Alfred-Wegener-Institut, Helmholtz-Zentrum für Polar- und Meeresforschung
Bremerhaven

Oxygen and Silicon Stable Isotopes of Diatom Silica: Reconstructing Changes in Surface Water Hydrography and Silicic Acid Utilization in the Late Pleistocene Subarctic Pacific

Dissertation zur Erlangung des akademischen Grades
eines Doktors der Naturwissenschaften

Dr. rer. nat.

am Fachbereich Geowissenschaften der
Universität Bremen

vorgelegt von
Edith Maier

Bremerhaven, März 2014

Gutachter:
Prof. Dr. Ralf Tiedemann
Prof. Dr. Gerhard Bohrmann

Eidesstattliche Erklärung

Hiermit versichere ich an Eides statt, die vorliegende Arbeit selbstständig und ohne Zuhilfenahme anderer als der hier angegebenen Quellen angefertigt zu haben. Alle Anführungen, die direkt oder indirekt übernommen wurden, sind als solche kenntlich gemacht.

Bremerhaven, 05.03.2014

Edith Maier

Abstract

Millennial-scale climate variability has been detected globally throughout late Pleistocene paleoenvironmental records, yet the trigger and response mechanisms remain under debate. It has been suggested that deglacial variations in upper ocean stratification in high latitudes and associated changes in thermohaline overturning circulation might have played a key role in changing atmospheric CO_2 concentrations ("polar stratification hypothesis"), but information to evaluate this relationship in the subarctic Pacific are scarce. Oceanic-atmospheric CO_2 exchange also strongly depends on the efficiency of the biological pump, which is closely coupled to the nutrient cycle. This thesis examines the relationship between past changes in subarctic Pacific upper ocean stratification and nutrient (silicic acid) utilization, using oxygen ($\delta^{18}O_{diat}$) and silicon ($\delta^{30}Si_{diat}$) stable isotopes of diatom silica, for the first time at millennial-scale resolution. In combination with new information on subsurface temperature/salinity, paleoproductivity and iceberg discharge from the Cordilleran Ice Sheet as well as additional information e.g. on sea ice distribution and sea surface temperatures, this thesis aims to improve the understanding of subarctic Pacific climate development from the last glacial to interglacial period (~50-6 ka BP). The $\delta^{18}O_{diat}$ and $\delta^{30}Si_{diat}$ measurements were performed using a new instrumentation set-up, which allows for the efficient combined silica $\delta^{18}O$ and $\delta^{30}Si$ analysis and requires a comparatively low amount of silica material (~1.5-2.0 mg).

The results of this thesis are presented in three manuscripts. Apart from introducing the new instrumentation set-up, the first manuscript investigates potential isotope effects on $\delta^{18}O_{diat}$ and $\delta^{30}Si_{diat}$ associated with (1) contamination with non-diatom silicates (e.g. clay minerals, radiolarians) and (2) species-related isotope effects (vital effects and environmental effects, e.g. related to seasonality). The results demonstrate the importance of high-purity diatom samples for isotope analysis and support previous findings indicating the absence of discernable species-related silicon isotope effects. Observed vital and/or environmental effects influencing diatom $\delta^{18}O_{diat}$ highlight the necessity to separate diatom samples according to species or species groups, assigned to the same environmental boundary conditions, to obtain reliable isotopic results.

The second manuscript concentrates on the relationship between upper ocean stratification, nutrient utilization and paleoproductivity from the last glacial to interglacial period (~25-6 ka BP). Consistent with the "polar stratification hypothesis", glacial data indicate stratified, fresh and highly utilized surface waters, as well as low productivity. The deglacial period (~17.5-11.7 ka BP) is characterized by a sequence of paleoceanographic events occurring in surface waters. These can be linked to changes in sea-ice and water mass formation in the subarctic Pacific realm as well as to changes in the strength of the Atlantic Meridional Overturning Circulation (AMOC), but do not mirror the deglacial pattern of the Heinrich Stadial (HS) 1 cooling (~17.5-14.6 ka BP) or Bølling/Allerød (B/A) warming (~14.6-12.8 ka BP), recorded in Greenland ice cores. An indicated increased availability of silicic acid during early HS1 is possibly associated with an increased formation of North Pacific Intermediate Water, characterized by a comparatively high silicic acid concentration. An alternative explanation might be an increased silicic acid supply to surface waters related to deep convective overturning. However, surface waters are still fresh and stratified during that time,

questioning conditions favorable for deep convection. At ~16 ka BP, prior to the onset of the B/A, it is suggested that upper ocean stratification weakens in response to a change to sea-ice-free conditions, which increases the supply of saline, silicic acid rich waters into the euphotic zone as well as productivity. With the onset of the Bølling, upwelling may have been further facilitated by the increased AMOC, which could explain the observed maximum in productivity as well as the saline and weakly utilized surface waters during the B/A. The increased upwelling and observed decoupling of silicic acid utilization and productivity during late HS1 and the B/A might indicate an decreased efficiency of the biological pump, suggesting that the subarctic Pacific may have been a source region of atmospheric CO_2 during late HS1 and the B/A.

The third manuscript focuses on the subarctic Pacific climate development during Marine Isotope Stage 3 (~50-29 ka BP). Proxy data provide evidence of millennial-scale variabilities in surface water stratification, which are associated with changes in upwelling intensity. These changes seem to be closely correlated to millennial-scale changes in AMOC intensity, indicating rapid teleconnections between the North Atlantic and the subarctic Pacific. Massive iceberg discharge coeval with the HS4 event of enhanced ice-rafted debris deposition in the North Atlantic – an analogy also observed during HS1 – suggests a close link between the developments of the Cordilleran Ice Sheet and the Laurentide Ice Sheet. Following HS4, proxy data point towards a strengthening of upper ocean stratification. Evidence of increased seasonal contrasts in sea surface temperatures, related to the strengthened upper ocean stratification, might indicate an increased moisture transport on the North American continent, possibly accelerating ice-sheet growth.

In conclusion, this study provides the first $\delta^{18}O_{diat}$ and $\delta^{30}Si_{diat}$ data at millennial-scale resolution from the subarctic Pacific, analyzed with a new and efficient instrumentation set-up. The isotopic data show a consistent picture of millennial-scale variabilities in upper ocean stratification and silicic acid utilization during the last ~50 ka BP and demonstrate the high potential of combined $\delta^{18}O_{diat}$ and $\delta^{30}Si_{diat}$ analysis especially for, but not restricted to, marine regions characterized by a low biogenic carbonate content like the subarctic Pacific and the Southern Ocean.

Zusammenfassung

Spätpleistozäne Paläoumweltrekonstruktionen zeichnen deutlich Klimavariabilitäten auf der Jahrtausendskala nach, jedoch sind die Ursachen- und Wirkungsmechanismen Gegenstand gegenwärtiger Diskussion. Es gibt Hinweise, dass deglaziale Änderungen in der Stratifizierung des Oberflächenwassers (OF) in hohen Breiten und damit assoziierte Änderungen in der thermohalinen Zirkulation eine Schlüsselrolle hinsichtlich Veränderungen atmosphärischer CO_2-Konzentrationen spielen („Polar-Stratifizierungs-Hypothese“). Neben der OF-Stratifizierung hängt der CO_2-Austauch zwischen Ozean und Atmosphäre unter anderem auch stark von der Effizienz der biologischen Pumpe ab, welche eng an den Nährstoffkreislauf gekoppelt ist. Diese Dissertation untersucht die Beziehung zwischen vergangenen Änderungen in der OF-Stratifizierung und der Nährstoffnutzung, genauer Kieselsäurenutzung, des subarktischen Pazifiks. Hierfür wurden stabile Sauerstoff- und Siliziumisotope aus Diatomeensilikat ($\delta^{18}O_{diat}$, $\delta^{30}Si_{diat}$) analysiert, erstmalig in einer Auflösung auf der Jahrtausendskala. Mit Hilfe der $\delta^{18}O_{diat}$- und $\delta^{30}Si_{diat}$-Daten, in Kombination mit neuen Informationen über oberflächennahe Wassertemperatur/-salinität, den Einfluss von Eisbergen und der Paläoproduktivität, sowie zusätzlichen Informationen hinsichtlich Meereisverbreitung und OF-Temperaturen, ist es das Ziel dieser Arbeit, zu einem besseren Verständnis der Klimaentwicklung des subarktischen Pazifiks vom letzten Glazial bis zum heutigen Interglazial (~50.000-6.000 Jahre) beizutragen. Die $\delta^{18}O_{diat}$- und $\delta^{30}Si_{diat}$-Messungen wurden mit Hilfe einer neuen Messapparatur durchgeführt, welche eine effiziente kombinierte $\delta^{18}O$- und $\delta^{30}Si$-Analyse ermöglicht, und zudem vergleichsweise wenig Silikatmaterial benötigt (~1,5-2,0 mg).

Die Ergebnisse dieser Dissertation sind in drei Manuskripten aufgeführt. Neben der Einführung der neuen Messapparatur untersucht das erste Manuskript potentielle Isotopeneffekte auf die $\delta^{18}O_{diat}$- und $\delta^{30}Si_{diat}$-Signale, welche (1) mit der Kontamination durch andere Silikate (z.B. Tonminerale, Radiolarien) und speziesabhängigen Isotopeneffekten (Vitaleffekte und Umwelteffekte, z.B. verbunden mit Saisonalität) einhergehen können. Die Ergebnisse zeigen die Wichtigkeit hochreiner Diatomeenproben für die Isotopenanalysen und unterstützen zudem frühere Ergebnisse, die keine erkennbaren speziesabhängigen Silizium-isotopeneffekte anzeigen. Das $\delta^{18}O_{diat}$-Signal hingegen zeigt Beeinflussung durch Vital- und/oder Umwelteffekte an. Es ist somit notwendig, Diatomeenproben hinsichtlich einzelner Arten oder Gattungen zu trennen, welche an die gleichen Umweltbedingungen gebunden sind, um verlässliche Isotopenergebnisse zu erhalten.

Das zweite Manuskript konzentriert sich auf die Beziehung zwischen OF-Stratifizierung, Nährstoffnutzung und Paläoproduktivität vom letzten Glazial ins Interglazial (~25.000-6.000 Jahre). In Übereinstimmung mit der „Polar-Stratifizierungs-Hypothese“ weisen die glazialen Daten auf eine Stratifizierung der Meeresoberfläche hin, gekennzeichnet durch salzarmes und stark nährstoffgenutztes Oberflächenwasser, sowie eine geringe Produktivität. Das Deglazial (~17.500-11.700 Jahre) ist charakterisiert durch eine Abfolge paläozeanographischer Ereignisse, welche sich mit Änderungen der Meereisbedeckung und der Wassermassen-produktion im subarktischen Pazifik sowie mit Änderungen in der Zirkulationsschleife im Nordatlantik (AMOC) in Verbindung bringen lassen. Sie spiegeln allerdings nicht das

deglaziale Muster der Heinrich Stadial (HS) 1- Abkühlung (~17.500-14.640 Jahre) oder der Bølling/Allerød (B/A)-Erwärmung (~14.640-12.850 Jahre) wider, überliefert aus grönländischen Eiskernen. Die Daten weisen auf ein erhöhtes Vorhandensein von Kieselsäure während des frühen HS1 hin, welche sich möglicherweise mit einer erhöhten Formationsrate von Nordpazifischem Zwischenwasser erklären lässt, welches eine vergleichsweise hohe Silikatkonzentration aufweist. Eine alternative Erklärung wäre ein erhöhter Kieselsäureeintrag in das Oberflächenwasser aufgrund einer erhöhten, tiefgreifenden Ozeanumwälzung. Das salzarme Oberflächenwasser zeigt jedoch an, dass die Voraussetzungen für eine derartige Umwälzung während dem frühen HS1 nicht gegeben sind. Die Daten zeigen außerdem, dass vor ~16.000 Jahren, bevor das B/A beginnt, die OF-Stratifizierung aufgrund eines Wechsels zu meereisfreien Bedingungen geschwächt wird, was zu einer Erhöhung sowohl des Eintrags von salz- und nährstoffreichem Wasser in die euphotische Zone, als auch der Produktivität führt. Das Produktivitätsmaximum und das salzreiche, gering genutzte Oberflächenwasser während des B/A lässt sich mit dem „Anspringen“ der AMOC zu Beginn des Bøllings erklären, welches den Auftrieb von tieferem Wasser verstärkt. Der hohe Auftrieb und die von der Kieselsäurenutzung entkoppelte Produktivität während des späten HS1 und des B/A könnten auf eine geringere Effektivität der biologischen Pumpe hinweisen und damit andeuten, dass der subarktische Pazifik eine Quellregion für atmosphärisches CO_2 während des späten HS1 und des B/A gewesen ist.

Das dritte Manuskript untersucht die Klimaentwicklung des subarktischen Pazifiks während des Marinen Isotopen Stadiums 3 (~50.000-29.000 Jahre). Die Daten liefern Hinweise auf Variabilitäten in der OF-Stratifizierung auf der Jahrtausendskala, welche mit Änderungen im Auftrieb von kaltem, salz- und nährstoffreichem, tieferem Wasser assoziiert sind. Diese Variabilitäten scheinen eng mit Änderungen der AMOC-Intensität korreliert zu sein, was auf schnelle Übertragungsmechanismen zwischen dem Nordatlantik und dem subarktischen Pazifik hinweist. Ein massiver Eintrag von Eisbergen in den Nordpazifik ist zeitgleich mit dem erhöhten Eintrag von Eisbergen in den Nordatlantik während HS4 – diese Übereinstimmung besteht auch während des HS1 – und deutet auf eine enge Verknüpfung der Entwicklungen des Kordilleren- und des Laurentischen Eisschilds hin. Nach dem HS4 zeigen die Daten eine Verstärkung der OF-Stratifizierung an. Hinweise auf erhöhte saisonale Kontraste in den Oberflächenwassertemperaturen, gekoppelt an die verstärkte Stratifizierung, könnten auf einen erhöhten Feuchtigkeitstransport auf den nordamerikanischen Kontinent hindeuten, der möglicherweise das Wachstum der nordamerikanischen Eisschilde gefördert hat.

Diese Arbeit zeigt die ersten $\delta^{18}O_{diat}$- und $\delta^{30}Si_{diat}$-Daten aus dem subarktischen Pazifik auf der Jahrtausendskala. Diese Daten wurden mit einer neuen und effizienten Messapparatur gemessen. Die Isotopendaten zeichnen ein konsistentes Bild der Variabilität von OF-Stratifizierung und Kieselsäurenutzung während der letzten ~50.000 Jahre und zeigen das hohe Potential einer kombinierten $\delta^{18}O_{diat}$- und $\delta^{30}Si_{diat}$-Analyse speziell für, aber nicht beschränkt auf, marine Gebiete, die sich durch einen geringen Anteil an biogenem Karbonat auszeichnen – wie z.B. der subarktische Pazifik und der Südozean.

Acknowledgments

First of all I want to thank my supervisor Prof. Ralf Tiedemann for giving me the opportunity to do my Ph.D. on this wonderful topic and for his support throughout my study. I am particularly grateful for the support and motivation of Andrea Abelmann and Rainer Gersonde throughout the last few years. Thanks for the constructive comments and reviews on all the abstracts, presentations and papers over the years. Thank you also for providing such excellent sample material. Unfortunately I was not yet at the AWI, when the Innovative NOrth Pacific EXperiment (INOPEX) cruise took place. I also want to thank Prof. Michael Sarnthein for providing additional sample material. A special thank you to Prof. Gerhard Bohrmann who nicely accepted to review my thesis.

This work would have taken much longer without the help of Ulrike Böttjer, Birgit Glückselig and Ruth Cordelair, who did most of the purification of the diatom samples. Thank you so much, it was worth all the effort. Working with the mass spectrometers would have been impossible without the help of Prof. emerit. Hans Friedrichsen, Bernhard Chapligin and Hanno Meyer, who I could always reach even when they were on holiday or baby break. Thanks to Ute Bock for introducing me into the world of energy dispersive spectrometry. Jian Ren and Oliver Esper are thanked for sharing knowledge on subarctic Pacific diatom species with me and for the diatom countings. Marianne Warnkross is gratefully acknowledged for picking foraminifera and Silke Steph for foraminiferal isotopic measurements.

During my Ph.D. I was part of the AWI graduate school POLMAR. Thanks to the coordinators Jelle Bijma, Claudia Hanfland and Claudia Sprengel for providing a platform to easily get in contact with fellow Ph.D. students from other departments and for the various expert and soft skill courses.

However, the last years have not been just about diatom isotopes – thankfully. I have been lucky to find some friends in Bremen and Bremerhaven. My special thanks go to Verena, who was always there as a friend and to Sarah, who was the best and funniest possible office mate. I never want another one.

I am deeply thankful to my beloved mother for always supporting me and for letting me go my own way. My deepest gratitude to Philipp for his patience and moral support during my Ph.D. years, especially the last one, and for his decision to move to Bremen – thank you for being my best friend!

Contents

Chapter 1 – Introduction

1.1 General introduction and outline

The Northern Hemisphere climate during the Late Pleistocene was characterized by millennial-scale climate variabilities, recorded across the entire Northern Hemisphere, including Greenland ice cores (Dansgaard et al., 1993; Svensson et al., 2008) as well as sediment records from the North Atlantic (e.g. Bond et al., 1993) and the North Pacific (Kotilainen and Shackleton, 1995; Kiefer et al., 2001; Hendy et al., 2002; Riethdorf et al., 2013b; Fig. 1.1). Millennial-scale oscillations between cold and warm phases in the Northern Hemisphere over the deglaciation from the last glacial to the modern interglacial period (~17.5-11.7 ka BP), but also during Marine Isotope Stage (MIS) 3 (~57-29 ka BP), have been related to changes in the strength of the Atlantic Meridional Overturning Circulation (AMOC) (Max et al., 2012; Menviel et al., 2014), which exerts a strong control on the distribution of water masses and the storage of nutrients and CO_2 (Kuhlbrodt et al., 2007; Fig. 1.2). Despite the similar pattern of North Atlantic and North Pacific climate variabilities, the temporal relationship between millennial-scale changes in both regions, as well as the transmission mechanisms, are still not well known. Reasons for this include the limitations of age model constraints, but also the relative scarcity of paleoceanographic studies from the subarctic Pacific. An important aspect for the poor paleoceanographical knowledge of the glacial-to-interglacial development of the subarctic Pacific relative to the North Atlantic is the general great water depth of the North Pacific. The lack of carbonate in most North Pacific sediments, related to the corrosive North Pacific deep waters, limit the application of well-established proxies from carbonaceous fossils, e.g. foraminiferal stable isotope geochemistry.

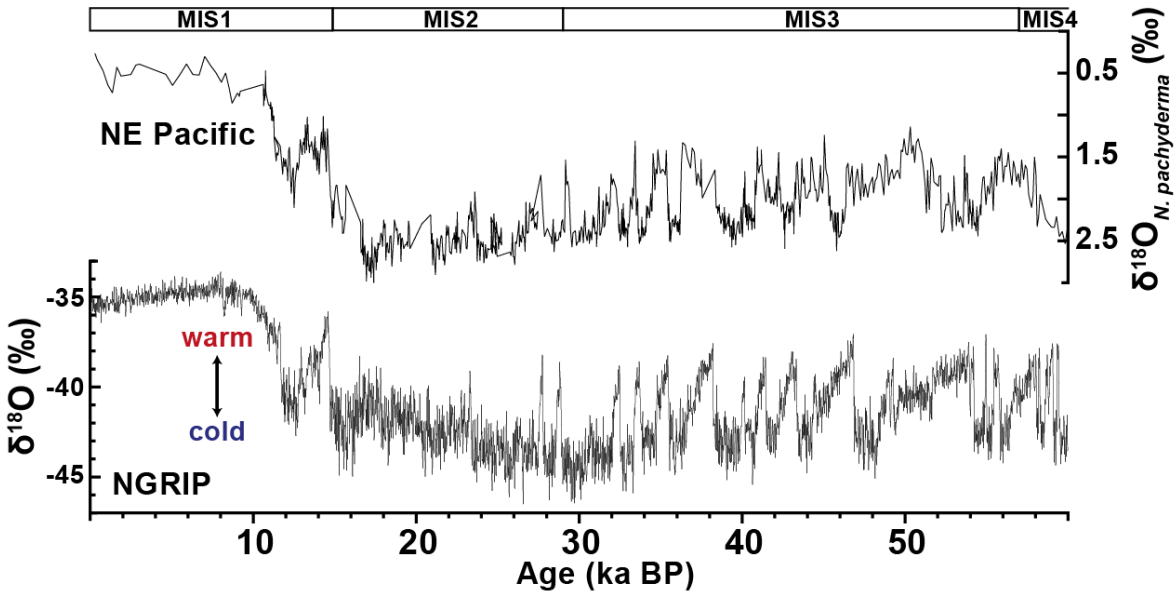

Figure 1.1. Planktic foraminiferal (*Neogloboquadrina pachyderma*$_{sin}$) oxygen isotope record from the North-East (NE) Pacific Core ODP893 (Hendy et al., 2007) and oxygen isotope record from the North Greenland Ice Core Project (NGRIP) ice core (GICC05 timescale) (Andersen et al., 2006; Svensson et al., 2006, 2008).

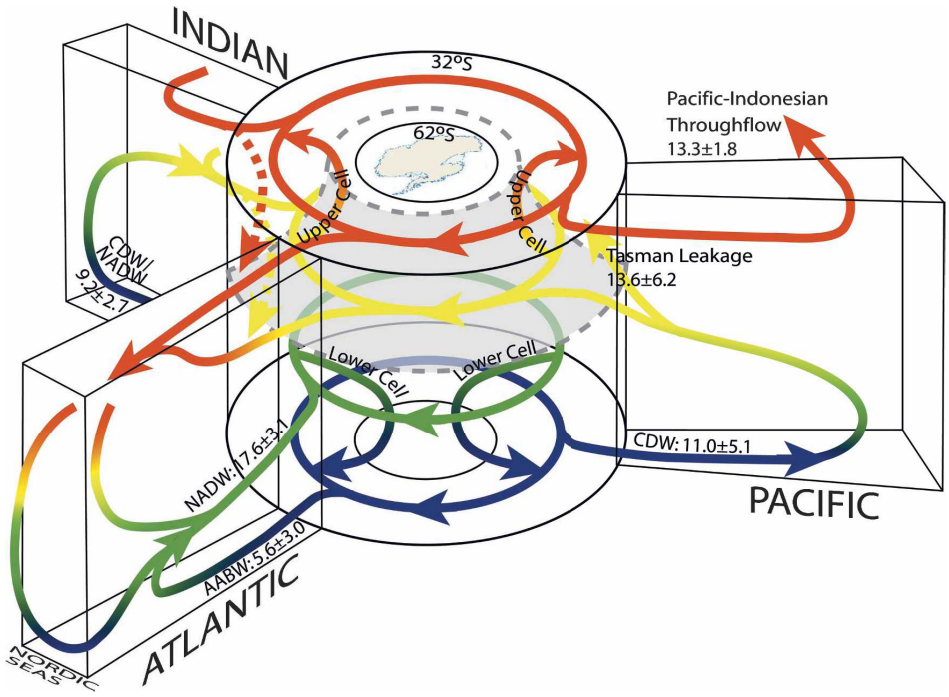

Figure 1.2. Schematic of modern global ocean meridional overturning circulation. Colors indicate different density ranges and roughly correspond to upper (red), intermediate (yellow), deep (green) and bottom (blue) waters. NADW: North Atlantic Deep Water; AABW: Antarctic Bottom Water; CDW: Circumpolar Deep Water. The grey dashed line divides the upper and the lower global overturning cells in the Southern Ocean. Numbers indicate water transport in Sverdrup (figure taken from Lumpkin and Speer, 2007).

It was a central purpose of the Innovative NOrth Pacific EXperiment (SO202-INOPEX; 04/2009-08/2011) project to decipher the role of the subarctic Pacific realm in global climate development and glacial-to-interglacial forcing, using a multi-proxy approach as well as new and innovative methodologies. In this thesis, which was embedded in the SO202-INOPEX project, fairly new proxies, oxygen and silicon stable isotopes of diatom silica ($\delta^{18}O_{diat}$, $\delta^{30}Si_{diat}$), are used to reconstruct changes in subarctic Pacific surface water hydrography and nutrient utilization during the last 50 ka BP. Diatom are ideal candidates to reconstruct surface water conditions since they are photosynthetic algae, which are constrained to the euphotic zone during their lifetime. Considering the rather low content of biogenic silica in subarctic Pacific sediments (e.g. Gebhardt et al., 2008; Kohfeld and Chase, 2011), it was crucial to use a method for $\delta^{18}O_{diat}$ and $\delta^{30}Si_{diat}$ analysis, which requires comparatively small amounts of diatom silica. Therefore a (partly) new instrumentation set-up allowing for the combined $\delta^{18}O_{diat}$ and $\delta^{30}Si_{diat}$ analysis, where both proxies are measured on the same sample aliquot, was developed in the first place.

The following sub-chapters of this introduction provide a general introduction to the oceanography and nutrient cycling of the present-day subarctic Pacific (*Section 1.2.1*), give an overview on the state of subarctic Pacific paleoceanographic research related to this thesis (*Section 1.2.2*), introduce $\delta^{18}O_{diat}$ and $\delta^{30}Si_{diat}$ as paleoceanographic proxies (*Section 1.3*), formulate the aims of this thesis (*Section 1.4*) and state the author´s contribution to the manuscripts (*Section 1.5*). *Chapter 2* introduces the used study material as well as the applied methods, including a brief overview of the diatom sample preparation and the new instrumentation set-up. *Chapter 3* shortly describes the age model construction applied to the studied sediment cores. *Chapters 4, 5* and *6* contain the manuscripts which are either published or in preparation and include the main results of this thesis. *Chapter 4* introduces the new instrumentation set-up in detail, which was used to measure the subarctic Pacific $\delta^{18}O_{diat}$ and $\delta^{30}Si_{diat}$ records. Based on these data *Chapters 4, 5 and 6* address the main paleoceanographic research questions of this thesis. Following the manuscripts, *Chapter 7* concludes this thesis and provides perspectives for future work.

1.2 The subarctic Pacific

1.2.1 Present-day oceanography and nutrient cycling

The present-day surface circulation in the subarctic Pacific is dominated by the cyclonic motion of the Subarctic Gyre, which contains two smaller, distinct cyclonic circulation systems: the Western Subarctic Gyre in the West and the Alaskan Gyre in the East (Fig. 1.3A). To the south the Subarctic Gyre is bound by the eastward flowing Subarctic Current, which brings relatively warm waters into the North-East (NE) Pacific. The Alaskan Stream (AS), which binds the Subarctic Gyre to the north, transports waters back into the North-West (NW) Pacific along the Aleutian Islands. Several passages between the Aleutian Islands allow for Alaskan Stream waters to enter the Bering Sea, where surface waters follow a cyclonic motion before they are mainly transported back into the subarctic Pacific via the East Kamchatka Current (EKC). Subsurface circulation strongly follows surface water circulation, but a subsurface undercurrent transports waters from the eastern tropical North Pacific northwards into the subarctic Pacific (Dodimead et al., 1963).

A dominant feature of the subarctic Pacific is the steep salinity-driven stratification (halocline), which limits the input of cold, salty and nutrient-rich deeper waters into the surface water layer and allows for the development of a seasonal thermocline and for large seasonal contrasts in sea surface temperatures (SST). The low salinity surface waters (Fig. 1.3B) are sustained by a large freshwater flux and relatively small regional evaporation (Warren, 1983; Emile-Geay et al., 2003). Due to the riverine influx of freshwater from the North American Cordillera the subarctic NE Pacific surface waters are slightly fresher relative

to NW Pacific surface waters. The halocline prevents the formation of deep waters in the subarctic Pacific realm. Intermediate water formation is restricted to the marginal Sea of Okhotsk (SoO) (Fig. 1.3A), from where intermediate waters are transported into the North Pacific (Talley, 1993).

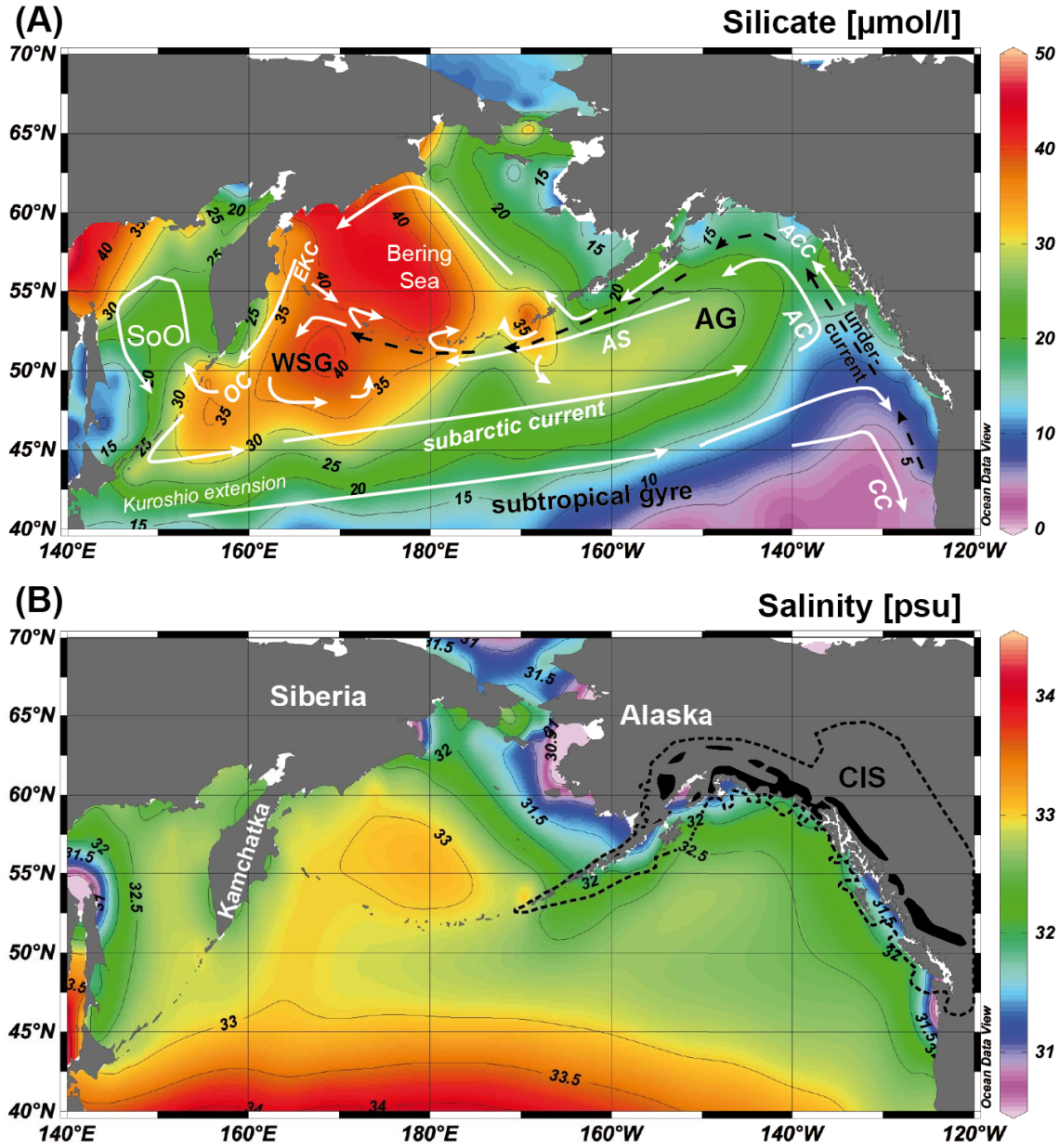

Figure 1.3. (A) Mean silicic acid concentration of subarctic Pacific surface waters (Garcia et al., 2010) as well as (sub-)surface water currents (after Dodimead et al., 1963; Stabeno et al., 2004): AC Alaska Current; ACC: Alaska Coastal Current; AS Alaskan Stream; EKC: East Kamchatka Current; OC: Oyashio Current; CC: California Current; SoO: Sea of Okhotsk; WSG: Western Subarctic Gyre ; AG: Alaskan Gyre. The dashed black line marks the subsurface undercurrent. **(B)** Mean annual sea surface salinity of the subarctic Pacific (Locarnini et al., 2010) and distribution of modern glaciers in the North American Cordillera (black areas) as well as the maximum extent of the Cordilleran Ice Sheet (CIS) during the last glacial (black dashed contour; after Clague and James, 2002; Kaufman et al., 2011). The maps were created with Ocean Data View (www.odv.awi.de).

Furthermore, the halocline strongly influences nutrient cycling in the subarctic Pacific. The limited exchange with deeper waters results in strong vertical macronutrient (silicic acid, nitrate) gradients, which largely coincide with the halocline (Andreev et al., 2002). Nutrients are brought into the euphotic zone mainly by autumn/winter mixing. In response to the thermocline development, in combination with increasing light availability, diatom-dominated phytoplankton blooms develop during spring and nutrients are progressively consumed over the course of spring and summer (Harrison et al., 1999). With the breakdown of the thermal stratification during autumn, new nutrients are transported into the euphotic zone, resulting in a second bloom. Water column profiles from the NW Pacific show low concentrations of silicic acid in the surface waters, related to the uptake of silicic acid by silicifying organisms, mainly diatoms, during biomineralisation (Reynolds et al., 2006). In the depth range between 100-1200 m the dissolution of sinking biogenic silica leads to an increase in silicic acid concentrations (Reynolds et al., 2006). Deeper waters are characterized by the mixing of two water masses with high silicic acid concentrations: North Pacific Deep Water and Antarctic Bottom Water (Reynolds et al., 2006).

Due to the incomplete consumption of the macronutrients (silicic acid, nitrate) in surface waters over the course of the year, the modern open subarctic Pacific is a high nutrient, low chlorophyll (HNLC) area, particularly pronounced in the NW Pacific (Fig. 1.3A). Iron-deficiency may be a major reason for modern incomplete nutrient utilization (Tsuda et al., 2003; Boyd et al., 2004). Most iron is brought to the euphotic zone by lateral and vertical mixing (Johnson et al., 2005; Measures et al., 2005), but dust, mainly originating from Asian deserts (Duce and Tindale, 1991), is another important iron source to the open subarctic Pacific (Mahowald et al., 2006). Despite the HNLC surface waters, biological activity and carbon export efficiency is high in the modern subarctic Pacific, making it a net sink of atmospheric CO_2 (Honda, 2003; Ayers and Lozier, 2012).

1.2.2 State of subarctic Pacific paleoceanograpic research related to this thesis

It is a burning issue in current paleoclimate research to improve the understanding of the mechanisms driving earth´s climate variabilities, including changes in atmospheric CO_2 concentrations, on glacial-to-interglacial as well as millennial time scales, to better estimate future climate and environmental development (Jansen et al., 2007). Deglacial variations in high latitude upper ocean stratification and associated changes in thermohaline overturning circulation are thought to have contributed to changes in past atmospheric pCO_2 ("polar stratification hypothesis") (Jaccard et al., 2005; Sigman et al., 2010), documented in Antarctic ice cores (e.g. Lüthi et al., 2008; Parennin et al., 2013). Destratification in the Southern Ocean is suggested to have been a significant contributing mechanism (amongst others) to the last deglacial rise in atmospheric pCO_2 (Skinner et al., 2010; Burke and Robinson, 2012).

However, recent studies also indicate last deglacial destratification in the subarctic Pacific, potentially resulting in the release of CO_2 to the atmosphere (Galbraith et al., 2007; Gebhardt et al., 2008). Whether destratification and the associated upwelling of deep, nutrient- and CO_2-rich water led to oceanic CO_2 release from subarctic Pacific surface waters strongly depends on the efficiency of the biological pump, which removes CO_2 from the atmosphere by biological productivity in the photic zone and transfers it to the deep ocean interior. The biological pump is closely coupled to subarctic Pacific nutrient dynamics, including (1) the input of micronutrients, particularly iron (Tsuda et al., 2003), and (2) the input and utilization of macronutrients like silicic acid and nitrate (Haug et al., 1999; Boyd et al., 2004; Galbraith et al., 2008). Recent studies found a close link between nutrient (nitrate) utilization, export production and upper ocean stratification on glacial-to-interglacial timescales (Galbraith et al., 2008; Brunelle et al., 2010), strengthening the "polar stratification hypothesis". However, this relationship is less clear on millennial time scales, e.g. during the last deglaciation. In contrast to studies arguing for enhanced vertical mixing during that time (Galbraith et al., 2007; Gebhardt et al., 2008), it has recently been assumed that the co-occurrence of high productivity and nutrient utilization during the Bølling/Allerød (B/A; ~14.6-12.8 ka BP) might have been related to a transient stratification event (Lam et al., 2013).

Another important modern paleoceanographic research question addresses possible changes in water mass formation in the subarctic Pacific during the last deglaciation, related to a variable strength of the halocline. Water mass formation in the modern subarctic Pacific realm is restricted to the formation of North Pacific Intermediate Water (NPIW) originating in the marginal Sea of Okhotsk (Talley, 1993). In contrast, studies with general circulation models suggested that during Heinrich Stadial 1 (HS1; ~17.5-14.6 ka BP) a weakening of the halocline, related to significant reduction in the strength of the AMOC, resulted in the formation of deep-water in the subarctic Pacific, maintained by an enhanced poleward transport of salt from the subtropics (Okazaki et al., 2010; Menviel et al., 2012). However, whether deep-water formation occurred in the North Pacific or not is still controversial. Recent sediment core studies found evidence of increased ventilation only in the mid-depth North Pacific during HS1, which was attributed to an increased formation rate of NPIW (Jaccard and Galbraith, 2013; Max et al., 2013).

While a large amount of studies have been dealing with the instabilities of ice sheets close to the North Atlantic region of modern deep-water formation (e.g. MacAyeal, 1993; Van Krefeld et al., 2000; Dyke, 2004), information on instabilities of the Cordilleran Ice Sheet (CIS), their temporal relationship to other Northern Hemisphere ice-sheet instabilities and on the mechanism of CIS iceberg discharge are scarce. The CIS is thought to have had a marine basis during the last glacial (Fig. 1.3B; Kaufman et al., 2011) and parts of MIS3 (Hendy and Cosma, 2008). The extent of the last glacial CIS relative to today indicates that a large amount

of freshwater must have entered the North Pacific, which, however, is yet largely undetected in the open subarctic Pacific.

Since similar patterns of millennial-scale climate variabilities have been detected in sediments from the subarctic Pacific (Kotilainen and Shackleton, 1995; Kiefer et al., 2001; Riethdorf et al., 2013b) and the North Atlantic (Bond et al., 1993; Maslin et al., 1995) as well as within the Greenland ice cores (Andersen et al., 2006; Svensson et al., 2008), the paleoclimate community has tried to decipher responsible trigger mechanisms of, and response mechanisms to, millennial-scale climate variability. Some sediment core studies (Kiefer et al., 2001; Kiefer and Kienast, 2005), as well as modeling studies (Saenko et al., 2004; Okazaki et al., 2010), argue for an out-of-phase relationship between the North Atlantic and the North Pacific climate development, ultimately related to oceanic readjustments in response to changes in the AMOC. Other studies suggest an in-phase behavior between both oceanic regions (Mikolajewicz et al., 1997; Galbraith et al., 2007; Okumura et al., 2009; Max et al., 2012), primarily associated with atmospheric teleconnections. Regional changes in sea-ice extent played an important role in shaping the Southern Ocean deglacial climate (WAIS Divide Project members, 2013), giving rise to the hypothesis that changes in sea-ice, which was also present in the last glacial and early deglacial subarctic Pacific (De Vernal and Pederson, 1997; Méheust et al., in prep.), might have also influenced subarctic Pacific climate on a regional scale.

1.3 Diatom $\delta^{18}O_{diat}$ and $\delta^{30}Si_{diat}$ as proxies for paleoceanographic changes

Paleoceanographic reconstructions in sediments with a low or absent content of biogenic carbonate but a comparatively elevated amount of biogenic opal, like the subarctic Pacific, require a specific set of proxies. Within this study $\delta^{18}O_{diat}$ and $\delta^{30}Si_{diat}$ are used to reconstruct past changes in surface water hydrography and nutrient (silicic acid) utilization and improve the understanding of the subarctic Pacific paleoceanographic topics mentioned above (*Section 1.2.2*).

Diatoms are photosynthetic algae with a siliceous frustule consisting of amorphous silica ($SiO_2 * nH_2O$), which is composed of inner silica tetrahedrons and a hydrous outer layer (Fig. 1.4). They dominate the modern marine silica cycle and are believed to account for more than 50% of primary production and opal export in coastal environments and nutrient rich open ocean regions (Nelson et al., 1995; Tréguer and De la Rocha, 2013). As diatoms are constrained to the euphotic zone during their lifetime, proxy data obtained from diatoms provide information on the surface water layer. It has been successfully demonstrated that $\delta^{30}Si_{diat}$ can be used to trace past changes in silicic acid utilization (De la Rocha et al., 1998;

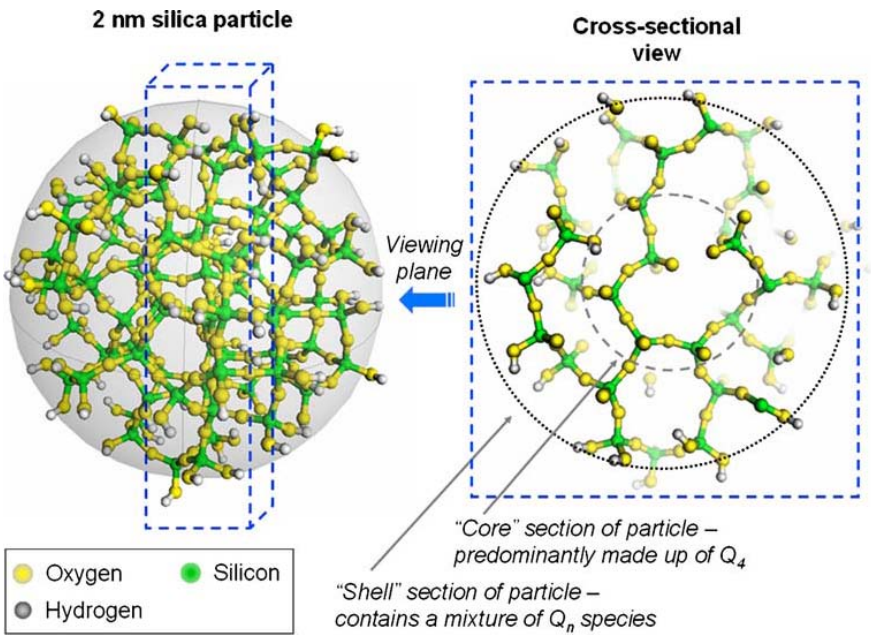

Figure 1.4. General structure of biogenic silica (figure taken from Leng et al. (2009).

Brzezinski et al., 2002; Reynolds et al., 2008; Egan et al., 2013). The silicon isotope signal preserved in diatom silica is mainly a function of (1) the supply rate and the concentration of silicic acid transported to the surface waters as well as the (2) net use of the available silicic acid. Diatoms utilize silicic acid during biomineralization, where they preferentially incorporate the lighter isotope (^{28}Si) into their frustules. Silicon isotope fractionation is mass-dependent with a fractionation factor of ca. -1.1 ± 0.4‰ (De la Rocha et al., 1997; Milligan et al., 2004) for a closed (Rayleigh-type) system like the modern subarctic Pacific (Fig. 1.5; Reynolds et al., 2006), which is characterized by seasonal stratification. The $\delta^{18}O_{diat}$, similar as the $\delta^{18}O$ of foraminifera, is mainly influenced by changes in global ice volume, temperature and the $\delta^{18}O$ of ambient seawater. There is a direct relationship between ambient water temperature and diatom oxygen isotopes, with a coefficient of ca. -0.2‰/°C (Crespin et al., 2010; Dodd and Sharp, 2010), indicating that $\delta^{18}O_{diat}$ may be used as a paleothermometer. The $\delta^{18}O_{diat}$ analysis has been successfully applied in the marine realm, e.g. by reconstructing changes in surface water temperature (Shemesh et al., 1992) and sea surface salinity in the North Pacific realm (Sancetta et al., 1985; Swann et al., 2006) as well as in the Southern Ocean (Shemesh et al., 1994; Pike et al., 2013; Swann et al., 2013). To date, $\delta^{18}O_{diat}$ represents the only proxy tracing back physical properties like salinity at the polar ocean surface, since oxygen isotope measurements of the most prominent calcareous planktic foraminifera in polar sediments, *Neogloboquadrina pachyderma* sinistral (*N. pachyderma*$_{sin}$), mirror subsurface rather than surface water conditions (Bauch et al., 2002, see also Riethdorf et al., 2013a).

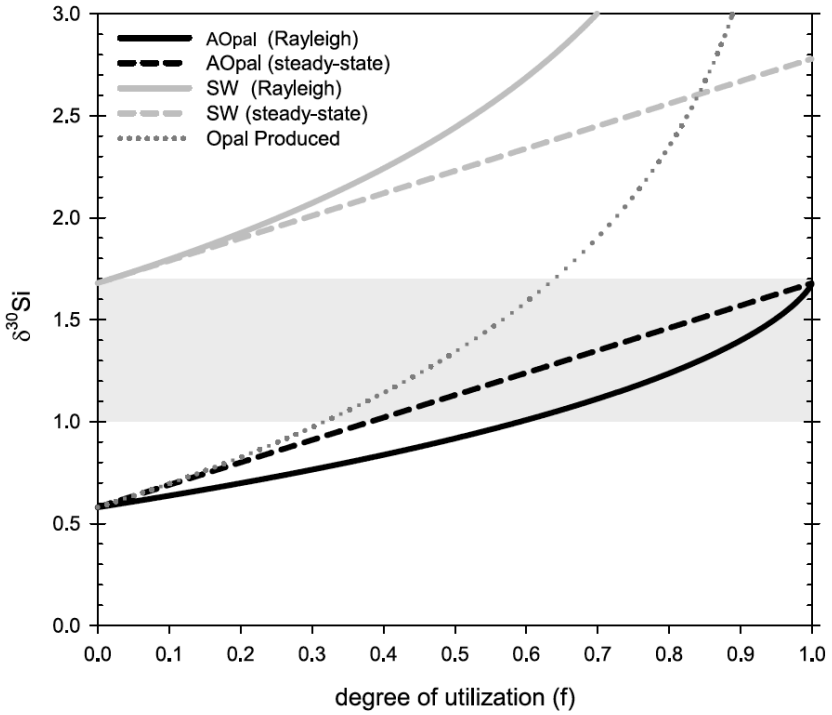

Figure 1.5. Theoretical changes in $\delta^{30}Si$ of seawater (grey lines) and accumulated biogenic opal (black lines) as a function of the fraction of silicic acid removed from seawater with an initial $\delta^{30}Si$ of seawater of +1.7‰. Opal precipitation generally follows either a Rayleigh-type fractionation model (solid lines) or a steady state system (dashed lines) behavior, with a fractionation factor of -1.1‰. The dotted line indicates the instantaneous composition of the diatoms growing under a Rayleigh-type fractionation model (figure taken from Reynolds et al., 2008).

Generally, $\delta^{18}O_{diat}$ and $\delta^{30}Si_{diat}$ measurements are performed on multi-species samples, where species-related isotope effects might affect the $\delta^{18}O_{diat}$ and $\delta^{30}Si_{diat}$, similar to biogenic carbonates (Wefer and Berger, 1991). Such isotope effects include vital effects as well as environmental effects, which are related to potential differences in depth habitat and life strategies of distinct diatom species or species groups (e.g. seasonally different blooming periods). It is commonly believed that $\delta^{30}Si_{diat}$ is not affected by inter-species fractionation effects (De la Rocha et al., 1997). In contrast, culture (Brandriss et al., 1998; Schmidt et al., 2001), sediment trap (Moschen et al., 2005) and marine sediment core (Shemesh et al., 1995; Swann et al., 2007, 2008) studies provide contradicting results regarding species-related oxygen isotope effects. Non-controversial, however, is the high importance of studying pure diatom samples, since contamination of the diatom samples with non-diatom silicates, i.e. non-biogenic silicates (e.g. clay minerals) and/or non-diatom biogenic silicates (e.g. radiolarians) might bias the diatom isotopic values (Brewer et al., 2008; Chapligin et al., 2012; Egan et al., 2012).

1.4 Aims of this thesis

Using a new instrumentation set-up allowing for the combined (biogenic) silica $\delta^{18}O_{diat}$ and $\delta^{30}Si_{diat}$ analysis (*Chapter 4*), this thesis provides for the first time $\delta^{30}Si_{diat}$ data from the last glacial to interglacial period (~50-6 ka BP) as well as $\delta^{18}O_{diat}$ and $\delta^{30}Si_{diat}$ records at millennial-scale resolution from the subarctic Pacific (*Chapters 4, 5, 6*). This data are used to improve the current understanding of millennial-scale variability in the subarctic Pacific. Since the most recent studies of Swann et al. (2007, 2008) suggest vital effects influencing the subarctic Pacific $\delta^{18}O_{diat}$, this thesis also contains a case study from NW Pacific sediments to further evaluate the potential influence of species-related isotope effects on $\delta^{18}O_{diat}$ and $\delta^{30}Si_{diat}$ (*Chapter 4*). Using the obtained $\delta^{18}O_{diat}$ and $\delta^{30}Si_{diat}$ data, in combination with new subsurface *N. pachyderma*$_{sin}$ $\delta^{18}O$ and $\delta^{13}C$ data, biogenic opal data, core logging data and ice-rafted debris (IRD) data, as well as previously published nitrogen isotope data (Galbraith et al., 2008; Studer et al., 2013), diatom counting data (Ren et al., in prep.), alkenone-based sea surface temperature (SST) and sea-ice data (Méheust, 2014; Méheust et al., in prep.), this thesis aims to answer the following questions (Q):

Question 1: ***How sensitive are the $\delta^{18}O_{diat}$ and $\delta^{30}Si_{diat}$ signals to isotopic effects related to (1) a potential sample contamination (e.g. clay minerals, radiolarians) and/or (2) the diatom species composition (vital and environmental effects)?***

(see *Chapter 4*)

Question 2: ***What is the meltwater history of the Cordilleran Ice Sheet (CIS) during the last 50 ka and how is it related to the meltwater history of the Laurentide Ice Sheet (LIS)?***

(see *Chapters 5, 6*)

Question 3: ***Do the $\delta^{18}O_{diat}$ and $\delta^{30}Si_{diat}$ signals support the hypothesis of deep-water formation in the subarctic Pacific during HS1?***

(see *Chapter 5*)

Question 4: ***What is the timing of paleoceanographic changes of surface water properties (e.g. salinity, silicic acid utilization) in the subarctic Pacific relative to climate changes in the North Atlantic realm during the last deglaciation and what are possible trigger mechanisms?***

(see *Chapter 5*)

Question 5: ***What was the subarctic Pacific´s role during the last deglacial rise in pCO_2?***

(see *Chapter 5*)

Question 6: ***What happens in the subarctic Pacific in response to changes in the Atlantic Meridional Overturning Circulation during MIS3?***

(see *Chapter 6*)

Question 7: ***How did the strength in the halocline vary over MIS3 and what are the implications for North American ice-sheet growth?***

(see *Chapter 6*)

1.5 Author´s contribution

Manuscript 1 (*Chapter 4*):

I developed analytical test series (memory test, initial silica sample weight) and performed the $\delta^{18}O_{diat}$ and $\delta^{30}Si_{diat}$ measurements for the down-core records. I wrote the entire manuscript. The co-authors Hans Friedrichsen and Bernhard Chapligin, supported by Hanno Meyer, did most of the technical implementation of the new instrumentation set-up. Hans Friedrichsen adjusted the MAT 252 Isotope Ratio Mass Spectrometer (IRMS) for silicon isotope analyses. Oliver Esper and Jian Ren did the diatom counting for the estimation of diatom species contributions. All co-authors reviewed and discussed the drafts of the manuscript.

Manuscript 2 and 3 (*Chapters 5 and 6*):

I performed the $\delta^{18}O_{diat}$ and $\delta^{30}Si_{diat}$ analyses and the contamination assessment of diatom samples. Jian Ren did the diatom counting for the estimation of diatom species contributions, Marie Méheust provided alkenone-based SST and information on sea-ice and Bernhard Chapligin supported the $\delta^{18}O_{diat}$ analyses. I wrote the entire manuscript. Andrea Abelmann, Rainer Gersonde and Ralf Tiedemann contributed to the interpretation of the data.

Chapter 2 – Material and methods

2.1 Study material

This study uses two different kinds of study material (Table 2.1). To test the new instrumentation set-up (*Chapter 4*) several silica standards were used (Table 2.1A). To address the research questions of this thesis (*Section 1.4*) two sediment cores from the subarctic NE and NW Pacific were studied (Fig. 2.1). The kasten Core SO202-27-6 was recovered from the subarctic NE Pacific (Patton Seamounts) during the SO202-INOPEX cruise 2009 (Gersonde and SO202-INOPEX Participants, 2010). The complete core was studied, allowing for paleoclimatic investigations from the MIS3 to the mid-Holocene (Table 2.1B; *Chapter 3*). Furthermore, the upper 1.06 m of NW Pacific piston Core MD01-2416 (Detroit Seamount), recovered during the WEPAMA cruise 2001 (Bassinot et al., 2002), was investigated. This section represents a time period from the B/A to the mid-Holocene (*Chapter 3*).

Table 2.1. Study material used in this thesis. **(A)** Standard materials used including the supplying institutes: IAEA: International Atomic Energy Agency, Austria; AWI: Alfred Wegener Institute Helmholtz Centre for Polar and Marine Research, Germany; NERC: National Environmental Research Council, Great Britain; UCSB: University of California in Santa Barbara, USA. **(B)** Studied sediment cores including studied time period (see *Chapter 3*).

(A)

standard	type	Supplier	Reference ($\delta^{30}Si$)
NBS-28	reference quartz standard	IAEA	Gröning (2007)
PS1772-8_{bsis}	marine diatom standard	AWI	this study
BFC	lacustrine diatom standard	NERC	Leng and Sloane (2008)
Diatomite	natural diatom standard	UCSB	Reynolds et al. (2007)
Big Batch	highly fractionated silica	UCSB	Reynolds et al. (2007)

(B)

Core	Latitude	Longitude	Water depth	Core recovery	Studied core section	Studied time period	Core type
SO202-27-6	54.296°N	149.597°W	2919 m	2.89 m	0 - 2.89 m	~50 - 7 ka BP	kasten core
MD01-2416	51.268°N	167.725°E	2317 m	44.75 m	0 - 1.06 m	~14 - 6 ka BP	piston core

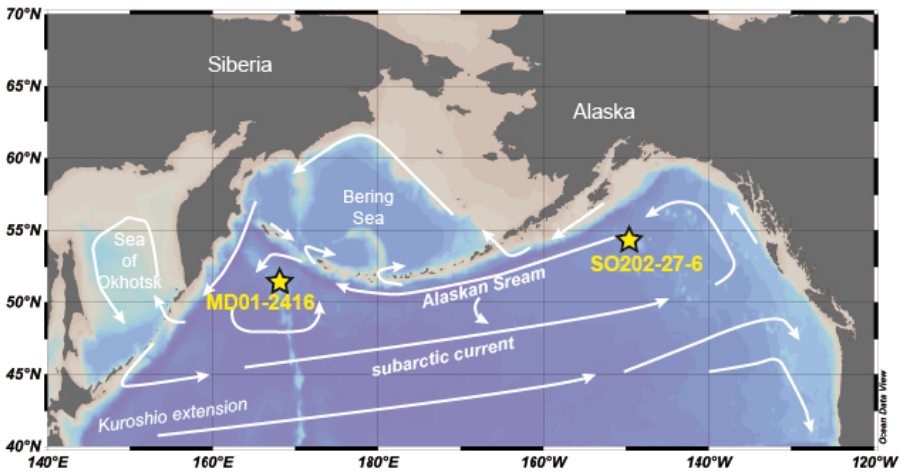

Figure. 2.1. Locations of studied sediment cores and surface water circulation (after Dodimead et al., 1963).

2.2 Methods

2.2.1 $\delta^{18}O_{diat}$ and $\delta^{30}Si_{diat}$

2.2.1.1 Purification of diatom material and diatom sample composition

Bulk sediment samples from kasten Core SO202-27-6 (2-cm slices) and piston Core MD01-2416 (2-cm and 4-cm slices) were prepared for diatom isotope analysis using a combination of physical and chemical treatments. A detailed overview on the preparation process, as well as the estimation of diatom sample composition, is given in *Sections 4.2.2 and 5.3.1*.

Briefly, bulk samples were first liberated from carbonates and organic matter using HCl and H_2O_2, before they were sieved into different fractions. Following a first heavy liquid separation, where most of the lithic fragments were removed, a fraction was chosen to be prepared further for isotope analysis using various sieving steps, sonication and treatments with heavy liquids. A central criterion for the choice of this fraction was a high content of diatom silica relative to other biogenic silicates (radiolarians, sponge spicules). To estimate (1) the diatom species composition of the final purified diatom samples and (2) the contamination with non-diatom biogenic silicates (radiolarians, sponge spicules), microscopic slides and scanning electron microscope (SEM) samples were prepared. Contributions of individual diatom species and non-diatom biogenic silicates were estimated following a quantification approach described in *Sections 4.2.2 and 5.3.1*. Purified diatom samples were checked for contamination with non-biogenic silicates (rock fragments, minerals) via determination of elemental compositions using energy dispersive spectrometry (EDS) and inductively coupled plasma optical emission spectrometry (ICP-OES) (Chapligin et al., 2012; *Sections 4.2.2, 5.3.1*). Al_2O_3 was used as a tracer for contamination of non-biogenic silicates (Brewer et al., 2008; Chapligin et al., 2012) following the quantification approach described in *Sections 4.2.2 and 5.3.1*. To decipher the influence of non-biogenic silicates on the measured $\delta^{18}O_{diat}$ and $\delta^{30}Si_{diat}$ records of Core SO202-27-6, mass balance corrections based on Brewer at al. (2008) were applied, thereby removing the potential isotopic effects of the non-biogenic contamination.

2.2.1.2 Silica $\delta^{18}O$ and $\delta^{30}Si$ measurements

All (diatom) silica $\delta^{18}O$ values presented in this thesis were measured at the Alfred Wegener Institute Helmholtz Centre for Polar and Marine Research (AWI, Potsdam) according to Chapligin et al. (2010). Within the framework of this thesis I participated in the development of an instrumentation, which allows for the additional measurement of $\delta^{29}Si$ and $\delta^{30}Si$ from the same sample aliquot, i.e. the combined (biogenic) silica $\delta^{18}O$ and $\delta^{30}Si$ analysis. In close cooperation with Hans Friedrichsen (MS Analysentechnik; Free University, Berlin), Bernhard Chapligin and Hanno Meyer (both AWI, Potsdam), a SiF_4 separation line was attached to the

high-performance laser fluorination line for (biogenic) silica $\delta^{18}O$ analysis presented by Chapligin et al. (2010) (Fig. 2.2). *Chapter 4* contains a detailed description of the new SiF_4 separation line (Fig. S4.1), which allows for the separation of the SiF_4 gas produced during laser fluorination. The SiF_4 was analyzed for $\delta^{29}Si$ and $\delta^{30}Si$ using a modified MAT 252 IRMS situated at the new opal isotope laboratory of the AWI (Bremerhaven). Furthermore, *Chapter 4* presents analytical tests documenting the purity of the SiF_4 gas (Fig. S4.2) and the precision, accuracy (Table 4.1) and required silica sample weight of the combined instrumentation set-up (Fig. S4.3).

For the combined measurement 1.5-2.0 mg of pure (diatom) silica was used (except for the analytical test to determine the minimum required sample weight (Fig. S4.3)). Values are reported in the common δ-notation vs. V-SMOW (Vienna Standard Mean Ocean Water) for oxygen isotopes and vs. NBS-28 for silicon isotopes. Analytical precision was better than 0.25‰ for $\delta^{18}O_{diat}$ (Chapligin et al., 2011) and better than 0.12‰ for $\delta^{30}Si_{diat}$ measurements (Table 4.1).

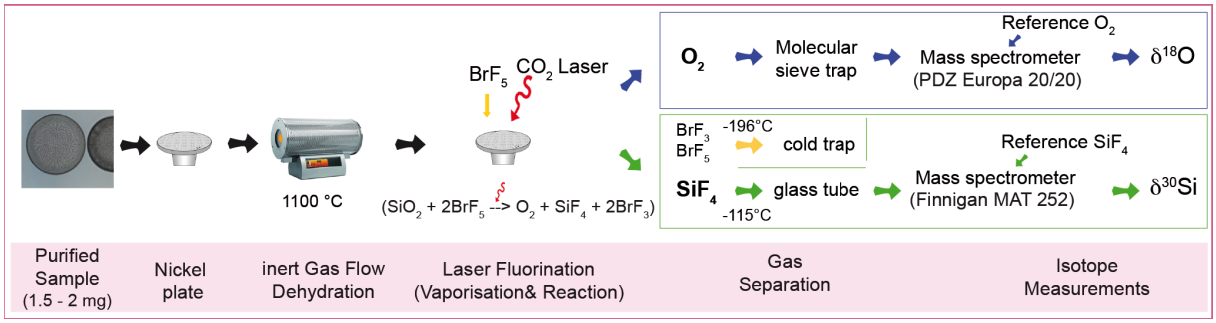

Figure 2.2. Flowchart of the instrumentation set-up for the combined (biogenic) silica oxygen and silicon stable isotope analysis (modified after Chapligin et al., 2010).

2.2.2 *N. pachyderma*$_{sin}$ oxygen ($\delta^{18}O_{Nps}$) and carbon ($\delta^{13}C_{Nps}$) measurements

Planktic foraminifera *N. pachyderma*$_{sin}$ from Core SO202-27-6 were picked from the 125-250 µm fraction, at some depths from the 315-400 µm or the >400 µm fraction. Isotope measurements were performed at the AWI (Bremerhaven) using a MAT 251 IRMS directly coupled to an automated carbonate preparation device (Kiel I) and calibrated via NIST-19 international standard to the PDB scale. All values are given in δ-notation vs. V-PDB (Vienna Pee Dee Belemnite). The precision of the measurements at 1σ, based on repeated analyses of an internal laboratory standard (Solnhofen limestone) over a 1-year period, was better than 0.08‰ and 0.06‰ for oxygen and carbon isotopes, respectively. Since *N. pachyderma*$_{sin}$ is believed to calcify at the bottom of the thermocline in the subarctic Pacific realm (Bauch et al., 2002), the $\delta^{18}O_{Nps}$ and $\delta^{13}C_{Nps}$ records are used as proxies for changes in subsurface water development (temperature, salinity, nutrients).

2.2.3 X-ray fluorescence (XRF) core logging

Core SO202-27-6 was measured at 1 cm resolution using an Avaatech X-ray fluorescence (XRF) core scanner located at the AWI (Bremerhaven) to determine the relative elemental composition (counts per second; cps). Three measurements with varying tube voltages (10 kV, 30 kV, 50 kV) were performed at 1 mA and a counting time of 30 seconds. The relatively light elements Si, Ti, Fe and Ca presented in this study were obtained from the scan at 10 kV. The Fe and Ca intensity records were used to help creating the age model of SO202-27-6 (see *Chapter 3; Sections 5.4, 6.3*) and the Si/Ti ratio as supporting information on relative changes in the content of biogenic opal within the sediment.

2.2.4 Biogenic opal

Biogenic opal concentration of Core SO202-27-6 was measured on bulk samples à ~20 mg at the AWI (Bremerhaven), using the automated leaching method of Müller and Schneider (1993). The opal content was extracted with 1M NaOH at 85°C and the opal concentration was measured by continuous flow analysis with molybdate-blue spectrophotometry. Biogenic opal (weight-%) values were calculated from the biogenic silica concentration adding 10% H_2O bound in the skeleton and correcting for the concentrations of salt in the input sample, following Kuhn (2013). When information on dry bulk density was available, biogenic opal concentrations were converted into mass accumulation rates (MAR) of opal, compensating for effects of percentage dilution of biogenic silica by other sediment particles. Furthermore, the Si/Ti ratio from XRF core logging (*Section 2.2.3*) was used as supporting information on relative changes in the concentration of biogenic opal. Changes in biogenic opal concentration and opal MAR were used as qualitative indicators for changes in export production and, to a first order degree, in paleoproductivity.

2.2.5 Ice-rafted debris (IRD)

As indicator for input and relative changes in ice-rafted debris (IRD) the weight-% of lithic fragments of the >250-µm fraction was estimated. Therefore the >250-µm fraction was sieved from the heavy fraction after the first heavy liquid separation for diatom isotope sample preparation. The obtained weight-% was then normalized to the complete heavy fraction (>63 µm). Dropstones (defined as pebble-to-cobble sized IRD) are not included in this calculation.

2.2.6 Radiocarbon

About 4.0 mg of planktic foraminifer *N. pachyderma*$_{sin}$ were picked from the 125-250 µm fraction at different depths of Core SO202-27-6 and were analyzed for radiocarbon by accelerator mass spectrometry (AMS) at the National Ocean Science AMS facility (NOSAMS) at Woods Hole Oceanographic Institution, USA. Radiocarbon was used to help creating the age model of SO202-27-6 (see *Chapter 3; Sections 5.4, 6.3*).

Chapter 3 – Age constraints

This thesis provides new proxy data from sediment cores SO202-27-6 (NE Pacific) and MD01-2416 (NW Pacific) (Fig. 2.1). Within the frame of this thesis a chronology for Core SO202-27-6 was generated and the chronology of Core MD01-2416 was slightly modified for the studied time interval from the chronology originally presented by Sarnthein et al. (2007) and recently improved by Sarnthein et al. (2013).

Age model construction for the North Pacific realm is a challenging task considering the low biogenic carbonate content of most North Pacific sediments and the poor knowledge of paleo-^{14}C reservoir ages of North Pacific surface waters. Age models covering the last 40 ka are usually largely based on few planktic foraminiferal ^{14}C ages and assuming a constant surface water reservoir age. The applied constant reservoir age differs among different studies by several hundred years across different oceanographic settings (e.g. NE Pacific, NW Pacific, Sea of Okhotsk, Bering Sea, continental margin setting, open sea) as well as concerning cores located close to each other (e.g. De Vernal and Pederson, 1997; Galbraith et al., 2007; Davies et al., 2011; Max et al., 2012). Some authors (Galbraith et al., 2007; Lund et al., 2011) use large errors for reservoir ages (≥200 a) to cover the published variability of (paleo-)reservoir ages. Accordingly, errors in the age models are usually in the order of several hundred years for the last deglaciation, and even higher concerning the MIS3, which complicates the evaluation of the relative timing of millennial-scale climate variability in the North Pacific and the North Atlantic regions. Consequently, the paleoclimatic relationship between both regions is either described as out-of-phase (Kiefer et al., 2001; Kiefer and Kienast, 2005) or as in-phase (Galbraith et al., 2007; Max et al., 2012).

Concerning the last termination Sarnthein et al. (2007) proposed a different approach to date subarctic North Pacific sediments. This suggestion was based on ^{14}C-plateau tuning, where suites of planktic ^{14}C plateaus of high-resolution ^{14}C chronologies from different core locations were tuned to the reference ^{14}C-plateaus from ODP Site 1002 (Cariaco Basin) (Sarnthein et al., 2007), which have been chronologically tied to ^{230}Th-dated Hulu Cave speleothem records (Hughen et al., 2004). The high-resolution ^{14}C record from a laminated core recovered from Japanese Lake Suigetsu (Bronk Ramsey et al., 2012) recently offered a new and independent opportunity to tie the marine ^{14}C-plateaus to atmospheric ^{14}C-plateaus. Sediment cores studied by Sarnthein et al. (2013) include NW Pacific Core MD01-2416 investigated in this thesis and NE Pacific Core MD02-2489, which is located close to the studied Core SO202-27-6 (Fig 5.1).

3.1 SO202-27-6

The age model of the upper part of Core SO202-27-6 (0-88.5 cm) was constructed using its proximity to the well-dated Core MD02-2489. A detailed description of the age model is presented in *Section 5.4*. Briefly, three ^{14}C-Plateaus identified within the Core MD02-2489

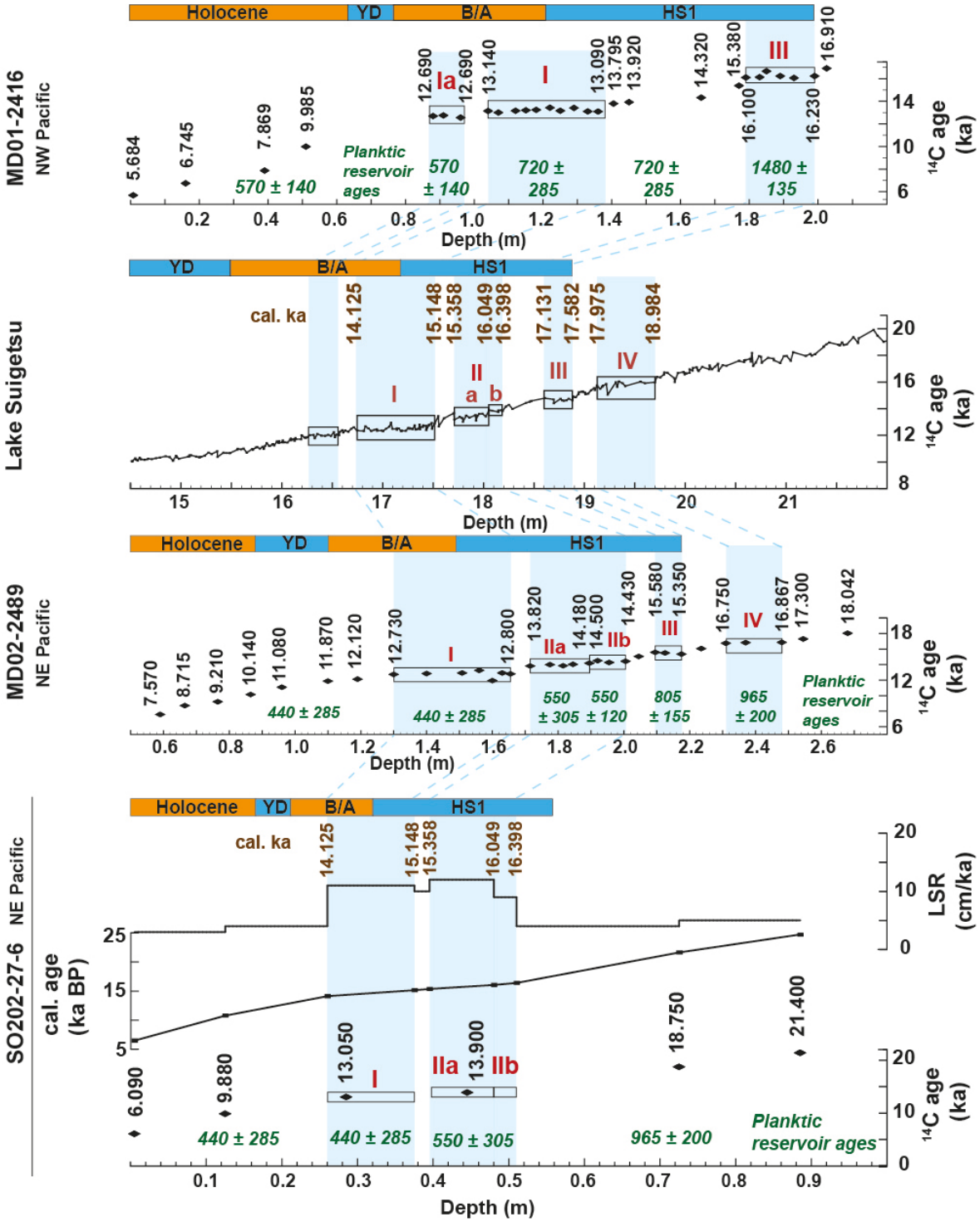

Figure 3.1. Principle of age model construction for cores MD01-2416, MD02-2489 and SO202-27-6. The assignment of the ^{14}C-plateau boundaries to Core SO202-27-6 is based on proxy data not shown here, but in Fig. 5.3. Used data: Planktic reservoir ages from Sarnthein et al. (2013); MD01-2416 ^{14}C ages from Sarnthein et al. (2007); Lake Suigetsu ^{14}C record from Bronk Ramsey et al. (2012); MD02-2489 ^{14}C ages from Gebhardt et al. (2008). ^{14}C-plateau within ^{14}C record of Core MD02-2489 after Sarnthein et al. (2007). Red Roman numbers indicate ^{14}C-plateaus (I, IIa, IIb, III, IV) following the classification of Sarnthein et al. (2007).

(Sarnthein et al., 2013) were assigned to Core SO202-27-6, using a combination of raw planktic ^{14}C ages, XRF data and biogenic opal data (Fig. 3.1; for details see Fig 5.3; Table 5.1). The plateau boundary ages (calibrated ages) of the assigned plateaus were determined by correlation of the assigned ^{14}C- plateau boundaries to the respective ^{14}C-plateau boundaries identified in the high-resolution Lake Suigetsu radiocarbon record, which has an independent age model determined by varve counting (Bronk Ramsey et al., 2012). SO202-27-6 ^{14}C dates outside the ^{14}C-plateaus were calibrated with the CALIB 7.0 software and the Marine13 calibration dataset (Stuiver and Reimer, 1993; Reimer et al., 2013), using reservoir ages determined for Core MD02-2489 by Sarnthein et al. (2013). In between the determined calibrated ages linear interpolation was used to create the age model.

The age model of the lower part of Core SO202-27-6 (88.5-289 cm) is based on calibrated planktic ^{14}C ages (calibrated as described above and using a constant reservoir age (965 ± 200 a) in combination with tuning of proxy data to NGRIP oxygen isotope (Andersson et al., 2006; Svensson et al., 2006, 2008) and dust records (Ruth et al., 2007). This part of the age model is described in detail in *Section 6.3*.

3.2 MD01-2416

The first manuscript (*Chapter 4*) uses the chronology for Core MD01-2416 originally published by Sarnthein et al. (2007). This manuscript was published before the chronology of Core MD01-2416 was first improved by Sarnthein et al. (2013) and then slightly updated over the course of this thesis (Fig. 3.1; for details see *Section 5.4*). The $\delta^{18}O_{diat}$ and $\delta^{30}Si_{diat}$ data presented in this manuscript cover a time interval from the B/A to mid-Holocene, no matter, which of the age models applied in this study is used (Fig. 3.2). Therefore, the paleoceanographic interpretations within the first manuscript (Chapter 4) are not challenged by the further developed age model.

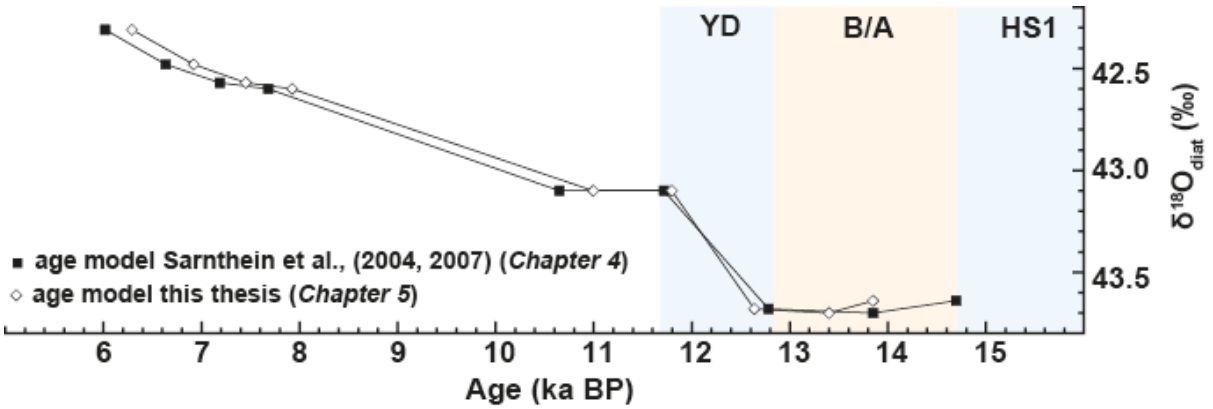

Figure 3.2. Comparison of age models for Core MD01-2416 used in this study for the time period covered by diatom isotopes, exemplarily shown for $\delta^{18}O_{diat}$ values (>63-µm fraction) presented in *Chapter 4*. The age model based on Sarnthein et al. (2004, 2007) was used in *Chapter 4* and the age model created in this thesis was used in *Chapter 5*.

Chapter 4 - Combined oxygen and silicon isotope analysis of diatom silica from a deglacial subarctic Pacific record

Maier, E.[1], Chapligin, B.[2], Abelmann, A.[1], Gersonde, R.[1], Esper, O.[1], Ren, J.[1], Friedrichsen, H.[3], Meyer, H.[2], Tiedemann, R.[1]

[1]Alfred Wegener Institute, Helmholtz Centre for Polar and Marine Research, Bremerhaven, Germany
[2]Alfred Wegener Institute, Helmholtz Centre for Polar and Marine Research, Potsdam, Germany
[3]Free University of Berlin, Berlin, Germany

Published in Journal of Quaternary Science (2013), doi: 10.1002/jqs.2649

Abstract

We present a SiF_4 separation line, coupled to a laser fluorination system, which allows for an efficient combined silica $\delta^{18}O$ and $\delta^{30}Si$ analysis (50 minutes/sample). The required sample weight of 1.5-2.0 mg allows for high-resolution isotope studies on biogenic opal. Besides analytical tests, the new instrumentation set-up was used to analyse two marine diatom fractions (>63 µm, 10-20 µm) with different diatom species compositions extracted from a Bølling/Allerød-Holocene core section (MD01-2416, North-West (NW) Pacific) in order to evaluate the palaeoceanographic significance of the diatom isotopic signals and to address isotopic effects related to contamination and species-related isotope effects (vital and environmental effects). While $\delta^{30}Si$ offsets between the two fractions were not discernable, supporting the absence of species-related silicon isotope effects, systematic offsets occur between the $\delta^{18}O$ records. Although small, these offsets point to species-related isotope effects, as bias by contamination can be discarded. The new records strengthen the palaeoceanographic history during the last deglaciation in the NW Pacific characterized by a sequence of events with varying surface water structure and biological productivity. With such palaeoceanographic evolution it becomes unlikely that the observed systematic $\delta^{18}O$ offsets signal seasonal temperature variability. This calls for reconsideration of vital effects, generally excluded to affect $\delta^{18}O$ measurements.

4.1 Introduction

Oxygen and silicon stable isotope studies on diatom valves have become promising palaeoceanographic tools. While diatom oxygen isotope ($\delta^{18}O_{diat}$) analysis is increasingly used to obtain information on changes in physical parameters of surface waters (Mikkelsen et al., 1978; Shemesh et al., 1994; Swann, 2010), diatom silicon isotopes ($\delta^{30}Si_{diat}$) are

interpreted to infer changes in local silicic acid utilization (De la Rocha et al., 1998; De la Rocha, 2006; Reynolds et al., 2008). Recently, Bailey et al. (2011) demonstrated the link between water mass structure and nutrient utilization for the late Pliocene subarctic Pacific, while Swann et al. (2010) illustrated the potential of a coupled interpretation of both $\delta^{18}O_{diat}$ and $\delta^{30}Si_{diat}$ for lacustrine environments.

Similar to biogenic carbonates (Wefer and Berger, 1991; Hoogakker et al., 2010) species-related isotope effects may potentially affect the isotopic records of diatom valves. Such isotope effects include fractionation effects (vital effects), e.g. kinetic and metabolic effects, but also environmental effects, which may result from differences in the habitat and live strategies of distinct diatom species and species groups, e.g. seasonally different blooming periods. Considering their potential to bias the isotopic records, often derived from multi-species samples, it is of great importance to know if, and to what extend, the diatom isotope records can be influenced by such effects. While early diatom culture experiments (De la Rocha et al., 1997) showed no evidence of inter-species fractionation of silicon isotopes, the recent study of Sutton et al. (2013) provided first hints at inter-species fractionation. Concerning $\delta^{18}O_{diat}$ neither culture (Brandriss et al., 1998; Schmidt et al., 2001) nor sediment trap (Moschen et al., 2005) studies revealed conclusive evidence of species-related oxygen isotope effects. Marine sediment core studies, however, present contradictory results. While earlier studies did not find species-related oxygen isotope effects (Juillet-Leclerc and Labeyrie, 1987; Shemesh et al., 1995; Chapligin et al., 2012), Swann et al. (2007, 2008) detected offsets of up to 3.51‰ in the $\delta^{18}O$ records between two marine diatom size fractions, which might be linked to such effects. The magnitude of the offsets, however, could not be conclusively explained, highlighting the need for further investigations.

The combined extraction of oxygen and silicon from silicates has been known for about 40 years (Epstein and Taylor, 1970). While early work using the combined approach concentrated on lunar and meteoritic rocks (Epstein and Taylor, 1970; Molini-Velsko et al., 1986), Leng and Sloane (2008) adapted the method for biogenic silica by including the removal of exchangeable oxygen present in diatom valves, which is a key requirement of sample preparation prior to $\delta^{18}O_{diat}$ analysis. The instrumentation for combined $\delta^{18}O_{diat}$ and $\delta^{30}Si_{diat}$ analysis presented by Leng and Sloane (2008) requires an initial weight of 5-10 mg of pure diatom silica, thus exceeds other fluorination-based instrumentations that, however, solely perform $\delta^{18}O_{diat}$ analysis (Chapligin et al., 2010; Dodd and Sharp, 2010).

Here we present combined $\delta^{18}O$ and $\delta^{30}Si_{diat}$ records using an efficient and partly new instrumentation setup. Besides analytical test documenting the precision, accuracy and required sample weight of the new setup we include a down core record from a deglacial-Holocene sediment sequence recovered on Detroit Seamount, North-West (NW) Pacific (Core

MD01-2416; Fig. 4.1). The obtained data sets are compared with other proxy records to better evaluate the palaeoceanographic significance of the diatom silica isotopic data, also addressing isotopic effects related to sample contamination and species-related isotope effects.

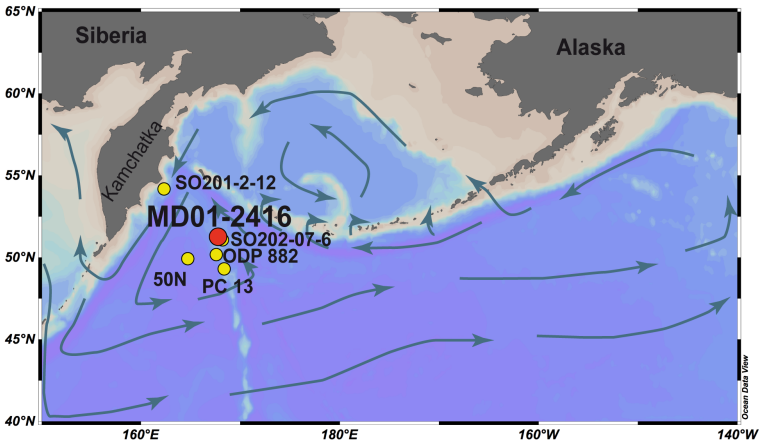

Figure 4.1. Location of Core MD01-2416 (51°16'N, 167°44'E, 2317 m), main surface water currents (after Dodimead et al., 1963) as well as location of ODP Site 882 (50°22'N, 167°36'E, 3243 m), Core PC 13 (49°43'N, 168°18'E, 2393 m), Core SO201-2-12 (53°59'N, 162°23'E, 2145 m), Core SO202-07-6 (51°16'N, 167°42'E, 2340 m) and Sediment trap Station 50N (50°01'N, 165°00'E, 3260 m).

4.2 Instrumentation, material and methods

4.2.1 Instrumentation

For fast routine combined silica $\delta^{18}O$ and $\delta^{30}Si$ analysis, we added a SiF_4 separation line to the high-performance laser fluorination system for silica $\delta^{18}O$ analysis described by Chapligin et al. (2010; Fig. 4.2). Generally, during laser fluorination O_2, SiF_4 and other fluorination by-products are generated. In the setup of Chapligin et al. (2010) the oxygen is directly separated after laser fluorination and measured for its isotopic composition using a PDZ Europa 2020, while SiF_4 and other by-products are trapped together at -196°C before being disposed. The newly connected SiF_4 separation line (at Alfred Wegener Institute, Potsdam), which consists of two cold traps, a pressure gauge and a battery of 13 Pyrex glass tubes for the storage of 13 distinct SiF_4 samples, allows the additional separation of the SiF_4 before silicon isotope analysis on a MAT 252 IRMS configured for $\delta^{29}Si$ and $\delta^{30}Si$ measurements (at Alfred Wegener Institute, Bremerhaven), according to a procedure described in the Supporting Information (Fig. S4.1). While Leng and Sloane (2008) and Molini-Velsko et al. (1986) use a temperature of about -80 °C for the separation of SiF_4 from by-products (mainly bromine compounds like BrF_3 and BrF_5), we propose a temperature of -115 °C (ethanol cooled down to freezing point with liquid N_2). The lower separation temperature minimizes the chance of contamination by even trace amounts of bromine compounds, but still allows a complete release of SiF_4. The purity of the SiF_4 is crucial as bromine compounds might be responsible

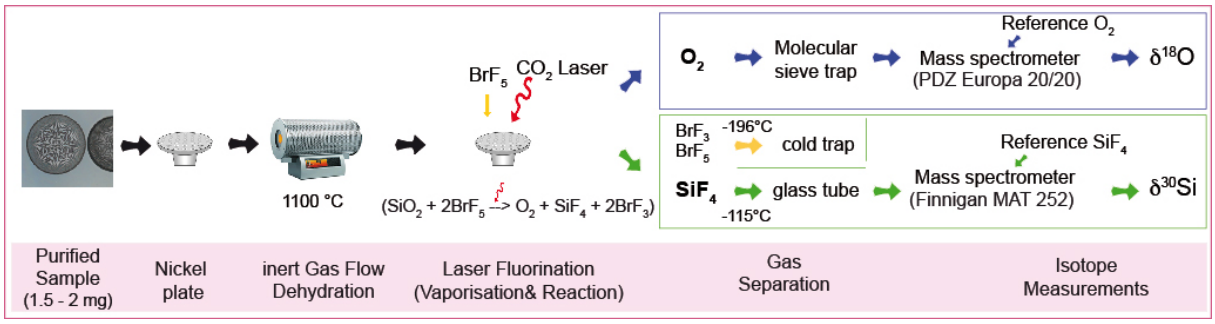

Figure 4.2. Flowchart of the instrumentation set-up for the combined oxygen and silicon stable isotope analysis (modified after Chapligin et al., 2010).

for interferences on m/z ratios of SiF_3^+, which biases the silicon isotope signals. Similar to Molini-Velsko et al. (1986), we separate the SiF_4 into Pyrex glass tubes. This allows a quick visual inspection of the SiF_4 sample purity, in addition to monitoring the $\delta^{29}Si/\delta^{30}Si$ ratios (see below), as yellowish bromine compounds would alter the color of the otherwise colorless SiF_4 sample. In total, a combined $\delta^{18}O$ and $\delta^{30}Si$ measurement takes about 50 min: 35 min for laser fluorination, O_2 and SiF_4 separation and oxygen isotope measurement plus 15 min for silicon isotope analyses.

The analytical precision of silicon isotope measurements was better than 0.09‰ ($\delta^{29}Si$; 1σ) and 0.12‰ ($\delta^{30}Si$; 1σ) for all used standard materials: the International Atomic Energy Agency (IAEA) reference standard NBS-28 and the additional working standards BFC, Diatomite, PS1772-8_{bsis} and Big Batch (Table 4.1). The standard deviation of single measurements (the SiF_4 within each Pyrex glass was measured with five repetitions) was lower, reaching a precision better than 0.05‰ for both $\delta^{29}Si$ and $\delta^{30}Si$ (determined on PS1772-8_{bsis}; 1σ; n=140). The average $\delta^{29}Si$ and $\delta^{30}Si$ values and standard deviations for BFC, Diatomite and Big Batch are in the range of published results (Reynolds et al., 2007; Leng and Sloane, 2008). Average $\delta^{29}Si$ and $\delta^{30}Si$ values of PS1772-8_{bsis}, previously introduced as a marine working standard for $\delta^{18}O$ measurements using the term PS1772-8 (Chapligin et al., 2010, 2011), were determined in this study (n=166) and are +0.68±0.07‰ (1σ) and +1.29±0.12‰ (1σ), respectively (Table 4.1).

Table 4.1. Reproducibility of $\delta^{29}Si$ and $\delta^{30}Si$ values for silicon isotope reference standard NBS-28 and the working standards PS1772-8_{bsis}, BFC, Diatomite and Big Batch.

Standard	$\delta^{29}Si$ (‰)	1σ (‰)	$\delta^{30}Si$ (‰)	1σ (‰)	n	Reference $\delta^{30}Si$ (‰)
NBS-28	+0.02	0.07	-0.01	0.10	65	0.00[a]
PS1772-8_{bsis}	+0.68	0.07	+1.29	0.11	166	this study
BFC	+0.06	0.09	+0.07	0.12	39	+0.13[b]
Diatomite	+0.59	0.08	+1.06	0.09	9	+1.26[c]
Big Batch	-5.38	0.06	-10.64	0.12	3	-10.48[c]

[a] *Gröning* (2007) [b] *Leng and Sloane* (2008) [c] *Reynolds et al.* (2007)

There is a mass-dependent fractionation between the $\delta^{29}Si/\delta^{30}Si$ ratios of the BFC and PS1772-8_{bsis} silicon isotope measurements (R^2=0.97; Fig. S4.2), indicating SiF_4 gas of high purity. The whole instrumentation (laser fluorination line, SiF_4 separation line and both mass spectrometers) is regarded free of memory effects (Fig. S4.3: A, B) and we recommend a sample weight of 1.5-2.0 mg for a single combined analysis (Fig. S4.3: C, D). More information on the procedure of the analytical tests is presented in the Supporting Information.

4.2.2 Material, sample preparation and contamination assessment

For our down-core study we analysed purified diatom samples from nine depths, collected from the uppermost 1 m of Core MD01-2416 (Detroit Seamount, NW Pacific; Fig. 4.1). The studied core section represents a time period spanning from the Bølling/Allerød (B/A) to the mid-Holocene (ca. 14.7-6.0 ka BP; Sarnthein et al., 2004; Gebhardt et al., 2008). Each sample contains diatoms extracted from a 4-cm-thick slice of sediment, each representing about 200-400 years. The very low content of biogenic opal in last glacial sediments (Gebhardt et al., 2008) prevented an extension of the records back into the last glacial.

The first step of the sample purification includes a chemical treatment with HCl and H_2O_2 to remove carbonates and organic material. After washing the residue to remove the chemicals the samples were sieved to obtain two size fractions from each sample, 10-20 µm and >63 µm. The selection of the two size fractions takes into account the size distribution of other biogenic opal particles, predominantly consisting of radiolarian skeletons, which are otherwise difficult to discard from diatom silica. The 18 size fraction subsamples were then further purified. Mineral grains were removed through density separations using specific sodium polytungstate solutions. Remaining radiolarians and sponge spicules were separated via several sieving and settling steps combined with ultrasonic treatments. The ultrasonic treatment represents an important prerequisite to assure that the diatom samples are as pure as possible for the isotope analyses as it also helps to remove clay minerals trapped within or adhered to diatom valves. Sonification may increase the number of fragmented diatom valves, but will not affect the overall composition of the two fractions. During the stepwise purification process each sample was checked several times under the light microscope before being selected for a final cleaning step with perchloric acid.

The composition of the purified fractions was determined under the light microscope using a Zeiss Axioplan I. Quantitative determination of the diatom species composition and its volumetric contribution to the measured opal was, to some extent, complicated by the occurrence of fragmented valves. To provide most appropriate estimates of the composition of both fractions we counted on average 330 particles at x400 (>63 µm) and x1000 (10-20 µm) magnification. Particles were defined as any piece of material within the counted

transects (e.g. complete and half diatom valves, radiolarians, minerals). Diatoms were identified following the taxonomy described by Sancetta (1982, 1987). Note that our calculations are based on the assumption that all particles contribute the same amount of opal to the purified sample, as a technique for precise quantification of silica contribution of individual diatom taxa is not yet available for application to series of fossil diatom samples. We preferred this counting approach to other techniques, e.g. area and volumetric estimations based on Morley et al. (2004) and Hillebrand et al. (1999), considering the occurrence of broken diatoms valves with various shapes, thicknesses and pore sizes (Fig. 4.3). To consider the environmental significance of the diatoms we classified the diatoms as spring/summer and autumn/winter diatom species following sediment trap studies in the subarctic Pacific (Takahashi, 1986; Takahashi et al., 1990), including Station 50N close to the core site location (Fig. 4.1; Onodera et al., 2005).

Multiple studies have illustrated the importance of using highly purified diatom material, particularly for oxygen isotope analysis (Morley et al., 2004; Brewer et al., 2008; Chapligin et al., 2012). The admixture of non-biogenic silicates with much lighter $\delta^{18}O$ values, ranging in general between 2 and 30‰ (Taylor, 1968; Sheppard & Gilg, 1996) compared with marine

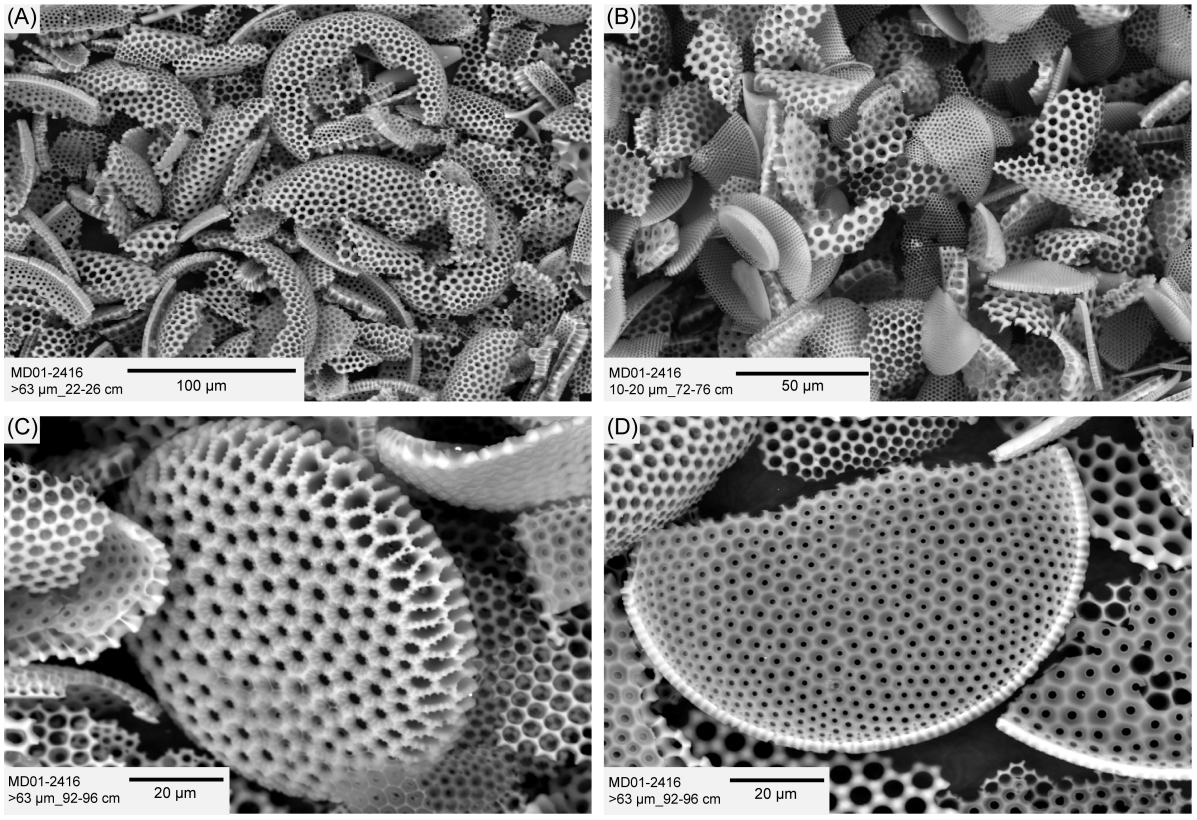

Figure 4.3. Scanning electron micrographs of purified MD01-2416 samples. There is no visible contamination with clay or other non-biogenic silicates. **(A, B)** Typical cleaned diatom samples of the two analysed size fractions **(A)** >63 µm and **(B)** 10-20 µm. An area of about this size (250 x 340 µm) was analysed with EDS. **(C)** *C. marginatus*. **(D)** Fragment of *C. oculus-iridis*.

$\delta^{18}O_{diat}$ values (>35‰), would lead to biased results and erroneous palaeoceanographic interpretations of the $\delta^{18}O_{diat}$ record. We thus applied (1) inductively coupled plasma optical emission spectrometry (ICP-OES), with 10 mg sample material according to Chapligin et al. (2012), and (2) energy dispersive X-ray spectrometry (EDS) under the scanning electron microscope, using about 0.3 mg sample material, to quantitatively assess the residual terrigenous contamination of the purified diatom samples. Analytically, best choice of both approaches is ICP-OES, given its in general lower detection limit and higher precision. However, two 10-20-µm samples only provided enough material for EDS analysis. EDS was performed using a Philips XL 30 ESEM scanning electron microscope equipped with an energy-dispersive system and a QUANTAX XFlash 5010-2405 SDD detector (Bruker AXS). The elemental composition was acquired through integration of X-ray intensities determined from an area of about 250 x 350 µm (Fig. 4.3), thereby using standardless quantification (P/B-ZAF). Results from ICP-OES and EDS are expressed as weight percentages of oxides, normalized to 100 wt%. By comparing the EDS results from PS1772-8_{bsis} with results for this material determined by Chapligin et al. (2012), we found that in our study Na_2O is comparatively overestimated, while SiO_2 is slightly underestimated (Table S4.1). All other oxide percentages are consistent, i.e. within a 0.1% uncertainty, to the results of Chapligin et al. (2012) and are close or below the general detection limit of 0.1% for EDS measurements.
Following Brewer et al. (2008) and Chapligin et al. (2012) we used the Al_2O_3 content as tracer for clay contamination. From the calculated SiO_2 and Al_2O_3 percentages we estimated the maximum amount of residual terrigenous contamination, assuming a SiO_2/Al_2O_3 ratio of 2.2 (Eggimann et al., 1980) for potential North Pacific clay residuals and presuming that all measured Al_2O_3 stems from residual clay minerals.

4.2.3 Combined $\delta^{18}O_{diat}$ and $\delta^{30}Si_{diat}$ analysis

The oxygen and silicon isotope compositions of all 18 purified diatom samples were generally measured twice, or three times, when standard deviations of duplicates exceeded the analytical reproducibility (1σ) of 0.25‰ for silica $\delta^{18}O$ (Chapligin et al., 2010) or 0.12‰ for $\delta^{30}Si$ (Table 4.1). Exceptionally, we repeated the measurement more often. All samples were measured against a reference gas (O_2 and SiF_4; both Linde) with known isotopic composition, calibrated to NBS-28. The isotopic compositions are reported in the common δ-notation relative to the IAEA primary reference standards V-SMOW (for $\delta^{18}O$) and NBS-28 (for $\delta^{29}Si$, $\delta^{30}Si$), respectively.

4.3 Results

4.3.1 Oxygen and silicon isotopes

The $\delta^{30}Si_{diat}$ values obtained from the >63-µm and the 10-20-µm fractions range between 1.19 and 1.49‰ (Table 4.2). At all depths the differences in $\delta^{30}Si_{diat}$ between the two fractions are within the analytical reproducibility of the measurements and neither of the two fractions shows constantly heavier or lighter values than the other. The $\delta^{30}Si_{diat}$ values mostly range around 1.3‰ and display a slight decrease throughout the Holocene, thus follow a trend similar to the bulk $\delta^{15}N$ (Galbraith et al., 2008) and the biogenic opal records (Gebhardt et al., 2008) from the same core (Fig. 4.6). In contrast, during the B/A the $\delta^{30}Si_{diat}$ values display a decoupling from the bulk $\delta^{15}N$ and the opal record.

The $\delta^{18}O_{diat}$ values of the >63-µm fraction range between 42.3 and 43.8‰, while the $\delta^{18}O_{diat}$ signal of the 10-20-µm fraction varies between 41.9 and 43.5‰ (Table 4.2). The $\delta^{18}O_{diat}$ records of both fractions decrease about 1.3‰ from the B/A to the Holocene and positively correlate in trend and amplitude to the $\delta^{18}O$ record of planktic, subsurface-dwelling, foraminifera *Neogloboquadrina pachyderma*$_{sin}$ reported by Gebhardt et al. (2008) from the same core. There is a small systematic offset of about 0.45‰ in $\delta^{18}O_{diat}$ between the two size fractions, with the smaller fraction being systematically lighter than the bigger fraction. This offset exceeds the general analytical reproducibility of 0.25‰. Furthermore, the offset is at most depths greater than the combined individual reproducibility of both $\delta^{18}O_{diat}$ values. There are only two exceptions at 64 and 84 cm core depth, where the offset is close to zero. In these samples, however, the individual reproducibility of the $\delta^{18}O_{diat}$ value from one of the two fractions is comparatively low, which calls for cautious interpretation of these $\delta^{18}O_{diat}$ values.

Table 4.2. $\delta^{18}O$ and $\delta^{30}Si$ values as well as standard deviations (SD) of diatom samples from Core MD01-2416.

	Oxygen						Silicon					
	>63 µm			10-20 µm			>63 µm			10-20 µm		
Sample depth (cm)	$\delta^{18}O_{AVG}$ (‰)	SD (‰)	n	$\delta^{18}O_{AVG}$ (‰)	SD (‰)	n	$\delta^{30}Si_{AVG}$ (‰)	SD (‰)	n	$\delta^{30}Si_{AVG}$ (‰)	SD (‰)	n
4-8	+42.31	0.29	2	+41.91	0.02	2	+1.19	0.01	2	+1.26	0.01	2
12-16	+42.48	0.10	4	+42.04	0.26	3	+1.37	0.11	3	+1.27	0.06	3
22-26	+42.57	0.20	2	+42.05	0.15	4	+1.31	0.06	2	+1.29	0.12	2
32-36	+42.60	0.09	2	+42.31	0.04	2	+1.30	0.04	2	+1.39	0.10	3
52-56	+43.10	0.08	3	+42.66	0.28	4	+1.30	0.04	2	+1.37	0.09	3
62-66	+43.10	0.04	2	+43.26	0.53	6	+1.43	0.01	2	+1.49	0.12	6
72-76	+43.68	0.13	3	+43.16	0.08	2	+1.46	0.01	2	+1.38	0.05	2
82-86	+43.65	0.41	5	+43.53	0.13	2	+1.32	0.02	3	+1.32	0.03	2
92-96	+43.64	0.05	2	+43.16	0.01	2	+1.34	0.01	2	+1.26	0.04	2

4.3.2 Diatom species compositions and contamination

Potential reasons for isotopic offsets between the two size fractions include (1) differences in contamination with non-biogenic silicates (e.g. clays) and non-diatom biogenic silicates (e.g. radiolarians), as well as (2) diatom species-related isotope effects. The latter are related to differences in diatom species composition and include species-related fractionation effects as well as environmental effects. Environmental effects may affect diatom samples, if they contain species or species groups dwelling during different blooming periods at different environmental conditions (e.g. surface water temperature).

Contamination by non-biogenic silicates and non-diatom biogenic silicates is generally extremely low and was estimated to range between 0 and 2.1% and 0 and 2.3% in the two fractions (Table S4.2). Optical counting and ICP-OES/EDS analyses point to a slightly higher contamination in the smaller fraction, with offsets between 0 and 0.9% (Table 4.3). While results from ICP-OES/EDS suggest the presence of trace amounts of clays in all diatom samples, light microscopy reveals non-biogenic silicates only in some of the samples (Table S4.2). Trace amounts of residual clays trapped within or adhered to the diatom frustules, which could not be detected by light microscopy, might explain this discrepancy. Regarding non-diatom biogenic silicates, we found no offset in the content of radiolarians and siliceous sponge spicules between both fractions, which contribute together <0.5% to each fraction. In six 10-20-µm samples, we found few specimen of the siliceous dinoflagellate *Actiniscus pentasterias* (0-1.6%), which was absent in the bigger fraction.

Table 4.3. Offsets of isotopic values (>63 µm minus 10-20 µm fraction), offsets in non-biogenic silica contamination (estimated from particle counts and content of Al_2O_3 determined by ICP-OES or EDS, where in bold italics) and differences in the relative abundance of spring/summer species (10-20 µm minus >63 µm fraction), which equals the relative abundance of *Thalassiosira* spp. and *Actinocyclus* spp. in the 10-20 µm fraction.

Sample depth (cm)	Offset $\delta^{18}O$ (>63 µm minus 10-20 µm) (‰)	offset $\delta^{30}Si$ (>63 µm minus 10-20 µm) (‰)	Offset non-biogenic silica contamination (10-20 µm minus >63 µm) (%)		offset *Thalassiosira spp.* + *Actinocyclus spp.* *(10-20 µm minus >63 µm)* (%)
			light microscopy	ICP-OES / ***EDS***	
4-8	+0.40	-0.07	+0.5	+0.30	+20.9
12-16	+0.44	+0.10	+0.3	+0.79	+19.3
22-26	+0.52	+0.02	+0.0	+0.80	+33.8
32-36	+0.29	-0.09	+0.3	+0.59	+13.0
52-56	+0.45	-0.07	+0.6	***+0.69***	+28.1
62-66	*+0.16**	-0.11	+0.0	+0.59	+30.8
72-76	+0.52	+0.09	+0.0	+0.43	+40.5
82-86	*+0.12**	+0.00	+0.3	+0.39	+45.6
92-96	+0.48	+0.08	+0.3	***+0.93***	+49.5
mean offset	**+0.44**	**-0.01**	**+0.3**	**+0.61**	**+31.3**
SD offset	0.08	0.08	+0.2	0.21	+12.4

*Value excluded from mean offset calculation considering the relatively high standard deviations (see Table 4.2)

Considering the diatom species composition, the >63-µm fraction solely (98.5-100%) consists of *Coscinodiscus* species (*C. oculus-iridis*, *C. marginatus*, *Coscinodiscus spp.*; Table S4.2, Fig. 4.4, Fig. S4.4), which have their main fluxes in autumn/early winter according to Takahashi (1986) and Takahashi et al. (1990). The smaller fraction contains up to 49.5% of diatom species with peak fluxes in spring/summer. This includes *Thalassiosira* spp. (mainly *T. trifulta* group) and *Actinocyclus* spp. (*A. curvatulus, A. ochotensis, A. oculatus*). Other diatoms, which could not be classified as spring/summer or autumn/winter diatoms, contribute 1.0-7.8% to the 10-20-µm fraction. Strongly fragmented *Coscinodiscus*, attributed to the same species as found in the large fraction, account for the remaining portion.

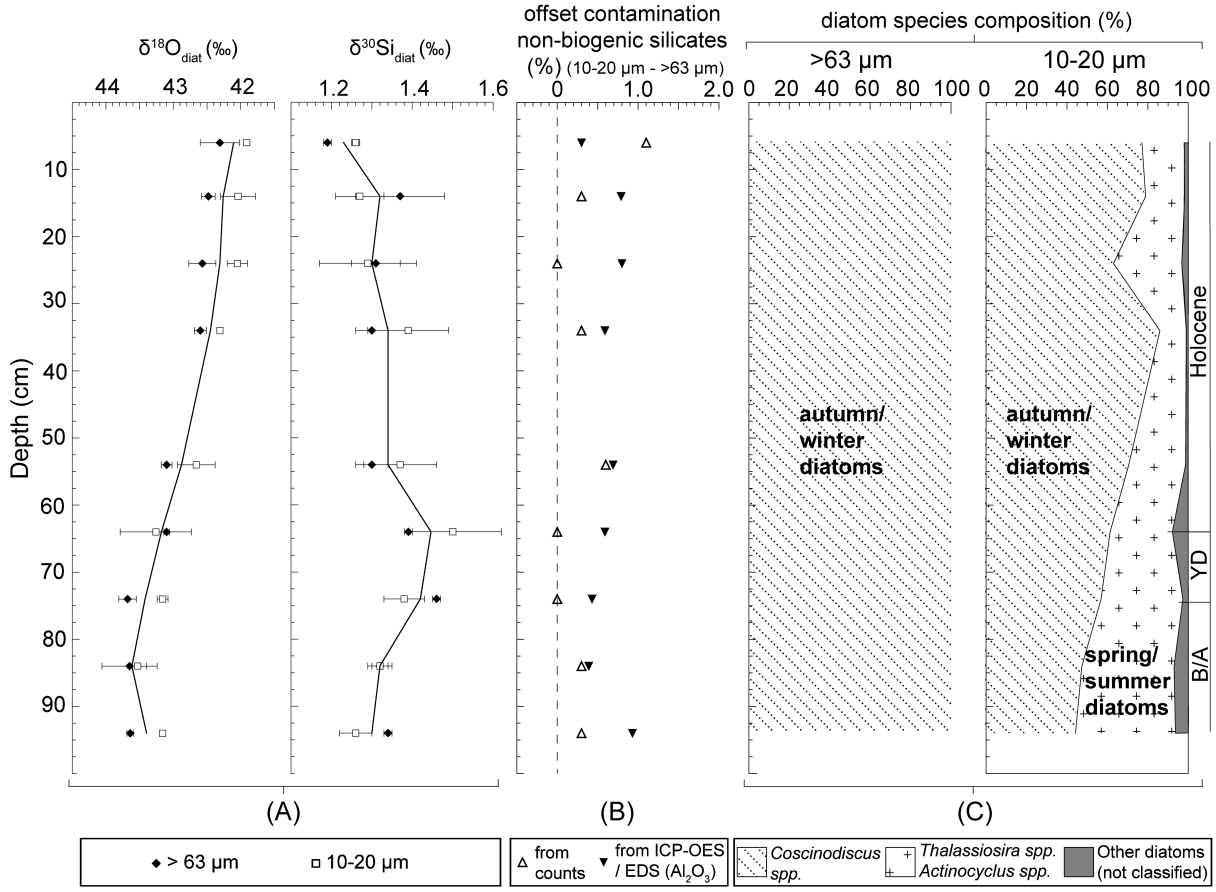

Figure 4.4. Down-core results from the 10-20-µm and >63-µm fraction of Core MD01-2416. **(A)** Oxygen and silicon isotopes. **(B)** Percentages of non-biogenic silica contamination (calculated from counts and Al_2O_3 percentages determined by ICP-OES/EDS). **(C)** Classification of diatom species composition in autumn/winter and spring/summer diatom species based on sediment trap studies of Takahashi (1986) and Takahashi et al. (1990).

4.4 Size fraction-related isotope records

4.4.1 $\delta^{30}Si_{diat}$ records

Despite the differences in contamination with non-biogenic silicates and diatom species compositions within the >63-µm and the 10-20-µm fraction the offsets between the $\delta^{30}Si_{diat}$ values are at all depths within the analytical reproducibility of the measurements and neither of the two fractions shows constantly heavier or lighter $\delta^{30}Si_{diat}$ values than the other. The absence of a notable and systematic $\delta^{30}Si_{diat}$ offset illustrates the negligible influence of the <1% difference in contamination, which can be explained by the, if present at all, rather small difference between $\delta^{30}Si_{diat}$ values and the $\delta^{30}Si$ of clay minerals. Even a hypothetical difference in clay contamination of 2.0% with a clay $\delta^{30}Si$ as low as -2.5‰ (clay $\delta^{30}Si$ range between about -2.5 and +1.8‰ according to Douthitt, 1982; Ding et al., 1996 and Ziegler et al., 2005) would shift the isotopic value of a 100% clean diatom sample with a $\delta^{30}Si_{diat}$ signal of 1.50‰ by only 0.08‰, which would be well within the analytical reproducibility of the silicon isotope measurements. Our observations furthermore indicate that species-related silicon isotope effects are not discernable, which supports findings of experiments suggesting that diatom silicon isotope fractionation is species-independent (De la Rocha et al., 1997).

4.4.2 $\delta^{18}O_{diat}$ records

As outlined above, the observed offsets in the $\delta^{18}O_{diat}$ values of the studied fractions occur systematically and their average value of 0.45‰ exceeds the analytical uncertainty of silica $\delta^{18}O$ measurements. Offsets in $\delta^{18}O_{diat}$ records from two diatom fractions with species compositions similar to the fractions investigated herein have previously been reported by Swann et al. (2008) from the nearby ODP Site 882 (Fig. 4.1). However, this study of Pleistocene $\delta^{18}O_{diat}$ variability reveals a non-systematic offset about fourfold larger than the one we observe, which could not be explained conclusively. This calls for more detailed analysis and discussion of potential causes of $\delta^{18}O_{diat}$ offsets, in particular differences in contamination and species composition.

4.4.2.1 Effect of contamination

Potential contamination in our diatom fractions may be related to the presence of non-diatom biogenic silicates and/or non-biogenic silicates (Table S4.2). We exclude non-diatom biogenic silicates as a responsible factor for the observed offset in $\delta^{18}O$. First, the amount of radiolarians and sponge spicules is in both fractions below 0.5%, with no systematic offset, and the few oxygen isotope analyses of radiolarian tests and sponge spicules showed that their oxygen isotopes generally range between ca. 34 and 45‰ (Matheney and Knauth, 1989; Jochum et al., 2012), which is about the same isotopic range as for marine diatom silica

(Shemesh et al., 1995; Swann, 2010). Secondly, considering the existing calibrations for oxygen isotope fractionation between biogenic silica and water (e.g. Juillet-Leclerc and Labeyrie, 1987; Matheney and Knauth, 1989), the on average 0.5% higher abundance of the siliceous dinoflagellate *A. pentasterias* in the 10-20-µm fraction also cannot account for the observed 0.45‰ offset, even though the life strategy of *A. pentasterias* and the true magnitude of its oxygen isotope fractionation is unknown. A 0.5% higher abundance in the 10-20-µm fraction would only decrease the offset by maximum 0.05‰, assuming an *A. pentasterias* $\delta^{18}O$ of 34.0‰ and a $\delta^{18}O_{diat}$ of 44.0‰.

Previous studies (Morley et al., 2004; Brewer et al., 2008; Chapligin et al., 2012) demonstrated the correlation between measured $\delta^{18}O$ of diatom samples and contamination with non-biogenic silicates (tephra, clay minerals, rock fragments), with higher contamination levels resulting in lower $\delta^{18}O_{diat}$ values. To fully account for the observed offset in $\delta^{18}O_{diat}$ the smaller fraction would need to be 1.3% more contaminated by non-biogenic silicates than the bigger fraction (assuming a rather low $\delta^{18}O$ of 10.0‰ for non-biogenic silicates and a $\delta^{18}O_{diat}$ value of 44.0‰ for a 100% clean diatom sample). For a reduction of the offset in $\delta^{18}O_{diat}$ below the analytical reproducibility of $\delta^{18}O$ measurements the contamination in the smaller fraction would need to be >0.7%. The average offset in contamination with non-biogenic silicates determined by optical counting of 0.3 ± 0.4% (Table 4.3) is too low to explain the $\delta^{18}O_{diat}$ offset, while estimations from ICP-OES/EDS (0.6 ± 0.2%) reduce the $\delta^{18}O_{diat}$ offset close to the analytical reproducibility. Calculations from ICP-OES/EDS, however, might overestimate the contamination, and thus its offset, since we therein assume that all aluminium derives from clay minerals. However, diatoms structurally incorporate some Al into their frustules during biomineralisation (Gehlen et al., 2002) and rapid early diagenesis of settled diatom valves usually leads to a further increase in the Al/Si ratio (Van Cappellen et al., 2002). Since there is furthermore no statistically significant correlation between the offsets in $\delta^{18}O_{diat}$ and in contamination with non-biogenic silicates (R^2=0.24 and P=0.26 (light microscopy); R^2=0.07 and P=0.58 (ICP-OES/EDS); Fig. 4.5A), we suggest that even though minor differences (<1%) in non-biogenic contamination occur, they are not the major responsible factor for the observed offset in the $\delta^{18}O_{diat}$.

4.4.2.2 Species-related oxygen isotope effects

In contrast to the statistically insignificant correlation between $\delta^{18}O_{diat}$ offsets and the degree in contamination (Fig. 4.5A) we note that the $\delta^{18}O_{diat}$ offsets covary with the relative abundance of spring/summer diatoms *Thalassiosira* spp. and *Actinocyclus* spp. in the 10-20-µm fraction. Increasing numbers of spring/summer diatoms result in increasing offsets (R^2=0.59; Fig. 4.5B). This relationship is statistically significant (P=0.04) and points to

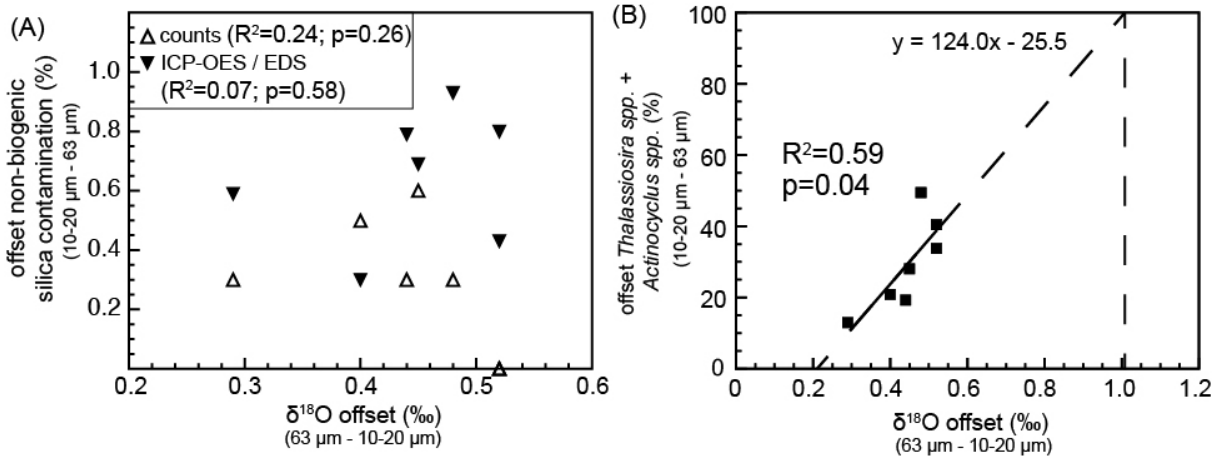

Figure 4.5. (A) Crossplot between the offset in $\delta^{18}O_{diat}$ and contamination with non-biogenic silicates, which was calculated from (1) counts under the light microscope and (2) Al_2O_3 percentages determined by ICP-OES or EDS (see Table 4.3). (B) Crossplot between the offset in $\delta^{18}O_{diat}$ and the offset in the abundance of spring/summer diatoms, which equals the abundance of the diatoms *Thalassiosira* spp. and *Actinocyclus* spp. in the 10-20-µm fraction.

species-related isotope effects being responsible for the observed $\delta^{18}O_{diat}$ offsets. Species-related isotope effects include (1) inter- and intraspecific fractionation effects, so-called vital effects, and (2) environmental effects.

According to available studies, summarized by Swann and Leng (2009), diatoms are commonly believed to precipitate their frustules in equilibrium with ambient seawater, with vital effects regarded as being non-existent or within the analytical uncertainty of the $\delta^{18}O$ measurements. In the absence of studies dealing with vital effects of the marine diatom species recorded in our samples, it is not possible to further determine the presence and magnitude of such effects in our $\delta^{18}O_{diat}$ records. However, we can evaluate the potential of environmental effects, in particular seasonal differences in diatom growth rates, sea surface temperature (SST) and surface water salinity (SSS), to explain the correlation between the observed offset and the relative abundance of *Thalassiosira spp*. and *Actinocyclus spp.*.

Based on culture studies, Schmidt et al. (2001) suggested that oxygen isotope fractionation is influenced by diatom growth rates, with less fractionation occurring in faster growing diatoms. Fertilization experiments demonstrated that the deposition of dissolved iron in the high-nutrient, low-chlorophyll waters of the subarctic North Pacific induces rapidly developing phytoplankton blooms (e.g. Tsuda et al., 2003). Such enhancements of phytoplankton growth rates could lower the $\delta^{18}O_{diat}$ values of the 10-20-µm fraction containing spring/summer diatoms considering that dust-borne iron deposition on the North Pacific increases in spring during modern (interglacial) times (Takeda, 2011).

The modern subarctic NW Pacific is characterized by strong seasonal SST contrasts reaching up to 8 °C between late summer (ca. 10 °C) and late winter (ca. 2 °C), and more smoothed seasonal contrast of 2.5 °C between spring/summer and autumn/winter periods (Locarnini et

al., 2010). Considering a diatom temperature coefficient (relationship between $\delta^{18}O_{diat}$ and temperature) ranging between -0.5‰ °C^{-1} (Shemesh et al., 1992) and -0.2‰ °C^{-1} (Moschen et al., 2005; Dodd and Sharp, 2010) $\delta^{18}O_{diat}$ values of modern spring/summer species should range between 0.5 and 1.25‰ lower than $\delta^{18}O_{diat}$ values of autumn/winter species. An extrapolation of the relation between the relative abundance of spring/summer diatoms (*Thalassiosira* spp. and *Actinocyclus* spp.) and the $\delta^{18}O_{diat}$ offsets to a hypothetical diatom sample containing a 100% spring/summer signal results in a theoretical maximum offset of 1.01‰ (Fig. 4.5B) between a 100% spring/summer and a 100% autumn/winter diatom sample. This suggests that seasonal temperature changes may have the potential to explain the $\delta^{18}O_{diat}$ offset between the two diatom size fractions.

It has previously been estimated that the low seasonal salinity gradient in surface waters of the modern subarctic North Pacific (ca. 0.5 p.s.u. between late summer (ca. 32.7 p.s.u.) and late winter (ca. 33.2 p.s.u.; Antonov et al., 2010)) corresponds to annual variations in surface water $\delta^{18}O$ of 0.13-0.14‰ (Swann et al., 2008). Such low values range within the analytical reproducibility of $\delta^{18}O$ measurements of 0.25‰, thus could not be detected by $\delta^{18}O$ analysis.

In the following we will further test the plausibility of the different mechanisms' impact on the $\delta^{18}O_{diat}$ offset by consideration of the palaeoceanographic development in the study area derived from the new isotope data in concert with available studies.

4.5 Palaeoceanographic implications

The $\delta^{18}O_{diat}$ record is not indicative of anomalies in SST or SSS over the B/A warming, the Younger Dryas (YD) cooling and the early Holocene warming period represented in the studied core section (Fig. 4.6). The close relationship between the $\delta^{18}O_{diat}$ records and the $\delta^{18}O$ record of the planktic foraminifer *N. pachyderma$_{sin}$* in trend and amplitude suggests that the trend of the $\delta^{18}O_{diat}$ records represents an ice volume signal rather than a signal reflecting Northern Hemisphere climate evolution at the last glacial-interglacial transition as documented at high resolution in Greenland ice core records (NGRIP members, 2004). However, although Max et al. (2012) state a close coupling of the climate variability between the North Atlantic and North Pacific, SST records obtained from the subarctic NW Pacific display only a weak B/A warming and YD cooling. This is true for an alkenone-based record obtained west of the studied core location (Core SO201-02-12, Max et al., 2012) (Fig. 4.1), which displays a trend similar to the $\delta^{18}O$ records obtained from the studied core section (Fig. 4.6). Yet unpublished diatom transfer function-based SST records from the studied core section (J. Ren, R. Gersonde, O. Esper, unpubl. data) and alkenone-based SST from the nearby Core SO202-07-6 (M. Méheust, R. Stein, K. Fahl, unpubl. data; Fig. 4.1) support the presence of such deglacial SST development.

In the modern subarctic North Pacific vertical mixing of surface waters with deeper water masses is limited by a strong halocline, which developed during the onset of the Northern Hemisphere glaciation (Haug et al., 1999; Swann et al., 2006). During the last glacial period enhanced stratification is proposed for the subarctic Pacific (Jaccard et al., 2005), but the transition to modern conditions is not well understood (Brunelle et al., 2010). The pattern of the $\delta^{18}O$ and SST records suggest less stratified surface waters since the B/A, supporting previous evidence of enhanced vertical mixing after 15 ka BP at this site (Gebhardt et al., 2008). Enhanced vertical mixing during the B/A is also supported by apparently decoupled $\delta^{30}Si_{diat}$ from bulk $\delta^{15}N$ and opal concentration data during that time (Fig. 4.6). As silicon and nitrogen isotopes are subject to stable isotope fractionation during the formation of opaline skeletons and organic matter, with a discrimination against the heavier isotopes (^{30}Si; ^{15}N), both $\delta^{30}Si$ and $\delta^{15}N$ have the potential to document temporal changes in nutrient (silicic acid or nitrate) utilization (De la Rocha, 2006). We regard our $\delta^{30}Si_{diat}$ signals to reflect silicic acid utilization, as species-related silicon isotope effects can be neglected (see *Section 4.4.1*) and whole-ocean changes in silicic acid $\delta^{30}Si$ are not likely to modulate our signal considering the oceanic residence time of silicon of about 10 ka (Tréguer and De la Rocha, 2013). In contrast, the interpretation of the $\delta^{15}N$ signal may be additionally complicated, e.g. by advection of

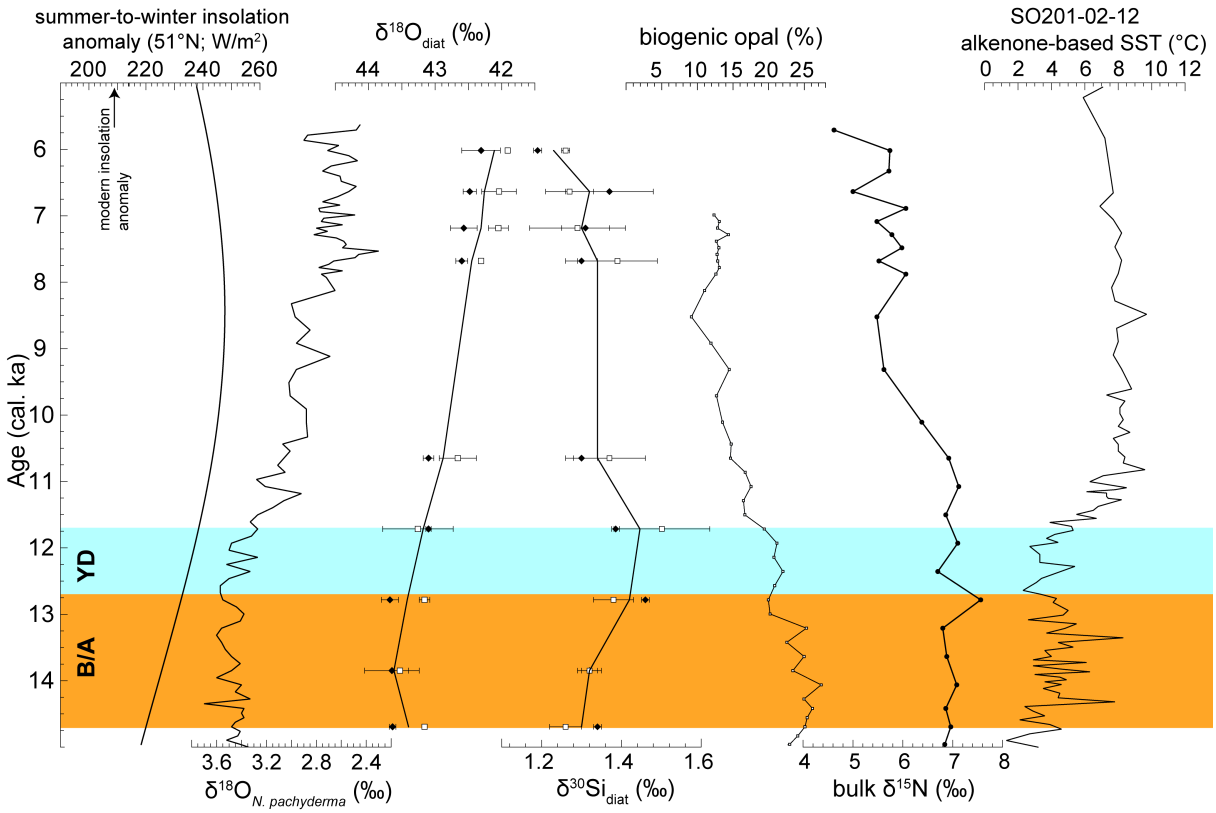

Figure 4.6. From left to right: mean summer-to-winter insolation anomaly (calculated after Laskar et al., 2004), proxy data of Core MD01-2416: $\delta^{18}O$ record of subsurface-dwelling foraminifera *N. pachyderma*$_{sin}$ (Gebhardt et al., 2008), $\delta^{18}O_{diat}$ and $\delta^{30}Si_{diat}$ records displaying surface conditions, biogenic opal content (Gebhardt et al., 2008), bulk $\delta^{15}N$ record of Galbraith et al. (2008). To the far right the alkenone-based SST record of Core SO201-2-12 (Max et al., 2012) is displayed.

subsurface waters from the Eastern Tropical North Pacific (Brunelle et al., 2010), where enhanced denitrification is proposed to occur especially during the B/A (Galbraith et al., 2013). Brunelle et al. (2010) could not relate the high $\delta^{15}N_{diat}$ during the B/A obtained from Core PC13, close to the studied core site (Fig. 4.1), to either denitrification or increased nitrate utilization. The decoupled $\delta^{30}Si$ records could be interpreted to indicate enhanced fueling of the productivity zone with subsurface waters characterized by a comparatively greater denitrification signal. This interpretation is consistent with the suggestion of increased vertical mixing as trigger for the high export of biogenic opal in the subarctic Pacific during the B/A (Kohfeld and Chase, 2011).

Slightly elevated $\delta^{30}Si_{diat}$ values during the YD might display a short re-establishment of enhanced surface water stratification, causing less advection of the silicic acid. The stronger surface water stratification is potentially associated with the presence of sea ice (Max et al., 2012) in the far NW Pacific during that time. Enhanced YD stratification might smooth summer SST cooling of surface waters in the study area at a time of increasing summer insolation. The slight decrease of the $\delta^{30}Si_{diat}$ values from the YD to the mid-Holocene is consistent with a slight decrease in bulk $\delta^{15}N$ and $\delta^{15}N_{diat}$ from the studied section and other subarctic Pacific cores (Fig. 4.6; Galbraith et al., 2008; Brunelle et al., 2010), indicating a decrease in nutrient (silicic acid and nitrate) utilization in the subarctic NW Pacific. Such a decrease is also mirrored by declining biogenic opal concentrations (Fig. 4.6). The observed changes in nutrient utilization and productivity are likely linked with the finding of Riethdorf et al. (2013a) suggesting an enhancement of the thermal mixed layer stratification and related increase in seasonal temperature contrasts, comparable to modern conditions, developing since the Early Holocene.

The palaeoceanographic picture developed from the new opal isotope data together with other palaeoceanograpic records from the study area allows for a critical review of the potential mechanisms related to the occurrence of the offset in $\delta^{18}O_{diat}$ values between the two diatom size fractions and related diatom species compositions. It appears that a rather consistent offset occurs at distinctly different surface water mass structure conditions, (1) enhanced vertical mixing during the B/A, (2) enhanced stratification during the YD and (3) conditions close or comparable to modern with enhanced seasonal sea surface temperature contrasts. This impedes a simple explanation of the mechanism responsible for the observed offsets. It appears difficult to relate the offset to seasonal SST differences, although the temperature range calculated from the offset is not unlikely. However it is rather implausible that the seasonal differences remain more or less stable at time periods characterized by distinctly different surface water conditions. The same is true for a mechanism related to diatom growth rates. In the modern subarctic NW Pacific, the supply of dissolved iron due to autumn/winter

vertical mixing is supposedly more important than the average input of soluble dust-borne iron (Brown et al., 2005; Measures et al., 2005), suggesting nutrient-rich subsurface waters to be the most important source for both autumn and spring blooms. Dust-induced spring blooms might play a bigger role during the YD, where dust deposition was probably elevated in the Northern Hemisphere (Ruth et al., 2007). However, the $\delta^{18}O_{diat}$ offset observed during that time does not indicate a change in diatom growth rates.

At the bottom line, a significant impact by environmental effects to explain the observed $\delta^{18}O_{diat}$ offset appears to be unlikely. This requires reconsideration of vital effects as primary factor to generate the $\delta^{18}O_{diat}$ offsets between different groups of diatom species, and thus calls for more efforts to study this effect on modern and fossil materials.

The $\delta^{18}O_{diat}$ offsets reported by Swann et al. (2008) from a Quaternary record recovered at ODP Site 882, thus in the vicinity of our core (Fig. 4.1), are fourfold higher compared with our measurements. These offsets occur between two diatom fractions with species compositions comparable to the compositions reported herein. The offset has been attributed to some kind of vital effect, but in contrast to our study, the offset could not be linked to diatom species compositions. It can be speculated that the differences in the magnitude of the offset reported by Swann et al. (2008) and herein could arise from differences in the purity of the analysed samples. Hints for this speculation can be based on the finding that the offsets display a non-systematic pattern and that interglacial ODP 882 $\delta^{18}O_{diat}$ measurements display generally lower (ca. 29-43‰) values than those obtained from the Holocene in Core MD01-2416 (≥42‰). This could indicate a general higher presence of clays in the ODP 882 samples.

4.6 Summary and conclusions

A new instrumentation setup provides a powerful tool for highly efficient combined silica $\delta^{18}O$ and $\delta^{30}Si$ analysis. The setup requires relatively low sample weights of ca. 1.5 mg, thus enabling routine application of both proxies on sediments with a biogenic opal content as low as about 10%. Routine measurements take only 50 minutes in total for one combined analysis. As such the setup easily allows multiple repetitions of oxygen and silicon isotope measurements to improve the precision of the $\delta^{18}O$ and $\delta^{30}Si$ values. However, continuing effort is needed to further reduce the sample weight in order to make the method feasible on sediments with even lower biogenic opal content.

The down-core analysis of two diatom size fractions (>63 µm and 10-20 µm) with different species compositions extracted from a core section representing the B/A to the mid-Holocene (Core MD01-2416, Detroit Seamount) reveals $\delta^{30}Si_{diat}$ and $\delta^{18}O_{diat}$ records that strengthen the development of NW Pacific palaeoceanography together with other available proxy records. This includes a sequence of events attributed to the B/A warming, the YD cooling and the

development towards modern conditions starting in the early Holocene. This development is characterized by changes in water mass structure and biological productivity.

Extensive testing of the methodological steps to prepare purified diatom samples for isotopic measurements reveals that the applied method allows for both $\delta^{30}Si_{diat}$ and $\delta^{18}O_{diat}$ measurements not or insignificantly biased by contamination with non-biogenic silicates and non-diatom biogenic silicates. Careful purification of the samples and additional screening of elemental compositions (e.g. by ICP-OES; EDS) represent a crucial prerequisite to avoid disturbances and misinterpretations of the isotopic measurements by contamination.

The repeated measurement of the two size fractions results in non-systematic $\delta^{30}Si_{diat}$ offsets between the two fractions with $\delta^{30}Si_{diat}$ value deviations in the range of the analytical reproducibility of the measurements. As such, species-related silicon isotope effects are not discernable. The offset observed in the $\delta^{18}O_{diat}$ is systematic and related to the species composition of the small diatom fraction. The magnitude of the offset suggests that seasonal temperature changes may have the potential to explain the offset. However, it is rather implausible that the seasonal differences remain more or less stable at time periods characterized by distinctly different surface water conditions. The same is true for a mechanism related to diatom growth rates. This requires reconsideration of vital effects as primary factor to generate the rather constant $\delta^{18}O_{diat}$ offsets.

The isotope measurements obtained with the new instrumental setup show the strong relevance of this approach to enhance palaeoceanographic interpretations of water mass structure and nutrient utilization. However, a number of technical improvements are still required, including further sample size reduction and the development of routine methods for more appropriate quantification of the opal contributed by the different components (species and species groups, fragmented and non-fragmented) to allow for best possible interpretation of diatom isotope records. Another remaining knowledge gap concerns the study of potential vital effects that may impact the isotopic signals.

Acknowledgements

This study is part of the Innovative NOrth Pacific EXperiment (INOPEX) project, which was funded by the Bundesministerium für Bildung und Forschung, Germany (BMBF). We gratefully acknowledge Michael Sarnthein for providing the bulk samples of Core MD01-2416 and Melanie Leng (BFC) as well as Mark Brzezinski (Big Batch, Diatomite) for supplying working standards. Ulrike Böttjer, Birgit Glückselig and Ruth Cordelair are thanked for their extensive laboratory work to purify the diatom samples and we thank Cindy Springer for laboratory support during oxygen isotope analysis. Ingrid Stimac and Ute Bock helped during ICP-OES and EDS analysis, respectively. Finally, we thank Antony Long and two anonymous reviewers for their constructive suggestions to improve the manuscript.

Supporting information to:

"Combined oxygen and silicon isotope analysis of diatom silica from a deglacial subarctic Pacific record"

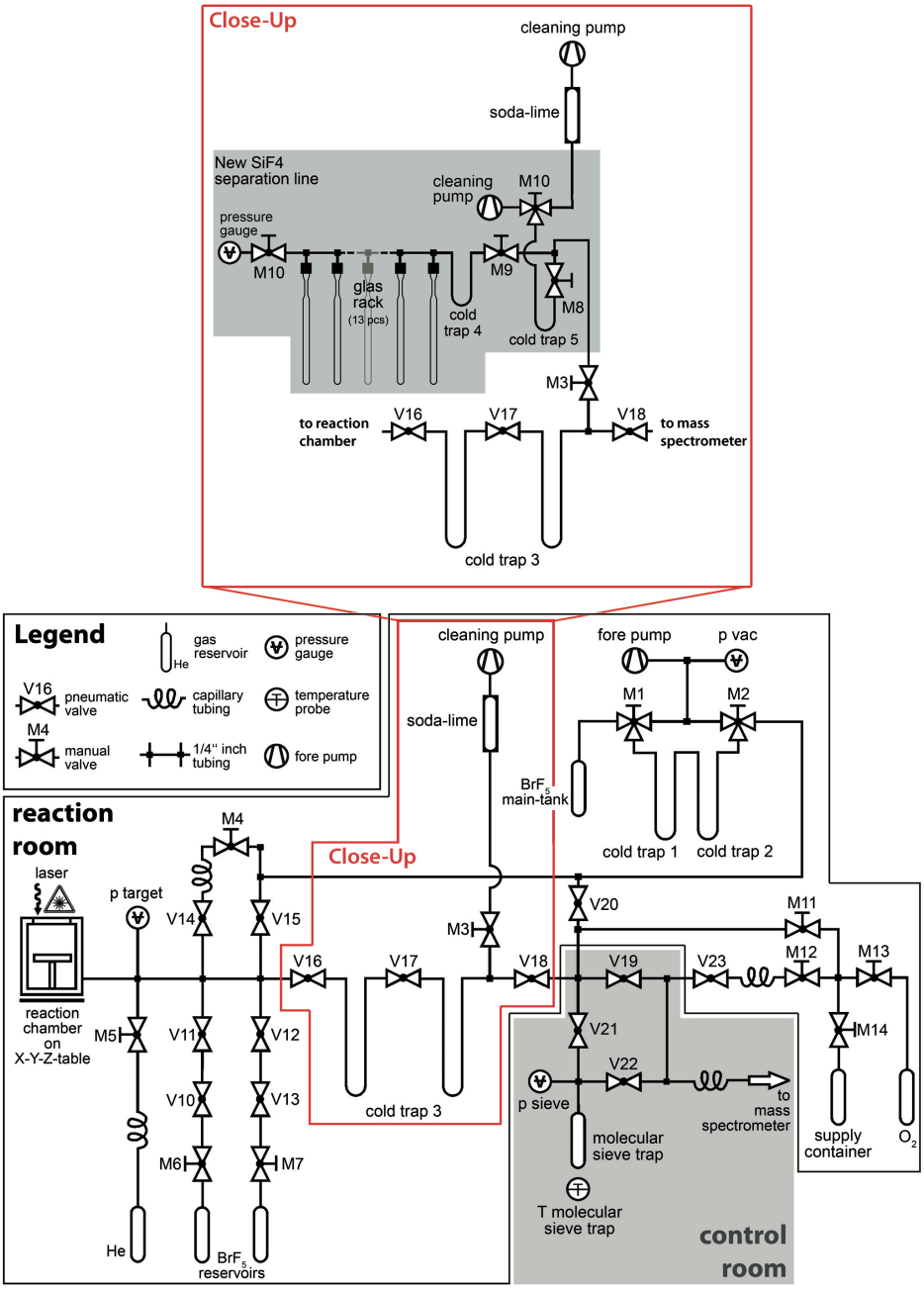

Figure S4.1. Valve chart of the laser fluorination line (Chapligin et al., 2010) with the new SiF_4 separation line (connection via M3). The separation of SiF_4 from other laser fluorination products (except O_2, which was already separated earlier) is performed according to the following procedure:
Starting point: All laser fluorination products (except O_2) are trapped in CT 3 (V16, V18 and M3 closed, V17 open) while the SiF_4 separation line is pumped down to < 1 x 10^{-3} mbar (M8, M9, M10 open, CT 5 at -196°C). Separation: CT 3 is heated from -196°C to room temperature, while CT 4 is cooled to -196°C. Then M3 is opened for 3 minutes. After all gases are transferred to CT 4, M9 is closed and CT 4 is warmed to -115°C (ethanol cooled down to freezing point with liquid N_2) to release the SiF_4 while other products stay trapped. When all SiF_4 is liberated from CT 4 a dewar containing liquid N_2 is placed underneath one of the pyrex glass tubes to freeze the SiF_4 into the tube. To ensure SiF_4 purity (Ding et al., 1996) each glass tube contains a few zinc particles (room temperature). The glass is then melted off and stored until silicon isotope analysis using a MAT252 IRMS suitable for $\delta^{29}Si$ and $\delta^{30}Si$ measurements. CT 4 is warmed to room temperature and M9 is opened to condense all by-products in CT 5 before they are disposed via a waste line (natron pellets). The separation of SiF_4 can be carried out during routine oxygen isotope measurements without major loss of time. In order to keep the whole procedure as fast as possible, we use an additional cold trap, CT 4, that otherwise is not necessarily needed in the setup. However, in order to get CT 3 ready for the next sample as quick as possible, we transferred all fluorination by-products (except O_2) to CT 4, before CT 3 was pumped to <1 x 10^{-4} and cooled down to -196°C to trap the next sample.

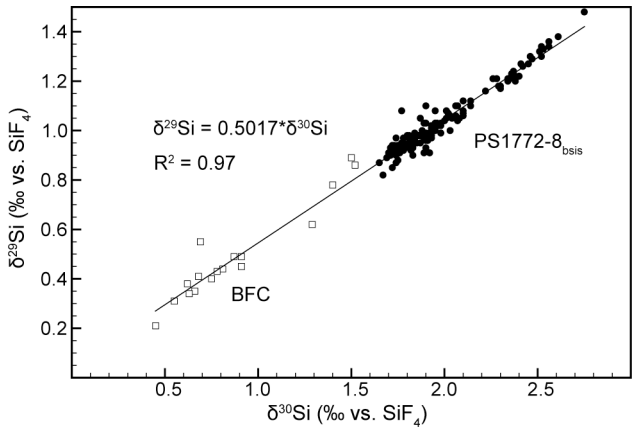

Figure S4.2. Crossplot of $\delta^{29}Si$ and $\delta^{30}Si$ of PS1772-8_{bsis} (black dots; n=140) and BFC (open squares; n=17), showing a mass-dependent fractionation of the silicon isotopes and the high purity of the SiF_4 samples.

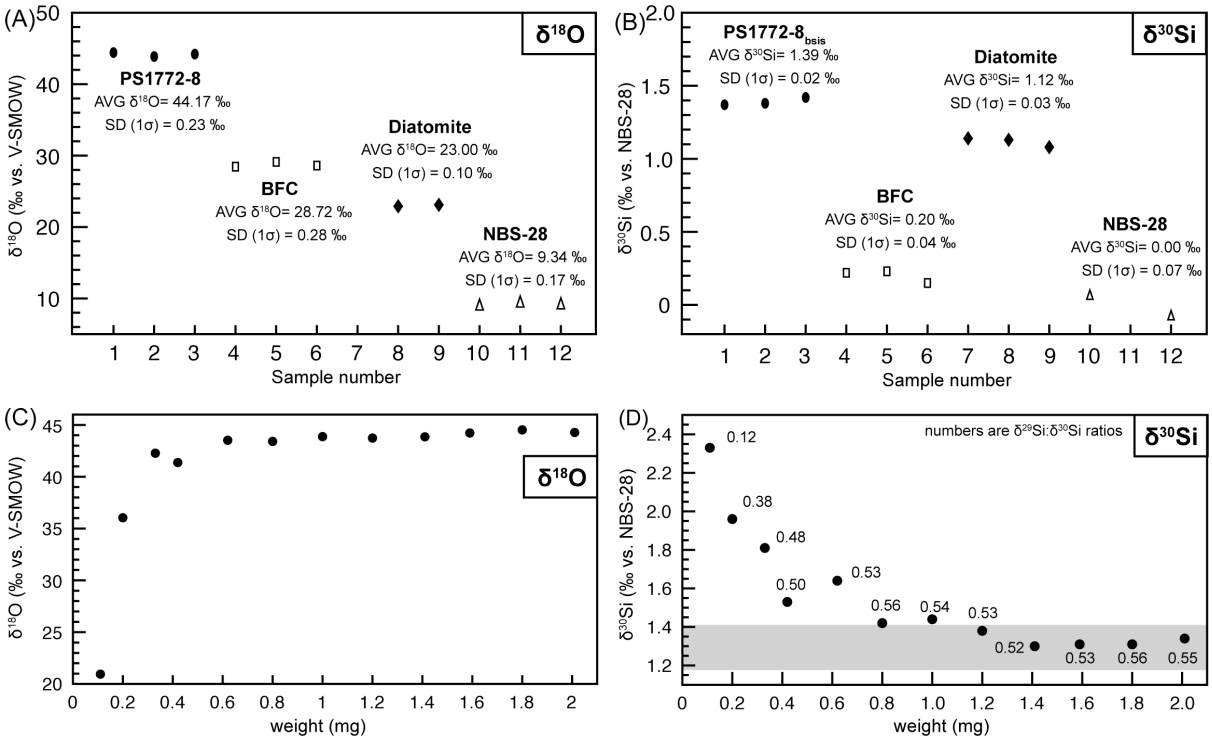

Figure S4.3. (A, B) To test if the whole instrumentation is free of memory effects the three diatom working standards and NBS-28 were measured in a continuous sample set of 12 pyrex glass tubes, with each standard measured three times. Within the sample set of 12 pyrex glass tubes, that contains four different (working) standards and each standard material three times in a row, neither oxygen isotope measurements (Fig. S4.3A) nor silicon isotope measurements (Fig. S4.3B) showed notable memory effects. Thus, the whole instrumentation (laser fluorination line, SiF_4 separation line and both mass spectrometers) is regarded to be free of any memory effects. **(C, D)** We furthermore evaluated the required minimum weight of pure diatom material for an accurate combined measurement by analysing 12 samples of PS1772-8_{bsis} consecutively, with different sample weights from 0.1 to 2.0 mg. The last two tests were performed using a different batch of PS1772-8_{bsis} ($\delta^{18}O$ = +44.15±0.19 ‰; n=22) than the one presented in Chapligin et al. (2010; 2011). The minimum sample weight regarding silicon isotope measurements is 1.2 mg (Fig. S4.3D), below which the $\delta^{30}Si$ values are out of the determined frame of +1.29±0.12 ‰ (1σ) for PS1772-8_{bsis} (grey bar). With decreasing sample weight $\delta^{30}Si$ values are increasing successively. According to Brzezinski et al. (2006), this increase may result from preferential loss of $^{28}SiF_4$. As the $\delta^{29}Si/\delta^{30}Si$ ratios get smaller with decreasing sample weight below 0.6 mg there may be an additional gas present in the SiF_4 sample, which might interfere with the $^{30}SiF_3^+$ ion on m/z ratio 87. Even though $\delta^{29}Si/\delta^{30}Si$ ratios indicate that this gas seems negligible above weights of 0.6 mg a stable signal is not reached below a minimum weight of 1.2 mg. For silica $\delta^{18}O$ measurements Chapligin et al. (2010) recommended a sample weight of 1.5-2.0 mg (determined on BFC and NBS-28) to avoid any mass-related corrections. Our $\delta^{18}O_{diat}$ data from PS1772-8_{bsis} (Fig. S4.3C) support these results for this instrumentation. Thus the minimum weight of purified diatom material required for an accurate combined $\delta^{18}O_{diat}$ and $\delta^{30}Si_{diat}$ measurement using the presented setup is about 1.5 mg.

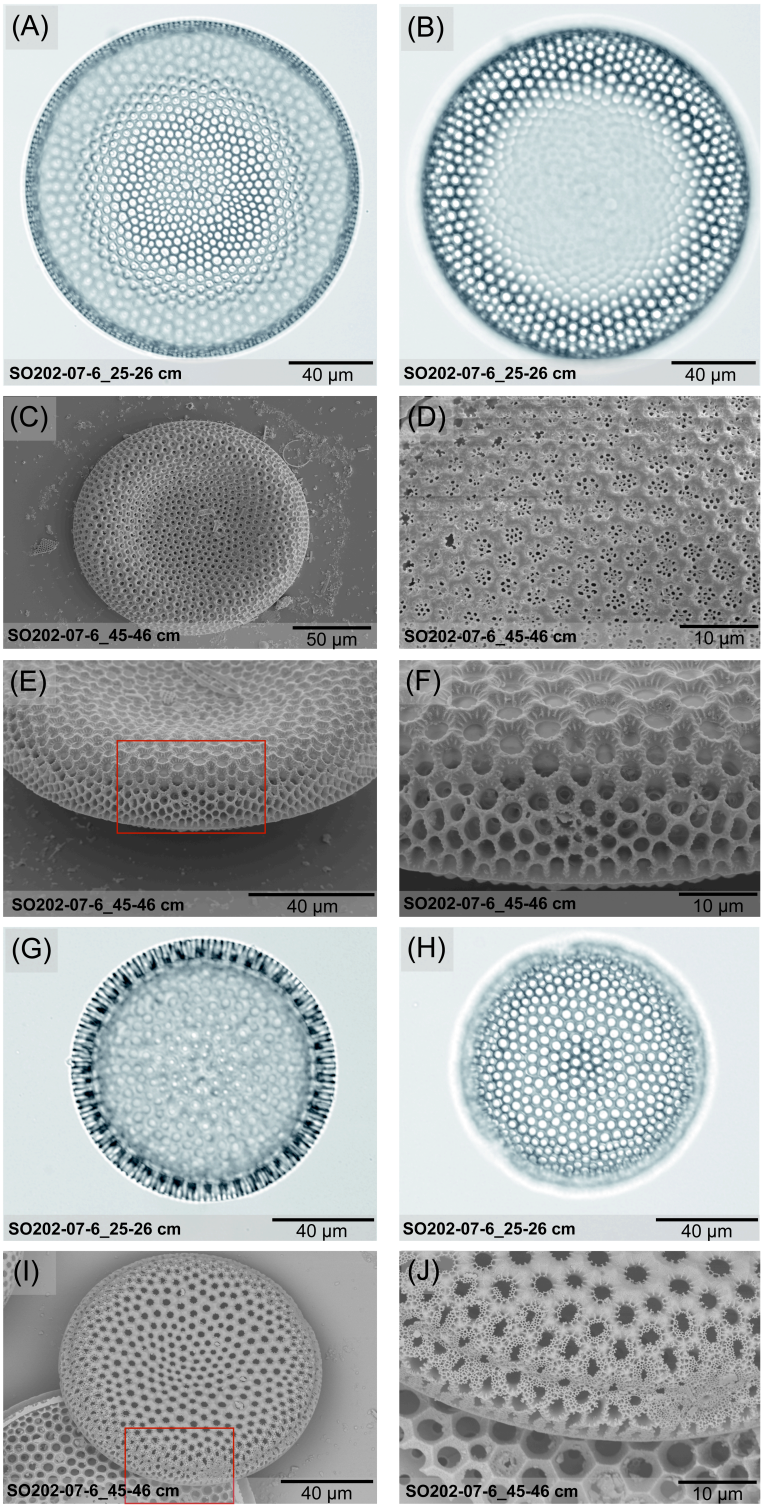

Figure S4.4. SEM and light microscopic pictures of (A)-(F) *Coscinodiscus oculus-iridis* and (G)-(J) *Coscinodiscus marginatus* from Core SO202-07-6 (50°16'N, 147°42'E, 2340 m), located close to MD01-2416. **(A)-(B)** Light microscopic pictures of *C. oculus-iridis* on two focal planes showing the (A) small margin and the central area with the rosette as well as (B) the decreasing size of areolae towards the margin. **(C)-(F)** SEM pictures of *C. oculus-iridis*. (C) External view showing the central depression. (D) Areolae with velum. (E) External view with the typical quincunx areolae in the marginal zone. (F) Detail of (E) showing the quincunx area with smaller areolae and the external openings of labiate processes right above the quincunx rows. **(G)-(H)** Light microscopic pictures of *C. marginatus* on two focal planes: (G) the coarse radially striated margin and (H) the center with no clear depression and no rosette. **(I)-(J)** SEM pictures of *C. marginatus* showing (I) no change of areolae size from the center to the margin and (J) the elongated mantle areolae with remnants of the velum (detail of (I)).

Table S4.1. Elemental compositions, determined by EDS and ICP-OES analysis, of (A) working standard PS1772-8_{bsis} and of (B) the 10-20 µm and >63 µm fraction of Core MD01-2416, including the estimated contamination with non-biogenic silicates.

(A)

PS1772-8$_{bsis}$	SiO_2	Al_2O_3	Na_2O	CaO	K_2O	MgO	FeO	TiO_2
EDS	98.95	0.12	0.61	0.06	0.13	0.09	0.05	0.01
EDS*	99.6	bdl	0.2	bdl	0.1	0.2	bdl	bdl
ICP-OES	99.29	0.08	0.45	0.04	0.06	0.05	0.01	bdl

*from Chapligin et al. (2012)

(B)

	EDS								
MD01-2416	SiO_2	Al_2O_3	Na_2O	CaO	K_2O	MgO	FeO	TiO_2	estimated non-biog. silicate contamination
10-20 µm									
4-8 cm	99.12	0.25	0.34	0.07	0.11	0.01	0.08	0.02	1.4
12-16 cm	99.17	0.20	0.37	0.04	0.09	0.02	0.09	0.02	1.3
22-26 cm	99.01	0.28	0.39	0.05	0.13	0.03	0.08	0.03	1.6
32-36 cm	99.03	0.24	0.41	0.03	0.11	0.05	0.08	0.05	1.5
52-56 cm	98.83	0.31	0.48	0.04	0.14	0.04	0.10	0.06	1.9
62-66 cm	99.00	0.20	0.52	0.02	0.11	0.05	0.09	0.01	1.4
72-76 cm	98.99	0.20	0.52	0.01	0.12	0.05	0.07	0.04	1.5
82-86 cm	98.89	0.27	0.55	0.06	0.14	0.04	0.05	0.00	1.7
92-96 cm	98.61	0.34	0.58	0.07	0.16	0.06	0.13	0.03	2.1
> 63 µm									
4-8 cm	99.17	0.10	0.50	0.03	0.12	0.02	0.06	0.00	1.1
12-16 cm	99.18	0.12	0.48	0.03	0.11	0.03	0.05	0.00	1.1
22-26 cm	99.07	0.18	0.53	0.02	0.13	0.01	0.05	0.01	1.3
32-36 cm	99.14	0.07	0.57	0.02	0.11	0.01	0.06	0.02	1.0
52-56 cm	99.08	0.11	0.62	0.02	0.13	0.00	0.04	0.00	1.2
62-66 cm	99.07	0.12	0.59	0.01	0.11	0.03	0.06	0.01	1.2
72-76 cm	99.13	0.10	0.57	0.02	0.11	0.01	0.04	0.02	1.1
82-86 cm	98.94	0.12	0.70	0.02	0.14	0.02	0.05	0.01	1.3
92-96 cm	99.03	0.11	0.64	0.02	0.12	0.03	0.05	0.00	1.2

	ICP-OES								
MD01-2416	SiO_2	Al_2O_3	Na_2O	CaO	K_2O	MgO	FeO	TiO_2	estimated non-biog. silicate contamination
10-20 µm									
4-8 cm	99.31	0.19	0.32	0.05	0.06	0.03	0.03	0.01	1.1
12-16 cm	99.07	0.25	0.39	0.10	0.09	0.05	0.04	0.01	1.4
22-26 cm	99.08	0.27	0.38	0.09	0.08	0.03	0.05	0.01	1.5
32-36 cm	99.15	0.23	0.36	0.10	0.08	0.03	0.04	0.01	1.3
52-56 cm	-	-		-	-	-	-	-	-
62-66 cm	99.18	0.20	0.41	0.06	0.07	0.03	0.04	0.01	1.2
72-76 cm	99.26	0.15	0.42	0.03	0.07	0.03	0.03	0.01	1.0
82-86 cm	99.27	0.14	0.42	0.04	0.07	0.03	0.03	0.01	1.0
92-96 cm	-	-		-	-	-	-	-	-
> 63 µm									
4-8 cm	99.47	0.12	0.34	0.03	0.00	0.01	0.01	0.00	0.8
12-16 cm	99.48	0.06	0.33	0.05	0.05	0.01	0.00	0.00	0.6
22-26 cm	99.46	0.06	0.36	0.04	0.05	0.01	0.00	0.00	0.7
32-36 cm	99.42	0.07	0.39	0.03	0.06	0.01	0.01	0.00	0.7
52-56 cm	99.46	0.04	0.41	0.02	0.05	0.01	0.00	0.00	0.6
62-66 cm	99.45	0.04	0.41	0.03	0.05	0.01	0.00	0.00	0.6
72-76 cm	99.47	0.04	0.43	0.01	0.06	0.01	0.00	0.00	0.6
82-86 cm	99.44	0.03	0.45	0.01	0.06	0.01	0.00	0.00	0.6
92-96 cm	99.41	0.03	0.45	0.03	0.06	0.01	0.00	0.00	0.7

Table S4.2. Composition of purified diatom samples of the (A) >63 µm fraction and the (B) 10-20 µm fraction, determined by light microscopy.

(A)

		> 63 µm counts								
Diatom species	state of particle	4-8 cm	12-16 cm	22-26 cm	32-36 cm	52-56 cm	62-66 cm	72-76 cm	82-86 cm	92-96 cm
Coscinodiscus marginatus	complete	7	8	4	9	12	8	2	2	7
	1/2	13	17	10	21	22	18	8	18	10
	1/4	59	46	108	175	165	122	87	171	45
Coscinodiscus oculus-iridis	complete	2	2	-	-	-	3	2	-	3
	1/2	16	8	1	4	5	15	9	5	24
	1/4	200	210	130	89	84	130	140	75	180
Coscinodiscus spp.	complete	-	-	-	-	-	1	-	-	1
	1/2	-	-	-	-	-	-	-	-	2
	1/4	21	26	48	26	31	26	61	52	59
Actinocyclus ochotensis	complete	-	-	-	-	-	-	-	1	-
	1/2	-	-	-	-	-	-	-	-	-
	1/4	-	-	-	-	-	-	-	-	-
Actinocyclus actinochilus	complete	-	-	-	1	-	-	-	-	-
	1/2	-	-	-	-	-	-	-	-	-
	1/4	-	-	-	-	-	-	-	-	-
Thalassiosira spp.	complete	-	-	1	-	-	-	1	2	-
	1/2	1	-	-	-	-	1	-	-	-
	1/4	1	1	2	-	-	-	1	-	-
Stephanopyxis turris	complete	-	-	-	-	-	-	-	1	-
	1/2	-	-	-	-	-	-	-	-	-
	1/4	-	-	-	-	-	-	-	-	-
Eucampia antarctica	complete	-	-	-	-	-	-	-	1	-
	1/2	-	-	-	-	-	-	-	-	-
	1/4	-	-	-	-	-	-	-	-	-
Radiolaria		1	1	2	3	1	-	-	1	-
Non-biogenic silicates (%)		2	-	-	-	-	-	-	-	-
Sum		**323**	**319**	**306**	**328**	**320**	**324**	**311**	**329**	**331**
Diatoms (%)		99.1	99.7	99.3	99.1	99.7	100.0	100.0	99.7	100.0
Non-*Coscinodiscus* diatoms (%)		0.6	0.3	1.0	0.3	0.0	0.3	0.6	1.5	0.0
Total contamination (%)		0.9	0.3	0.7	0.9	0.3	0.0	0.0	0.3	0.0
Non-diatom biogenic silicates (%)		0.3	0.3	0.7	0.9	0.3	0.0	0.0	0.3	0.0
Non-biogenic silicates (%)		0.6	0.0	0.0	0.0	0.0	0.0	0.0	0.0	0.0

(B)

		10-20 µm counts								
Diatom species	state of particle	4-8 cm	12-16 cm	22-26 cm	32-36 cm	52-56 cm	62-66 cm	72-76 cm	82-86 cm	92-96 cm
Actinocyclus curvatulus	complete	9	9	12	6	7	3	6	6	7
	1/2	2	1	1	-	1	-	2	1	-
	1/4	-	-	-	-	-	-	-	-	-
Actinocyclus ochotensis	complete	9	9	15	5	10	4	2	1	2
	1/2	1	-	-	-	-	1	-	-	-
	1/4	-	-	-	-	-	-	-	-	-

Table S4.2. (B) (continued).

		10-20 µm counts								
Diatom species	state of particle	4-8 cm	12-16 cm	22-26 cm	32-36 cm	52-56 cm	62-66 cm	72-76 cm	82-86 cm	92-96 cm
Actinocyclus oculatus	complete	6	1	3	1	4	-	-	-	1
	1/2	-	-	-	-	-	-	-	-	-
	1/4	-	-	-	-	-	-	-	-	-
Coscinodiscus marginatus	complete	2	2	2	2	-	1	3	1	3
	1/2	3	5	1	3	3	3	-	1	2
	1/4	8	4	9	8	6	3	10	-	10
Coscinodiscus radiatus	complete	1	-	-	-	-	3	-	1	1
	1/2	-	1	-	-	-	1	2	3	1
	1/4	-	-	-	-	-	-	-	5	-
Coscinodiscus oculus-iridis	complete	-	-	-	-	-	-	-	-	1
	1/2	1	-	-	-	-	-	-	-	-
	1/4	-	-	2	1	-	-	-	-	-
Coscinodiscus spp.	complete	-	-	-	-	-	-	-	-	-
	1/2	1	-	1	-	-	-	-	1	-
	1/4	250	250	181	250	202	200	200	150	150
Thalassiosira trifulta	complete	22	15	31	7	20	15	47	24	41
	1/2	4	10	4	3	8	10	68	23	38
	1/4	1	2	7	-	1	3	10	11	59
Thalassiosira spp.	complete	4	8	9	2	15	8	4	8	14
	1/2	3	8	9	10	10	19	13	12	8
	1/4	10	1	4	5	5	40	1	66	17
Thalassiosira antarctica	complete	1	-	9	1	3	3	-	4	1
var. borealis	1/2	-	-	1	-	-	-	-	-	-
	1/4	-	-	-	-	-	-	-	-	-
Stephanopyxis turris	complete	2	-	5	1	1	3	9	7	16
	1/2	1	-	-	-	-	2	1	2	1
	1/4	-	-	-	-	-	-	-	-	1
Actinoptychus senarius	complete	-	-	1	-	-	-	-	-	-
	1/2	-	-	-	-	-	-	-	-	-
	1/4	-	-	-	-	-	-	-	-	-
Rhizosolenia hebetata	complete	4	6	4	1	3	1	-	2	-
	1/2	-	-	-	-	-	-	-	-	-
	1/4	-	-	-	-	-	-	-	-	-
Porosira glacialis	complete	-	-	-	-	-	-	-	-	-
	1/2	-	-	-	-	-	1	-	-	-
	1/4	-	-	-	-	-	-	-	-	-
Stellarima stellaris	complete	-	-	-	1	-	4	-	1	1
	1/2	-	-	-	-	-	9	-	4	3
	1/4	-	-	-	-	-	7	-	8	2
Radiolaria		1	-	2	-	1	-	-	-	1
Siliceous sponge spicules		-	-	2	-	1	-	-	-	-
Actiniscus pentasterias		4	1	-	3	5	1	2	-	-
Non-biogenic silicates (%)		4	1	-	1	2	-	-	1	1
Sum		**354**	**334**	**315**	**311**	**308**	**345**	**380**	**343**	**382**
Diatoms (%)		97.5	99.4	98.7	98.7	97.1	99.7	99.5	99.7	99.5
Total Contamination (%)		2.5	0.6	1.3	1.3	2.9	0.3	0.5	0.3	0.5
Non-diatom biogenic silicates (%)		1.4	0.3	1.3	1.0	2.3	0.3	0.5	0.0	0.3
Non-biogenic silicates (%)		1.1	0.3	0.0	0.3	0.6	0.0	0.0	0.3	0.3

Chapter 5 – Surface water hydrography and nutrient dynamics of the deglacial subarctic Pacific – evidence from diatom oxygen and silicon stable isotopes

Maier, E.[1], Abelmann, A[1], Gersonde, R.[1], Méheust, M.[1], Chapligin, B.[2], Ren, J. [1], Tiedemann, R.[1]

[1]Alfred Wegener Institute Helmholtz Centre for Polar and Marine Research, Bremerhaven, Germany
[2]Alfred Wegener Institute Helmholtz Centre for Polar and Marine Research, Potsdam, Germany

to be submitted to Paleoceanography

Abstract

Deciphering deglacial changes in subarctic Pacific upper ocean stratification and nutrient utilization might provide important information on deglacial subarctic Pacific climate development and oceanic-atmospheric CO_2 exchange. This study presents new oxygen ($\delta^{18}O_{diat}$) and silicon ($\delta^{30}Si_{diat}$) stable isotope data, as well as new biogenic opal, subsurface foraminiferal $\delta^{18}O$ and core logging data, which give new insights into the spatial and temporal evolution of the hydrography, silicic acid utilization and productivity of the subarctic Pacific surface waters over the last glacial-interglacial transition.

Our data indicate enhanced glacial surface water stratification in the North-East (NE) Pacific, in accordance with previous studies from the subarctic Pacific realm. This stratification was related to the melting of sea-ice and icebergs, which probably discharged from the Cordilleran Ice Sheet (CIS). As surface water stratification limits the supply of nutrients from below, it provides a plausible explanation for the high glacial silicic acid utilization despite low productivity. Stratification persists into the Heinrich Stadial 1 (HS1) and the fresh surface waters during early HS1 question an increased poleward salt transport into the subarctic Pacific and thus the formation of deep-water, recently proposed for that time interval. However, a decrease in silicic acid utilization during the early HS1, when productivity is still low, indicates an increased availability of silicic acid. Ruling out deep convection, this might have been associated with the recently proposed increased North Pacific Intermediate Water formation during HS1.

At ~16 ka BP, our data indicate high silicic acid utilization and further enhanced surface water stratification in response to a massive input of freshwater, likely originating from the CIS. This meltwater input coincides with enhanced ice-rafted debris (IRD) sedimentation at the Californian margin and the Heinrich 1 IRD event in the North Atlantic, indicating a close,

dominantly atmospheric, link between the deglaciation of the CIS and the Laurentide Ice Sheet.

The Bølling/Allerød (B/A) is characterized by an increased supply of saline, silicic acid rich waters into the euphotic zone and a maximum in productivity, possibly associated with the invigorated Atlantic Meridional Overturning Circulation (AMOC). However, our data indicate that this change towards increased vertical mixing and productivity occurs prior to the onset of the Bølling. We suggest that the contemporaneous pre-Bølling change to sea-ice-free conditions in the subarctic Pacific, possibly related to a quicker response to Northern Hemisphere insolation forcing relative to the North Atlantic, might have triggered this pre-Bølling paleoceanographic change in the subarctic Pacific by weakening surface water stratification. With the onset of the Bølling, upwelling might have been further facilitated by the increased AMOC. The increased upwelling and observed decoupling of silicic acid utilization and export production in both the NE and North-West (NW) Pacific during late HS1 and the B/A might indicate an decreased efficiency of the biological pump, suggesting that the subarctic Pacific might then have been a source region of atmospheric CO_2 during late HS1 and the B/A.

5.1 Introduction

Deglacial variations in thermohaline overturning circulation are thought to have played a key role in changing atmospheric CO_2 concentrations via changes in upper ocean stratification in high latitudes (Sigman et al., 2010). Deglacial destratification especially in the Southern Ocean may have provided a pathway for CO_2 exchange between the deep ocean and the atmosphere during Heinrich Stadial 1 (HS1) (Skinner et al., 2010; Burke and Robinson, 2012), thereby increasing atmospheric CO_2 concentrations as recorded in ice cores (Monnin et al., 2001; Schmitt et al., 2012; Parennin et al., 2013). During the past decade the subarctic Pacific received increased paleoceanographic attention with the aim to examine its potential for influencing the nutrient cycle and the oceanic release of CO_2 via deep/intermediate-water formation, upwelling and associated changes in biogenic productivity. Today, the subarctic Pacific is considered a weak sink for CO_2 (Lèfevre et al., 1999; Ayers and Lozier, 2012), despite the existence of oceanic high nutrient-low chlorophyll (HNLC) regions, especially in the North-West (NW) Pacific (Fig. 5.1). Accordingly, changes in subarctic Pacific upper ocean stratification and/or biological nutrient utilization and export production have the potential to effectively influence the oceanic-atmospheric gas exchange.

Today, the subarctic Pacific is characterized by a steep salinity stratification, with the low-salinity surface waters sustained by a large freshwater flux and relatively small regional evaporation (Warren, 1983; Broecker et al., 1990). As a consequence of the halocline no deep-water is formed in the modern subarctic Pacific realm and intermediate water formation

is restricted to the marginal Sea of Okhotsk. However, these conditions may have been different during HS1. Recent studies with general circulation models (Okazaki et al., 2010; Chikamoto et al., 2012) suggest an enhanced poleward transport of salt from the subtropics to the subarctic Pacific during HS1, which preconditioned the generation of deep convective overturning in the North Pacific. However, whether deep-water formation occurred in the North Pacific or not is still a matter of debate (Jaccard, 2012; Jaccard and Galbraith, 2013; Max et al., 2013).

In addition to evidence for downwelling in the subarctic Pacific realm during the HS1 and the Younger Dryas (YD), there is evidence for deglacial upwelling that might have led to enhanced biological productivity during the Bølling-Allerød (B/A) (Galbraith et al., 2007; Kohfeld and Chase, 2011). Whether upwelling of deep, CO_2-rich water led to oceanic CO_2 release in subarctic Pacific strongly depends on the efficiency of the biological pump, which removes CO_2 from the atmosphere by biological productivity in the photic zone and transfers it to the deep ocean interior. Diatom silicon isotope records ($\delta^{30}Si_{diat}$) provide valuable information on changes in the degree of nutrient (silicic acid) utilization in surface waters (De la Rocha et al., 1998; Brzezinski et al., 2002; Reynolds et al., 2008; Maier et al., 2013), which is a function of silicic acid supply and use. Thus, $\delta^{30}Si_{diat}$ may be useful to assess changes in the efficiency of the biological pump. During biomineralization diatoms preferentially incorporate the lighter isotope (^{28}Si) into their frustules, with a mass-dependent fractionation of ca. -1.1 ± 0.4‰ (De la Rocha et al., 1997; Milligan et al., 2004) for a closed system like the subarctic Pacific (Reynolds et al., 2006), where nutrients (silicic acid, nitrate, iron) are brought to the euphotic zone by vertical mixing during autumn/winter (Harrison et al., 1999). While the last glacial interval in the NW Pacific realm and marginal seas is characterized by low biogenic productivity and high nutrient (nitrate) utilization, possibly related to a strong surface water stratification and increased iron availability (Brunelle et al., 2007; 2010), the relationship between export production, nutrient utilization and the strength of surface water stratification is less clear for the last deglaciation. Recently, the co-occurence of high export production and high diatom nitrogen isotope values ($\delta^{15}N_{diat}$) values during the B/A has been related to a transient stratification event (Lam et al., 2013). However, comparatively low $\delta^{30}Si_{diat}$ indicate low silicic acid utilization during the B/A and, together with diatom oxygen isotope records ($\delta^{18}O_{diat}$), point to an increased influx of silicic acid into the NW Pacific productivity zone during the B/A (Maier et al., 2013).

Here, we present diatom $\delta^{18}O_{diat}$ and $\delta^{30}Si_{diat}$ records from the open North-East (NE) Pacific (Core SO202-27-6, Gulf of Alaska), to investigate the development of surface waters in the open subarctic NE Pacific over the last glacial-interglacial transition. The isotopic results are compared to deglacial $\delta^{18}O_{diat}$ and $\delta^{30}Si_{diat}$ records from the NW Pacific (Core MD01-2416,

western subarctic gyre) (Maier et al., 2013; this study). The low biogenic opal concentration of ~5 wt-% (Gebhardt et al., 2008; this study) during the last glacial and HS1 did not allow for a pre-Bølling extension of the NW Pacific isotopic records, while the kasten core from the NE Pacific provided enough diatom material for isotope analyses of the glacial and early deglacial period. Our results, in combination with new subsurface foraminiferal *Neogloboquadrina pachyderma*$_{sin}$ stable isotope data ($\delta^{18}O_{Nps;}$ $\delta^{13}C_{Nps}$), X-ray fluorescence (XRF) data, biogenic opal data, as well as previously published nitrogen isotope data (Galbraith et al., 2008; Studer et al., 2013), diatom counting data (Ren et al., in prep.) and alkenone-based sea surface temperature (SST) and sea-ice data (Méheust et al., in prep.),

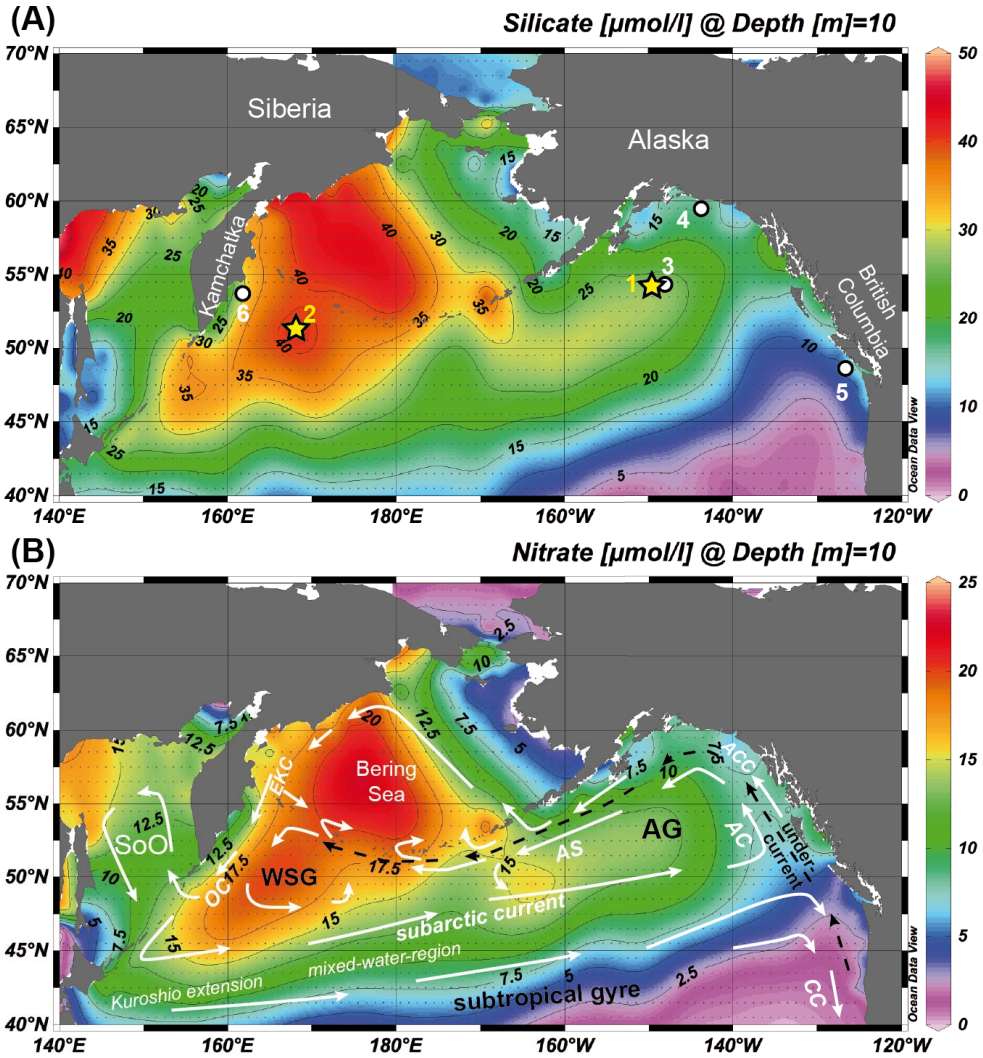

Figure 5.1. (A) Mean annual silicic acid concentration of subarctic Pacific surface waters (Garcia et al., 2010) as well as locations of cores investigated in this study (yellow stars) and of other cores mentioned in the text (white circles): **1)** SO202-27-6 (54°18'N, 149°36'W, 2929 m); **2)** MD01-2416 (51°16'N, 167°44'E, 2317 m) and SO202-07-6 (51°16'N, 167°42'E, 2340 m); **3)** MD02-2489 (54°34'N, 148°55'W, 3640 m) and ODP 887 (54°22'N, 148°27'W, 3633 m); **4)** EW0408-85JC (59°33'N, 144°9'W, 682 m); **5)** MD02-2496 (48°58'N, 127°2'W, 1243 m); **6)** SO201-2-12 (53°59'N, 162°23'E, 2145 m). **(B)** Mean annual nitrate concentration of the subarctic Pacific surface waters (Garcia et al., 2010) as well as (sub-)surface water currents (after Dodimead et al., 1963): AC: Alaska Current; ACC: Alaska Coastal Current; AS: Alaskan Stream; EKC: East Kamchatka Current; OC: Oyashio Current; CC: California Current. SoO: Sea of Okhotsk; WSG: western subarctic gyre; AG: Alaskan gyre. The dashed black line represents the subsurface countercurrent. The maps were created with Ocean Data View (www.odv.awi.de).

provide excellent information into the spatial and temporal evolution of the hydrography and silicic acid utilization of subarctic Pacific surface waters. Our data (1) give new insights into the deglacial meltwater history of the CIS, thereby questioning an increased poleward salt transfer during HS1 (as suggested by model results), (2) indicate a pre-Bølling climatic change and (3) suggest deep vertical mixing during late HS1 and the B/A, with the subarctic Pacific likely acting as a source of atmospheric CO_2.

5.2 Modern regional oceanography and nutrient cycling

The surface circulation in the modern subarctic Pacific is dominated by the wind-driven cyclonic motion of the Subarctic Gyre, which contains two prominent cyclonic circulation systems: the Western Subarctic Gyre in the West and the Alaskan Gyre in the East (Fig. 5.1). The shelf circulation in the NE Pacific is largely isolated from the open ocean circulation, but confined to the high speed Alaskan Coastal Current (ACC), which is strongly influenced by freshwater input from the coast (Allen et al., 1983; Stabeno et al., 2004). Several passages between the Aleutian Islands allow for subarctic Pacific waters to enter the Bering Sea, where surface waters follow a cyclonic motion. The East Kamchatka Current brings surface waters back into the subarctic Pacific through the Kamchatka Strait. Subsurface circulation strongly resembles surface water circulation, but a subsurface countercurrent transports waters from the eastern tropical North Pacific into the subarctic Pacific (Dodimead et al., 1963).

Nutrient cycling in the subarctic Pacific is strongly linked to the permanent halocline, which limits diapycnal vertical mixing between the nutrient-rich deeper waters and the more nutrient-depleted surface waters, resulting in strong vertical macronutrient (silicic acid, nitrate) gradients that largely coincide with the halocline (Andreev et al., 2002). After the input of nutrients by autumn/winter mixing diatom-dominated phytoplankton blooms develop during spring due to the formation of a shallow thermocline in combination with increasing light availability (Harrison et al., 1999). Over the course of spring and summer nutrients are progressively consumed. During autumn, cooling of surface waters and the breakdown of the thermal stratification brings new nutrients into the euphotic zone, resulting in a second bloom. The autumn bloom is generally dominated by coccolithophores, but certain diatom genera, e.g *Coscinodiscus* spp., flourish under autumn conditions (Takahashi, 1986; Kemp et al., 2000). Water column profiles from the NW Pacific show increased $\delta^{30}Si(OH)_4$ values towards the surface (Reynolds et al., 2006), related to the silicon isotope fractionation of diatoms (De la Rocha et al., 2000). In the depth range between 100-1200m the dissolution of sinking biogenic silica brings lighter silicon isotopes to intermediate depths and leads to a downward increase in Si concentrations (Reynolds et al., 2006). Deeper waters are characterized by high silicic acid concentrations and are composed of North Pacific Deep Water, likely influenced by Antarctic Bottom Water below ca. 1500m (Reynolds et al., 2006).

5.3 Material and Methods

We sampled the top 91 cm of kasten Core SO202-27-6 from the open Gulf of Alaska (Patton Seamount, NE Pacific) (Fig. 5.1), which was recovered during the Innovative NOrth Pacific EXperiment (INOPEX) cruise in summer 2009. The core was sampled every 4-5 cm for combined diatom $\delta^{18}O_{diat}$ and $\delta^{30}Si_{diat}$ analysis, every 4 cm for $\delta^{18}O$ and $\delta^{13}C$ analysis of planktic foraminifer *N. pachyderma*$_{sin}$ and every 1-4cm for the determination of the biogenic opal concentration. Furthermore, we increased the resolution of the previously published diatom $\delta^{18}O_{diat}$ and $\delta^{30}Si_{diat}$ record from the NW Pacific Core MD01-2416 (Fig. 5.1; Maier et al., 2013) by intercalating six new $\delta^{18}O_{diat}$ and $\delta^{30}Si_{diat}$ measurements over the deglacial to Holocene period.

5.3.1 Diatom sample preparation and diatom sample composition

Sixteen bulk samples (2-cm-thick) from kasten Core SO202-27-6, and six bulk samples (2-cm-thick) from piston Core MD01-2416, were prepared for diatom isotope analyses using a combination of physical and chemical treatments (Maier et al., 2013). Briefly, after samples were liberated from carbonates and organic matter, samples were prepared using various sieving steps, sonication and treatments with heavy liquids. After a first heavy liquid separation, where most of the lithic fragments were removed, we chose the 100-125 µm fraction for Core SO202-27-6 to be purified further. Prior to the sonication procedure, which led to the shattering of certain amounts of diatom valves, we prepared microscopic slides to estimate the diatom species composition. On average ca. 200 biogenic opal components (diatoms, radiolarians, sponge spicules) were counted using a Zeiss Axioskop I at x400 magnification, following the counting approach described in Maier et al. (2013). Diatoms were identified following the taxonomy of Sancetta (1982, 1987). Since the continuative sonication separates the majority of radiolarians and sponge spicules from the diatom material

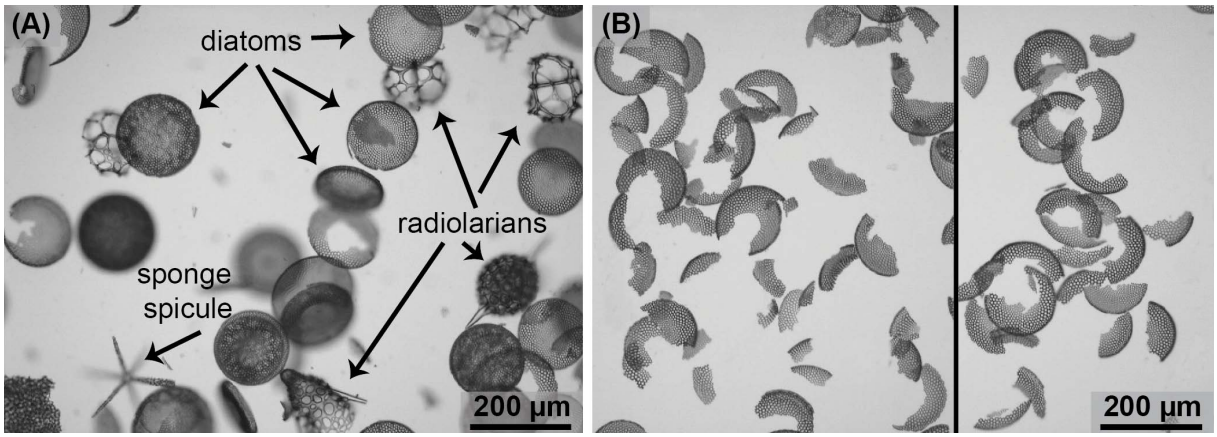

Figure 5.2. SO202-27-6 diatom sample from core depth 77-79 cm in two steps of purification process (pictures were taken using a ProgRes C10 plus digitale camera coupled to a Zeiss Axioplan II light microscope). **(A)** Diatom sample after heavy liquid separation and prior to sonification. **(B)** Purified diatom sample.

(Fig. 5.2), thereby enriching the diatom material, the radiolarian/sponge spicule content, in contrast to the diatom species composition, cannot be regarded largely representative of the final purified diatom sample. This is however, particularly important for the $\delta^{30}Si_{diat}$ record, since siliceous sponge spicules have shown to harbor $\delta^{30}Si$ values ranging from ca. +0.5‰ and -5.7‰ (Hendry and Robinson, 2012), and $\delta^{30}Si$ values of radiolarians may be as low as ca. – 3.1‰ (A. Abelmann, pers. comm.), while $\delta^{30}Si_{diat}$ values are generally harboring positive values (e.g. De la Rocha et al., 1998; Brzezinski et al., 2002; Maier et al., 2013). The contribution of radiolarians and sponge spicules to the final purified diatom samples was estimated under a Philips XL 30 ESEM scanning electron microscope by counting on average ~340 silica particle equivalents at x350 magnification. Concerning Core MD01-2416, we purified the >63 µm fraction, based on two reasons. First, the samples should be comparable to the samples presented by Maier et al. (2013). Second, the low biogenic opal concentration in the sediment (<5-10 wt-%) did not allow for a further limitation of the >63 µm fraction.

As contamination with non-biogenic silicates (rock fragments, minerals) may influence especially the oxygen isotope value of biogenic silica (Brewer et al., 2008), all purified diatom samples were checked for such contamination using energy dispersive spectrometry (EDS) (Chapligin et al., 2012; Maier et al., 2013). At two depths of Core SO202-27-6 (10 cm and 22 cm) additional inductively coupled plasma optical emission spectrometry (ICP-OES) measurements according to Chapligin et al. (2012) were performed to assure on the validity of EDS measurement. We used Al_2O_3 as a tracer for contamination of non-biogenic silicates (Brewer et al., 2008; Maier et al., 2013) following the conservative quantification approach described by Maier et al., (2013), i.e. assuming a comparatively high SiO_2/Al_2O_3 ratio of 2.2 (Eggiman et al., 1980) for non-biogenic silicates and that all Al comes from contamination by non-biogenic silicates. To decipher the influence of non-biogenic silicates on the measured $\delta^{18}O_{diat}$ and $\delta^{30}Si_{diat}$ signals we used mass balance corrections based on Brewer at al. (2008), thereby removing the potential isotopic effects of the non-biogenic silicates according to the following equations:

$$\delta^{18}O_{model} = \delta^{18}O_{diat} + (\%cont \times \delta^{18}O_{cont}) \quad (1)$$

$$\delta^{30}Si_{model} = \delta^{30}Si_{diat} + (\%cont \times \delta^{30}Si_{cont}) \quad (2)$$

where $\delta^{18}O_{diat}$ and $\delta^{30}Si_{diat}$ are the measured isotopic values, %cont is the EDS-determined non-biogenic silicate contamination and $\delta^{18}O_{cont}$ and $\delta^{30}Si_{cont}$ are the isotopic values for the contamination. The $\delta^{30}Si$ of non-biogenic silicates ranges between ca. -2.5 and +1.8 ‰ (Douthitt, 1982; Ding et al., 1996; Ziegler et al., 2005), while their $\delta^{18}O_{cont}$ signal usually range from +2 ‰ to +30 ‰ (Taylor, 1968; Sheppard and Gilg, 1996). To cover the possible range of the influence from such a contamination we applied two different $\delta^{18}O_{cont}$ values (0 ‰, +20.00 ‰) and $\delta^{30}Si_{cont}$ values (-2.50 ‰, +1.80 ‰).

5.3.2 Stable isotope measurements

To monitor surface water conditions 22 purified diatom samples, 16 samples from Core SO202-27-6 and six samples from Core MD01-2416, were measured at the Alfred Wegener Institute Helmholtz Centre for Polar and Marine Research (AWI) (Potsdam and Bremerhaven), using combined silica $\delta^{18}O$ and $\delta^{30}Si$ analyses according to Maier et al. (2013) and Chapligin et al. (2010) and 1.5-2.0 mg of purified diatom material. Values are reported in the common δ-notation vs. V-SMOW (Vienna Standard Mean Ocean Water) for oxygen isotopes and vs. NBS-28 for silicon isotopes. Analytical precision was better than 0.25‰ for $\delta^{18}O_{diat}$ (Chapligin et al., 2011) and better than 0.12‰ for $\delta^{30}Si_{diat}$ measurements (Maier et al., 2013). Diatom samples were measured at least twice when enough purified material was available.

Information on the subsurface water development was achieved by analyzing the $\delta^{18}O$ and $\delta^{13}C$ values of planktic foraminifer *Neogloboquadrina pachyderma*$_{sin}$., which are believed to calcify at the bottom of the thermocline (Bauch et al., 2002). *N. pachyderma*$_{sin}$ were picked from the 125-250 µm (19 samples), the 315-400 µm (2 samples) and the >400 µm (1 sample) fraction. Isotope measurements were performed at the AWI (Bremerhaven) using a MAT 251 mass spectrometer directly coupled to an automated carbonate preparation device (Kiel I) and calibrated via NIST-19 international standard to the PDB scale. All values are given in δ-notation vs. V-PDB (Vienna Pee Dee Belemnite). The precision of the measurements at 1σ, based on repeated analyses of an internal laboratory standard (Solnhofen limestone) over a 1-year period, was better than 0.08‰ and 0.06‰ for oxygen and carbon isotopes, respectively.

5.3.3 Estimation of local surface seawater $\delta^{18}O$ ($\delta^{18}O_{sw}$)

We estimated past changes in sea surface salinity (SSS) in the NE Pacific from local surface $\delta^{18}O_{sw}$ by correcting the $\delta^{18}O_{diat}$ record for temperature and global ice-volume/sea level. $\delta^{18}O_{diat}$ was corrected for temperature using the approach of Juillet-Leclerc and Labeyrie (1987) and the alkenone-based SSTs from Méheust et al. (in prep.). $\delta^{18}O_{sw}$ was then corrected for global ice-volume/sea level, using the approach of Waelbroeck et al. (2002). Considering the poor knowledge of the relationship between salinity and $\delta^{18}O_{sw}$ for the studied site, we used the estimated local surface $\delta^{18}O_{sw}$ as first-order indicator for changes in SSS.

5.3.4 X-ray fluorescence (XRF) core logging

The relative elemental composition (counts per second; cps) of Core SO202-27-6 was measured at 1 cm resolution using an Avaatech X-ray fluorescence (XRF) core scanner located at the AWI (Bremerhaven). Altogether three measurements were performed at 1 mA with varying tube voltages (10 kV, 30 kV, 50 kV) to allow for the mapping of a large quantity of elements. Counting time was set to 30 seconds. The relatively light elements Si, Ti, Fe and

Ca presented here were obtained from the scan at 10 kV. We used the Fe and Ca XRF records to help creating an age model (see *Section 5.3*) and the Si/Ti ratio as supporting information on relative changes in the content of biogenic opal within the sediment.

5.3.5 Biogenic opal

We determined the concentration of biogenic opal within 33 bulk samples of Core SO202-27-6 à ca. 20 mg at the AWI (Bremerhaven), following the automated leaching method of Müller and Schneider (1993). Biogenic opal (weight-%) values were calculated from the biogenic silica concentration adding 10% H_2O bound in the skeleton and correcting for the concentrations of salt in the input sample after Kuhn (2013). Weight-% of biogenic opal from 10 samples, of which we had information on dry bulk density, were converted into mass accumulation rates (MAR) of opal to compensate for effects of percentage dilution of biogenic silica by other sediment particles. As supporting information on relative changes in the concentration of biogenic opal we used the Si/Ti ratio from XRF core logging (see *Section 5.3.4*). We use the changes in biogenic opal concentration, opal mass accumulation rates (MAR) and Si/Ti as qualitative indicators for changes in export production and paleoproductivity.

5.3.6 Radiocarbon

Six samples of planktic foraminifer *Neogloboquadrina pachyderma*$_{sin}$ were picked from the 125-250 µm fraction of Core SO202-27-6 and analysed for radiocarbon by accelerator mass spectrometry (AMS) at the National Ocean Science AMS facility (NOSAMS) at Woods Hole Oceanographic Institution (Table 5.1).

5.4 Chronologies

To create the age model for Core SO202-27-6 we used its proximity to Core MD02-2489, for which an independent age model has been created, based on the ^{14}C–plateau tuning procedure of Sarnthein et al. (2007), by Gebhardt et al. (2008). This age model was recently improved by Sarnthein et al. (2013), who correlated the marine ^{14}C-plateaus, detected within the high-resolution ^{14}C record of Core MD02-2489 (Gebhardt et al., 2008; Sarnthein et al., 2013), to atmospheric ^{14}C-plateaus, identified within the very well calibrated, high-resolution Lake Suigetsu record of atmospheric ^{14}C (Bronk Ramsey et al., 2012). We assigned a suite of three ^{14}C-plateaus identified within Core MD02-2489 (Plateaus I, IIa and IIb) to Core SO202-27-6, using a combination of raw ^{14}C ages and the correlation of XRF and biogenic opal data (Fig. 5.3). Based on this assignment we determined five age control points, which are the calibrated ages of the ^{14}C-plateau boundaries. Outside of the plateaus we calibrated the raw ^{14}C ages of Core SO202-27-6 with the CALIB 7.0 software and the Marine13 calibration dataset (Stuiver and Reimer, 1993; Reimer et al., 2013), using different reservoir ages (Table

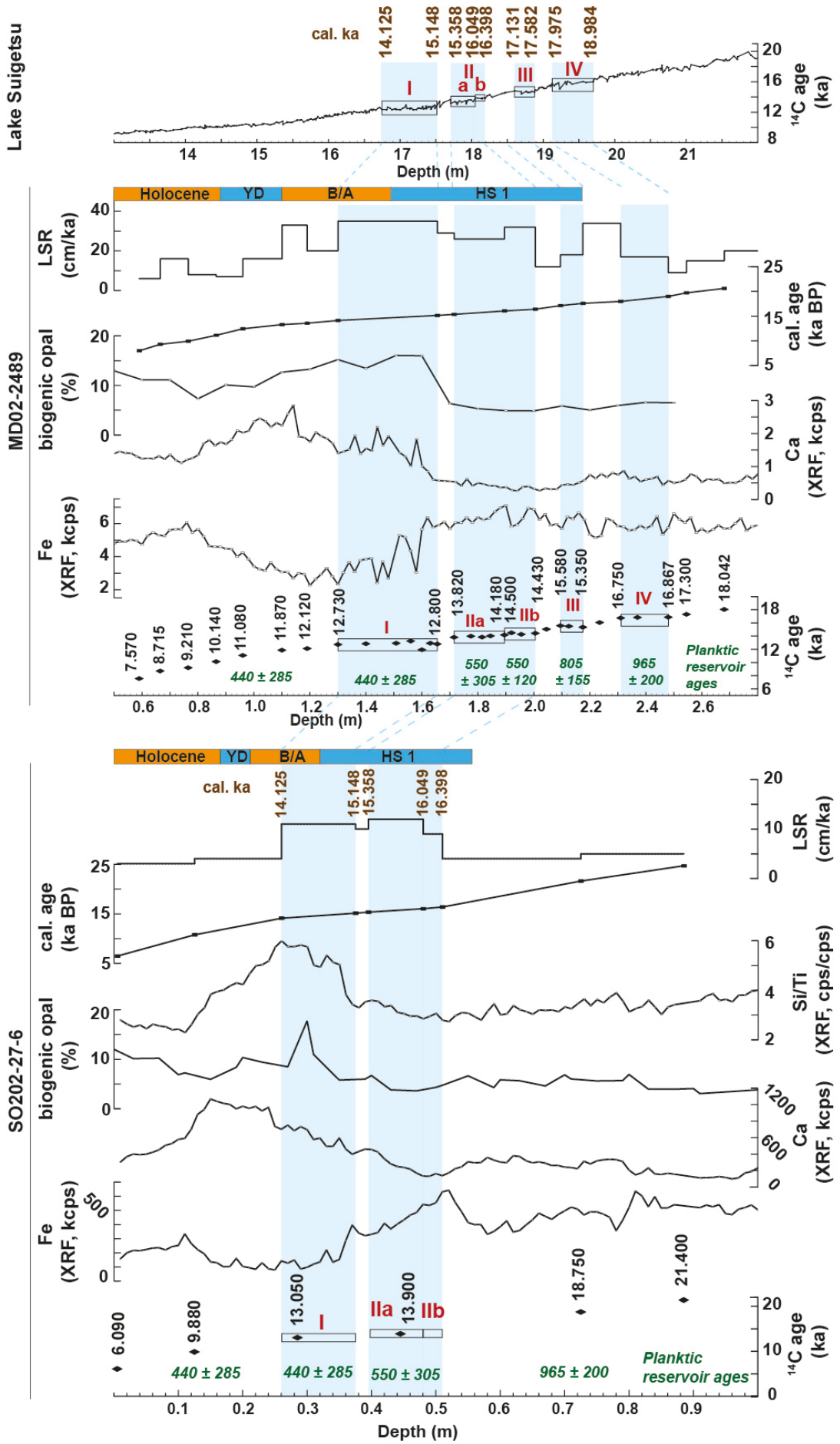
Lake Suigetsu
cal. ka
14.125
15.148
15.358
16.049
16.398
17.131
17.582
17.975
18.984
I
II
a b
III
IV
14C age (ka)
Depth (m)
MD02-2489
Holocene
YD
B/A
HS 1
LSR (cm/ka)
biogenic opal (%)
cal. age (ka BP)
Ca (XRF, kcps)
Fe (XRF, kcps)
7.570
8.715
9.210
10.140
11.080
11.870
12.120
12.730
12.800
13.820
14.180
14.500
14.430
15.580
15.350
16.750
16.867
17.300
18.042
440 ± 285
550 ± 305
550 ± 120
805 ± 155
965 ± 200
Planktic reservoir ages
SO202-27-6
Si/Ti (XRF, cps/cps)
6.090
9.880
13.050
13.900
18.750
21.400
440 ± 285
550 ± 305
965 ± 200

Figure 5.3.

Figure 5.3. Age models of cores SO202-27-6 and MD02-2489. Used data: Lake Suigetsu record of atmospheric ^{14}C from Bronk Ramsey et al. (2012). Core MD02-2489: The ^{14}C record is taken from Gebhardt et al. (2008) and Sarnthein et al. (2013) and biogenic opal and XRF data are from Gebhardt et al., 2008). Planktic reservoir ages according to Sarnthein et al. (2013). Red Roman numbers indicate ^{14}C-plateaus (I, IIa, IIb, III, IV) following the classification of Sarnthein et al. (2007).

5.1). We applied a reservoir age of 440 ± 285 a for the ^{14}C values above Plateau I and of 965 ± 200 a for the ^{14}C values below Plateau IIb, which correspond to the reservoir ages determined by Sarnthein et al. (2013) for the time of the ^{14}C-plateau closest to the ^{14}C age. In between the nine determined age control points (correlated calibrated ^{14}C plateau age boundaries and calibrated ^{14}C ages) we used linear interpolation to create our age model.

Compared to Sarnthein et al. (2013) we set slightly different boundaries for some ^{14}C-plateaus within the Lake Suigetsu radiocarbon record, resulting in slightly different calibrated ages for the start and end of concerned ^{14}C-plateaus. The average deviation between our calibrated ^{14}C-plateau boundary ages and the ages determined by Sarnthein et al. (2013) is 57 ± 92 a, with a maximum and minimum deviation of 240 a and 0 a, respectively. Based on this shift we created new age models for the uppermost sections of Cores MD01-2416 and MD02-2489 (Fig. 5.3; Table S5.1) as follows: We correlated three ^{14}C-plateaus within the radiocarbon record of MD01-2416 (Plateaus Ia, I, II) and five ^{14}C-plateaus within the radiocarbon record of MD02-2489 (Plateaus I, IIa, IIb, III, IV) to the Lake Suigetsu atmospheric ^{14}C record. Regarding MD01-2416, this is in contrast to Sarnthein et al. (2013), who suggested that parts of Plateau IIa and IIb are also visible in the ^{14}C record. We calibrated the raw ^{14}C ages of MD02-2489 and MD01-2416 outside of the identified ^{14}C-plateaus using the CALIB 7.0 software as described above (Table S5.1). For the calibration we applied the reservoir ages determined by Sarnthein et al. (2013) for the respective ^{14}C-plateaus (Fig. 5.3, Table S5.1).

The proxies from cores MD01-2416 and MD02-2489 shown in this study are plotted against the updated timescale. It is important to note that the updated age models of both Sarnthein et al. (2013) and this study support a pre-Bølling paleoceanographic change in NE Pacific Core MD02-2489, as originally presented by Gebhardt et al. (2008) and observed in Core SO202-27-6 (see *Section 5.6.2.3*). This is in contrast to the NW Pacific Core MD01-2416, which showed a pre-Bølling paleocenographic change on the original timescale (Sarnthein et al., 2007), but which was shifted close to the HS1-B/A boundary by the updated age models (Figs. 5.5, 5.6). However, we suggest that a pre-Bølling paleocenographic change represents a true feature of both the NE and the NW Pacific sites, based on three arguments. First, a shift of the observed paleoceanographic change in the Core SO202-27-6 to the HS1-B/A boundary would require a planktic reservoir age of about 1500 years, which is several hundred years higher than all known previously calculated/assumed reservoir ages for this time slice in the NE Pacific (e.g. De Vernal and Pederson, 1997; Kovanen and Easterbrook, 2002; Galbraith et

Table 5.1. Planktic (*N. pachyderma*$_{sin}$) radiocarbon ages and calibrated ages of Core SO202-27-6. Reservoir ages were assigned from nearby Core MD02-2489 (Sarnthein et al., 2013). Uncertainties of the ^{14}C plateau boundaries (1σ) were coarsely estimated as the sum of the ^{14}C dating errors of the marine and the correlated Lake Suigetsu ^{14}C samples plus the error of the Lake Suigetsu varve counting. Since the assigned plateau boundaries are in between ^{14}C ages we used the higher ^{14}C error.

								Calib 7.0 calibrated ages (ka BP)			
Sample ID	Depth (cm)	^{14}C age (ka)	^{14}C age error (a)	Reservoir age (a)	Calibrated ages (ka BP)	Derivation of cal. age	Uncertainty plateau boundaries (a; 1σ)	Median (ka BP)	2σ min (ka BP)	2σ max (ka BP)	Relative area under probability distribution
OS-85661	0.5	6.090	30	440 ± 285	**6.493**	Calib 7.0	-	6.493	5.878	7.156	1
OS-85752	12.5	9.880	30	440 ± 285	**10.781**	Calib 7.0	-	10.781	10.077	11.681	1
-	26.5	-	-	440 ± 285	**14.125**	Plateau I	318	-	-	-	-
OS-87903	28.5	13.050	55	440 ± 285	14.347	Plateau I	-	-	-	-	-
-	37.5	-	-	440 ± 285	**15.148**	Plateau I	334	-	-	-	-
-	39.5	-	-	550 ± 305	**15.358**	Plateau IIa	371	-	-	-	-
OS-85753	44.5	13.900	30	550 ± 305	15.764	Plateau IIa	-	-	-	-	-
-	48.0	-	-	550 ± 305/120	**16.049**	Plat. IIa/IIb	464	-	-	-	-
-	51.0	-	-	550 ± 120	**16.398**	Plateau IIb	373	-	-	-	-
OS-87888	72.5	18.750	70	965 ± 200	**21.640**	Calib 7.0	-	21.640	21.044	22.220	1
OS-87894	88.5	21.400	120	965 ± 200	**24.732**	Calib 7.0	-	24.732	24.119	25.333	1

bold: age control points

al., 2008; Gebhardt et al., 2008; Lund et al., 2011). Second, a tight constraint of the HS1-B/A boundary in NW Pacific Core SO202-07-6, based on the similarity of deglacial patterns between proxies of atmospheric dust from SO202-07-6 (Fig. 5.1) and the NGRIP ice core (Ruth et al., 2007) (Appendix A.1), showed a pre-Bølling change of paleoceanographic proxies, e.g. increase in biogenic opal content, taken from the same homogenized samples as the dust samples (S. Serno, unpubl. data). Third, pollen data from an independently dated (varve counted) Japanese Lake Suigetsu sediment core also indicate a paleoclimate change preceding the onset of the Bølling event in the North Atlantic (Nakagawa et al., 2003).

5.5 Results

5.5.1 Diatom species composition and contamination

Various studies have demonstrated the importance to consider diatom species composition and potential contamination with non-diatom silicates when interpreting $\delta^{18}O_{diat}$ and $\delta^{30}Si_{diat}$ records (Brewer et al., 2008; Swann et al., 2008; Chapligin et al., 2012; Egan et al., 2012; Maier et al., 2013). The contamination with non-biogenic silicates (minerals, rock fragments) is generally below 4.0% for all measured diatom samples from both sediment cores, with two exceptions from Core SO202-27-6: the core top sample (4.2%) and the lowermost sample of the studied section (6.0%). NE Pacific samples are on average twice as contaminated (2.6%) as the NW Pacific samples (1.2%). The non-biogenic silicates contamination of diatom samples from Core MD01-2416 varies between 1.0 and 1.7% (Maier et al., 2013; this study, Table S5.2), while the diatom samples from Core SO202-27-6 are more heterogeneous regarding the contamination with non-biogenic silicates (1.1-6.0%). The mass-balance

corrections for Core SO202-27-6 show that even though a removal of the isotopic effects due to contamination results in a shift towards lighter (or heavier, which is the case for some $\delta^{30}Si_{diat}$ samples assuming a $\delta^{30}Si_{cont}$ of +1.8‰) values, the deglacial to Holocene variations are far from being leveled out (Fig. 5.4), indicating that the large amplitudes occurring in the isotopic records are not attributed to contamination with non-biogenic silicates.

Maier et al. (2013) demonstrated that the effects of non-diatom biogenic silicates on the isotopic signals are negligible for the MD01-2416 samples. Concerning SO202-27-6, the microscopic slides prior to sonication show a high occurrence of radiolarians (47% and 62% of all counts) in the 53-cm and 57-cm samples, while radiolarian occurrence was between 3 and 34% in all other pre-sonication slides. Counts of SEM samples of the purified diatom samples show that the content of radiolarians is generally reduced to ~5% (between 1 and 10%) in the purified samples and the radiolarian contents within the 53-cm and 57-cm samples are not higher than the contents within the samples directly below and above (Table S5.3). Sponge spicules are estimated to contribute between 0 and 3% in the pre-sonication samples, while the final purified samples contain sponge spicules between 0 and 1% (Table S5.3). Maier et al. (2013) showed that the diatom species composition of the >63 µm fraction of Core MD01-2416 solely (98.5-100%) consists of the diatom genus *Coscinodiscus*.

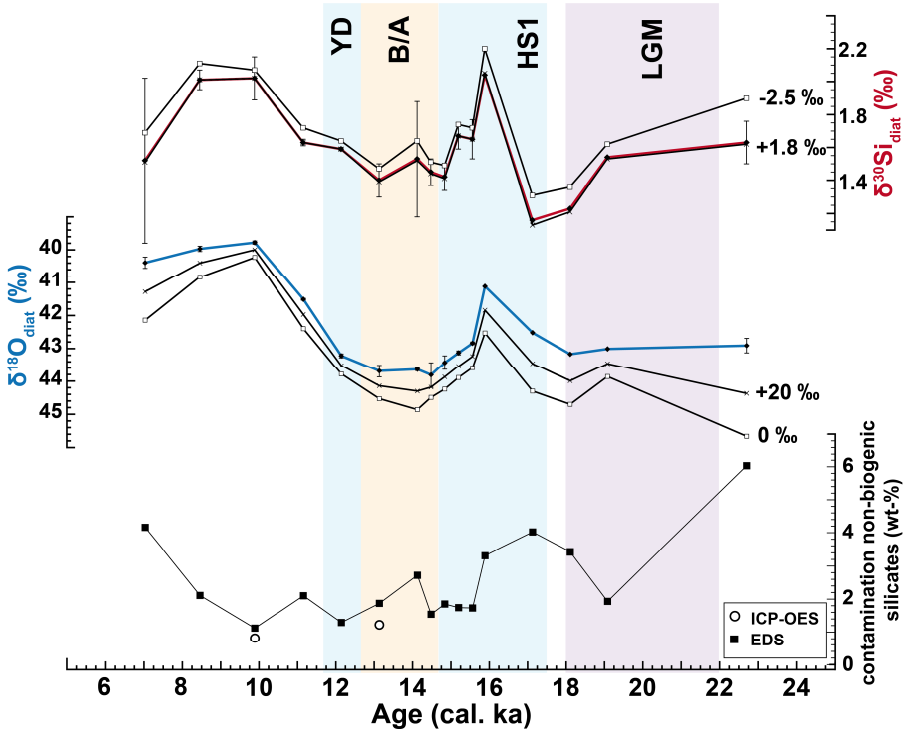

Figure 5.4. (bottom) Contamination with non-biogenic silicates estimated by ICP-OES and EDS. (middle and top) Measured $\delta^{18}O_{diat}$ (blue curve) and $\delta^{30}Si_{diat}$ (red curve) including isotopic curves mass-balance corrected for contamination with non-biogenic silicates estimated by EDS and using two different theoretical $\delta^{18}O_{cont}$ and $\delta^{30}Si_{cont}$ values each (black curves).

Qualitative checking of the additional MD01-2416 samples prior to isotope analysis supported the absolute dominance of *Coscinodiscus* species for the >63 µm diatom samples. The pre-sonication SO202-27-6 diatom samples were also dominated (93.7-100%) by *Coscinodiscus* species, with a strong dominance of *C. marginatus* (83-98%) over *C. oculus-iridis* (2-11%). Since the diatom samples of both studied cores are largely composed of *Coscinodiscus* species, possible species-related isotope effects are minimized and cannot explain $\delta^{18}O_{diat}$ and $\delta^{30}Si_{diat}$ variabilities. Based on modern diatom fluxes from the subarctic Pacific (Takahashi, 1986; Onodera et al., 2005) we suggest that the *Coscinodiscus* $\delta^{30}Si_{diat}$ and $\delta^{18}O_{diat}$ records reflect predominantly autumn conditions (surface water $\delta^{18}O$, SSS, relative silicic acid utilization) of surface waters, assuming that the growing period of *Coscinodiscus* did not change over the last 25 ka BP.

5.5.2 Glacial-interglacial variabilities in the NE Pacific

The $\delta^{18}O_{diat}$ record of Core SO202-27-6 shows a glacial-interglacial amplitude of ca. 3‰ between about +43.0‰ during the last glacial and +40.0‰ during the Early Holocene, which is about twice as large as the glacial-interglacial amplitude of ca. 1.3‰ observed in the subsurface $\delta^{18}O_{Nps}$ record (glacial: ca. +3.8‰, Holocene: ca. +2.5 ‰) (Fig. 5.5h, i). Subsurface $\delta^{13}C_{Nps}$ values are about 0.4‰ lower during the last glacial than during the Holocene (Fig. 5.5j), which largely corresponds to the mean global glacial-interglacial shift of -0.32‰ (Duplessy et al., 1988), reflecting the decreased terrestrial biosphere during glacials. Glacial $\delta^{30}Si_{diat}$ values are at intermediate level (ca. +1.60‰), but lower than $\delta^{30}Si_{diat}$ values from the Early Holocene (ca. +1.90‰) (Fig. 5.5g; Table S5.4). The differences between glacial and Holocene export production are low (Fig. 5.5d-f; Table S5.5). Biogenic opal concentration is slightly lower (~5 wt-%) during glacials compared to the Holocene (~9 wt-%). Opal MAR are low during both the glacial period and the Holocene (~20 $g*cm^2\ ka^{-1}$), while Si/Ti ratio suggests even slightly higher concentration of biogenic opal in LGM compared to Holocene sediments.

5.5.3 Deglacial variabilities in the NE Pacific

There is a large similarity of deglacial variabilities between the surface water $\delta^{18}O_{diat}$ and $\delta^{30}Si_{diat}$ records as well as between subsurface $\delta^{18}O_{Nps}$ and $\delta^{13}C_{Nps}$ records of Core SO202-27-6, however with isotopic records shifting mostly in opposing directions (Fig. 5.5g-j). Starting from intermediate(-to-high) $\delta^{18}O_{diat}$ values around +43.0‰ during the last glacial, the $\delta^{18}O_{diat}$ gets lighter during the start of the HS1. At ~16 ka BP, the $\delta^{18}O_{diat}$ shows an excursion of ~ 1.0‰ to lighter $\delta^{18}O_{diat}$ (+41.1‰), after which $\delta^{18}O_{diat}$ values get subsequently heavier throughout the end of HS1, reaching the heaviest $\delta^{18}O_{diat}$ values around (+43.8‰) during the B/A and the YD. The $\delta^{18}O_{diat}$ record shows a large shift of nearly 4.0‰ to lighter $\delta^{18}O_{diat}$

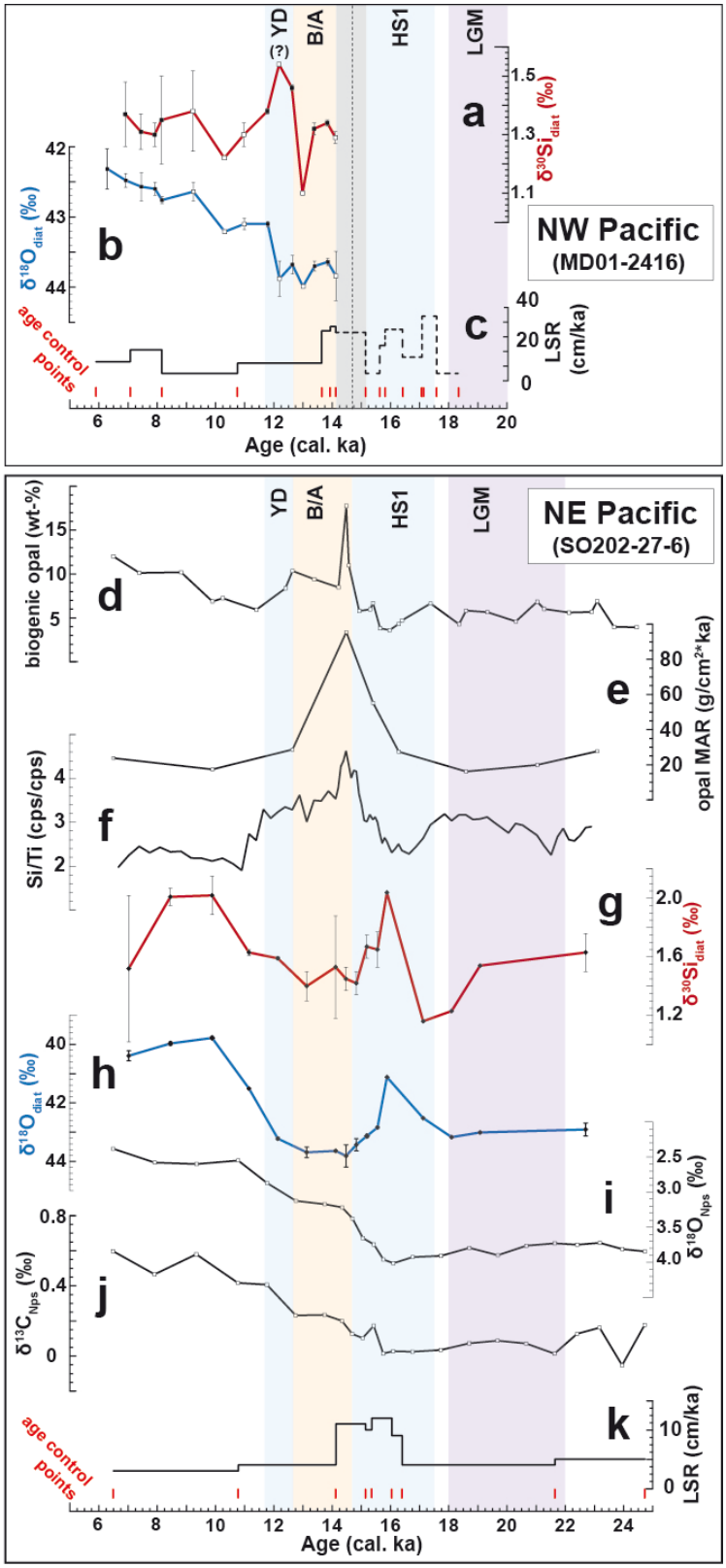

Figure 5.5. **(a)-(c)** Proxy data of NW Pacific Core MD01-2416: **(a)** $\delta^{30}Si_{diat}$ (Maier et al., 2013: black squares; this study: open squares), **(b)** $\delta^{18}O_{diat}$ (Maier et al., 2013: black squares; this study: open squares), **(c)** linear sedimentation rate (LSR) and age control points. We suggest that the calculated HS1-B/A boundary (vertical pointed line), is located further up-core within the marked ^{14}C plateau (grey box; see also *Section 5.4*). This may be possible considering that the HS1-B/A boundary is calculated by linear interpolation between the ^{14}C-plateau boundaries. Alternatively there might be a hiatus of a few centimeters located within upper part of the ^{14}C plateau. Accordingly the age model before ~14.2 ka BP is not well constrained and is therefore marked by a dashed LSR. **(d)-(k)** Proxy data of NE Pacific Core SO202-27-6: **(d)** biogenic opal, **(e)** Si/Ti ratio, **(f)** opal MAR, **(g)** $\delta^{30}Si_{diat}$, **(h)** $\delta^{18}O_{diat}$, **(i)** $\delta^{18}O_{Nps}$, **(j)** $\delta^{13}C_{Nps}$, **(k)** LSR and age control points.

values during the early Holocene, reaching a minimum in $\delta^{18}O_{diat}$ of +39.8 ‰ at around 9.8 ka BP. Reconstructed estimated local surface $\delta^{18}O_{sw}$ (= $\delta^{18}O_{diat}$ - $\delta^{18}O_{GIV}$ – SST) shows the same deglacial pattern as $\delta^{18}O_{diat}$, indicating a dominant control of local changes in surface water salinity on the $\delta^{18}O_{diat}$ (Fig. 5.6o). At ~16 ka BP surface $\delta^{18}O_{sw}$ indicates a massive drop in SSS, after which SSS increases, reflecting relatively saline upper surface waters throughout the B/A and YD. Following the YD surface $\delta^{18}O_{sw}$ points to decreasing salinity with lowest levels during the Early Holocene.

After glacial $\delta^{30}Si_{diat}$ values around +1.59‰, the $\delta^{30}Si_{diat}$ record shifts to lighter values during the start of the HS1, displaying the most depleted $\delta^{30}Si_{diat}$ value of +1.16‰ around 17 ka BP (Fig. 5.5g). At ~16 ka BP, contemporaneous with the large excursion to lighter $\delta^{18}O_{diat}$, the $\delta^{30}Si_{diat}$ record shifts about 0.9‰ in the opposite direction, displaying its most enriched value of +2.04‰. Following this excursion $\delta^{30}Si_{diat}$ gets subsequently lighter, reaching intermediate levels (+1.46‰) during the B/A. After the B/A, when $\delta^{18}O_{diat}$ gets lighter, $\delta^{30}Si_{diat}$ values get subsequently heavier, reaching +2.02‰ during the Early Holocene at ~9.8 ka BP.

$\delta^{18}O_{Nps}$ stays at its glacial high level (ca. +3.8‰) and $\delta^{13}C_{Nps}$ at its glacial low level (ca. +0.1‰) until ~16 ka BP, when $\delta^{18}O_{Nps}$ becomes progressively lighter and $\delta^{13}C_{Nps}$ gets progressively heavier until the Early Holocene (Fig. 5.5i-j). The episodic drop to lighter $\delta^{18}O$, as recorded by $\delta^{18}O_{diat}$, is not visible in the $\delta^{18}O_{Nps}$ record. The deglacial increase/decrease happens in two steps. After a first decrease in $\delta^{18}O_{Nps}$ of about 0.8‰ and increase in $\delta^{13}C_{Nps}$ of about 0.1‰ during the late HS1, $\delta^{18}O_{Nps}$ values stay around +3.2‰ and $\delta^{13}C_{Nps}$ around +0.2‰ throughout the B/A. In a second step $\delta^{18}O_{Nps}$ subsequently decreases about 0.6‰, reaching a $\delta^{18}O_{Nps}$ plateau around +2.6‰ after ~10.1 ka BP, while $\delta^{13}C_{Nps}$ increases about 0.3‰ with Holocene $\delta^{13}C_{Nps}$ values of ca. +0.5‰.

Biogenic opal concentration (~5 wt-%) and opal MAR (20 $g*cm^2\ ka^{-1}$) are low during the last glacial and early HS1, and the Si/Ti record indicates even slightly lower opal concentrations during the early HS1 compared to the end of the last glacial period (Fig. 5.5d,f). At ~16 ka BP, contemporaneous with the large decrease in $\delta^{30}Si_{diat}$ and the increase in $\delta^{18}O_{diat}$, all three biogenic opal indicators point to an increase in biological productivity. Highest productivity is indicated during the early Bølling (~14.5 ka BP), when $\delta^{30}Si_{diat}$ values are at intermediate levels. During that time biogenic opal concentrations is about 3-4 times larger (~18 wt-%) and opal MAR about 5 times larger (~96 $g*cm^2\ ka^{-1}$) than during the glacial period. Shortly after this brief peak productivity decreases continuously until reaching low productivity levels, similar to glacial values, during the early Holocene, when $\delta^{30}Si_{diat}$ values are high.

5.5.4 Intercalated new $\delta^{18}O_{diat}$ and $\delta^{30}Si_{diat}$ data from the NW Pacific

The 6 new $\delta^{18}O_{diat}$ data points from NW Pacific core MD01-2416, intercalated into the record presented by Maier et al. (2013), show relatively high $\delta^{18}O_{diat}$ values around +43.9‰ during the B/A and the YD and early Holocene $\delta^{18}O_{diat}$ values of about +42.9‰. The ca. 1.0‰ decrease in $\delta^{18}O_{diat}$ occurs relatively abrupt at the transition from the YD to Holocene. The new $\delta^{30}Si_{diat}$ data show similar values during the B/A and the Early Holocene, but elevated $\delta^{30}Si_{diat}$ values during the YD, when $\delta^{18}O_{diat}$ is high.

5.6 Discussion

5.6.1 Glacial surface water stratification and enhanced silicic acid utilization in the NE Pacific

Surface $\delta^{18}O_{sw}$ data, in combination with SST data (Méheust et al., in prep.), indicate that the glacial NE Pacific surface waters were cold and fresh (Fig. 5.6o, s). Fresh surface waters are supported by the high content of IRD, suggesting that melting icebergs influenced the LGM surface water layer, leading to stratified surface waters. Icebergs most likely originated from the Cordilleran Ice Sheet, considering that dropstones from nearby ODP Site 887 (Fig. 5.1) provenance from SE Alaska (McKelvey et al., 1995). Seasonal melting of sea-ice, which seems to have been present in the open NE Pacific during the LGM (De Vernal and Pederson, 1997; Méheust et al., in prep.), might have further strengthened glacial surface water stratification. Enhanced glacial stratification provides a plausible explanation for the combination of intermediate $\delta^{30}Si_{diat}$ and low productivity, since a strengthened stratification would have largely reduced the flux of nutrients from below, thus limiting productivity and leading to enhanced silicic acid utilization. Our results are in concert with previous studies on bulk $\delta^{15}N$ and $\delta^{15}N_{diat}$ from the subarctic Pacific and its marginal seas (Brunelle et al., 2007; 2010; Galbraith et al., 2008), which likewise associated low productivity in combination with high nutrient (nitrate) utilization to strengthened surface water stratification.

The studies of Brunelle et al. (2007; 2010) and Galbraith et al. (2008) on bulk $\delta^{15}N$ and $\delta^{15}N_{diat}$ showed that nitrate utilization in the subarctic Pacific was near complete during the last glacial. Intermediate $\delta^{30}Si_{diat}$ values indicate a relatively high utilization of silicic acid, but utilization seems to have been not complete (~80%, if we assume a closed system and that the highest measured $\delta^{30}Si_{diat}$ value of +2.04‰ corresponds to complete silicic acid utilization). The relatively lower utilization of silicic acid compared to nitrate might be related to an elevated iron-to-macronutrient supply ratio. This seems likely, considering a suggested increased input of dust into the glacial subarctic Pacific surface waters (Mahowald et al., 2006; Lam et al., 2013). With increased iron supply the growth of non-siliceous phytoplankton might have been stimulated, as observed in iron fertilization experiment in the

subarctic Pacific (Marchetti et al., 2006; Tsuda et al., 2007). Moreover, an elevated iron-to-macronutrient supply ratio might generally lower diatom Si/N uptake ratios below the Si/N supply ratio (Takeda, 1998). Another possibility might have been an enhanced growth of weakly silicified diatom species with comparatively low Si/N uptake ratios due to an increased iron-to-macronutrient supply in the glacial NE Pacific. Iron fertilization experiments in the subarctic Pacific showed a high growth rate of *Chaetoceros* sp., weakly silicified diatoms with low Si/N uptake ratios (Brzezinski, 1985), upon iorn addition (Takeda and Tsuda, 2005; Takeda, 2011). A relative abundance of ~15% of *Chaetoceros* resting spores (r.sp.) in the diatom species composition from last glacial sediments of nearby Core MD02-2489 (Fig. 5.6k; Ren et al., in prep.), indicates that the less complete utilization of silicic acid compared to nitrate might have been associated, at least in part, with the overall diatom species composition.

5.6.2 Deglaciation

5.6.2.1 Early deglacial decrease in silicic acid utilization in NE Pacific surface waters

After the LGM the $\delta^{30}Si_{diat}$ values decrease, suggesting decreased silicic acid utilization during the early HS1 (Fig. 5.6n). It has recently been suggested that a drop in $\delta^{15}N_{diat}$, visible within subarctic Pacific records during HS1 (Brunelle et al., 2010; Galbraith et al., 2008; Studer et al., 2013) might be associated with an increase in the abundance of radiolarians within the measured samples, considering that radiolarians generally harbor $\delta^{15}N$ values lower than $\delta^{15}N_{diat}$ (Studer et al., 2013). Even though the $\delta^{30}Si$ values of radiolarians have been found to be as low as ca. -3‰ in subarctic Pacific sediments (A. Abelmann, pers. comm.), we think it unlikely that radiolarians are responsible for the decreased $\delta^{30}Si$ values, as the abundance of radiolarians is not higher in the respective purified diatom samples compared to the samples directly below and above (Table S5.3B).

Considering that export production stays at low glacial levels during the early HS1 (Fig. 5.6m), the shift to lower $\delta^{30}Si_{diat}$ is suggested to be related to (1) a decreased iron-to-macronutrient ratio, (2) an increased supply rate of silicic acid to the euphotic zone and/or (3) an increased concentration of the supplied silicic acid. A recent study from the NW Pacific indicates that the dust flux from Asian loess did not decrease until the B/A (Lam et al., 2013), suggesting that the input of Asian dust in the NE Pacific also did not lessen during the HS1. Dust flux from Alaska has been identified as a source of iron to the modern open Gulf of Alaska (Boyd et al., 1998; Crusius et al., 2011). However, even though we clearly need more information on the variations in dust flux from Alaska into the NE Pacific to better evaluate the influence of Alaskan dust on the $\delta^{30}Si_{diat}$, we assume that the input of Alaskan dust was not higher during the early HS1 compared to the LGM to overcompensate for the decrease in Asian dust. We therefore suggest that the lower $\delta^{30}Si_{diat}$ values are not linked to atmospheric

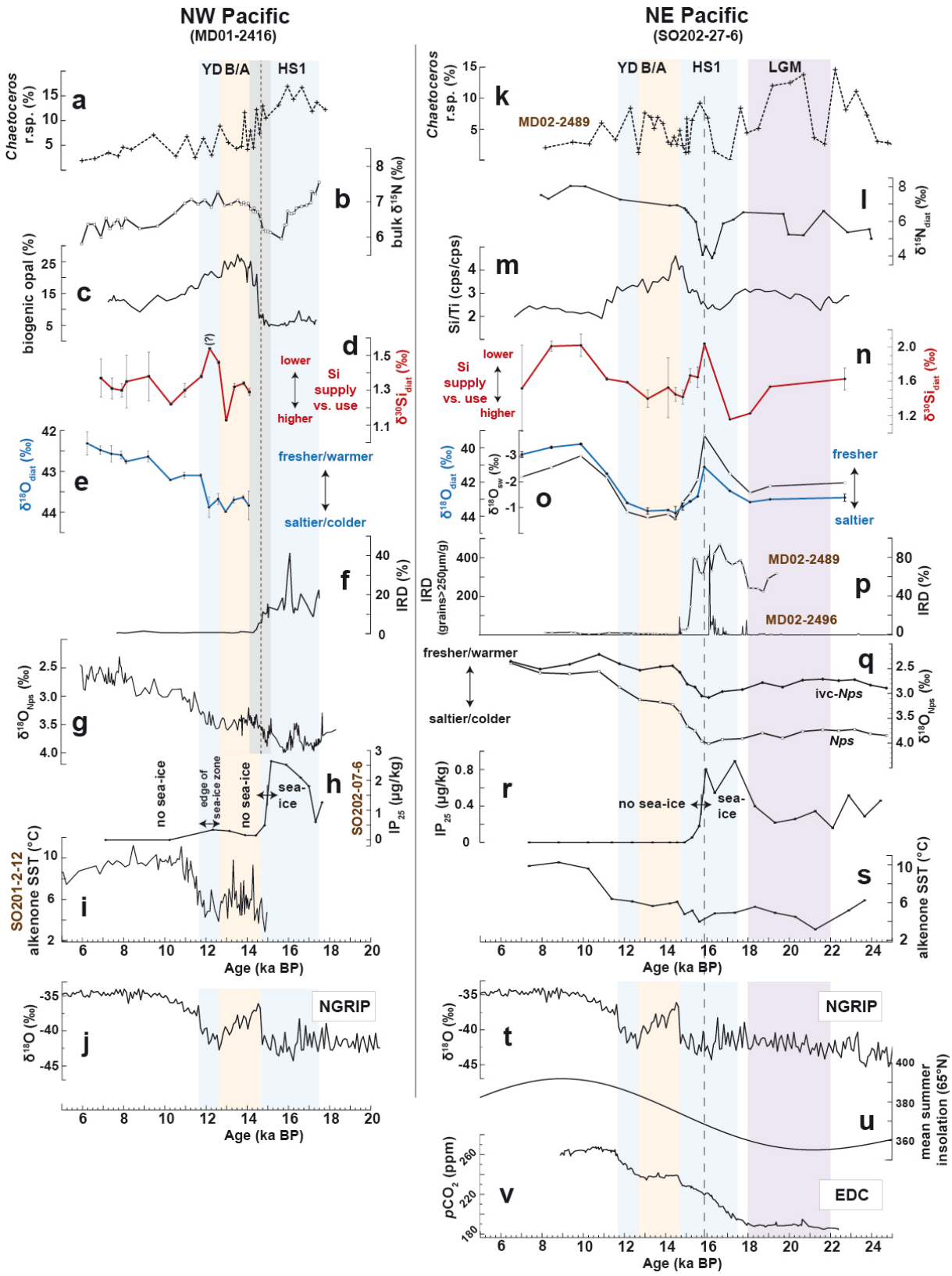

Figure 5.6. **(a)-(i)** Proxy data from NW Pacific Core MD01-2416 (on the timescale presented in this study; grey box and pointed line as in Fig. 5.5; age model before ~14.2 ka BP not well constrained): **(a)** *Chaetoceros* r.sp. relative abundance (Ren et al., in prep.), **(b)** bulk $\delta^{15}N$ (Galbraith et al., 2008), **(c)** biogenic opal concentration (Gebhardt et al., 2008), **(d)** $\delta^{30}Si_{diat}$ and **(e)** $\delta^{18}O_{diat}$ (both Maier et al., 2013; this study) **(f)** IRD data and **(g)** subsurface $\delta^{18}O_{Nps}$ (both Gebhardt et al., 2008); **(h)** IP_{25} data from Core SO202-07-6 (Méheust et al., in prep.), **(i)** alkenone-based SST from Core SO201-2-12 (Max et al., 2012); **(j)** NGRIP $\delta^{18}O$ (Andersen et al., 2006; Rasmussen et al., 2006; Vinther et al., 2006); **(k)-(s)** Proxy data from NE Pacific Core SO202-27-6, except

when mentioned otherwise: **(k)** *Chaetoceros* r.sp. relative abundance (Ren et al., in prep.), **(l)** $\delta^{15}N_{diat}$ (Studer et al., 2013), **(m)** Si/Ti ratio, **(n)** $\delta^{30}Si_{diat}$, **(o)** $\delta^{18}O_{diat}$ and surface $\delta^{18}O_{sw}$ records **(p)** IRD data from cores MD02-2489 (Gebhardt et al., 2008; on the time scale presented in this paper) and MD02-2496 (Hendy and Cosma, 2008), **(q)** subsurface $\delta^{18}O_{Nps}$, (measured and ice-volume corrected (ivc)) **(r)** IP_{25} data and **(s)** alkenone-based SST (both Méheust et al., in prep.); **(t)** NGRIP $\delta^{18}O$ (Andersen et al., 2006; Rasmussen et al., 2006; Vinther et al., 2006); **(u)** mean summer insolation at 65°N (Laskar et al., 2004); **(v)** EPICA Dome C (EDC) pCO_2 (Parrenin et al., 2013). The dashed line during the HS1 marks the freshwater and silicic acid utilization anomalies at ~16 ka BP and the onset of paleoceanographic changes.

iron input, indicating that changes in the hydrographic structure or oceanographic changes are likely responsible for the decrease in silicic acid utilization.

An increased flux of silicic acid to the euphotic zone might generally be accomplished by reduced strength of surface water stratification. Lam et al. (2013) recently suggested that during HS1 deep convective mixing in the NW Pacific brought nutrient-rich waters to the surface. Deep-water ventilation ages from NE Pacific Core MD02-2489 (Fig. 5.1), close to the studied core site SO202-27-6, support the hypothesis of deep convective mixing in the subarctic Pacific during the early HS1 (Sarnthein et al., 2013). Deeper mixing would provide a plausible explanation for the observation that $\delta^{15}N_{diat}$ (Studer et al., 2013) does not simultaneously decrease with $\delta^{30}Si_{diat}$. The remineralisation depth of silicic acid is deeper than for nitrate, i.e. the maximum nitrate concentration can be found around 600 m, while the maximum silicic acid concentration is reached between 1500-2000 m (Dugdale and Wilkerson, 2001; Harrison et al., 2004; Reynolds et al., 2006). Thus the Si/N ratio increases with depth and deeper mixing should lead to a decrease in $\delta^{30}Si_{diat}$ relative to $\delta^{15}N$.

However, our $\delta^{18}O_{diat}$ and surface $\delta^{18}O_{sw}$ records do not support deep vertical mixing. An important precondition to enable deep convective overturning in the subarctic Pacific during HS1 has been suggested to be an enhanced poleward transport of salt from the subtropics to the subarctic Pacific, resulting in surface waters dense enough to allow for the formation of deep-water (Okazaki et al., 2010; Chikamoto et al., 2012; Menviel et al., 2012). However, in contrast to an earlier study in the open subarctic NE Pacific, which indicated warmer and more saline surface waters during HS1 (De Vernal and Pederson, 1997), our surface $\delta^{18}O_{sw}$ data do not indicate an increase in SSS during the HS1 (Fig. 5.6o). Our data thus question conditions favorable for deep convective overturning. Support for this comes from subsurface $\delta^{18}O_{sw}$ data from the far NW Pacific, which also show relatively fresh upper ocean waters during HS1 (Riethdorf et al., 2013a).

Another possible mechanism to increase the supply rate/concentration of silicic acid to the euphotic zone involves increased lateral advection of silicic acid related to circulation changes affecting the subsurface waters and/or the intermediate water body. Today, intermediate waters in the North Pacific, which constitute the major source of nutrients for phytoplankton in the open subarctic Pacific, are largely influenced by North Pacific Intermediate Water

(NPIW) (Sarmiento et al., 2004). NPIW is largely confined to the subtropical gyre but also influences the subarctic Pacific (Reynolds et al., 2006; Sarmiento et al., 2004). Compared to intermediate waters from the Southern Ocean the NPIW is characterized by a relatively high silicic acid content (Sarmiento et al., 2004). An increased intensity of NPIW formation thus might have led to an increased supply of silicic acid to intermediate waters of the subarctic Pacific and, through upwelling, also to surface waters. Recent studies indeed showed that the formation rate of NPIW likely increased during HS1 (Jaccard and Galbraith, 2013; Max et al., 2013). Increased NPIW formation would also provide an explanation for the diverging $\delta^{15}N_{diat}$ and $\delta^{30}Si_{diat}$ (Fig. 5.6l, n), since NPIW is characterized by a positive Si/N ratio (Sarmiento et al., 2004). An intensified NPIW formation thus might have lead to a relative increase in silicic acid compared to nitrate.

5.6.2.2 Massive freshwater input into the NE Pacific during HS1

Following low $\delta^{30}Si_{diat}$ of ca. +1.2‰ at ~17.5 ka BP, the highest $\delta^{30}Si_{diat}$ value of ca. +2.0‰ occurs at ~16 ka BP (Fig. 5.6n). Export production stays low over this time interval (Fig. 5.6m), suggesting that the peak of high $\delta^{30}Si_{diat}$ is related to a largely reduced supply of silicic acid at ~16 ka BP, resulting in a high utilization of the available silicic acid. Contemporaneous with the peak of high $\delta^{30}Si_{diat}$ a peak of low $\delta^{18}O_{diat}$ and surface $\delta^{18}O_{sw}$ values can be observed, indicating a massive freshening of surface waters (Fig. 5.6o). The combination of high $\delta^{30}Si_{diat}$ and low surface $\delta^{18}O_{sw}$ points to enhanced surface water stratification at ~16 ka BP, potentially in response to a massive meltwater input. Since subsurface $\delta^{18}O_{Nps}$ and $\delta^{13}C_{Nps}$ data do not show any perturbation to lighter/heavier values (Fig. 5.5i,j; Fig. 5.6q), the freshwater and nutrient utilization anomaly seems to be restricted to surface waters.

Hypothesis to explain a massive freshwater flux into the NE Pacific include atmospheric and/or oceanographic factors destabilizing the Cordilleran Ice Sheet (CIS), thereby leading to rapid discharge/melting of Cordilleran ice. The $\delta^{18}O_{diat}$/surface $\delta^{18}O_{sw}$ minimum occurs during times of a high IRD deposition in the subarctic NE Pacific and moderate IRD deposition in the NW Pacific (Fig. 5.6f, p). Unfortunately, the low biogenic opal concentration prevented an obtaining of glacial/early deglacial NW Pacific $\delta^{18}O_{diat}$ data. Similar to the NE Pacific, however, the subsurface $\delta^{18}O_{Nps}$ record does not show any freshwater event (Fig. 5.6g; Gebhardt et al., 2008), suggesting that a possible freshwater anomaly, as indicated by the IRD data, was restricted to the upper surface waters. Since no ice sheet was present over eastern Siberia during the LGM (Brigham-Grette et al., 2001), we suggest that the CIS was the common source for the NE and NW Pacific IRD; icebergs were likely transported westward from the CIS by the Alaskan Stream. The $\delta^{18}O_{diat}$ minimum

furthermore coincides with (1) an IRD peak found in the eastern North Pacific (Core MD02-2496) (Fig. 5.1; Hendy and Cosma, 2008) and (2) Heinrich Event 1 (H1) in the North Atlantic, which is characterized by a high deposition of IRD (Fig. 5.7; Bard et al., 2000) associated with the episodic discharge of icebergs from the Laurentide Ice Sheet (LIS) (Heinrich, 1988; Hemming, 2004).

The coinciding events in the North Atlantic and the North Pacific suggest a close link between the deglacial meltwater histories of the LIS and the CIS. This link might be related to the common external forcing of increasing summer insolation (Fig. 5.6u), indicating an increased rate of summer melting. Alternatively, processes happening in the North Atlantic during HS1, particularly associated with the reduction/shutdown of the Atlantic Meridional Overturning Circulation (AMOC) (McManus et al., 2004), might have triggered rapid climate change in the North Pacific realm via atmospheric and/or oceanic teleconnections, e.g. through sea level rise (Rohling et al., 2004) or oceanic/atmospheric warming (Clark et al., 2007; Hendy and Cosma, 2008).

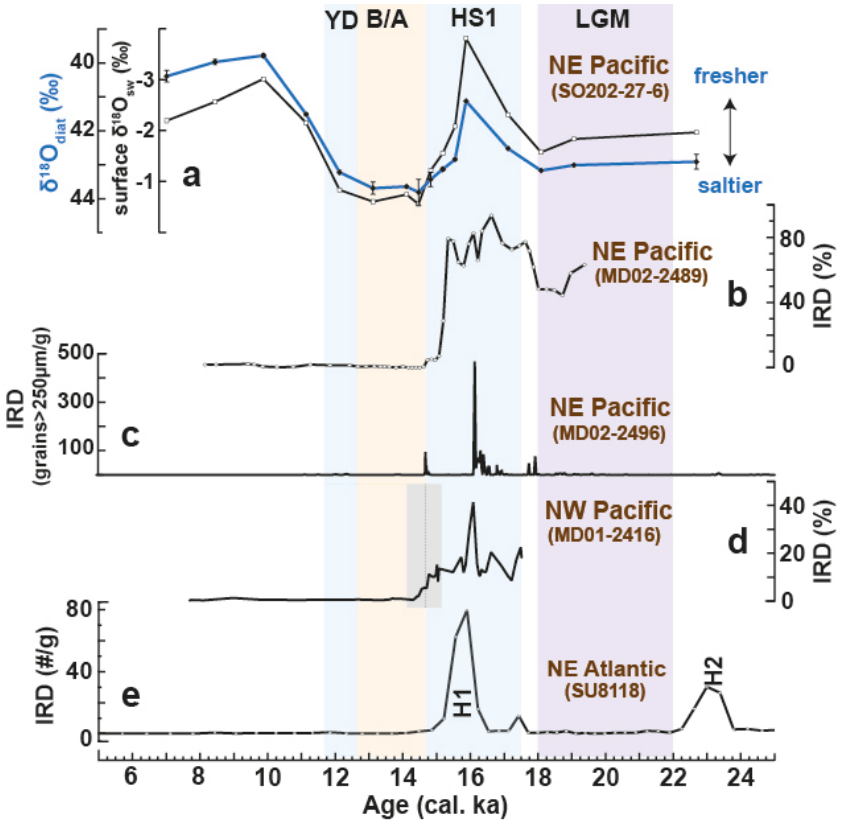

Figure 5.7. **(a)** $\delta^{18}O_{diat}$ and surface $\delta^{18}O_{sw}$ records from NE Pacific Core SO202-27-6; **(b)-(e)** IRD data from NE Pacific cores **(b)** MD02-2489 (Gebhardt et al., 2008; on the time scale presented in this paper) and **(c)** MD02-2496 (Hendy and Cosma, 2008), as well as from **(d)** NW Pacific Core MD01-2416 (Gebhardt et al., 2008; on the time scale presented in this paper; grey box and pointed line as in Fig. 5.5) and **(e)** NE Atlantic Core SU8118 (Bard et al., 2000).

During times of maximum ice extent the CIS covered coastal Alaska and the Alaska Peninsula and flowed to the outer margin of the continental shelf, from where icebergs were discharged into the NE Pacific (Mann and Hamilton, 1995; Kaufman et al., 2011). Between 19.0-14.5 ka BP the eustatic sea level rose about 8-20 m (Carlson and Clark, 2012). Increasing sea level may be of importance for the retreat of glaciers with marine grounding lines (Flückinger et al., 2006; Alley et al., 2007). However, only rapid changes in sea level >10 m might have acted as a forcing factor to synchronize ice sheet retreat (Alley et al., 2007), e.g. due to the stabilizing effect of subglacial sedimentation on glacier grounding lines (Anandakrishnan et al., 2007).

Since the Bering Strait is closed during HS1, oceanic teleconnections from the North Atlantic via the Arctic Ocean can be discarded for the transmission of rapid climate changes. The atmospheric circulation and air-sea interaction in the Northern Hemisphere seems to be fundamentally influenced by processes happening in the Atlantic and the tropical Pacific (Alexander et al., 2002; Okumura et al., 2009), but the response of the North Pacific to the changes in the strength of the AMOC is controversial. Some modeling studies suggest an increased advection of warm, salty surface waters from the subtropical Pacific into the subarctic Pacific (Kiefer, 2010; Okazaki et al., 2010) in response to the reduction/shutdown of the AMOC, arguing that a southward shift of the Intertropical Convergence Zone might have resulted in a reduced export of moisture from the Atlantic to the tropical Pacific (Leduc et al., 2007). Such a warming might have accelerated iceberg discharge into the North Pacific (Hendy and Cosma, 2008). However, this hypothesis is not supported by our $\delta^{18}O_{diat}$ data as well as other (sub-)surface temperature/salinity data from the subarctic Pacific, indicating cold and fresh (sub-)surface waters in the NE and NW Pacific during most of HS1 (Fig. 5.6i, o, q, s; Max et al., 2012; Riethdorf et al., 2013a; Méheust et al., in prep.). These proxy data are supported by modeling studies arguing for a slight cooling and freshening of the subarctic North Pacific surface waters during HS1 (Okumura et al., 2009; MIROC model of Chikamoto et al., 2012), related to an enhanced Aleutian low (Okumura et al., 2009). Such a cooling might have increased Cordilleran ice-sheet growth, ultimately resulting in enhanced iceberg calving, a scenario similar, even though much smaller scaled, to the scenario proposed for the North Atlantic (Clark et al., 2007). However, despite smaller, regionally constrained, glacier re-advances the CIS largely retreated during the HS1 (Mann and Hamilton, 1995). Off Charlotte Islands the CIS had retreated from the outer continental shelf before ~16-15 ^{14}C ka BP (Mann and Peteet, 1994), the ice margin had retreated to Kodiak Island before ~14.7 ^{14}C ka BP (~17.9 ka BP) (Mann and Peteet, 1994) and glaciers in SE Alaska had retreated close to their modern position by ~13.5 ^{14}C (~16.3 ka BP) (Mann and Hamilton, 1995). Furthermore, iceberg calving from the southern CIS into the North Pacific during HS1 seems to have been related to ice retreat, not ice advance (Hendy and Cosma, 2008).

The rapid retreat of the southern CIS leading to the HS1 IRD event in the eastern North Pacific might be associated with regional atmospheric warming, which might not be mirrored in the SST records due to a dampening influence of melting ice (Hendy and Cosma, 2008). A dominant atmospheric control on the freshwater flux into the North Pacific is supported by the switch from extensive sea-ice cover towards seasonal sea-ice at the beginning of HS1 (Méheust et al., in prep.), assuming that, similar to the Southern Ocean, atmospheric forcing (Holland and Kwok, 2012) and local orbital forcing (WAIS Divide Project Members, 2013) are mainly controlling sea-ice advance and retreat. Furthermore, episodic meltwater outbursts from glacial lakes point towards an atmospheric forcing. Ice dam failure repeatedly led to meltwater floods from glacial Lake Missoula (Hendy, 2009; Benito and O´Connor, 2003). Missoula flood deposits exposed along the Columbia River were mostly emplaced before ca. 15.6 ka BP (Benito and O´Connor, 2003). Particularly during the LGM and HS1, when the subarctic front is displaced southward (Sabin and Pisias, 1996; Okumura et al., 2009), megaflood events from glacial Lake Missoula might have had the potential to reach the open NE Pacific. Also likely influencing the study site area are megafloods related to the drainage of Alaskan glacial Lake Atna into the NE Pacific, which occurred at least two times between ~26-15.5 ka BP (Wiedmer et al., 2010). While most of the freshwater entering the Gulf of Alaska today is transported along the coast within the ACC and does not mix offshore (Weingartner et al., 2005), megaflood events probably had an impact on the open NE Pacific surface waters.

5.6.2.3 Pre-Bølling paleoceanographic change

After ~16 ka BP the $\delta^{30}Si_{diat}$ record decreases by about 0.5‰ until reaching a plateau with intermediate $\delta^{30}Si_{diat}$ values during the B/A (Fig. 5.6n). The decline in silicic acid utilization is accompanied by an increase in export production, which culminates during the Bølling (Figs. 5.5d-f; 5.6m). The decoupling of $\delta^{30}Si_{diat}$ and export production is also observed in the NW Pacific during the B/A (Fig. 5.6c, d; Maier et al., 2013). Both the NE and the NW Pacific records thus indicate a strongly enhanced supply of silicic acid into subarctic Pacific surface waters that is not compensated by the increasing net use of silicic acid. Furthermore after ~16 ka BP our surface $\delta^{18}O_{sw}$ record points to a rapid increase of SSS, coeval with a change from seasonal-sea-ice to sea-ice-free conditions (Fig. 5.6o, r; Méheust et al., in prep.). Throughout the B/A surface waters seem to have been relatively saline. Based on these proxy data we suggest an increased upwelling of deeper saline and nutrient rich waters into the surface waters during the late HS1 and the B/A. A strong vertical mixing during the B/A is in accordance with previous studies from the subarctic Pacific (Galbraith et al., 2007; Gebhardt et al., 2008; Maier et al., 2013), supporting the hypothesis of an increased input of nutrients as

primary cause for the peak in export production in the subarctic Pacific realm during the Bølling (Galbraith et al., 2007; Kohfeld and Chase, 2011). This is in contrast to the recent study of Lam et al. (2013) suggesting transient stratification, possibly associated with meltwater-pulse 1a (MWP-1a), as responsible trigger. However, our diatom isotope records do not provide any evidence for freshwater stratification during the time of MWP-1a (Fig. 5.6o), which starts around the HS1-B/A boundary at 14.6 ka BP (Carlson and Clark, 2012; Deschamps et al., 2012). Furthermore, since the contribution of the CIS to the eustatic sea level rise of ca. 14-18 m associated with MWP-1a (Deschamps et al., 2012) was probably less than 1m (Carlson and Clark, 2012), freshwater input from the CIS related to MWP-1a might have been restricted to settings influenced by the ACC (e.g. Core EW0408-85JC) (Fig. 5.1; Davies et al., 2011) and may not have reached the open NE Pacific. Furthermore, the high $\delta^{15}N_{diat}$ values during the B/A in the NW Pacific, interpreted by Lam et al. (2013) to represent changes in nitrate utilization, are more likely related to increased denitrification in the equatorial North Pacific (Brunelle et al., 2010; Maier et al., 2013), same as suggested for the NE Pacific (Galbraith et al., 2008). An increased denitrification signal of subsurface waters during times of increased vertical mixing provides a conclusive explanation for the decoupled $\delta^{30}Si_{diat}$ and $\delta^{15}N$ records during the B/A (Fig. 5.6c, d, l, n; Maier et al., 2013; this study).

The observed pre-Bølling paleoceanographic change indicated by proxy data from the NE Pacific Core SO202-27-6, assumed to represent a true feature of the North Pacific region (see *Section 5.4*), is in accordance with proxy data from other North Pacific cores. Diatom concentration data from the NE Pacific show a pre-Bølling increase in *Neodenticula seminae* (Ren et al., in prep.), which today flourish in moderately warm (ca. 6-7°C) and saline surface waters (Sancetta, 1982; Barron et al., 2009). Planktic foraminiferal $\delta^{18}O$ records from the continental slope of the Gulf of Alaska start to decrease, synchronous with our $\delta^{18}O_{Nps}$, around 16 ka BP (Davies et al., 2011). Furthermore, temperatures of (sub-)surface waters in the NW Pacific (Riethdorf et al., 2013a), the NE Pacific (Gebhardt et al., 2008) and the subtropical eastern North Pacific (Hendy et al., 2002; Hill et al., 2006) increase prior to the B/A. Increasing subsurface temperatures of about 2-3°C, as suggested for the NE Pacific (Gebhardt et al., 2008), could well explain the ca. 0.6‰ decrease in ice-volume/sea level corrected (after Waelbroeck et al., 2002) subsurface $\delta^{18}O_{Nps}$ during late HS1, assuming a relationship between temperature and $\delta^{18}O_{Nps}$ of ca. 0.28°C/‰ (Mulitza et al., 2003).

The pre-Bølling paleoceanographic change in the subarctic Pacific indicates that a dominant Northern Hemisphere atmospheric control on subarctic Pacific paleoclimate, as suggested for the early HS1, might have been superimposed by an additional forcing after ~16 ka BP. Out-of-phase behaviour between North Pacific paleotemperature records and North Atlantic climate observed in the NE Pacific off Oregon (Mix et al., 1999) and on the Alaskan margin

(Davies et al., 2011) have been interpreted to reflect a combined Northern and Southern Hemisphere control on North Pacific climate, possibly related to a fast (few decades) propagation of southern-sourced surface water changes via the deeper ocean (Masuda et al., 2010). The pre-Bølling decrease in $\delta^{18}O_{Nps}$ and increase in SST coincides with warming in the Southern Ocean (WAIS Divide Project Members, 2013), thus indicating that Southern Hemisphere forcing on deglacial subarctic Pacific climate might have also influenced the deglacial open subarctic Pacific. However, our data show that the pre-Bølling paleoceanographic change in the NE Pacific occurs coeval with a switch towards sea-ice free conditions (Fig. 5.6r) and recently, an increase in local insolation forcing has been inferred as cause for sea-ice decline in the Southern Ocean and Antarctic warming (WAIS Divide Project Members, 2013). Accordingly, a quicker response of the North Pacific region to changes in Northern Hemisphere insolation relative to the North Atlantic region might have triggered the pre-Bølling switch towards sea-ice free conditions and (sub-)surface warming in the subarctic Pacific. In order to explain the pre-Bølling paleoclimate change recorded in Lake Suigetsu, Nakagawa et al. (2003) likewise proposed a temporal difference between the regional responses of the North Pacific and the North Atlantic climate to changes in solar insolation.

We therefore suggest that changes in Northern Hemisphere insolation might have resulted in the switch to sea-ice free conditions at ~16 ka BP. The weakened surface water stratification related to the sea-ice decline may have facilitated an increased input of nutrient-rich deeper waters, stimulating biological productivity. At the start of the Bølling, when the AMOC accelerated and invigorated the influx of southern-sourced, nutrient-rich deep waters into the North Pacific (McManus et al., 2004), maybe with an even higher silicic acid concentration as a result of less exchange with lower latitude upper water masses as suggested for the Atlantic (Meckler et al., 2013), upwelling amplified and nutrient supply to the surface waters increased, further promoting productivity (Galbraith et al., 2007; Gebhardt et al., 2008). Iron supply related to the inundation of continental shelve areas during rapid sea level rise associated with MWP-1a, might have further stimulated productivity during the Bølling (Davies et al., 2011), but seems to have been only of subordinate importance (Lam et al., 2013).

5.6.3 Evidence for sea-ice induced surface water stratification in the NW Pacific during the YD

The $\delta^{30}Si_{diat}$ record from the NW Pacific indicates a slight increase in silicic acid utilization during the YD, which is accompanied by a decrease in biogenic opal concentration (Fig. 5.6c, d). This was previously observed by Maier et al. (2013) and is supported by the additional YD $\delta^{30}Si_{diat}$ data point measured within this study. It is important to note that the standard deviation of this value, which is the highest $\delta^{30}Si_{diat}$ value of this record and is composed of

two isotopic measurements, is exceptionally high (0.52‰; Table S.5.2). Unfortunately we could not perform a third measurement since there was not enough purified diatom material available. Nevertheless, even without this data point the record shows an increase in silicic acid utilization following the B/A (Fig. 5.6d). In contrast to the HS1 in the NE Pacific the slightly increased $\delta^{30}Si_{diat}$ record in the NW Pacific is not accompanied by lower $\delta^{18}O_{diat}$ values, arguing against surface water stratification as a result of increased input of freshwater. However, Méheust et al. (in prep.) suggest that during the YD the area of the NW Pacific study site represents the marginal zone of winter sea-ice expansion originating from the Bering Sea (Fig. 5.6h). Seasonal melting of sea-ice might have resulted in increased surface water stratification and a shallowed thermocline. This would have reduced the available silicic acid, leading to a relative increase in silicic acid utilization. Even though sea-ice formation has a strong effect on salinity, the effects on the $\delta^{18}O_{sw}$ signal are relatively low, thereby explaining the high $\delta^{18}O_{diat}$.

5.6.4 Early Holocene surface water development

While the absolute $\delta^{18}O_{diat}$ values are similar during the B/A and the YD in the NE and the NW Pacific, during the Early Holocene the $\delta^{18}O_{diat}$ record from the NW Pacific shifts about 1.4‰ and the $\delta^{18}O_{diat}$ record from the NE Pacific shifts about 4.0‰ towards lighter values (to ca. +42.4‰ and ca. +40.0‰, respectively; Fig. 5.6e, o). Alkenone-based SST indicate a warming of about 4°C both in the NW and the NE Pacific (Fig. 5.6i, s; Max et al., 2012; Méheust et al., in prep.). Assuming a relationship between $\delta^{18}O_{diat}$ and water temperature of ca. -0.2‰/°C (Dodd and Sharp, 2010), the decrease of ca. 1.4‰ in the NW Pacific can be largely explained by SST warming, the change in global ice volume and development to fresher (sub-)surface waters, as indicated by decreasing subsurface $\delta^{18}O_{sw}$ in the far NW Pacific (Riethdorf et al., 2013a). In contrast the NE Pacific seems to be subject to an additional major freshening accounting for ca. 2.5‰ in the $\delta^{18}O_{diat}$ record. Since the shift in subsurface $\delta^{18}O_{Nps}$ and the absolute $\delta^{18}O_{Nps}$ values are similar in the NE and the NW Pacific (Fig. 5.6g, q), such a freshwater anomaly between both regions would need to be restricted to surface waters.

Today, the surface waters in NW Pacific are slightly more saline compared to NE Pacific surface waters (Antonov et al., 2010), with an estimated $\delta^{18}O_{sw}$ anomaly between both regions of ca. 0.6‰ (Bigg and Rohling, 2000). This W-E difference is related to the riverine influx of freshwater from the Cordilleran mountains into the NE Pacific, which is transported westward with the Alaskan Stream into the western subarctic gyre (Fig. 5.1). If the W-E difference in Early Holocene $\delta^{18}O_{diat}$ was entirely linked to differences in the freshwater budget, e.g precipitation vs. evaporation or riverine influx, the freshwater budget anomaly would need to

be about four times higher compared to today. Mechanisms that could explain a general freshening of Early Holocene subarctic Pacific surface waters include an intensified East Asian summer monsoon (Dykoski et al., 2005; Wang et al., 2005), which, however, would not likely result in NE Pacific surface waters four times fresher compared to the NW Pacific. Furthermore increased temperatures might have resulted in relatively increased ablation of Cordilleran ice. The vast majority of glaciers of the Cordilleran Ice Sheet, however, retreated before ~11.5 ka BP (Mann and Hamilton, 1995; Dyke, 2004) and the majority of relatively small-scaled freshwater inputs would likely not reach the open NE Pacific, but would be transported away with the ACC (Weingartner et al., 2005).

Since there is no conclusive climate-induced explanation for the large shift to low Early Holocene $\delta^{18}O_{diat}$ values in the NE Pacific, a bias of the uppermost three $\delta^{18}O_{diat}$ values of the NE Pacific Core SO202-27-6 (ca. 10-6 ka BP) towards lower $\delta^{18}O_{diat}$ values needs to be reconsidered. While we can exclude contamination as a major contributor to the low $\delta^{18}O_{diat}$ within the uppermost three diatom samples of Core SO202-27-6 (0-11 cm; Fig. 5.4), the process of silica maturation, generally assumed not to overprint the relative paleoenvironmental surface water signal (Swann and Leng, 2009), needs to be taken into account. Different studies have shown that $\delta^{18}O_{diat}$ signals of (sub-)fossil diatoms are enriched in ^{18}O compared to fresh diatoms (Schmidt et al., 1997; Brandriss et al., 1998; Moschen et al., 2006). This deviation has first been attributed to partial dissolution of the frustule, which was assumed to primarily affect isotopically light hydroxyl groups (Brandriss et al., 1998). Later, using infrared absorption spectrometry, Schmidt et al. (2001) and Moschen et al. (2006) demonstrated that the enrichment in ^{18}O is more likely related to secondary isotope exchange reactions. Since the silica maturation process leads to a structural change of the frustules involving the decline of hydroxyl oxygen (Dodd and Sharp, 2010), it may be possible that the early stage maturation process is not yet completed for the uppermost three diatom samples of Core SO202-27-6. The relative shift in the Early Holocene $\delta^{18}O_{diat}$ record might thus be lower than observed, i.e. the freshening of NE Pacific waters might be more moderate.

Nevertheless, a W-E difference can also be observed concerning the evolution of Early to mid Holocene nutrient utilization. While both the NE and the NW Pacific cores are characterized by rather low biogenic opal concentrations, $\delta^{30}Si_{diat}$ and $\delta^{15}N$ values are high in the NE Pacific, but comparatively low in the NW Pacific (Fig. 5.6b, d, l, n), indicating a different development of surface waters in both regions of the subarctic Pacific. However, both might be related to the development towards modern low-salinity, HNLC conditions with a higher utilization occurring in the modern NE Pacific compared to the NW Pacific. Following the YD, where stratification due to sea-ice melting has been constrained to the uppermost surface waters in the NW Pacific, a freshening of surface and subsurface waters during the Early

Holocene (Sarnthein et al., 2004; Riethdorf et al., 2013a; this study) might indicate a comparatively lower stratification of the uppermost water masses associated with a deepening of the winter mixed-layer, possibly resulting in an increased relative supply of nutrients. Since in the context of iron fertilization the Holocene decrease in atmospheric iron (Lam et al., 2013) might have increased the relative need for silicic acid, the nutrient input should have been high enough to compensate for the increased silicic acid demand. In the NE Pacific, where there has been no sea-ice induced stratification during the YD (Méheust et al., in prep.), the Early Holocene warming and freshening might have led to more stratified upper ocean waters and a relative increase in nutrient utilization. Clearly, more studies are needed to test these hypotheses. In particular, near future studies should evaluate the modern distribution of $\delta^{30}Si$ in the water columns of the NE and NW Pacific in combination with *in situ* captured/sediment trap/core top diatoms.

5.6.5 Links to deglacial rise in atmospheric pCO_2

The deglacial rise in atmospheric pCO_2 of ~90 ppm has mainly been attributed to outgassing of CO_2 related to the upwelling of old, CO_2-enriched deep waters in the Southern Ocean during HS1 and the YD (Schmitt et al., 2012; Parrenin et al., 2013), but some of the CO_2 might have degassed from the subarctic Pacific (Galbraith et al., 2007; Gebhardt et al., 2008). The observed pre-Bølling increase in deep convective mixing coincides with a deglacial rise in atmospheric CO_2 of about 20 ppm (Fig. 5.6v; Parrenin et al., 2013), ~10 ppm during late HS1 and ~10 ppm over the HS1-B/A transition. The decoupling of $\delta^{30}Si_{diat}$ and export production, pointing to an excess supply of silicic acid to the photic zone, indicate a comparatively low efficiency of the biological pump during late HS1 and the B/A, despite the increased export. The observed decline in *Chaetoceros* r.sp., in the NW Pacific during late HS1 (Fig. 5.6a) supports the hypothesis of a decreased efficiency of the biological pump, considering that *Chaetoceros* species are weakly silicified diatoms, which indicate a comparatively large export of carbon relative to silica (Abelmann et al., 2006). We therefore suggest that the subarctic Pacific has been a source of atmospheric CO_2 during late HS1 and the B/A.

5.7 Conclusions

This study presents new $\delta^{18}O_{diat}$ and $\delta^{30}Si_{diat}$ data, along with $\delta^{18}O_{Nps}$, $\delta^{13}C_{Nps}$ and export production data from the deglacial subarctic Pacific, which allow for new insights into the spatial and temporal evolution of the hydrography and silicic acid utilization of subarctic Pacific surface waters. Our results show that deglacial changes in the $\delta^{18}O_{diat}$ record are primarily controlled by changes in surface $\delta^{18}O_{sw}$, i.e. SSS, and do not mirror deglacial climate variabilities like the North Atlantic B/A warming or YD cooling. Silicic acid

utilization seems to be closely associated with changes in surface water stratification, but may be subordinately influenced by other factors including iron availability and silicic acid concentration.

The last glacial is characterized by low productivity and fresh as well as highly utilized surface waters, supporting previous studies indicating strong glacial surface water stratification in the subarctic Pacific realm. During the early HS1 silicic acid utilization decreases, while paleoproductivity stays low and surface waters stay fresh, indicating an increase in the advection of silicic acid supply despite strongly stratified surface waters. Such an increased silicic acid supply might be related to an increase in the formation rate of NPIW. At ~16 ka BP our data suggest a pulse of freshwater into the NE Pacific, likely related to extensive iceberg discharge. The synchronicity of the freshwater pulse with the H1 IRD event in the North Atlantic indicates a close link between the CIS and LIS meltwater histories and we suggest a dominant atmospheric control on the CIS deglaciation. Furthermore, the fresh surface waters in the NE Pacific during early-mid HS1 argue against the inflow of salty subtropical water required for the formation of deep-water in the subarctic Pacific realm, previously suggested for that time.

Our data indicate a pre-Bølling paleoceanographic change in the subarctic NE Pacific, characterized by an increase in the supply of saline, silicic-acid rich waters into the euphotic zone, leading to weakly stratified upper waters throughout the B/A in the subarctic NE and the NW Pacific. We suggest that the contemporaneous pre-Bølling change to sea-ice-free conditions in the subarctic Pacific, possibly related to a quicker response to Northern Hemisphere insolation forcing relative to the North Atlantic, might have triggered the pre-Bølling paleoceanographic change in the subarctic Pacific. The maximum in export production and the weakly stratified upper waters during the Bølling are likely linked to AMOC acceleration at the start of the Bølling, which might have invigorated the influx of southern-sourced, nutrient-rich deep waters into the North Pacific.

During late HS1 and the B/A an observed decoupling of silicic acid utilization and export production in both the NE and NW Pacific indicates an excess supply of silicic acid, which overcompensates for the increasing net use of silicic acid. This suggests a decreased efficiency of the biological pump, indicating that the subarctic Pacific might have been a source region of atmospheric CO_2 during late HS1 and the B/A.

In the NW Pacific a slight increase in silicic acid utilization during the YD seems to have been related to increased surface water stratification due to melting sea-ice. In contrast, the NE Pacific was not stratified during the YD. The Early Holocene evolution of NW and NE Pacific surface waters might represent the evolution towards modern HNLC conditions, i.e. slightly fresher and better utilized surface waters in the NE Pacific compared to the NW Pacific.

This study demonstrates that the $\delta^{18}O_{diat}$ and $\delta^{30}Si_{diat}$ provide valuable information of past changes in subarctic Pacific surface water conditions. However, in addition to further down-core studies on suitable sediment cores to test the abovementioned sequence of paleoclimatic events, research is needed on the process of silica maturation, especially in the marine realm, considering the differences between fresh and (sub-)fossil $\delta^{18}O_{diat}$. Furthermore, to allow for a more precise evaluation of (relative and absolute) down-core changes in $\delta^{30}Si_{diat}$, future studies should investigate the distribution of silicon isotopes throughout the subarctic Pacific water column and the relationship between the $\delta^{30}Si$ of surface water silicic acid and the $\delta^{30}Si$ signals of *in situ* captured diatoms, diatoms from sediment traps as well as from core tops.

Acknowledgements

This study was embedded in the Innovative NOrth Pacific Experiment (INOPEX), funded by the Bundesministerium für Bildung und Forschung (BMBF). We gratefully acknowledge Michael Sarnthein for providing the additional bulk samples from Core MD01-2416. We thank Ulrike Böttjer, Birgit Glückselig and Ruth Cordelair for the thorough purification of the diatom material and Gerhard Kuhn for the salt-correction of biogenic opal concentration data. Silke Steph is thanked for analyzing *N. pachyderma*$_{sin}$ oxygen and carbon isotopes and Marianne Warnkross for picking *N. pachyderma*$_{sin}$ for isotope analysis and radiocarbon dating.

Supporting information to:

"Surface water hydrography and nutrient dynamics of the deglacial subarctic Pacific – evidence from diatom and silicon stable isotopes"

Table S5.1. Planktic (*N. pachyderma*$_{sin}$) radiocarbon ages of **(A)** Core MD01-2416 (Sarnthein et al., 2004; 2007), and **(B)** Core MD02-2489 (Gebhardt et al., 2008), including newly calibrated ages. Reservoir ages were taken from Sarnthein et al. (2013). The uncertainty of each plateau boundary was calculated as the sum of the Lake Suigetsu varve counting error (Bronk Ramsey et al., 2012) plus the analytical ^{14}C age errors of the plateau boundary of Lake Suigetsu (Bronk Ramsey et al., 2012) and the respective cores (Sarnthein et al., 2004, 2007; Gebhardt et al., 2008).

(A) MD01-2416

Depth (cm) MD01-2416	^{14}C ages (ka) (Sarnthein et al.,2004; 2007)	^{14}C age error (a) (Sarnthein et al., 2004; 2007)	Reservoir age (a) (Sarnthein et al., 2013)	Calibrated ages (ka BP)	Derivation of cal. age	Uncertainty plateau boundaries (a; 1σ)	Calib 7.0 calibrated ages (ka BP)			
							Median (ka BP)	2σ min (ka BP)	2σ max (ka BP)	Relative area under probability distribution
0.75	5.684	30	570 ± 140	**5.900**	Calib 7.0	-	5.900	5.590	6.208	1
16	6.745	33	570 ± 140	**7.077**	Calib 7.0	-	7.077	6.751	7.386	1
39	7.869	36	570 ± 140	**8.161**	Calib 7.0	-	8.161	7.863	8.437	1
51	9.985	45	570 ± 140	**10.754**	Calib 7.0	-	10.754	10.390	11.131	1
87	-	-	570 ± 140	**13.640**	Plateau Ia	223	-	-	-	-
88	12.690	50	570 ± 140	13.670	Plateau Ia	-	-	-	-	-
91	12.750	60	570 ± 140	13.759	Plateau Ia	-	-	-	-	-
96	12.555	60	570 ± 140	13.908	Plateau Ia	-	-	-	-	-
97	-	-	570 ± 140	**13.938**	Plateau Ia	256	-	-	-	-
104	13.140	60	720 ± 285	**14.125**	Plateau I	343	-	-	-	-
107	13.000	60	720 ± 285	14.215	Plateau I	-	-	-	-	-
112	13.160	70	720 ± 285	14.366	Plateau I	-	-	-	-	-
115	13.205	55	720 ± 285	14.456	Plateau I	-	-	-	-	-
118	13.240	80	720 ± 285	14.546	Plateau I	-	-	-	-	-
122	13.430	90	720 ± 285	14.667	Plateau I	-	-	-	-	-
125	13.160	80	720 ± 285	14.757	Plateau I	-	-	-	-	-
129	13.410	80	720 ± 285	14.877	Plateau I	-	-	-	-	-
133	13.100	90	720 ± 285	14.998	Plateau I	-	-	-	-	-
136	13.090	60	720 ± 285	15.088	Plateau I	-	-	-	-	-
138	-	-	720 ± 285	**15.148**	Plateau I	304	-	-	-	-
140.5	13.795	60	720 ± 285	**15.631**	Calib 7.0	-	15.631	14.586	16.542	1
145	13.920	65	720 ± 285	**15.818**	Calib 7.0	-	15.818	14.916	16.766	1
166	14.320	45	720 ± 285	**16.414**	Calib 7.0	-	16.414	15.579	17.294	1
177	15.380	70	1480 ± 135	***17.086***	Calib 7.0	-	17.825	17.086	18.537	1
179	16.100	90	1480 ± 135	**17.131**	Plateau III	415	-	-	-	-
183	16.130	90	1480 ± 135	17.125	Plateau III	-	-	-	-	-
185	16.660	90	1480 ± 135	17.182	Plateau III	-	-	-	-	-
189	16.230	90	1480 ± 135	17.297	Plateau III	-	-	-	-	-
193	16.060	90	1480 ± 135	17.411	Plateau III	-	-	-	-	-
199	16.230	90	1480 ± 135	**17.582**	Plateau III	411	-	-	-	-
202.5	16.910	80	1480 ± 135	***18.332***	Calib 7.0	-	18.684	18.332	18.992	1

bold: age control points

bold + italic: calibrated ages is not median age

Table S5.1. (continued).

(B) MD02-2489

Depth (cm) MD02-2489	^{14}C ages (ka) (Gebhardt et al., 2008)	^{14}C age error (a) (Gebhardt et al., 2008)	Reservoir age (a) (Sarnthein et al., 2013)	Calibrated ages (ka BP)	Derivation of cal. age	Uncertainty plateau boundaries (a; 1σ)	Calib 7.0 calibrated ages (ka BP)			
							Median (ka BP)	2σ min (ka BP)	2σ max (ka BP)	Relative area under probability distribution
59.0	7.570	40	440 ± 285	**8.003**	Calib 7.0	-	8.003	7.434	8.579	1
66.5	8.715	45	440 ± 285	**9.310**	Calib 7.0	-	9.310	8.587	10.092	1
76.5	9.210	50	440 ± 285	**9.933**	Calib 7.0	-	9.933	9.247	10.660	1
86.5	10.140	70	440 ± 285	**11.135**	Calib 7.0	-	11.135	10.327	12.070	1
96.0	11.080	60	440 ± 285	**12.445**	Calib 7.0	-	12.445	11.540	13.143	0.997
110.0	11.870	30	440 ± 285	**13.297**	Calib 7.0	-	13.297	12.714	13.873	1
119.0	12.120	70	440 ± 285	**13.567**	Calib 7.0	-	13.567	12.862	14.249	1
130.0	12.730	35	440 ± 285	**14.125**	Plateau I	318	-	-	-	-
140.0	12.840	70	440 ± 285	14.409	Plateau I	-	-	-	-	-
150.8	12.918	65	440 ± 285	14.722	Plateau I	-	-	-	-	-
156.0	13.250	70	440 ± 285	14.864	Plateau I	-	-	-	-	-
160.0	11.935	45	440 ± 285	14.978	Plateau I	-	-	-	-	-
163.0	12.920	90	440 ± 285	15.063	Plateau I	-	-	-	-	-
165.5	12.800	90	440 ± 285	**15.149**	Plateau I	334	-	-	-	-
171.5	13.820	80	550 ± 305	**15.358**	Plateau IIa	371	-	-	-	-
177.5	13.990	80	550 ± 305	15.588	Plateau IIa	-	-	-	-	-
181.5	13.850	80	550 ± 305	15.742	Plateau IIa	-	-	-	-	-
184.5	14.030	80	550 ± 305	15.857	Plateau IIa		-	-	-	-
189.5	14.180	80	550 ± 305/120	**16.049**	Plateau IIa/IIb	464	-	-	-	-
192.0	14.500	70	550 ± 120	16.112	Plateau IIb	-	-	-	-	-
195.5	14.270	80	550 ± 120	16.239	Plateau IIb	-	-	-	-	-
200.5	14.430	90	550 ± 120	**16.398**	Plateau IIb	373	-	-	-	-
204.5	15.050	90	*NA*	16.724	interpolated	-	-	-	-	-
209.5	15.580	90	805 ± 155	**17.131**	Plateau III	415	-	-	-	-
212.5	15.500	95	805 ± 155	17.225	Plateau III	-	-	-	-	-
217.5	15.350	90	805 ± 155	**17.582**	Plateau III	411	-	-	-	-
223.5	16.060	80	*NA*	17.763	interpolated	-	-	-	-	-
231.0	16.750	110	965 ± 200	**17.975**	Plateau IV	563	-	-	-	-
237.0	16.830	110	965 ± 200	18.331	Plateau IV	-	-	-	-	-
248.0	16.867	65	965 ± 200	**18.984**	Plateau IV	526	-	-	-	-
254.5	17.300	90	965 ± 200	**19.709**	Calib 7.0	-	19.709	19.135	20.250	1
268.0	18.042	65	965 ± 200	**20.595**	Calib 7.0	-	20.595	20.048	21.145	1
520.0	30.521	170	*NA*	**33.500**	estimated*	-	-	-	-	-

bold: age control points

Table S5.2. Contamination of purified diatom samples with non-biogenic silicates estimated from SiO_2 and Al_2O_3 percentages determined **(A)** by ICP-OES for Core SO202-27-6 and **(B, C)** by EDS for Cores (B) SO202-27-6 and (C) MD01-2416.

(A)

		ICP-OES		
SO202-27-6 Depth (cm)	**Age (ka BP)**	**SiO_2 assumed (%)**	**Al_2O_3 (%)**	**non-biogenic silicate contamination (%)**
9-11	9.888	99.51	0.15	0.81
21-23	13.134	99.09	0.14	1.22

(B)

		EDS		
SO202-27-6 Depth (cm)	**Age (ka BP)**	**SiO_2 (%)**	**Al_2O_3 (%)**	**non-biogenic silicate contamination (%)**
1-3	7.029	98.1	1.0	4.2
5-6	8.458	98.9	0.5	2.1
9-11	9.888	99.3	0.2	1.1
13-15	11.153	98.9	0.4	2.1
17-19	12.143	99.1	0.2	1.3
21-23	13.134	98.8	0.3	1.9
25-27	14.125	98.2	0.4	2.7
29-31	14.481	98.8	0.2	1.5
33-35	14.837	98.7	0.2	1.8
37-39	15.198	98.8	0.3	1.7
41-43	15.561	98.9	0.3	1.7
45-47	15.886	97.9	0.6	3.3
53-55	17.129	97.7	0.8	4.0
57-59	18.105	98.0	0.7	3.4
61-63	19.080	98.6	0.3	1.9
77-79	22.703	96.9	1.4	6.0
Avg		98.5	0.5	2.6
SD (1σ)		0.6	0.3	1.3

(C)

		EDS		
MD01-2416 Depth (cm)	**Age (ka BP)**	**SiO_2 (%)**	**Al_2O_3 (%)**	**non-biogenic silicate contamination (%)**
4-8*	6.292	99.17	0.10	1.1
12-16*	6.920	99.18	0.12	1.1
22-26*	7.454	99.07	0.18	1.3
32-36*	7.925	99.14	0.07	1.0
38-40	8.161	98.82	0.24	1.7
42-46	9.241	99.13	0.12	1.1
48-50	10.322	99.05	0.12	1.2
52-56*	10.995	99.08	0.11	1.2
62-66*	11.796	99.07	0.12	1.2
68-70	12.197	99.05	0.11	1.2
72-76*	12.638	99.13	0.10	1.1
78-80	12.999	98.86	0.14	1.4
82-86*	13.400	98.94	0.12	1.3
92-96*	13.849	99.03	0.11	1.2
102-106	14.125	98.98	0.09	1.2
Avg		99.0	0.1	1.2
SD (1σ)		0.1	0.0	0.2

*data from Maier et al. (2013)

Table S5.3. Composition of **(A)** pre-sonicated and **(B)** final purified SO202-27-6 diatom samples. **(A)** Relative abundances of diatoms, radiolarians and sponge spicules are related to the total counts and relative abundances of *Coscinodiscus marginatus* and *Coscinodiscus oculus-iridis* are related to the diatom species assemblage, determined by light microscopy. Note that the sample 29-31 cm is the only sample were non-*Coscinodiscus* diatoms contribute to the diatom species assemblage (5.3%). **(B)** All relative abundances are related to the total counts.

(A)

		light microscopy (pre-sonication)					
SO202-27-6 Depth (cm)	**Age (ka BP)**	**total counts**	**diatoms (%)**	**radiolarians (%)**	**sponge spicules (%)**	***C. marginatus* (% of diatom abundance)**	***C. oculus-iridis* (% of diatom abundance)**
1-3	7.029	201	96.5	3.5	0.0	97.4	2.6
5-6	8.458	216	84.3	15.3	0.5	94.5	5.5
9-11	9.888	159	88.1	10.7	1.3	97.1	2.9
13-15	11.153	221	62.4	34.4	3.2	94.9	5.1
17-19	12.143	158	88.6	11.4	0.0	95.0	5.0
21-23	13.134	215	88.8	9.8	1.4	93.7	6.3
25-27	14.125	123	91.1	8.9	0.0	92.9	7.1
29-31	14.481	169	88.8	11.2	0.0	83.3	11.3
33-35	14.837	213	92.5	7.0	0.5	96.4	3.6
37-39	15.198	154	92.2	7.1	0.6	97.9	2.1
41-43	15.561	139	84.2	13.7	2.2	98.3	1.7
45-47	15.886	189	76.2	23.3	0.5	97.2	2.8
53-55	17.129	217	53.5	46.5	0.0	92.2	7.8
57-59	18.105	354	36.4	62.1	1.4	94.6	5.4
61-63	19.080	233	70.0	29.2	0.9	84.7	9.2
77-79	22.703	224	84.8	14.3	0.9	94.7	5.3
Avg		199	79.9	19.3	0.8	94.1	5.2
SD (1σ)		54	16.5	16.2	0.9	4.3	2.7

(B)

		SEM (purified)					
SO202-27-6 Depth (cm)	**Age (ka BP)**	**total counts**	**diatoms (%)**	**radiolarians (%)**	**sponge spicules (%)**	**non-biogenic silicate contamination (%)**	**not identified (%)**
1-3	7.029	423	96.5	3.3	0	0.2	0
5-6	8.458	391	96.4	3.1	0	0.3	0.3
9-11	9.888	496	97.8	1.6	0.2	0.4	0
13-15	11.153	394	97.5	0.5	1.0	1.0	0
17-19	12.143	509	97.2	2.6	0	0.2	0
21-23	13.134	337	91.4	8.0	0	0.6	0
25-27	14.125	249	96.4	3.2	0	0.4	0
29-31	14.481	289	88.2	10.0	0.7	0.3	0.7
33-35	14.837	242	95.9	3.3	0	0.8	0
37-39	15.198	344	90.7	6.1	0	3.2	0
41-43	15.561	322	99.1	0.6	0	0.3	0
45-47	15.886	326	92.0	6.7	0.6	0.6	0
53-55	17.129	269	91.8	5.2	0	2.6	0.4
57-59	18.105	281	91.8	6.8	0	1.4	0
61-63	19.080	349	90.0	9.2	0	0.6	0.3
77-79	22.703	233	95.7	3.9	0	0.4	0
Avg		341	94.3	4.6	0.2	0.8	0.1
SD (1σ)		84	3.3	2.9	0.3	0.9	0.2

Table S5.4. Measured $\delta^{18}O_{diat}$ and $\delta^{30}Si_{diat}$ values of Cores **(A)** SO202-27-6 and **(B)** MD01-2416 including standard deviations (SD, 1σ) and number of isotopic measurements (n).

(A)

SO202-27-6							
Depth (cm)	Age (ka BP)	$\delta^{30}Si_{diat}$ (‰)	SD $\delta^{30}Si_{diat}$ (1σ; ‰)	n	$\delta^{18}O_{diat}$ (‰)	SD $\delta^{18}O_{diat}$ (1σ; ‰)	n
1-3	7.029	1.52	0.50	3	40.39	0.17	3
5-7	8.458	2.01	0.06	2	39.97	0.08	2
9-11	9.888	2.02	0.13	3	39.78	0.05	2
13-15	11.153	1.63	0.02	2	41.51	0.03	2
17-19	12.143	1.59	0.01	2	43.22	0.06	2
21-23	13.134	1.40	0.10	2	43.69	0.18	3
25-27	14.125	1.53	0.35	3	43.64	0.04	3
29-31	14.481	1.45	0.08	3	43.81	0.38	3
33-35	14.837	1.42	0.08	2	43.43	0.21	2
37-39	15.198	1.67	0.08	2	43.13	0.06	3
41-43	15.561	1.65	0.12	3	42.84	0.04	2
45-47	15.886	2.04	-	1	41.12	-	1
53-55	17.129	1.16	-	1	42.52	-	1
57-59	18.105	1.23	-	1	43.17	-	1
61-63	19.080	1.54	-	1	43.01	-	1
77-79	22.703	1.63	0.13	2	42.91	0.22	2

(B)

MD01-2416							
Depth (cm)	Age (ka BP)	$\delta^{30}Si_{diat}$ (‰)	SD $\delta^{30}Si_{diat}$ (1σ; ‰)	n	$\delta^{18}O_{diat}$ (‰)	SD $\delta^{18}O_{diat}$ (1σ; ‰)	n
4-8*	6.292	1.19	0.01	2	42.31	0.29	2
12-16*	6.920	1.37	0.11	4	42.48	0.10	3
22-26*	7.454	1.31	0.06	2	42.57	0.20	2
32-36*	7.925	1.30	0.04	2	42.60	0.09	2
38-40	8.161	1.35	0.15	2	42.76	0.05	2
42-46	9.241	1.38	0.14	3	42.64	0.13	4
48-50	10.322	1.22	-	1	43.21	-	1
52-56*	10.995	1.30	0.04	3	43.10	0.08	2
62-66*	11.796	1.38	0.01	2	43.10	0.04	2
68-70	12.197	1.54	0.52	2	43.88	0.25	2
72-76*	12.638	1.46	0.01	3	43.68	0.13	2
78-80	12.999	1.10	-	1	43.99	-	1
82-86*	13.400	1.32	0.02	5	43.70	0.07	3
92-96*	13.849	1.34	0.01	2	43.64	0.05	2
102-106	14.125	1.29	0.02	3	43.84	0.35	3

*isotope data from Maier et al. (2013)

Table S5.5. Proxy data of Core SO202-27-6. **(A)** $\delta^{18}O_{Nps}$ and $\delta^{13}C_{Nps}$ values; **(B**) biogenic opal content; **(C)** opal mass accumulation rates; **(D)** XRF intensities (Fe, Ca and Si/Ti ratios).

(A)

Depth (cm)	Age (ka BP)	$\delta^{18}O$ (‰) *Nps*	$\delta^{13}C$ (‰) *Nps*	Size fraction (µm)
0-1	6.493	2.385	0.598	125-250
4-5	7.922	2.582	0.466	125-250
8-9	9.352	2.603	0.580	125-250
12-13	10.781	2.553	0.417	125-250
16-17	11.772	2.873	0.407	125-250
20-21	12.763	3.127	0.232	125-250
24-25	13.753	3.175	0.235	125-250
28-29	14.347	3.22	0.201	125-250
32-33	14.703	3.378	0.126	125-250
36-37	15.059	3.657	0.103	125-250
40-41	15.439	3.748	0.173	>400
44-45	15.764	3.962	0.015	125-250
48-49	16.107	4.015	0.028	125-250
52-53	16.764	3.928	0.025	125-250
56-57	17.739	3.910	0.035	125-250
60-61	18.714	3.796	0.073	125-250
64-65	19.689	3.901	0.088	125-250
68-69	20.665	3.765	0.072	125-250
72-73	21.640	3.732	0.014	125-250
76-77	22.413	3.751	0.127	125-250
80-81	23.186	3.725	0.162	315-400
84-85	23.959	3.814	-0.052	315-400
88-89	24.732	3.847	0.178	125-250

(B)

Depth (cm)	Age (ka BP)	SiO2 (Gew%)
0-1	6.493	12
3-4	7.386	10
7-8	8.816	10
10-11	9.888	7
11-12	10.245	7
15-17	11.400	6
19-20	12.391	8
20-21	12.639	10
23-24	13.382	9
27-28	14.214	8
30-31	14.481	18
31-32	14.570	11
35-36	14.926	6
39-40	15.298	6
40-41	15.399	7
43-44	15.643	4
47-48	15.968	4
50-51	16.282	4
51-52	16.398	5
55-56	17.373	7
59-60	18.349	4
60-61	18.592	6
63-64	19.324	6
67-68	20.299	5
70-71	21.030	7
71-72	21.274	6
75-76	22.123	6
79-80	22.896	6
80-81	23.089	7
83-84	23.669	4
87-88	24.442	4

(C)

Depth (cm)	Age (ka BP)	Opal MAR (g/(cm2*ka))
0-1	6.493	24
10-11	9.888	17
20-21	12.639	29
30-31	14.481	96
40-41	15.399	55
50-51	16.282	27
60-61	18.592	16
70-71	21.030	20
80-81	23.089	28

Table S5.5. (continued).

(D)

Depth (cm)	Age (ka BP)	XRF			Depth (cm)	Age (ka BP)	XRF		
		Fe (cps)	Ca (cps)	Si/Ti (cps/cps)			Fe (cps)	Ca (cps)	Si/Ti (cps/cps)
1	6.672	104731	149744	1.98	51	16.398	149985	54060	2.36
2	7.029	107781	160505	2.25	52	16.642	155679	50490	2.28
3	7.386	107482	179962	2.45	53	16.886	171213	68159	2.45
4	7.744	104935	176828	2.31	54	17.129	154331	84726	2.64
5	8.101	106917	179897	2.43	55	17.373	130295	117858	2.94
6	8.458	105477	175967	2.32	56	17.617	123394	129278	3.06
7	8.816	104681	182799	2.34	57	17.861	124008	135124	3.19
8	9.173	98047	196291	2.18	58	18.105	121637	144686	3.04
9	9.530	97919	210582	2.18	59	18.349	114262	171946	3.17
10	9.888	100662	217745	2.12	60	18.592	116713	156529	3.17
11	10.245	103885	246838	2.18	61	18.836	127889	135680	3.06
12	10.602	102377	252492	2.05	62	19.080	127186	150658	3.08
13	10.905	107716	232884	1.90	63	19.324	114478	154913	3.12
14	11.153	82325	343187	2.73	64	19.568	118410	140561	2.99
15	11.400	97089	320880	2.59	65	19.811	115297	139094	2.88
16	11.648	71635	387743	3.29	66	20.055	124342	123026	2.76
17	11.896	72541	357148	3.09	67	20.299	126747	119028	2.97
18	12.143	63956	374529	3.23	68	20.543	124397	117498	2.93
19	12.391	68222	356364	3.35	69	20.787	128784	112986	2.82
20	12.639	66090	346450	3.29	70	21.030	127896	100113	2.71
21	12.886	59680	343759	3.62	71	21.274	129637	85915	2.47
22	13.134	69718	305852	3.01	72	21.518	108213	61259	2.25
23	13.382	62497	315354	3.50	73	21.737	118033	79309	2.67
24	13.630	58495	293276	3.48	74	21.930	125646	116630	2.86
25	13.877	56738	231679	3.71	75	22.123	127287	95137	2.60
26	14.125	60406	227146	3.53	76	22.316	122967	104003	2.58
27	14.214	62807	248132	3.78	77	22.510	125011	115549	2.70
28	14.303	66717	241181	4.27	78	22.703	117437	118272	2.88
29	14.392	68098	236726	4.40	79	22.896	109135	114328	2.90
30	14.481	66648	225043	4.63					
31	14.570	63177	208682	4.32					
32	14.659	67946	236835	4.01					
33	14.748	69595	233724	4.18					
34	14.837	75936	201380	4.16					
35	14.926	72998	215420	3.65					
36	15.015	76566	211101	3.40					
37	15.104	103203	165404	3.04					
38	15.198	112819	157739	3.02					
39	15.298	102409	181839	3.17					
40	15.399	103859	180319	3.06					
41	15.480	105162	180983	3.12					
42	15.561	119696	148001	3.00					
43	15.643	119816	93156	2.73					
44	15.724	140755	84299	2.52					
45	15.805	133905	92525	2.65					
46	15.886	144245	81589	2.56					
47	15.968	154566	69765	2.43					
48	16.049	158619	52041	2.31					
49	16.165	152824	48904	2.39					
50	16.282	151868	54213	2.50					

Chapter 6 – Millennial-scale variabilities in upwelling and halocline strength in the NE Pacific during Marine Isotope Stage 3

Maier, E.[1], Abelmann, A.[1], Gersonde, R.[1], Méheust, M.[1], Chapligin, B.[2], Ren, J.[1], Tiedemann, R.[1]

[1]Alfred Wegener Institute, Helmholtz Centre for Polar and Marine Research, Bremerhaven, Germany
[2]Alfred Wegener Institute, Helmholtz Centre for Polar and Marine Research, Potsdam, Germany

to be submitted to Earth and Planetary Science Letters

Abstract

The modern subarctic Pacific is characterized by a steep salinity-driven surface water stratification, which hampers the supply of saline and nutrient-rich deeper waters into the euphotic zone, limiting productivity. However, the strength of the halocline might have varied in the past. Here, we present diatom oxygen ($\delta^{18}O_{diat}$) and silicon ($\delta^{30}Si_{diat}$) stable isotope data from the open subarctic North-East (NE) Pacific (SO202-27-6; Gulf of Alaska), in combination with other proxy data (*Neogloboquadrina pachyderma*$_{sin}$ $\delta^{18}O$, biogenic opal, Ca and Fe intensities, IRD), to evaluate changes in surface water hydrography and productivity during Marine Isotope Stage (MIS) 3, characterized by millennial-scale temperature changes (Dansgaard-Oeschger (D-O) cycles) documented in Greenland ice cores.

From ca. 50-40 ka BP our proxy data show millennial-scale cyclicities, which can be correlated to D-O events. Periods coinciding with D-O interstadials are characterized by lower surface water stratification and increased upwelling intensity, resulting in high export production but low silicic acid utilization. During D-O stadials surface water stratification is relatively increased, probably related to increased freshwater discharge from the Cordilleran Ice Sheet. The close temporal correlation of the observed millennial-scale variabilities in upwelling intensity with changes in the intensity of the Atlantic Meridional Overturning Circulation indicates rapid teleconnections between the North Atlantic and the North Pacific. At ~39 ka BP our data indicate a meltwater event in the subarctic NE Pacific that coincides with the meltwater signal characterizing Heinrich stadial (HS) 4 in the North Atlantic, suggesting close similarities between the North Atlantic and NE Pacific meltwater histories. Following HS4 the $\delta^{18}O_{diat}$ and $\delta^{30}Si_{diat}$ data suggest generally fresher and better-utilized surface waters, possibly pointing towards a strengthening of the surface water stratification. This hypothesis is supported by $\delta^{18}O_{Nps}$ and alkenone-based sea surface temperatures (SST), possibly pointing towards increasing seasonal contrasts in SST in response to reduced

exchange with deeper waters. We suggest that an increased seasonality in SST during late MIS3 might have resulted in an increased moisture transport onto the North American continent during autumn, where increased snow accumulation might have accelerated ice sheet growth.

6.1 Introduction

During Marine Isotope Stage 3 (MIS3) (~57-29 ka BP) Greenland ice cores have revealed millennial-scale climate variabilities, so-called Dansgaard-Oeschger (D-O) cycles, shifting between cold stadials and warm interstadials (Dansgaard et al., 1993). Similar millennial-scale variabilities have also been observed in North Atlantic (Bond et al., 1993; Voelker et al., 2002) and North Pacific sediments (Kiefer et al., 2001; Hendy, 2010; Riethdorf et al., 2013b), and have been related to iceberg rafting from Northern Hemispheric ice-sheets (Kotilainen and Shackleton, 1995; Van Krefeld et al., 2000), associated with changes in the strength of Atlantic Meridional Overturning Circulation (AMOC) (Menviel et al., 2014). Progressively colder D-O cycles in North Atlantic sea surface temperatures, bundled into ~7 ka long Bond cycles, culminated in massive iceberg discharges dominantly from the Laurentide Ice Sheet (LIS), so-called Heinrich events (Bond et al., 1993; Hemming, 2004). Episodes of rapid, increased IRD deposition in the NE Pacific, coeval with Heinrich events in the North Atlantic (Hendy and Cosma, 2008) indicate a close link between the (de)glacial evolution of the LIS and the Cordilleran Ice Sheet (CIS). Recent evidence from diatom oxygen ($\delta^{18}O_{diat}$) and silicon ($\delta^{30}Si_{diat}$) isotopes from the deglacial subarctic NE Pacific (Maier et al., a, in prep.) further supports this link and highlights the potential of $\delta^{18}O_{diat}$ and $\delta^{30}Si_{diat}$ for reconstructing changes in surface water hydrography and nutrient dynamics.

The growth of Northern Hemisphere ice-sheets depends on various factors, including sufficiently cold temperatures and a sufficient moisture flux to the high latitudes. The North Pacific seems to have been the dominant moisture source allowing for the onset of Northern Hemisphere glaciation (Haug et al., 2005), and moisture transport from the North Pacific might have played an important role in shaping D-O dynamics (Kiefer et al., 2001). Today, the subarctic Pacific is characterized by a strong salinity stratification (permanent halocline), which has been first developed at the onset of Northern Hemisphere glaciation (Haug et al., 1999; Swann et al., 2006) and is sustained by different factors including the northward moisture flux of the East Asian monsoon (Emile-Geay et al., 2003). By enabling large seasonal contrasts in sea surface temperatures (SST), the existence of the permanent halocline is suggested to have been an important precondition for generating an adequate amount of moisture to initiate the Northern Hemisphere glaciation during times of global climate cooling (Haug et al., 2005), indicating that changes in the strength of the halocline might be an

important factor in modulating Northern Hemisphere ice-sheet growth.

This study presents $\delta^{18}O_{diat}$ and $\delta^{30}Si_{diat}$ records, as well as subsurface *Neogloboquadrina pachyderma*$_{sin}$ $\delta^{18}O$ ($\delta^{18}O_{Nps}$), Ca and Fe X-ray fluorescence (XRF) and biogenic opal records from the open subarctic NE Pacific (Core SO202-27-6; Gulf of Alaska) (Fig. 6.1) over MIS3 to early MIS2 (50-25 ka BP). Our proxies reveal clear millennial-scale variabilities in upper ocean stratification and upwelling intensity related to D-O cyclicities during the early MIS3 and suggest a close link between the (de)glacial evolution of the LIS and the CIS. Furthermore, in combination with alkenone-based SST (Méheust, 2014) our data indicate that the subarctic North Pacific might have acted as a moisture source for glacial ice accumulation on the North American continent eventually leading to glacial MIS2.

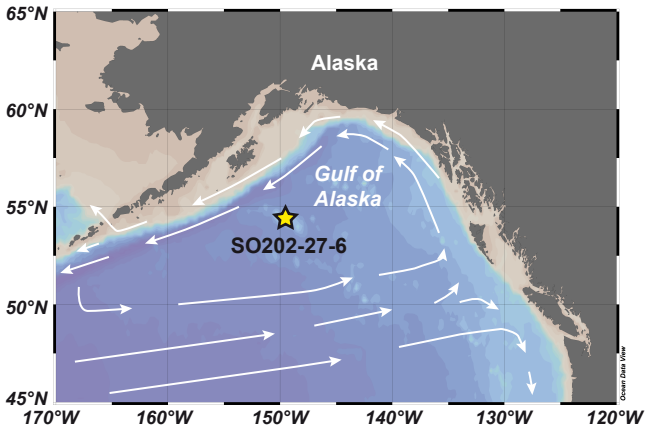

Figure 6.1. Location of the studied Core SO202-27-6 and main surface water currents (after Dodimead et al., 1963).

6.2 Material and Methods

The kasten Core SO202-27-6 from the Patton Seamount, open NE Pacific (54.296°N, 149.590°W, 2929 m) (Fig. 6.1) was sampled from 92 cm down to the base of the core at 289 cm. For combined $\delta^{18}O_{diat}$ and $\delta^{30}Si_{diat}$ analysis we purified 33 diatom samples (100-125 µm fraction) according to the procedure described in Maier et al. (2013). Briefly, bulk samples were liberated from carbonates and non-diatom silicates using a combination of physical and chemical treatments, including sonication and heavy liquid separation. To determine the diatom species composition microscopic slides were prepared for all diatom samples prior to the final (destructive) sonication process. We counted on average 170 components (diatom valves, radiolarians, sponge spicules) using a Zeiss Axioskop I light microscope at x400 magnification, following the counting approach described in Maier et al. (a, in prep.) and the diatom taxonomy of Sancetta (1982, 1987). We furthermore prepared scanning electron microscope (SEM) samples of eight purified diatom samples and estimated the contamination with non-diatom biogenic silicates (radiolarians, siliceous sponge spicules) by counting on

average 181 silica particle equivalents using a Philips XL 30 ESEM (see Maier et al. (a, in prep.) for details). The influence of residual non-biogenic silicates (e.g. clay minerals) on the isotopic signals was estimated using energy-dispersive spectrometry (EDS) as described in Maier et al. (2013). To assure the validity of the EDS measurements we additionally performed inductively coupled plasma optical emission spectrometry (ICP-OES) measurements on four diatom samples, according to Chapligin et al. (2012). Al_2O_3 was used as a tracer for non-biogenic silicates and mass balance corrections with two different $\delta^{18}O$ values (0 ‰, +20.00 ‰) and $\delta^{30}Si$ values (-2.50 ‰, +1.80 ‰) for the non-biogenic silicate contamination were applied, in accordance with their isotopic range (Fig. 6.2; see Maier et al. (a, in prep.) for details).

About 1.5-2.0 mg of purified diatom material was used to measure the $\delta^{18}O_{diat}$ and $\delta^{30}Si_{diat}$ composition using combined silica $\delta^{18}O$ and $\delta^{30}Si$ analysis according to Maier et al. (2013) and Chapligin et al. (2010). Values are reported in the common δ-notation vs. V-SMOW (Vienna Standard Mean Ocean Water) for oxygen isotopes and vs. NBS-28 for silicon isotopes. Analytical precision was better than 0.25‰ for $\delta^{18}O_{diat}$ (Chapligin et al., 2011) and better than 0.12‰ for $\delta^{30}Si_{diat}$ measurements (Maier et al., 2013). Diatom samples were measured at least twice when enough purified material was available.

Fifty $\delta^{18}O_{Nps}$ measurements were carried out using a MAT 251 mass spectrometer directly coupled to an automated carbonate preparation device (Kiel I) and calibrated via NIST-19 international standard to the PDB scale. *N. pachyderma*$_{sin}$ were picked from the 125-250 µm and the 315-400 µm fractions. All isotope values are given in δ-notation vs. V-PDB (Vienna Pee Dee Belemnite). The precision of the measurements at 1σ was better than 0.08‰.

We measured the relative elemental composition (counts per second; cps) at 1 cm resolution using an Avaatech X-ray fluorescence (XRF) core scanner. The elements Fe and Ca presented here were obtained from the scan performed at 1 mA, with a tube voltage of 10 kV and a counting time of 30 seconds.

As indicator for input and relative changes in ice-rafted debris (IRD) we calculated the weight-% of lithic fragments of the >250-µm fraction, sieved from the heavy fraction after the first heavy liquid separation (ρ=2.2-2.3 g*cm^{-3}) for diatom isotope sample preparation, and normalized the weight-% to the complete heavy fraction (>63 µm). Dropstones (pebble-to-cobble sized IRD) are not included in the calculation, but need to be considered for the interpretation of the IRD record.

The concentration of biogenic opal (weight-%) was determined within 53 bulk samples à ca. 20 mg, following the automated leaching method of Müller and Schneider (1993). Obtained results were corrected for salt concentrations in the input sample after Kuhn (2013).

Furthermore, six samples of *N. pachyderma*$_{sin}$ were picked from the 125-250-µm fraction and

analysed for radiocarbon by accelerator mass spectrometry (AMS) at the National Ocean Science AMS facility (NOSAMS) at Woods Hole Oceanographic Institution (Table 6.1).

6.3 Chronology

The chronology of the studied part of Core SO202-27-6 is based on calibrated planktic ^{14}C ages in combination with tuning of proxy data to NGRIP oxygen isotope (Andersson et al., 2006; Svensson et al., 2006, 2008) and dust records (Ruth et al., 2007) (Table 6.1). The six planktic ^{14}C ages, obtained between 103.4 cm and 243.5 cm, were calibrated using the Calib 7.0 software and the Marine13 calibration dataset (Stuiver and Reimer, 1993; Reimer et al., 2013). We applied a planktic reservoir age of 965 ± 200 a according to the oldest reservoir age determined by Sarnthein et al. (2013) for nearby Core MD02-2489 (^{14}C plateau IV). We are aware that the reservoir age was likely not constant throughout the MIS3, but there are no information available on local changes in reservoir ages during MIS3. Additional age control points, in between the calibrated ^{14}C ages and below 243.5 cm, were obtained by tuning different proxy data to NGRIP oxygen isotope (Andersson et al., 2006; Svensson et al., 2006, 2008) and dust records (Ruth et al., 2007) using AnalySeries 2.0.4.2 (Table 6.1; Fig. 6.3). In a first correlation we tuned the Ca XRF record and the $\delta^{18}O_{Nps}$ record to the NGRIP $\delta^{18}O$ record (Andersson et al., 2006; Svensson et al., 2006, 2008), assuming an overall in-phase behavior/synchronicity between increased Ca and biogenic opal concentrations and decreased $\delta^{18}O_{Nps}$ in the subarctic NE Pacific and warm periods in the North Atlantic region. This assumption is based on the at large positive correlation between the SO202-27-6 climate changes and the NGRIP $\delta^{18}O$ variabilites between ca. 25-6 ka BP (Maier et al., a, in prep) and

Table 6.1. Age constraints of the studied core section of SO202-27-6. Age control points (calibrated ages) derived from calibration of planktic ^{14}C ages are generally the median values, except for the values in italics.

							Calib 7.0 calibrated ages (a BP)			
^{14}C sample ID	depth (m)	^{14}C ages (ka)	^{14}C age error (a)	reservoir age (a)	calibrated ages (ka BP)	derivation of cal. age	Median	2σ min	2σ max	relative area under probability distribution
OS-87894	0.885*	21.400	120	965 ± 200	**24.732**	Calib 7.0	24.732	24.119	25.333	1
OS-87892	1.035	23.800	110	965 ± 200	**27.243**	Calib 7.0	27.243	26.669	27.634	1
OS-88043	1.395	28.300	140	965 ± 200	**30.958**	Calib 7.0	31.284	30.958	31.663	1
-	1.460	-	-	-	**32.710**	tuned	-	-	-	-
-	1.510	-	-	-	**33.490**	tuned	-	-	-	-
-	1.610	-	-	-	**34.950**	tuned	-	-	-	-
OS-87893	1.635	33.000	170	965 ± 200	**35.409**	Calib 7.0	36.018	35.409	36.574	1
-	1.670	-	-	-	**36.290**	tuned	-	-	-	-
-	1.710	-	-	-	**38.150**	tuned	-	-	-	-
-	1.810	-	-	-	**40.030**	tuned	-	-	-	-
-	1.910	-	-	-	**40.990**	tuned	-	-	-	-
OS-87899	1.975	38.400	310	965 ± 200	***41.365***	Calib 7.0	41.926	41.365	42.454	1
OS-87889	2.075	39.900	290	965 ± 200	***42.359***	Calib 7.0	42.873	42.359	43.409	1
OS-87898	2.435	42.800	600	965 ± 200	***44.151***	Calib 7.0	45.283	44.151	46.435	1
-	2.560	-	-	-	**47.010**	tuned	-	-	-	-
-	2.760	-	-	-	**49.150**	tuned	-	-	-	-
-	2.860	-	-	-	**49.650**	tuned	-	-	-	-

* data from Maier et al. (a, in prep.)

is consistent with previous MIS3 age models from the NE Pacific (Hendy et al., 2002; Cartapanis et al., 2011). In a second step we refined the position of the tuned age control points by additionally considering variabilities observed in the diatom isotope records and biogenic opal concentrations and assuming a positive relationship between NGRIP dust (Ruth et al., 2007) and Fe intensity. The final age model was generated through linear interpolation between the determined age control points.

6.4 Results

The contamination of the 33 purified diatom samples with non-biogenic silicates (minerals, rock fragments) generally ranges between 1.3 and 3.9% (Table S6.1), except for the uppermost two samples from the early MIS2 (5.3 and 7.6%). Since the mass-balance corrections of the isotopic values for this contamination do not at all even out the isotopic variations (Fig. 6.2), the observed patterns in the isotopic records do not result from such a contamination. Contamination with non-diatom biogenic silicates (radiolarians, sponge spicules) is on average 6 ± 6% prior to the final sonication procedure, but final purified samples are generally reduced (up to 100%) in contamination with non-diatom biogenic

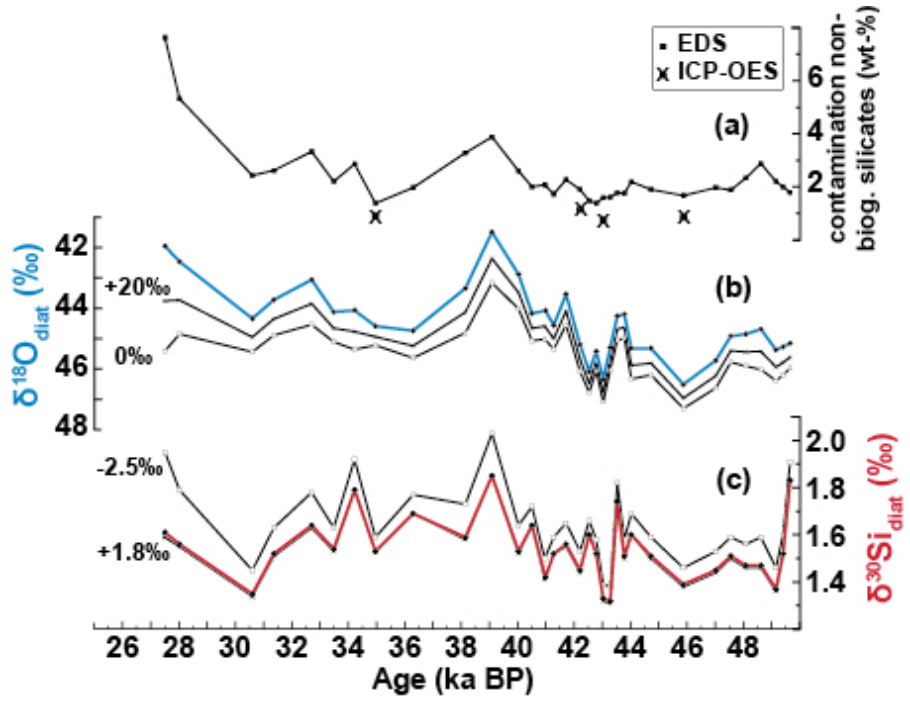

Figure 6.2. (a) Contamination with non-biogenic silicates determined by ICP-OES and EDS. **(b)** and **(c)** Measured $\delta^{18}O_{diat}$ (b, blue curve) and $\delta^{30}Si_{diat}$ (c, red curve) records and $\delta^{18}O_{diat}$ and $\delta^{30}Si_{diat}$ records mass-balance corrected for contamination with non-biogenic silicates based on EDS (black curves in (b) and (c)), using different theoretical $\delta^{18}O_{cont}$ and $\delta^{30}Si_{cont}$ values. Contamination with non-biogenic silicates determined by ICP-OES is less than that determined by EDS. Due to its lower detection limit and higher precision ICP-OES is generally to prefer over EDS (Chapligin et al., 2012). Thus, the actual maximum influence of such a contamination on the $\delta^{18}O_{diat}$ and $\delta^{30}Si_{diat}$ records is even less than shown. However, the required weight of 10 mg diatom material did not allow a complete down-core contamination assessment using ICP-OES.

silicates (Table S6.2), indicating a negligible influence on the isotopic signals. The diatom species assemblage of the samples is absolutely dominated by *Coscinodiscus* species (99.9 ± 0.4%), with a large contribution of *C. marginatus* (92.0 ± 11.3%) and a minor contribution of *C. oculus-iridis* (7.9 ± 11.3%).

The $\delta^{18}O_{diat}$ record shows a variation of about 5.0‰ between +41.49‰ (at ~39 ka BP) and +46.51‰ (at ~46 ka BP) and the $\delta^{30}Si_{diat}$ record varies about 0.53‰ between +1.32‰ (at ~43 ka BP) and +1.85‰ (at ~39 ka BP; Fig. 6.4c, f; Table S6.3). Thus, the lowest $\delta^{18}O_{diat}$ at ~39 ka BP coincides with the highest $\delta^{30}Si_{diat}$, as well as with HS4, characterized by a major IRD event recorded in the North Atlantic (Hemming, 2004). Furthermore, around that time the sediment is characterized by the occurrence of pebble- and cobble-sized dropstones (Fig. 6.3a), a peak of enriched subsurface $\delta^{18}O_{Nps}$ and a minimum in biogenic opal concentrations (Fig. 6.4d, g). Prior to HS4, the $\delta^{18}O_{diat}$ and $\delta^{30}Si_{diat}$ records as well as the biogenic opal record, the subsurface $\delta^{18}O_{Nps}$, the Ca and Fe intensity records and the IRD record from Core SO202-27-6 show distinct millennial-scale variabilities, consistent with D-O cycles in the NGRIP $\delta^{18}O$ record (Svensson et al., 2006, 2008). These variabilities are particularly pronounced for the time periods coeval to D-O cycles 12 and 11 (Fig. 6.4).

Time intervals contemporaneous to D-O interstadials are generally characterized by comparatively enriched $\delta^{18}O_{diat}$, but depleted subsurface $\delta^{18}O_{Nps}$. The $\delta^{30}Si_{diat}$ values are also depleted, while biogenic opal concentration and Ca intensities are high and Fe intensities as well as IRD are low. The amplitudes of millennial-scale variabilities of the oxygen isotope records are ca. 2.0-2.3‰ for surface $\delta^{18}O_{diat}$, and about 0.3‰ for subsurface $\delta^{18}O_{Nps}$. The millennial-scale amplitudes of the $\delta^{30}Si_{diat}$ record show a range of ca. 0.1-0.4‰ and biogenic opal concentrations vary between ca. 6% (D-O stadials) and ca. 30% (D-O interstadial 11). The internal structure of the millennial-scale cycles is characterized by a rapid increase in biogenic opal coincident with the start of the D-O interstadial, combined with a decrease in $\delta^{30}Si_{diat}$, followed by a gradual decline in biogenic opal and increase in $\delta^{30}Si_{diat}$. Following HS4 most proxy data from SO202-27-6 do not show clear millennial-scale cyclicities, except Ca and Fe intensities, but amplitudes are lower compared to the early MIS3. Following the peak of depleted $\delta^{18}O_{diat}$ and enriched $\delta^{30}Si_{diat}$ during HS4, the $\delta^{18}O_{diat}$ increases and the $\delta^{30}Si_{diat}$ decreases, but $\delta^{18}O_{diat}$ values are generally ca. 1.10‰ lighter and $\delta^{30}Si_{diat}$ are generally ca. 0.11‰ heavier during late MIS3 compared to the time period prior to HS4 (Fig. 6.4). A comparatively light $\delta^{30}Si_{diat}$ value of +1.35‰ at ~31 ka BP is accompanied by a biogenic opal concentration of 26%, while biogenic opal concentrations are generally below 15% during late MIS3. After HS4 the subsurface $\delta^{18}O_{Nps}$ values slightly decrease by about 0.3‰ before they continuously increase by about 0.5‰ between ~37 and ~25 ka BP.

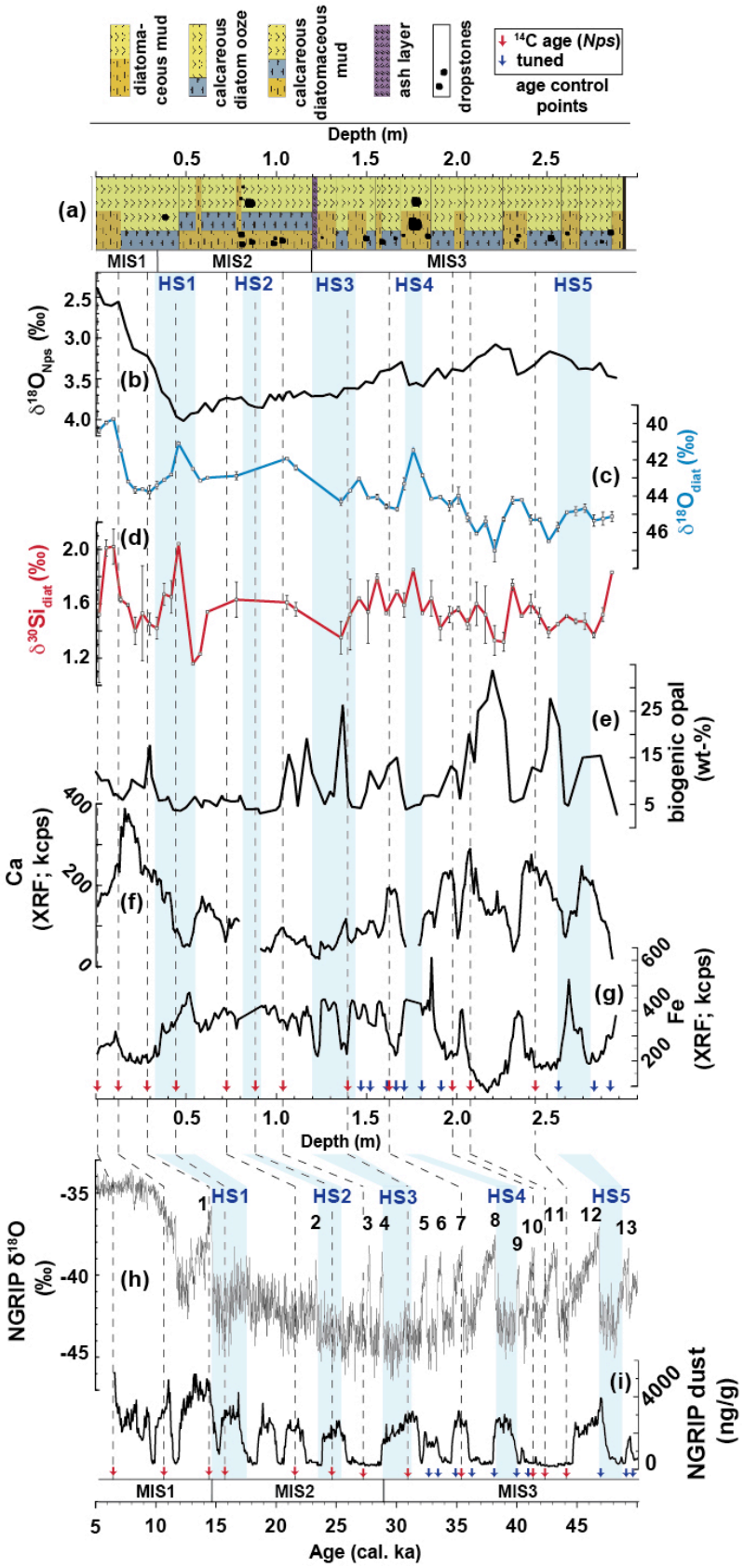

Figure 6.3. (a) Sediment core description scheme of SO202-27-6 (Gersonde, 2010); **(b)-(f)** Proxy data of Core SO202-27-6 versus depth (0-88.5 cm: Maier et al., 2013; below 88.5 cm: this study): **(b)** subsurface $\delta^{18}O_{Nps}$; **(c)** $\delta^{18}O_{diat}$; **(d)** $\delta^{30}Si_{diat}$; (e) biogenic opal concentration; **(f)** Ca intensity; **(g)** Fe intensity. Arrows mark the depths of age control points (0-88.5 cm: Maier et al., 2013; below 88.5 cm: this study). **(h)** NGRIP $\delta^{18}O$ record (Andersen et al., 2006; Svensson et al., 2006, 2008); **(i)** NGRIP dust record (Ruth et al., 2007), including SO202-27-6 age control points.

6.5 Discussion

6.5.1 Millennial-scale climate variabilities

The millennial-scale variabilities observed in various SO202-27-6 proxies from ca. 50-40 ka BP, including $\delta^{18}O_{diat}$, $\delta^{30}Si_{diat}$, $\delta^{18}O_{Nps}$ and biogenic opal concentration, are coeval to D-O cycles 13 to 10 in the NGRIP $\delta^{18}O$ record (Fig. 6.4). D-O interstadials are characterized by enriched $\delta^{18}O_{diat}$ (Fig. 6.4f). Since alkenone-based SST from the studied core show no clear millennial-scale cyclicities and SST generally varies only about 2 °C from ca. 60-40 ka BP (Fig. 6.4e; Méheust, 2014), the millennial-scale amplitudes of >2‰ in the $\delta^{18}O_{diat}$ record cannot have been largely modulated by variations in SST (assuming a relationship between diatom $\delta^{18}O$ and temperature of ca. -0.2‰/°C (Crespin et al., 2010; Dodd and Sharp, 2010)). The $\delta^{18}O_{diat}$ rather seems to reflect changes in surface water $\delta^{18}O$, which provide first-order information on changes in surface water salinity (SSS), thus indicating that SSS was considerably higher during D-O interstadials compared to stadials. Furthermore, during D-O interstadials 13 to 10 the $\delta^{30}Si_{diat}$ values are generally decreased relative to the stadials, while biogenic opal concentrations are elevated (Fig. 6.4c, d), pointing to an increased input of silicic acid into subarctic NE Pacific surface waters, which is not compensated by an increased export production. An excess availability of nutrients during interstadials is supported by the decreased bulk $\delta^{15}N$ values (Fig. 6.4b; Studer et al., 2013). We therefore suggest enhanced convective mixing during interstadial periods, resulting in increased upwelling of saline and nutrient-rich deeper waters into the euphotic zone compared to the stadials, which are generally characterized by enhanced IRD input (Fig. 6.4j), indicating stronger surface water stratification due to freshwater input related to iceberg discharge from the CIS.

In contrast to the $\delta^{18}O_{diat}$, the subsurface $\delta^{18}O_{Nps}$ record shows comparatively depleted values during interstadials and enriched values during stadials (Fig. 6.4g). Thus, the increased stadial freshwater input appears to have been confined to the subarctic surface waters. The subsurface $\delta^{18}O_{Nps}$ seems to primarily reflect changes in subsurface water temperature, with slightly increased temperatures (ca. 1°C, following the relationship of ca. 0.28°C/‰ between temperature and $\delta^{18}O_{Nps}$ (Mulitza et al., 2003) during interstadials compared to stadials. This observed pattern of the subsurface $\delta^{18}O_{Nps}$ record is consistent with the patterns of temperature variations recorded in NGRIP $\delta^{18}O$ record (Fig. 6.4k; Svensson et al., 2006, 2008) as well as of planktic foraminiferal water temperatures (Hendy and Kennett, 2000) and alkenone-based SST (Seki et al., 2002) from the California continental margin. The $\delta^{18}O_{Nps}$ record even mirrors gradual cooling of millennial-scale cold intervals, which is concordant with the cooling of subsequent D-O stadials observed over the Bond cycle in the NGRIP $\delta^{18}O$ NGRIP $\delta^{18}O$ record culminating in HS4.

Our data suggest an overall in-phase behavior between the North Atlantic and North Pacific climate variabilities during the observed period of millennial-scale variabilities from ca. 50-40 ka BP, further supported by the internal pattern of the millennial-scale variabilities in the studied core. A rapid increase in biogenic opal and decrease in $\delta^{30}Si_{diat}$ and $\delta^{18}O_{Nps}$ contemporaneous to rapid onset of D-O interstadials is followed by a gradual decline in biogenic opal and increase in $\delta^{30}Si_{diat}$ and $\delta^{18}O_{Nps}$, particularly pronounced during D-O event 11. Our results correspond to previous studies arguing for a predominantly atmospheric coupling of Northern Hemisphere (sub)surface water development during MIS3 (Mix et al., 1999; Riethdorf et al., 2013b), even though we are aware that absolute phasing between North Atlantic and North Pacific climate variations during MIS3 is difficult to determine. Our data indicate a close coupling between changes in upwelling intensity and in the strength of the AMOC, with periods of increased upwelling intensity in the subarctic NE Pacific coinciding with periods of intensified AMOC. The hypothesis is consistent with recent studies from the last deglaciation, which likewise suggest a close temporal link between upwelling intensity, nutrient supply and export production in the subarctic Pacific and the strength of the AMOC (Galbraith et al., 2007; Maier et al., a, in prep.). However, while a change to sea-ice free conditions during late HS1 seemed to have played a significant role in inducing vertical mixing in the subarctic NE Pacific in the first place (Maier et al., a, in prep.), the studied site can be regarded largely sea-ice free over the time of observed millennial-scale variabilities from ca. 50-40 ka (Méheust, 2014), indicating that changes in sea-ice cover did not largely influence changes in upwelling during that time.

6.5.2 Freshwater input from the CIS during HS4

At ~39 ka BP, coeval to HS4, a massive drop in $\delta^{18}O_{diat}$ and large increase in $\delta^{30}Si_{diat}$, combined with (slightly) reduced SST (Méheust, 2014), low biogenic opal concentration and an accumulation of (pebble-to-cobble sized) dropstones (Fig. 6.3; 6.4), indicate a strong surface water stratification due to a massive freshwater input from melting icebergs, which resulted in highly increased silicic acid utilization despite low export production. There is a close temporal correlation between this event of iceberg rafting from the CIS in the subarctic NE Pacific and HS4 in Greenland and the North Atlantic (Figs. 6.3; 6.4). The observed correlation supports earlier studies indicating that the CIS and the LIS both respond to a similar climate forcing (Hendy and Cosma, 2008; Maier et al., a, in prep.). As observed for the D-O stadials, the $\delta^{18}O_{Nps}$ does not decrease during HS4 (Fig. 6.4g), suggesting that even the massive freshwater input into the NE Pacific during HS4 did not influence subsurface

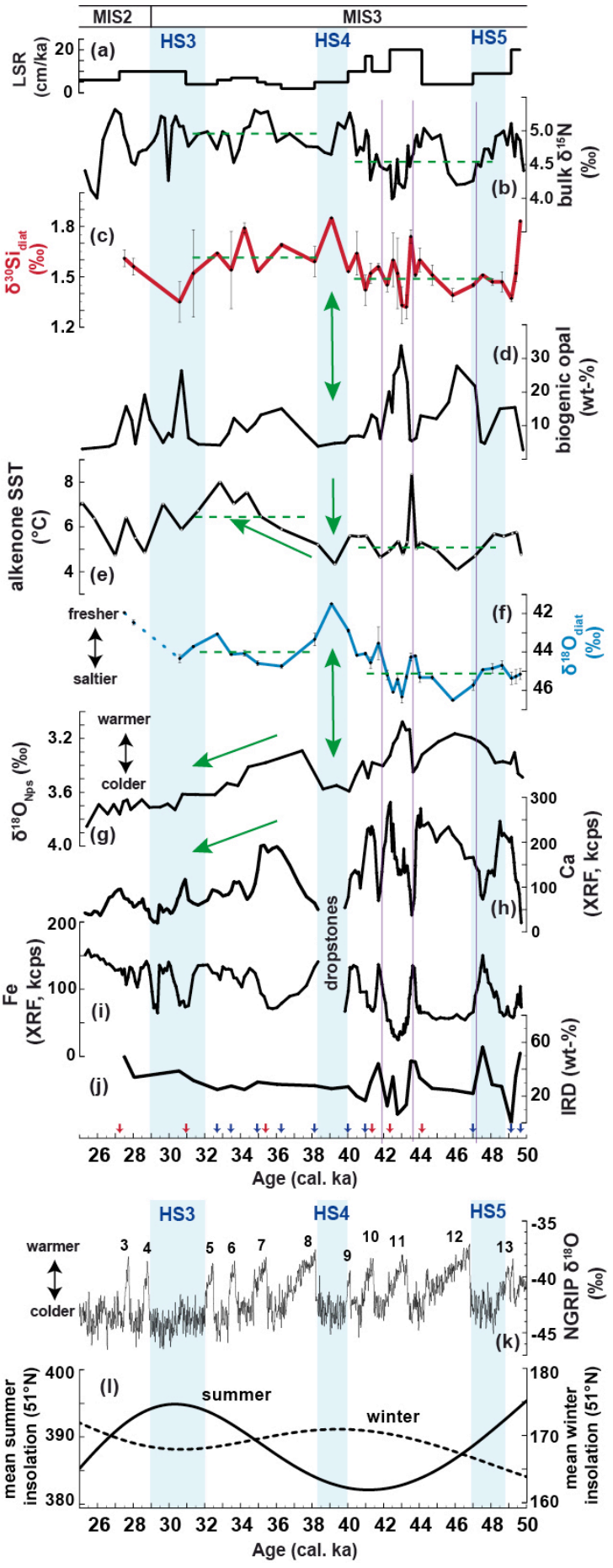
MIS2
MIS3
HS3
HS4
HS5
LSR (cm/ka)
(a)
bulk δ15N (‰)
(b)
δ30Sidiat (‰)
(c)
biogenic opal (wt-%)
(d)
alkenone SST (°C)
(e)
fresher
saltier
δ18Odiat (‰)
(f)
warmer
colder
δ18ONps (‰)
(g)
Ca (XRF, kcps)
(h)
dropstones
Fe (XRF, kcps)
(i)
IRD (wt-%)
(j)
Age (cal. ka)
NGRIP δ18O (‰)
(k)
(l)
summer
winter
mean summer insolation (51°N)
mean winter insolation (51°N)

Figure 6.4

Figure 6.4. (a)-(j) SO202-27-6 proxy data. **(a)** linear sedimentation rate; **(b)** bulk $\delta^{15}N$ data (Studer et al., 2013); **(c)** $\delta^{30}Si_{diat}$ data; **(d)** biogenic opal; **(e)** alkenone-based SST (Méheust et al., 2014); **(f)** $\delta^{18}O_{diat}$ data; **(g)** $\delta^{18}O_{Npa}$ **(h)** Ca intensity; **(i)** Fe intensity; **(j)** Estimation of IRD, dropstones excluded. Arrows mark the depths of age control points (red: planktic ^{14}C age; blue: tuned age); **(k)** NGRIP $\delta^{18}O$ (Andersen et al., 2006; Svensson et al., 2006, 2008) including the numeration of D-O cycles; **(l)** mean summer and winter insolation at 51°N (Laskar et al., 2004). Light blue intervals mark Heinrich stadials and purple vertical lines roughly correspond to onsets of D-O interstadials 12 to 10.

waters. In contrast, as stated above, the $\delta^{18}O_{Nps}$ shows its most enriched values during HS4 relative to the previous stadials, indicating particularly cold subsurface waters during that time, which is in concert with decreasing stadial temperatures within the Bond cycle in the NGRIP ice core culminating in HS4 (Fig. 6.4g, k). A similar situation of a large shift toward low $\delta^{18}O_{diat}$ with no effect on $\delta^{18}O_{Nps}$ has also been observed for the time coeval to the HS1 IRD event (Maier et al., a, in prep.).

The $\delta^{18}O_{diat}$ and $\delta^{30}Si_{diat}$ very well document strong surface water stratification during HS1 (Maier et al., a, in prep.) and HS4 (this study), but do not show equivalent comparable isotopic changes during HS5, HS3 and HS2 (Figs. 6.3; 6.4). During HS5 the diatom isotopic records show a slight shift towards lighter $\delta^{18}O_{diat}$ and heavier $\delta^{30}Si_{diat}$, but the amplitudes of the shifts are comparatively low, and there is no distinct accumulation of dropstones, pointing towards a comparatively small, albeit present, input of freshwater, more likely representing a "normal" D-O stadial. During the times of HS3 and HS2, the isotopic records do not show any indication of surface water stratification. One reason could be that our diatom isotope records do not cover the time frames of the IRD events within Heinrich stadials. This is the most likely explanation for the time of HS2, when the sediment contains a high amount of dropstones (Fig. 6.3a), but the biogenic opal concentration is below 5% (Maier et al., a, in prep.), preventing the preparation of purified diatom samples for diatom isotope analysis for that time interval. While this might also be a plausible explanation for the HS3 period, another possibility could be that, since the IRD event in the North Atlantic during HS3 is rather minor (Hemming, 2004), there might be no equivalent event in the North Pacific. This is supported by the lack of dropstones during that time (Fig. 6.3a). Furthermore, HS3 may not at all include a major ice-rafting event, but the elevated IRD during HS3 observed in the North Atlantic may be primarily caused by low amount of foraminifera rather than a large increase in coarse lithics (Gwiazda et al., 1996).

6.5.3 Halocline strengthening in the subarctic Pacific after HS4 as possible amplifier for ice-sheet growth

Following the massive episodic freshwater input during HS4 recorded by low $\delta^{18}O_{diat}$ and enriched $\delta^{30}Si_{diat}$, the $\delta^{18}O_{diat}$ record increases and $\delta^{30}Si_{diat}$ record slightly decreases (Fig. 6.4c,

f). However, the $\delta^{18}O_{diat}$ record levels off at generally lower, and the $\delta^{30}Si_{diat}$ record at generally higher, values compared to the time period prior HS4, indicating comparatively fresher and better-utilized surface waters during late MIS3. An increased utilization is supported by increased bulk $\delta^{15}N$ (Fig. 6.4b; Studer et al., 2013). In combination with comparatively low export production (Fig. 6.4d) the isotopic records point towards increased freshwater-induced surface water stratification following HS4. The rather low abundances of IRD and dropstones (Figs. 6.3a; 6.4j) as well as the cold Northern Hemisphere climate during the late MIS3 indicate that the freshwater did not originate from the CIS. Instead, the increased freshwater supply might be associated with an increased precipitation, indicated by an intensified late MIS3 East Asian Summer Monsoon (An, 2000).

Contemporaneous to the increased surface water stratification after HS4, alkenone-based SST increase by about 1.5 °C (Méheust, 2014), while the $\delta^{18}O_{Nps}$ record indicates a gradual cooling of subsurface waters (Fig. 6.4e, g). Since alkenones, produced by coccolithophores in the euphotic zone, are supposed to reflect late summer temperatures in the NE Pacific (Méheust et al., 2013), while *N. pachyderma* lives close or at the bottom of the thermocline (Bauch et al., 2002), where winter mixing mainly influences water temperatures, we suggest that these diverging temperature trends might be related to enhanced seasonality in SST. Similar to the modern situation, a strong low salinity surface water body might have not only largely limited the vertical exchange with deeper water masses but might have also allowed increased temperature contrasts within the shallow seasonal thermocline. This hypothesis is corroborated by close correlation between the alkenone-based SST and summer insolation, while the $\delta^{18}O_{Nps}$ record follows the winter insolation and the general Northern Hemisphere cooling (Fig. 6.4e, k, l).

A similar link between strong surface water stratification and increased seasonal SST contrasts in the subarctic Pacific has previously been described by Haug et al. (2005) at the onset of Northern Hemisphere glaciation, suggesting that despite a general Northern Hemisphere cooling an increased SST seasonality in the subarctic Pacific, related to the development of the halocline, could have allowed for an increased moisture flux onto the North American continent during autumn, when the continent was cold enough for the moisture to precipitate and accumulate as snow. We suggest that a similar mechanism, albeit on a much smaller scale, might have occurred during MIS3. A strengthening of surface water stratification following HS4 might have led to an increased autumn evaporation from subarctic Pacific surface waters and an increased snow accumulation on the North American continent, accelerating Northern Hemisphere ice-sheet growth. Our results indicate that the subarctic Pacific is not only a moisture source for Northern Hemisphere ice-sheets, but we suggest an important control of changes in subarctic Pacific surface water stratification on Northern Hemispheric moisture flux and ice-sheet growth.

6.5 Conclusions

New $\delta^{18}O_{diat}$ and $\delta^{30}Si_{diat}$ data from the open subarctic NE Pacific (SO202-27-6), as well as other new proxy data ($\delta^{18}O_{Nps}$, biogenic opal, Ca and Fe intensities) from Core SO202-27-6, show millennial-scale variabilities from ca. 50-40 ka BP, which can be related to D-O cycles in the NGRIP ice core. The combined interpretation of the proxy data provides a consistent picture regarding millennial-scale changes in silicic acid utilization, paleoproductivity and surface water hydrography. While subsurface $\delta^{18}O_{Nps}$ mirror the Northern Hemisphere millennial-scale temperature variability during MIS3, the $\delta^{18}O_{diat}$ seems to be mainly modulated by millennial-scale changes in SSS, probably related to changes in iceberg discharge from the CIS. Our data provide evidence of changes in surface water stratification associated with interstadial-to-stadial variations in upwelling intensity and freshwater input into the NE Pacific, with interstadials being characterized by increased upwelling of saline and nutrient-rich deeper waters, resulting in low silicic acid utilization despite high export production. These changes coincide with changes in the intensity of the AMOC, indicating rapid teleconnections between the North Atlantic and the North Pacific.

During HS4 our data indicate a massive freshwater input related to iceberg discharge into the NE Pacific, resulting in strong surface water stratification and high silicic acid utilization despite low export production. The temporal correlation to the HS4 IRD event in the North Atlantic indicates a close link between the LIS and CIS development.

Our $\delta^{18}O_{diat}$ and $\delta^{30}Si_{diat}$ data show that following HS4 surface waters are generally fresher and better utilized, possibly indicating a strengthening of surface water stratification. This hypothesis is supported by $\delta^{18}O_{Nps}$ and alkenone-based SST, pointing towards increasing seasonal contrasts in SST in response to less exchange with deeper waters. The increased seasonality in SST might have resulted in an increased moisture transport on the North American continent during autumn, where increased snow accumulation might have accelerated ice-sheet growth.

Acknowledgments

This study was part of the Innovative NOrth Pacific Experiment (INOPEX), funded by the Bundesministerium für Bildung und Forschung (BMBF). We thank Ulrike Böttjer, Birgit Glückselig and Ruth Cordelair for the thorough purification of the diatom samples for isotope analyses. Marianne Warnkross is thanked for picking planktic foraminifera for stable isotope analysis and radiocarbon dating. We gratefully acknowledge Silke Steph for performing the foraminiferal oxygen isotope analysis and Gerhard Kuhn for calculating salt-corrected biogenic opal concentrations.

Supporting information to:

"Millennial-scale variabilities in upwelling and halocline strength in the NE Pacific during Marine Isotope Stage 3"

Table S6.1. Contamination of purified diatom samples with non-biogenic silicates estimated from SiO_2 and Al_2O_3 percentages determined by **(A)** by ICP-OES and **(B)** EDS.

(A)

		ICP-OES		
Depth (cm)	Age (ka BP)	SiO_2 assumed (%)	Al_2O_3 (%)	non-biogenic silicate contamination (%)
160-162	34.959	99.30	0.09	0.90
205-207	42.210	99.16	0.15	1.16
220-222	43.031	99.34	0.04	0.75
250-252	45.871	99.30	0.08	0.87

(B)

		EDS		
Depth (cm)	Age (ka BP)	SiO_2 (%)	Al_2O_3 (%)	non-biogenic silicate contamination (%)
105-107	27.501	96.27	1.77	7.62
110-112	28.017	97.32	1.20	5.32
135-137	30.597	98.43	0.39	2.43
140-142	31.360	98.48	0.50	2.62
145-147	32.700	98.06	0.63	3.33
150-152	33.482	98.68	0.40	2.20
155-157	34.220	98.42	0.58	2.86
160-162	34.959	98.99	0.17	1.38
166-168	36.295	98.73	0.32	1.97
170-172	38.146	98.28	0.71	3.28
175-177	39.088	98.08	0.89	3.88
180-182	40.029	98.46	0.48	2.60
185-187	40.507	98.79	0.36	2.00
190-192	40.957	98.73	0.37	2.08
195-197	41.277	98.82	0.25	1.73
200-202	41.713	98.54	0.37	2.27
205-207	42.210	98.69	0.27	1.90
210-212	42.533	98.90	0.17	1.47
215-217	42.782	98.91	0.13	1.38
220-220	43.031	98.78	0.17	1.59
225-227	43.280	98.81	0.19	1.61
230-232	43.529	98.88	0.30	1.78
235-237	43.778	98.88	0.29	1.76
240-242	44.027	98.65	0.38	2.19
245-247	44.724	98.76	0.30	1.90
250-252	45.871	98.81	0.22	1.67
255-257	47.017	98.69	0.30	1.97
260-262	47.551	98.82	0.32	1.88
265-267	48.084	98.62	0.43	2.33
270-272	48.618	98.24	0.51	2.88
275-277	49.152	98.61	0.37	2.20
280-282	49.402	98.70	0.32	2.00
285-287	49.652	98.86	0.30	1.80

Table S6.2. Composition of **(A)** pre-sonicated and **(B)** several final purified diatom samples. **(A)** Relative abundances of diatoms, radiolarians and sponge spicules are related to the total counts and relative abundances of *C. marginatus* and *C. oculus-iridis* are related to the diatom species assemblage, determined by light microscopy. **(B)** All relative abundances are related to the total counts.

(A)

		light microscopy (pre-sonication)					
Depth (cm)	Age (ka BP)	total counts	diatoms (%)	radiolarians (%)	sponge spicules (%)	*C. marginatus* (% of diatom abundance)	*C. oculus-iridis* (% of diatom abundance)
105-107	27.501	173	85.5	13.29	1.16	81.8	18.2
110-112	28.017	169	92.9	5.92	1.18	82.2	17.8
135-137	30.597	202	93.6	6.44	0.00	54.0	46.0
140-142	31.360	150	92.0	7.33	0.67	50.0	50.0
145-147	32.700	159	93.8	5.00	1.25	91.3	8.0
150-152	33.482	115	95.7	3.48	0.87	97.3	2.7
155-157	34.220	166	94.0	4.82	1.20	94.9	5.1
160-162	34.959	171	95.9	2.92	1.17	98.2	1.8
166-168	36.295	172	97.7	1.74	0.58	95.8	4.2
170-172	38.146	194	99.0	0.52	0.52	96.4	3.6
175-177	39.088	261	73.9	25.29	0.77	96.4	3.6
180-182	40.029	246	97.2	2.85	0.00	97.1	2.9
185-187	40.507	122	94.3	2.46	3.28	93.0	7.0
190-192	40.957	137	89.1	8.76	2.19	96.7	3.3
195-197	41.277	136	92.6	6.62	0.74	100.0	0.0
200-202	41.713	106	98.1	0.94	0.94	96.2	3.8
205-207	42.210	167	99.4	0.60	0.00	98.8	1.2
210-212	42.533	144	99.3	0.69	0.00	98.6	1.4
215-217	42.782	157	99.4	0.64	0.00	94.2	5.8
220-222	43.031	295	99.3	0.68	0.00	93.5	6.5
225-227	43.280	136	97.8	2.21	0.00	82.7	17.3
230-232	43.529	140	97.9	1.43	0.71	94.2	5.8
235-237	43.778	173	89.6	9.83	0.58	98.7	1.3
240-242	44.027	145	95.9	4.14	0.00	98.6	1.4
245-247	44.724	177	95.5	4.52	0.00	97.6	2.4
250-252	45.871	149	98.0	1.34	0.67	99.3	0.7
255-257	47.017	164	99.4	0.61	0.00	95.7	4.3
260-262	47.551	160	96.3	3.75	0.00	96.1	3.9
265-267	48.084	194	88.1	10.82	1.03	98.2	1.8
270-272	48.618	166	89.8	7.83	2.41	94.0	6.0
275-277	49.152	159	89.9	9.43	0.63	93.0	7.0
280-282	49.402	230	90.0	7.83	2.17	88.9	9.2
285-287	49.652	175	92.0	4.57	3.43	92.5	6.8
Avg		170	94.0	5.1	0.9	92.0	7.9
SD (1σ)		40	5.3	5.0	0.9	11.3	11.3

(B)

		SEM (purified)					
Depth (cm)	Age (ka BP)	total counts	diatoms (%)	radiolarians (%)	sponge spicules (%)	non-biogenic silicate contamination (%)	not identified (%)
170-172	38.146	181	98.9	0.0	0	1.1	0.0
175-177	39.088	157	94.9	2.5	0	1.9	0.6
180-182	40.029	203	95.6	2.5	1.5	0.5	0.0
230-232	43.529	187	97.3	2.1	0	0.5	0.0
235-237	43.778	182	95.1	4.9	0	0.0	0.0
240-242	44.027	183	99.5	0.0	0	0.5	0.0
245-247	44.724	160	96.9	1.9	0.6	0.6	0.0
250-252	45.871	192	99.5	0.5	0	0.0	0.0
Avg		181	97.2	1.8	0.3	0.7	0.1
SD (1σ)		15	1.9	1.7	0.5	0.6	0.2

Table S6.3. Measured $\delta^{18}O_{diat}$ and $\delta^{30}Si_{diat}$ values of Core SO202-27-6 including standard deviations (SD) and number of isotopic measurements (n).

		Silicon			Oxygen		
Depth (cm)	Age (ka BP)	$\delta^{30}Si_{diat}$ (‰)	SD (1σ; ‰)	n	$\delta^{18}O_{diat}$ (‰)	SD (1σ; ‰)	n
105-107	27.501	1.61	0.05	2	41.95	0.04	2
110-112	28.017	1.56	0.05	3	42.46	0.13	3
135-137	30.597	1.35	0.12	2	44.34	0.21	2
140-142	31.360	1.52	0.26	3	43.72	0.05	2
145-147	32.700	1.64	-	1	43.06	-	1
150-152	33.482	1.54	0.23	3	44.12	0.04	2
155-157	34.220	1.79	0.03	2	44.07	0.15	3
160-162	34.959	1.53	0.00	2	44.59	0.13	2
166-168	36.295	1.69	0.01	2	44.74	0.10	3
170-172	38.146	1.59	0.09	2	43.34	0.33	2
175-177	39.088	1.85	-	1	41.49	-	1
180-182	40.029	1.53	-	1	42.88	0.08	2
185-187	40.507	1.64	0.13	3	44.17	0.01	2
190-192	40.957	1.42	0.09	2	44.08	0.09	3
195-197	41.277	1.52	0.06	3	44.56	0.29	3
200-202	41.713	1.56	0.02	2	43.54	0.85	3
205-207	42.210	1.45	0.04	2	45.20	0.24	2
210-212	42.533	1.60	0.16	2	46.09	0.00	2
215-217	42.782	1.52	0.21	2	45.42	0.28	2
220-222	43.031	1.33	0.11	4	46.34	0.32	3
225-227	43.280	1.32	0.07	2	45.29	0.12	2
230-232	43.529	1.74	0.04	2	44.26	0.21	2
235-237	43.778	1.51	0.01	2	44.20	0.05	2
240-242	44.027	1.60	0.07	2	45.32	0.26	2
245-247	44.724	1.51	0.06	2	45.32	0.10	2
250-252	45.871	1.39	0.04	3	46.51	0.02	2
255-257	47.017	1.45	0.01	2	45.72	0.26	2
260-262	47.551	1.51	-	1	44.92	0.03	2
265-267	48.084	1.47	0.02	2	44.85	0.25	2
270-272	48.618	1.47	0.06	2	44.69	0.23	2
275-277	49.152	1.37	0.02	2	45.37	0.32	2
280-282	49.402	1.52	0.05	3	45.27	0.36	4
285-287	49.652	1.83	-	1	45.15	0.28	2

Chapter 7 – Conclusions and outlook

7.1 Conclusions

It was the overall aim of this thesis to improve the current understanding of millennial-scale climate variability in the subarctic Pacific, including implications on oceanic-atmospheric CO_2 exchange, by reconstructing past changes in surface water stratification and silicic acid utilization. For this purpose, $\delta^{18}O_{diat}$ and $\delta^{30}Si_{diat}$ records from the NE and the NW Pacific were generated, using a new instrumentation set-up for the efficient combined (biogenic) silica $\delta^{18}O$ and $\delta^{30}Si$ analysis, i.e. where both proxies are measured from the same sample aliquot. This set-up requires a comparatively low silica sample weight of ~1.5-2.0 mg.

This thesis presents for the first time subarctic Pacific $\delta^{18}O_{diat}$ and $\delta^{30}Si_{diat}$ data at millennial-scale resolution. While the NE Pacific Core SO202-27-6 provides continuous $\delta^{18}O_{diat}$ and $\delta^{30}Si_{diat}$ records from the last glacial to the modern interglacial (~50-7 ka BP), the low biogenic opal content in the NW Pacific Core MD01-2416 during the last glacial and HS1 prevented a pre-Bølling extension of the isotopic record. Based on the obtained $\delta^{18}O_{diat}$ and $\delta^{30}Si_{diat}$ data, in combination with new data on subsurface water temperature/salinity, XRF data, biogenic opal data, as well as previously published nitrogen isotope data (Galbraith et al., 2008; Studer et al. 2013), diatom counting data (Ren et al., in prep.) and alkenone-based SST and sea-ice data (Méheust, 2014; Méheust et al., in prep.), this thesis improved the knowledge concerning the following questions (revisited from *Section 1.4*):

Question 1: ***How sensitive are the $\delta^{18}O_{diat}$ and $\delta^{30}Si_{diat}$ signals to isotopic effects related to (1) a potential sample contamination (e.g. clay minerals, radiolarians) and/or (2) the diatom species composition (species-related isotope effects like vital and environmental effects)?***

This thesis shows the necessity of analyzing high-purity diatom samples and strongly recommends a contamination assessment of purified diatom samples. No discernable species-related silicon isotope effects were detected, indicating that $\delta^{30}Si_{diat}$ is not highly sensitive to variations in diatom species compositions. Concerning $\delta^{18}O_{diat}$, species-related oxygen isotope effects, most likely vital effects, may bias the oxygen isotopic records, arguing for the need to separate diatom samples according to species or species groups, assigned to the same environmental boundary conditions, to obtain reliable isotopic results.

Question 2: ***What is the meltwater history of the Cordilleran Ice Sheet (CIS) during the last 50 ka and how is it related to the meltwater history of the Laurentide Ice Sheet (LIS)?***

Proxy data show that millennial-scale variabilities in upper ocean stratification during MIS3, related to changes in iceberg discharge, correlate well with D-O events. Furthermore, massive

iceberg-related freshwater fluxes into the open NE Pacific are observed, which are coeval to HS1 and HS4 IRD events in the North Atlantic. Thus, iceberg discharge from the CIS seems to be closely related to iceberg discharge from the LIS, indicating that both ice sheets respond to a similar forcing.

Question 3: ***Do the $\delta^{18}O_{diat}$ and $\delta^{30}Si_{diat}$ signals support the hypothesis of deep-water formation in the subarctic Pacific during HS1?***

In response to the shutdown of the AMOC during HS1, studies with general circulation models indicate enhanced sea surface salinity in the subarctic NE Pacific, related to an increased poleward transport of salty surface waters into the subarctic Pacific, as an important precondition for deep-water formation in the subarctic Pacific realm (Okazaki et al., 2010; Chikamoto et al., 2012). However, the NE Pacific $\delta^{18}O_{diat}$ record indicates fresh surface waters during that time, arguing against an increased advection of salty subtropical surface waters. The $\delta^{30}Si_{diat}$ record suggests increased availability of silicic acid during the early HS1, which might be associated with deep convection, but can be equally well explained by an increased formation rate of NPIW.

Question 4: ***What is the timing of paleoceanographic changes of surface water properties (e.g. salinity, silicic acid utilization) in the subarctic Pacific relative to climate changes in the North Atlantic realm during the last deglaciation and what are possible trigger mechanisms?***

Deglacial proxy data show a sequence of paleoceanographic events occurring in surface waters, which do not mirror the deglacial pattern of HS1 cooling or B/A warming as recorded in Greenland ice cores (NGRIP members, 2004). Following cool and stratified glacial and early deglacial surface waters, a massive meltwater input at ~16 ka BP occurs, coeval with the HS1 IRD event in the North Atlantic (e.g. Bard et al., 2000). This indicates a close link to the North Atlantic region and a predominantly atmospheric control on surface water development. After ~16 ka BP, prior to the onset of the Bølling, the upper ocean then destratified and upwelling of saline, silicic acid-rich deeper waters increased. This is contemporaneous with a change to sea-ice free conditions, indicating that sea-ice, related to insolation changes, played a dominant role on this pre-Bølling paleoceanographic change. The observed maximum in productivity during the Bølling, when upwelling intensity is high, correlates with the reinvigoration of the AMOC, suggesting that the intensified AMOC facilitated upwelling and productivity during the B/A.

Question 5: ***What was the subarctic Pacific´s role during the last deglacial rise in pCO_2?***

Proxy data indicate that destratification and related increased upwelling started in late HS1 (at ~16 ka BP), coeval with an increase in paleoproductivity. Silicic acid supply largely exceeds its net use, as indicated by decoupled $\delta^{30}Si_{diat}$ and paleoproductivity records in late HS1 and throughout the B/A. This relationship might point to a decreased efficiency of the biological pump, suggesting that the subarctic Pacific has been a source region of CO_2 to the atmosphere during late HS1 and the B/A. The subarctic Pacific thus might have contributed to the deglacial rise in pCO_2 of ~20 ppm, observed in Antarctic ice cores over that time interval (Schmitt et al., 2012; Parrenin et al., 2013).

Question 6: ***What happens in the subarctic Pacific in response to changes in the Atlantic Meridional Overturning Circulation during MIS3?***

Results indicate millennial-scale variabilities in upper ocean stratification, silicic acid utilization and paleoproductivity, which are associated with changes in upwelling intensity. These millennial-scale cycles can be assigned to D-O cycles 12 to 10 and positively correlate with changes in AMOC intensity, indicating rapid teleconnections between the North Atlantic and the North Pacific.

Question 7: ***How did the strength in the halocline vary over MIS3 and what are the implications for North American ice-sheet growth?***

Upper ocean stratification varied at millennial time scales prior to HS4. Following HS4, proxy data indicate a strengthening of the upper ocean stratification, characterized by lighter $\delta^{18}O_{diat}$ values and heavier $\delta^{30}Si_{diat}$. Increased stratification is further supported by evidence of increasing seasonal contrasts after HS4. It can be speculated that, in response to the increased SST seasonality, moisture transport on the North American continent might have increased during autumn, possibly accelerating ice-sheet growth.

7.2 Outlook

As the data presented in this thesis are the first $\delta^{18}O_{diat}$ and $\delta^{30}Si_{diat}$ data in the subarctic Pacific with a resolution high enough to detect millennial-scale variabilities, clearly further studies are needed to evaluate the presented conclusions. Nevertheless, the results are a good basis for future research and a high number of sediment cores across the subarctic Pacific and its marginal seas, e.g. recovered during the SO202-INOPEX or the SO201-KALMAR cruise, provide excellent premises for future down-core studies. Such studies might combine diatom isotope with clay mineral studies to reconstruct the source, pathway and extension of the detected freshwater input in the NE Pacific during HS1 and HS4. Furthermore, considering the importance of sea-ice on surface water stratification, a combined interpretation of changes in sea-ice, $\delta^{18}O_{diat}$ and $\delta^{30}Si_{diat}$ would allow distinguishing between stratification by freshwater or sea-ice. Moreover, while $\delta^{18}O_{diat}$ and $\delta^{30}Si_{diat}$ provide valuable information on surface water hydrography and silicic acid utilization, future isotope studies on surface and deeper living radiolarians as well as sponge spicules from benthic siliceous sponges might provide an opportunity to track past changes in water mass structures and nutrient dynamics. Recent calibration studies on sponge spicules (e.g. Hendry and Robinson, 2012) show that sponge $\delta^{30}Si$ indeed can be used as a proxy to track past changes in silicic acid concentration and the recent study of Abelmann et al. (in prep.) shows the potential of a combined diatom/radiolarian $\delta^{18}O$ and $\delta^{30}Si$ study for reconstructing hydrographic structures.

Based on the results of Reynolds et al. (2006), who presented a first look into the $\delta^{30}Si$ of silicic acid throughout the NW Pacific water column, a clearly necessary and logic next step would be to conduct a calibration study for $\delta^{30}Si_{diat}$ in the North Pacific and to evaluate the relationship between the $\delta^{30}Si$ of surface water silicic acid and of diatoms captured by plankton nets, but also of diatoms from sediment traps. Such a calibration would improve the proxy and allow for a more quantitative evaluation of the $\delta^{30}Si_{diat}$. Results may be compared to studies from the Southern Ocean, another HNLC region, where the core top calibration study of Egan et al. (2012) recently demonstrated the applicability of $\delta^{30}Si_{diat}$ as a qualitative proxy for silicic acid utilization.

Additionally, future work should try to further improve analytical requirements, including a further reduction of the required sample weight for (combined) isotope analyses and a further improvement of the diatom purification process. Development of a technique to separate single diatom species would allow for the investigation of seasonal effects. Recently, Swann et al. (2013) demonstrated the potential of season-specific $\delta^{18}O_{diat}$ records, showing seasonal variations in glacial discharge from the Antarctic Peninsula over the last deglaciation.

Data handling

All data presented in this study will be stored electronically and will be available online in the PANGAEA database (http://www.pangaea.de).

References

Abelmann A, Gersonde R, Cortese G, Kuhn G, Smetacek V. 2006. Extensive phytoplankton blooms in the Atlantic sector of the glacial Southern Ocean. *Paleoceanography* **21**: PA1013.

Abelmann A, Maier E, Chapligin B, Zhang X, Esper O, Gersonde R, Knorr G, Lohmann G, Friedrichsen H, Meyer H, Tiedemann R, Shemesh A. In preparation for Nature Geoscience. Sea ice induced Glacial/deglacial changes in surface and subsurface silicic acid utilization in the Southern Ocean.

Alexander MA, Bladé I, Newman M, Lanzante JR, Lau N-C, Scott JD. 2002. The Atmospheric Bridge: The Influence of ENSO Teleconnections on Air-Sea Interaction over the Global Oceans. *Journal of Climate* **15**: 2205-2231.

Allen JS, Beardsley, RC, Blanton JO, Boicourt WC, Butman B, Coachman LK, Huyer A, Kinder TH, Royer TC, Schumacher JD, Smith RL, Sturges W, Winant, CD. 1983. Physical oceanography of continental shelves. *Reviews of Geophysics and Space Physics* **21**: 1149-1181.

Alley RB, Anandakrishnan S, Dupont TK, Parizek BR, Pollard D. 2007. Effect of Sedimentation on Ice-Sheet Grounding-Line Stability. *Science* **315**: 1838-1841.

An Z. 2000. The history and variability of the East Asian paleomonsoon climate. *Quaternary Science Reviews* **19**: 171-187.

Anandakrishnan S, Catania GA, Alley RB, Horgan HJ. 2007. Discovery of Till Deposition at the Grounding Line of Whillans Ice Stream. *Science* **315**: 1835-1838.

Andersen KK, Svensson A, Johnsen SJ, Rasmussen SO, Bigler M, Röthlisberger R, Ruth U, Siggaard-Andersen M-L, Steffensen JP, Dahl-Jensen D, Vinther BM, Clausen HB. 2006. The Greenland Ice Core Chronology 2005, 15-42 ka. Part 1: Constructing the time scale. *Quaternary Science Reviews* **25**: 3246-3257.

Andreev A, Kusakabe M, Honda M, Murata A, Saito C. 2002. Vertical fluxes of nutrients and carbon through the halocline in the western subarctic Gyre calculated by mass balance. *Deep-Sea Research II **49***: 5577-5593.

Antonov JI, Seidov D, Boyer TP, Locarnini RA, Mishonov AV, Garcia HE, Baranova OK, Zweng MM, Johnson DR. 2010. *World Ocean Atlas 2009, Volume 2: Salinity*, US Government Printing Office, Washington DC.

Ayers JM, Lozier MS. 2012. Unraveling dynamical controls on the North Pacific carbon sink. *Journal of Geophysical Research: Oceans* **117**: C01017.

Bailey I, Liu Q, Swann GEA, Jiang Z, Sun Y, Zhao X, Roberts AP. 2011. Iron fertilisation and biogeochemical cycles in the sub-Arctic northwest Pacific during the late Pliocene intensification of northern hemisphere glaciation. *Earth and Planetary Science Letters **307***: 253-265.

Bard E, Rostek F, Turon J-L, Gendreau S. 2000. Hydrological Impact of Heinrich Events in the Subtropical Northeast Atlantic. *Science* **289**: 1321-1324.

Barron JA, Bukry D, Dean WE, Addison JA, Finney B. 2009. Paleoceanography of the Gulf of Alaska during the past 15,000 years: Results from diatoms, silicoflagellates and geochemistry. *Marine Micropaleontology* **72**: 176-195.

Bassinot FC, Baltzer A, Chen MT, DeDeckker P, Khuhnt W, Levitan M, Nürnberg D, Oba T, Prentice M, Sarnthein M, Situmorang M, Tiedemann R, Holbourn A, Kiefer T, Pflaumann U, Rothe S. 2002. Scientific Report of the WEPAMA Cruise, MD122/IMAGES VII.

Bauch D, Erlenkeuser H, Winckler G, Pavlova G, Thiede J. 2002. Carbon isotopes and habitat of polar planktic foraminifera in the Okhotsk Sea: the "carbonate ion effect" under natural conditions. *Marine Micropaleontology* **45**: 83-99.

Benito G, O´Connor JE. 2003. Number and size of last-glacial Missoula floods in the Columbia River valley between the Pasco Basin, Washington, and Portland, Oregon, *Geological Society of America Bulletin* **115**: 624-638.

Bigg GR, Rohling EJ. 2000. An oxygen isotope data set for marine waters. *Journal of Geophysical Research: Oceans* **105**: 8527-8535.

Bond G, Broecker W, Johnsen S, McManus J, Labeyrie L, Jouzel J, Bonani G. 1993. Correlations between climate records from North Atlantic sediments and Greenland ice. *Nature* **365**: 143-147.

Boyd PW, Wong CS, Merrill J, Whitney F, Snow J, Harrison PJ, Gower J. 1998. Atmospheric iron supply and enhanced vertical carbon flux in the NE subarctic Pacific: Is there a connection?. *Global Biogeochemical Cycles* **12**: 429-441.

Boyd PW, Law CS, Wong CS, Nojiri Y, Tsuda A, Levasseur M, Takeda S, Rivkin R, Harrison PJ, Strzepek R, Gower J, McKay RM, Abraham E, Arychuk M, Barwell-Clarke J, Crawford W, Crawford D, Hale M, Harada K, Johnson K, Kiyosawa H, Kudo I, Marchetti A, Miller W, Needoba J, Nishioka J, Ogawa H, Page J, Robert M, Saito H, Sastri A, Sherry N, Soutar T, Sutherland N, Taira Y, Whitney F, Wong S-K E, Yoshimura T. 2004. The decline and fate of an iron-induced subarctic phytoplankton bloom. *Nature* **428**: 549-553.

Brandriss ME, O'Neil JR, Edlund MB, Stoermer EF. 1998. Oxygen isotope fractionation between diatomaceous silica and water. *Geochimica et Cosmochimica Acta* **62**: 1119-1125.

Brewer TS, Leng MJ, Mackay AW, Lamb AL, Tyler JJ, Marsh NG. 2008. Unravelling contamination signals in biogenic silica oxygen isotope composition: the role of major and trace element geochemistry. *Journal of Quaternary Science* **23**: 321-330.

Brzezinski MA. Jones JL, Beucher CP, Demarest MS. 2006. Automated Determination of Silicon Isotope Natural Abundance by the Acid Decomposition of Cesium Hexafluosilicate. *Analytical Chemistry* **78**: 6109-6114.

Brzezinski MA, Pride CJ, Franck VM, Sigman DM, Sarmiento JL, Matsumoto K, Gruber N, Rau GH, Coale KH. 2002. A switch from $Si(OH)_4$ to NO_3^- depletion in the glacial Southern Ocean. *Geophysical Research Letters* **29**: 1564.

Brigham-Grette J. 2001. New perspectives on Beringian Quaternary paleogeography, stratigraphy, and glacial history. *Quaternary Science Reviews* **20**: 15-24.

Broecker WS, Peng T-H, Jouzel J, Russell G. 1990. The magnitude of global fresh-water transports of importance to ocean circulation. *Climate Dynamics* **4**: 73-79.

Bronk Ramsey C, Staff RA, Bryant CL, Brock F, Kitagawa H, Van der Pflicht J, Schlolaut G, Marshall MH, Brauer A, Lamb HF, Payne RL, Tarasov PE, Haraguchi T, Gotanda K, Yonenobu H, Yokoyama Y, Tada R, Nakagawa T. 2012. A Complete Terrestrial Radiocarbon Record for 11.2 to 52.8 kyr B.P. *Science* **338**: 370-374.

Brown MT, Landing WM, Measures CI. 2005. Dissolved and particulate Fe in the western and central North Pacific: Results from the 2002 IOC cruise. *Geochemistry Geophysics Geosystems* **6**: Q10001.

Brunelle BG, Sigman DM, Cook MS, Keigwin LD, Haug GH, Plessen B, Schettler G, Jaccard SL. 2007. Evidence from diatom-bound nitrogen isotopes for subarctic Pacific stratification during the last ice age and a link to North Pacific denitrification changes. *Paleoceanography* **22**: PA1215.

Brunelle BG, Sigman DM, Jaccard SL, Keigwin LD, Plessen B, Schettler G, Cook MS, Haug GH. 2010. Glacial/interglacial changes in nutrient supply and stratification in the western subarctic North Pacific since the penultimate glacial maximum. *Quaternary Science Reviews* **29**: 2579-2590.

Brzezinski MA. 1985. The Si:C:N ratio of marine diatoms: Interspecific variability and the effect of some environmental variables. *Journal of Phycology* **21**: 347-357.

Brzezinski MA, Pride CJ, Franck VM, Sigman DM, Sarmiento JL, Matsumoto K, Gruber N, Rau GH, Coale KH. 2002. A switch from $Si(OH)_4$ to NO_3^- depletion in the glacial Southern Ocean. *Geophysical Research Letters* 29: 1564.

Burke A, Robinson LF. 2012. The Southern Ocean's Role in Carbon Exchange During the Last Deglaciation. *Science* **335**: 557-561.

Carlson AE, Clark PU. 2012. Ice sheet sources of sea level rise and freshwater discharge during the last deglaciation. *Reviews of Geophysics* **50**: RG4007.

Cartapanis O, Tachikawa K, Bard E. 2011. Northeastern Pacific oxygen minimum zone variability over the past 70 kyr: Impact of biological production and oceanic ventilation. *Paleoceanography* **26**: PA4208.

Chapligin B, Meyer H, Friedrichsen H, Marent A, Sohns E, Hubberten H-W. 2010. A high-performance, safer and semi-automated approach for the $\delta^{18}O$ analysis of diatom silica and new methods for removing exchangeable oxygen. *Rapid Communications in Mass Spectrometry* **24**: 2655-2664.

Chapligin B, Leng MJ, Webb E, Alexandre A, Dodd JP, Ijiri A, Lücke A, Shemesh A, Abelmann A, Herzschuh U, Longstaffe FJ, Meyer H, Moschen R, Okazaki Y, Rees NH, Sharp ZD, Sloane HJ, Sonzogni C, Swann GEA, Sylvestre F, Tyler JJ, Yam R. 2011. Inter-laboratory comparison of oxygen isotope compositions from biogenic silica. *Geochimica et Cosmochimica Acta* **75**: 7242-7256.

Chapligin B, Meyer H, Bryan A, Snyder J, Kemnitz H. 2012. Assessment of purification and contamination correction methods for analysing the oxygen isotope composition from biogenic silica. *Chemical Geology* **300-301**: 185-199.

Chikamoto MO, Menviel L, Abe-Ouchi A, Ohgaito R, Timmermann A, Okazaki Y, Harada N, Oka A, Mouchet A. 2012. Variability in North Pacific intermediate and deep water ventilation during Heinrich events in two coupled climate models. *Deep-Sea Research Part II* **61**: 114-126.

Clague JJ, James TS. 2002. History and isostatic effects of the last ice sheet in southern British Columbia. *Quaternary Science Reviews* **21**: 71-87.

Clark PU, Hostetler SW, Pisias NG, Schmittner A, Meissner KJ. 2007. Mechanisms for an ~7-kyr Climate and Sea-Level Oscillation During Marine Isotope Stage 3. *Geophysical Monograph Series* **173**: 209-246.

Crespin J, Sylvestre F, Alexandre A, Sonzogni C, Paillès C, Perga M-E. 2010. Re-examination of the temperature-dependent relationship between $\delta\,^{18}O_{diatoms}$ and $\delta\,^{18}O_{lake\ water}$ and implications for paleoclimate inferences. *Journal of Paleolimnology* **44**: 547-557.

Crusius J, Schroth AW, Gassó S, Moy CM, Levy RC, Gatica M. 2011. Glacial flour dust storms in the Gulf of Alaska: Hydrologic and meteorological controls and their importance as a source of bioavailable iron. *Geophysical Research Letters* **38**: L06602.

Dansgaard W, Johnsen SJ, Clausen HB, Dahl-Jensen D, Gundestrup NS, Hammer CU, Hvidberg CS, Steffensen JP, Sveinbjörnsdottir AE, Jouzel J, Bond G. 1993. Evidence for general instability of past climate from a 250-kyr ice-core record. *Nature* **364**: 218-220.

Davies MH, Mix AC, Stoner JS, Addison JA, Jaeger J, Finney B, Wiest J. 2011. The deglacial transition on the Southeastern Alaska Margin: Meltwater input, sealevel rise, marine productivity, and sedimentary anoxia. *Paleoceanography* **26:** PA2223.

De la Rocha CL. 2006. Opal-based isotopic proxies of paleoenvironmental conditions. *Global Biogeochemical Cycles* **20**: GB4S09.

De la Rocha CL, Brzezinski MA, DeNiro MJ. 1997. Fractionation of silicon isotopes by marine diatoms during biogenic silica formation. *Geochimica et Cosmochimica Acta* **61**: 5051-5056.

De la Rocha CL, Brzezinski MA, DeNiro MJ, Shemesh A. 1998. Silicon-isotope composition of diatoms as an indicator of past oceanic change. *Nature* **395**: 680-683.

De la Rocha CL, Brzezinski MA, DeNiro MJ. 2000. A first look at the distribution of the stable isotopes of silicon in natural waters. *Geochimica et Cosmochimica Acta* **64**: 2467-2477.

De Vernal A, Pederson TF. 1997. Micropaleontology and palynology of core PAR87A-10: A 23,000 year record of paleoenvironmental changes in the Gulf of Alaska, northeast North Pacific. *Paleoceanography* **12**: 821-830.

Deschamps P, Durand N, Bard E, Hamelin B, Camoin G, Thomas AL, Henderson GM, Okuno JI, Yokoyama Y. 2012. Ice-sheet collapse and sea-level rise at the Bølling warming 14,600 years ago. *Nature* **483**: 559-564.

Ding T, Jiang S, Wan D, Li Y, Li J, Song H, Liu Z, Yao X. 1996. *Silicon Isotope Geochemistry*. Geological Publishing House, Beijing.

Dodd JP, Sharp ZD. 2010. A laser fluorination method for oxygen isotope analysis of biogenic silica and a new oxygen isotope calibration of modern diatoms in freshwater environments. *Geochimica et Cosmochimica Acta* **74**: 1381-1390.

Dodimead AJ, Favorite F, Hirano T. 1963. Salmon of the North Pacific Ocean, Part II. *Bulletin of the International North Pacific Fisheries Commission* **13**: 1-195.

Douthitt CB. 1982. The geochemistry of the stable isotopes of silicon. *Geochimica et Cosmochimica Acta* **46**: 1449-1458.

Duce RA, Tindale NW. 1991. Atmospheric transport of iron and its deposition in the ocean, *Limnology and Oceanography* **36**: 1715-1726.

Dugdale RC, Wilkerson FP. 2001. Sources and fates of silicon in the ocean: the role of diatoms in the climate and glacial cycles. *Scientia Marina* **65**: 141-152.

Duplessy JC, Shackleton NJ, Fairbanks RG, Labeyrie L, Oppo D, Kallel N. 1988. Deepwater source variations during the last climatic cycle and their impact on the global deepwater circulation. *Paleoceanography* **3**: 343-360.

Dyke AS. 2004. An outline of North American Deglaciation with emphasis on central and northern Canada. In: *Quaternary Glaciations: Extent and Chronology* (Ehlers J, Gibbard PL (eds.)). Elsevier, Amsterdam.

Dykoski CA, Edwards RL, Cheng H, Yuan D, Cai Y, Zhang M, Lin Y, Qing J, An Z, Revenaugh J. 2005. A high-resolution, absolute-dated Holocene and deglacial Asian monsoon record from Dongge Cave, China. *Earth and Planetary Science Letters* **233**: 71-86.

Egan KE, Rickaby REM, Hendry KR, Halliday AN. 2013. Opening the gateways for diatoms primes Earth for Antarctic glaciation. *Earth and Planetary Science Letters* **375**: 34-43

Egan KE, Rickaby REM, Leng MJ, Hendry KR, Hermoso MI, Sloane HJ, Bostock H, Halliday AN. 2012. Diatom silicon isotopes as a proxy for silicic acid utilisation: A Southern Ocean core top calibration. *Geochimica et Cosmochimica Acta* **96**: 174-192.

Eggimann DW, Manheim FT, Betzer PR. 1980. Dissolution and analyses of amorphous silica in marine sediments. *Journal of Sedimentary Petrology* **50**: 215-225.

Emile-Geay J, Cane MA, Naik N, Seager R, Clement AC, van Geen A. 2003. Warren revisited: Atmospheric freshwater fluxes and "Why is no deepwater formed in the North Pacific". *Journal of Geophysical Research* **108**: 3178.

Epstein, S., Taylor HPJ. 1970. Stable Isotopes, Rare Gases, Solar Wind, and Spallation Products. *Science* **167**: 533-535.

Flückiger J, Knutti R, White JWC. 2006. Oceanic processes as potential trigger and amplifying mechanisms for Heinrich events. *Paleoceanography* **21**: PA2014.

Galbraith ED, Jaccard SL, Pedersen TF, Sigman DM, Haug GH, Cook M, Southon JR, Francois R. 2007. Carbon dioxide release from the North Pacific abyss during the last deglaciation. *Nature* **449**: 890-894.

Galbraith ED, Kienast M, Jaccard SL, Pedersen TF, Brunelle BG, Sigman DM, Kiefer T. 2008. Consistent relationship between global climate and surface nitrate utilization in the western subarctic Pacific throughout the last 500 ka. *Paleoceanography* **23**: PA2212.

Galbraith ED, Kienast M, NICOPP working group members. 2013. The acceleration of oceanic denitrification during deglacial warming. *Nature Geoscience*. Doi:10.1038/NGEO1832.

Garcia HE, Locarnini RA, Boyer TP, Antonov JI, Zweng MM, Baranova OK, Johnson DR. 2010. *World Ocean Atlas 2009, Volume 4: Nutrients (phosphate, nitrate, silicate).* US Government Printing Office, Washington DC.

Gebhardt H, Sarnthein M, Grootes PM, Kiefer T, Kuehn H, Schmieder F, Röhl U. 2008. Paleonutrient and productivity records from the subarctic North Pacific for Pleistocene glacial terminations I to V. *Paleoceanography* **23**: PA4212.

Gehlen M, Beck L, Calas G, Flank AM, Van Bennekom AJ, Van Beusekom JEE. 2002. Unraveling the atomic structure of biogenic silica: Evidence of the structural association of Al and Si in diatom frustules. *Geochimica et Cosmochimica Acta* **66**: 1601-1609.

Gersonde R. 2010. Documentation of sediment core SO202-27-6. *Alfred Wegener Institute, Bremerhaven – Polarstern core repository.* Doi:10.1594/PANGAEA.733384

Gersonde R, SO202-INOPEX Participants. 2010. Cruise Report of the SO202-INOPEX cruise.

Gröning M. 2007. *Reference Sheet for Reference Materials*. International Atomic Energy Agency (IAEA), Vienna.

Gwiazda RH, Hemming SR, Broecker WS. 1996. Provenance of icebergs during Heinrich event 3 and the contrast to their sources during other Heinrich episodes. *Paleoceanography* **11**: 371-378.

Harrison P, Whitney F, Tsuda A, Saito H, Tadokoro K. 2004. Nutrient and Plankton Dynamics in the NE and NW Gyres of the Subarctic Pacific Ocean. *Journal of Oceanography* **60**: 93-117.

Harrison PJ, Boyd PW, Varela DE, Takeda S, Shiomoto A, Odate T. 1999. Comparison of factors controlling phytoplankton productivity int he NE and NW subarctic Pacific gyres. *Progress in Oceanography* **43**: 205-234.

Haug GH, Ganopolski A, Sigman DM, Rosell-Mele A, Swann GEA, Tiedemann R, Jaccard SL, Bollmann J, Maslin MA, Leng MJ, Eglinton G. 2005. North Pacific seasonality and the glaciation of North America 2.7 million years ago. *Nature* **433**: 821-825.

Haug GH, Sigman DM, Tiedemann R, Pedersen TF, Sarnthein M. 1999. Onset of permanent stratification in the subarctic Pacific Ocean. *Nature* **401**: 779-782.

Heinrich H. 1988. Origin and Consequences of Cyclic Ice Rafting in the Northeast Atlantic Ocean during the past 130,000 Years. *Quaternary Research* **29**: 142-152.

Hemming SR. 2004. Heinrich Events: massive Late Pleistocene detritus layers of the North Atlantic and their global climate imprint. *Reviews in Geophysics* **42**: RG1005.

Hendry KR, Robinson LF. 2012. The relationship between silicon isotope fractionation in sponges and silicic acid concentration: Modern and core-top studies of biogenic opal. *Geochimica et Cosmochimica Acta* **81**: 1-12.

Hendy I. 2009. A fresh perspective on the Cordilleran Ice Sheet. *Geology* **37**: 95-96.

Hendy IL. 2010. The paleoclimatic response of the Southern Californian Margin to the rapid climate change of the last 60 ka: A regional overview. *Quaternary International* **215**: 62-73.

Hendy IL, Cosma T. 2008. Vulnerability of the Cordilleran Ice Sheet to iceberg calving during late Quaternary rapid climate change events. *Paleoceanography* **23**: PA2101.

Hendy IL, Kennett JP. 2000. Dansgaard-Oeschger Cycles and the California Current System: Planktonic foraminiferal response to rapid climate change in Santa Barbara Basin, Ocean Drilling Program Hole 893A. *Paleoceanography* **15**: 30-42.

Hendy IL, Kennett JP, Roark EB, Ingram BL. 2002. Apparent synchroneity of submillennial scale climate events between Greenland and Santa Barbara Basin, California from 30-10 ka. *Quaternary Science Reviews* **21**: 1167-1184.

Hendy IL, Kennett JP, Roark EB, Ingram BL. 2007. Santa Barbara Basin ODP893A Planktonic Stable Isotope Data. *IGBP PAGES/World Data Center for Paleoclimatology, Data Contribution Series #2007-080*. NOAA/NCDC Paleoclimatology Program, Boulder CO, USA.

Hill TM, Kennett JP, Pak DK, Behl RJ, Robert C, Beaufort L. 2006. Pre-Bølling warming in Santa Barbara Basin, California: surface and intermediate water records of early deglacial warmth. *Quaternary Science Reviews* **25**: 2835-2845.

Hillebrand H, Dürselen C-D, Kischtel D, Pollingher U, Zohary T. 1999. Biovolume calculation for pelagic and benthic microalgae. *Journal of Phycology* **35**: 403-424.

Holland PR, Kwok R. 2012. Wind-driven trends in Antarctic sea-ice drift. *Nature Geoscience* **5** : 872-875.

Honda MC. 2003. Biological Pump in Northwestern North Pacific. *Journal of Oceanography* **59**: 671-684.

Hoogakker B, Elderfield H, Oliver K, Crowhurst S. 2010. Benthic foraminiferal oxygen isotope offsets over the last glacial-interglacial cycle. *Paleoceanography* **25**: PA4229.

Hughen K, Lehman S, Southon J, Overpeck J, Marchal O, Herring C, Turnbull J. 2004. ^{14}C Activity and Global Carbon Cycle Changes over the Past 50,000 years. *Science* **303**: 202-207.

Jaccard SL. 2012. Palaeoceanography: Pacific and Atlantic synchronized. *Nature Geoscience* **5**: 594-596.

Jaccard SL, Galbraith ED. 2013. Direct ventilation of the North Pacific did not reach the deep ocean during the last deglaciation. *Geophysical Research Letters* **40**: 199-203.

Jaccard SL, Haug GH, Sigman DM, Pedersen TF, Thierstein HR, Röhl U. 2005. Glacial/Interglacial Changes in Subarctic North Pacific Stratification. *Science* **308**: 1003-1006.

Jansen E, Overpeck J, Briffa KR, Duplessy J-C, Joos F, Masson-Delmotte V, Olago D, Otto-Bliesner BL, Peltier WR, Rahmstorf S, Ramesh R, Raynaud D, Rind D, Solomina O, Villalba R, Zhang D. 2007. Paleoclimate. In: *Climate Change 2007: The Physical Science Basis. Contribution of Working Group I to the Fourth Assessment Report of the Intergovernmental Panel on Climate Change* (Solomon S, Qin D, Manning M, Chen Z, Marquis M, Averyt KB, Tignor M, Miller HL (eds.)). Cambridge Univerity Press, Cambridge, UK and New York, NY, USA.

Jochum KP, Wang X, Vennemann TW, Sinha B, Müller WEG. 2012. Siliceous deep-sea sponge Monorhaphis chuni: A potential paleoclimate archive in ancient animals. *Chemical Geology* **300-301**: 143-151.

Johnson WK, Miller LA, Sutherland NE, Wong CS. 2005. Iron transport by mesoscale Haida eddies int he Gulf of Alaska. *Deep-Sea Research II* **52**: 933-953.

Juillet-Leclerc A, Labeyrie L. 1987. Temperature dependance of the oxygen isotopic fractionation between diatom silica and water. *Earth and Planetary Science Letters* **84**: 69-74.

Kaufman DS, Young NE, Briner JP, Manley WF. 2011. Alaska Palaeo-Glacier Atlas (Version 2). *Developments in Quaternary Science* **15**: 427-445.

Kemp AES, Pike J, Pearce RB, Lange CB. 2000. The "Fall dump" - a new perspective on the role of a "shade flora" in the annual cycle of diatom production and export flux. *Deep-Sea Research II* **49**: 2129-2154.

Kiefer T. 2010. When Still Waters Ran Deep. *Science* **329**: 290-291.

Kiefer T, Kienast M. 2005. Patterns of deglacial warming in the Pacific Ocean: a review with emphasis on the time interval of Heinrich event 1. *Quaternary Science Reviews* **24**: 1063-1081.

Kiefer T, Sarnthein M, Erlenkeuser H, Grootes PM, Roberts AP. 2001. North Pacific response to millenial-scale changes in ocean circulation over the last 60 kyr. *Paleoceanography* **16**: 179-189.

Kohfeld KE, Chase Z. 2011. Controls on deglacial changes in biogenic fluxes in the North Pacific Ocean. *Quaternary Science Reviews* **30**: 3350-3363.

Kotilainen AT, Shackleton NJ. 1995. Rapid climate variability in the North Pacific Ocean during the past 95,000 years. *Nature* **377**: 323-326.

Kovanen DJ, Easterbrook DJ. 2002. Paleodeviations of radiocarbon marine reservoir values for the northeast Pacific. *Geology* **30**: 243-246.

Kuhlbrodt T, Griesel A, Montoya M, Levermann A, Hofmann M, Rahmstorf S. 2007. On the driving processes of the Altantic meridional overturning circulation. *Reviews in Geophysics* **45**: RG2001.

Kuhn G. 2013. Don´t forget the salty soup: Calculations for bulk marine geochemistry and radionuclide geochronology. *Goldschmidt 2013 Conference Abstracts, Florence, Mineralogical Magazine.*

Kuzmin Y, Burr GS, Jull AJT. 2001. Radiocarbon reservoir correction ages in the Peter the Great Gulf, Sea of Japan, and eastern coast of the Kunashir, southern Kuriles (northwestern Pacific). *Radiocarbon* **43**: 477-481.

Lam PJ, Robinson LF, Blusztajn J, Li C, Cook MS, McManus JF, Keigwin LD. 2013. Transient stratification as the cause of the North Pacific productivity spike during deglaciation. *Nature Geoscience*. Doi:10.1038/NGEO1873

Laskar J, Robutel P, Joutel F, Gastineau M, Correia ACM, Levrard B. 2004. A long-term numerical solution for the insolation quantities of the Earth. *Astronomy & Astrophysics* **428**: 261-285.

Leduc G, Vidal L, Tachikawa K, Rostek F, Sonzogni C, Beaufort L, Bard E. 2007. Moisture transport across Central America as a positiv feedback on abrupt climatic changes. *Nature* **445**: 908-911.

Lefèvre N, Watson AJ, Cooper DJ, Weiss RF, Takahashi T, Sutherland SC. 1999. Assessing the seasonality of the oceanic sink for CO_2 in the northern hemisphere. *Global Biogeochemical Cycles* **13**: 273-286.

Leng MJ, Sloane HJ. 2008. Combined oxygen and silicon isotope analysis of biogenic silica. *Journal of Quaternary Science* **23**: 313-319.

Leng MJ, Swann GEA, Hodson MJ, Tyler JJ, Patwardhan SV, Sloane HJ. 2009. The Potential use of Silicon Isotope Composition of Biogenic Silica as a Proxy for Environmental Change. *Silicon* **1**: 65-77.

Locarnini RA, Mishonov AV, Antonov JI, Boyer TP, Garcia HE, Baranova OK, Zweng MM, Johnson DR. 2010. *World Ocean Atlas 2009, Volume 1: Temperature*. US Government Printing Office, Washington DC.

Lumpkin R, Speer K. 2007. Global Ocean Meridional Overturning. *Journal of Physical Oceanography* **37**: 2250-2562.

Lund DC, Mix AC, Southon J. 2011. Increased ventilation age of the deep northeast Pacific Ocean during the last deglaciation. *Nature Geoscience* **4**: 771-774.

Lüthi D, Le Floch M, Bereiter B, Blunier T, Barnola J-M, Siegenthaler U, Raynaud D, Jouzel J, Fischer H, Kawamura K, Stocker TF. 2008. High-resolution carbon dioxide concentration record 650,000-800,000 years before present. *Nature* **453**: 379-382.

MacAyeal DR. 1993. Binge/purge oscillations of the Laurentide Ice Sheet as a cause of the North Atlantic's Heinrich events. *Paleoceanography* **8**: 775-784.

Mahowald NM, Muhs DR, Levis S, Rasch PJ, Yoshioka M, Zender CS, Luo C. 2006. Change in atmospheric mineral aerosols in response to climate: Last glacial period, preindustrial, modern, and doubled carbon dioxide climates. *Journal of Geophysical Research* **111**: D10202.

Maier E, Chapligin B, Abelmann A, Gersonde R, Esper O, Ren J, Friedrichsen H, Meyer H, Tiedemann R. 2013. Combined oxygen and silicon isotope analysis of diatom silica from a deglacial subarctic Pacific record. *Journal of Quaternary Science* **28**: 571-581.

Maier E, Abelmann A, Gersonde R, Méheust M, Ren J, Chapligin B, Tiedemann R. a. In preparation for Paleoceanography. Surface water hydrography and nutrient dynamics of the deglacial subarctic Pacific – evidence from diatom oxygen and silicon stable isotopes.

Maier E, Abelmann A, Gersonde R, Méheust M, Chapligin B, Ren J, Tiedemann R. b. In preparation for Earth and Planetary Science Letters. Millennial-scale variabilities in upwelling and halocline strength in the NE Pacific during Marine Isotope Stage 3.

Mann DH, Peteet DM. 1994. Extent and Timing of the Last Glacial Maximum in Southwestern Alaska. *Quaternary Research* **42**: 136-148.

Mann DH, Hamilton TD. 1995. Late Pleistocene and Holocene Paleoenvironments of the North Pacific Coast. *Quaternary Science Reviews* **14**: 449-471.

Marchetti A, Juneau P, Whitney FA, Wong C-S, Harrison PJ. 2006. Phytoplankton processes during a mesoscale iron enrichment in the NE subarctic Pacific: Part II - Nutrient utilization. *Deep-Sea Research II* **53**: 2114-2130.

Maslin MA, Shackleton NJ, Pflaumann U. 1995. Surface water temperature, salinity, and density changes in the northeast Atlantic during the last 45,000 years: Heinrich events, deep water formation, and climatic rebounds. *Paleoceanography* **10**: 527-544.

Masuda S, Awahi T, Sugiura N, Matthews JP, Toyoda T, Kawai Y, Doi T, Kouketsu S, Igarashi H, Katsumata K, Uchida H, Kawano T, Fukasawa M. 2010. Simulated Rapid Warming of Abyssal North Pacific Waters. *Science* **329**: 319-322.

Matheney RK, Knauth LP. 1989. Oxygen-isotope fractionation between marine biogenic silica and seawater. *Geochimica et Cosmochimica Acta* **53**: 3207-3214.

Max L, Riethdorf J-R, Tiedemann R, Smirnova M, Lembke-Jene L, Fahl K, Nürnberg D, Matul A, Mollenhauer G. 2012. Sea surface temperature variability and sea-ice extent in the subarctic northwest Pacific during the past 15,000 years. *Paleoceanography* **27**: PA3213.

Max L, Lembke-Jene L, Riethdorf J-R, Tiedemann R, Nürnberg D, Kühn H, Mackensen A. 2013. Pulses of enhanced North Pacific Intermediate Water ventilation from the Okhotsk Sea and Bering Sea during the last deglaciation. *Climate of the Past Discussions* **9**: 6221-6253.

McKelvey BC, Chen W, Arculus RJ. 1995. Provenance of Pliocene-Pleistocene Ice-Rafted Debris, Leg 145, Northern Pacific Ocean. *Proceedings of the Ocean Drilling Program, Scientific Results* **145**: 195-204.

McManus JF, Francois R, Gherardi JM, Keigwin LD, Brown-Leger S. 2004. Collapse and rapid resumption of Atlantic meridional circulation linked to deglacial climate changes. *Nature* **428**: 834-837.

Measures CI, Brown MT, Vink S. 2005. Dust deposition to the surface waters of the western and central North Pacific inferred from surface water dissolved aluminum concentrations, *Geochemistry Geophysics Geosystems* **6**: Q09M03.

Meckler AN, Sigman DM, Gibson KA, Francois R, Martínez-Garcia A, Jaccard SL, Röhl U, Peterson LC, Tiedemann R, Haug GH. 2013. Deglacial pulses of deep-ocean silicate into the subtropical North Atlantic Ocean. *Nature **495***: 495-499.

Méheust M. 2014. Late Quaternary variability of sea-ice cover, surface-water temperature and terrigenous input in the subarctic North Pacific and the Bering Sea: A biomarker approach. PhD thesis, University of Bremen: 118 pp.

Méheust M, Fahl K, Stein R. 2013. Variability in modern sea surface temperature, sea ice and terrigenous input in the sub-polar North Pacific and Bering Sea: Reconstruction from biomarker data. *Organic Geochemistry* **57**: 54-64.

Méheust M, Maier E, Kühn H, Stein R, Fahl K, Gersonde R. In preparation for Quaternary Science Reviews. IP_{25} proxy records of sea-ice variability in the subarctic North Pacific and adjacent Bering Sea during the past 25,000 years.

Menviel L, Timmermann A, Elison Timm O, Mouchet A, Abe-Ouchi A, Chikamoto MO, Harada N, Ohgaito R, Okazaki Y. 2012. Removing the North Pacific halocline: Effects on global climate, ocean circulation and the carbon cycle, *Deep-Sea Research II* **61-64**: 106-113.

Menviel L, Timmermann A, Friedrich T, England MH. 2014. Hindcasting the continuum of Dansgaard-Oeschger variability: mechanisms, patterns and timing. *Climate of the Past* **10**: 63-77.

Mikkelsen N, Labeyrie L, Berger WH. 1978. Silica oxygen isotopes in diatoms: a 20,000 yr record in deep-sea sediments. *Nature* **271**: 536-538.

Mikolajewicz U, Crowley TJ, Schiller A, Voss R. 1997. Modelling teleconnections between the North Atlantic and North Pacific during the Younger Dryas. *Nature* **387**: 384-387.

Milligan AJ, Varela DE, Brzezinski MA, Morel FMM. 2004. Dynamics of silicon metabolism and silicon isotopic discrimination in a marine diatom as a function of pCO2. *Limnology and Oceanography* **49**: 322-329.

Mix AC, Lund DC, Pisias NG, Bodén P, Bornmalm L, Lyle M, Pike J. 1999. Rapid Climate Oscillations in the Northeast Pacific During the Last Deglaciation Reflect Northern and Southern Hemisphere Sources. *Geographical Monograph* **12**: 127-148.

Molini-Velsko C, Mayeda TK, Clayton RN. 1986. Isotopic composition of silicon in meteorites. *Geochimica et Cosmochimica Acta* **50**: 2719-2726.

Monnin E, Indermühle A, Dällenbach A, Flückiger J, Stauffer B, Stocker TF, Raynaud D, Barnola J-M. 2001. Atmospheric CO_2 Concentrations over the Last Glacial Termination, *Science* **291**: 112-114.

Morley DW, Leng MJ, Mackay AW, Sloane HJ, Rioual P, Battarbee RW. 2004. Cleaning of lake sediment samples for diatom oxygen isotope analysis. *Journal of Paleolimnology* **31**: 391-401.

Moschen R, Lücke A, Schleser GH. 2005. Sensitivity of biogenic silica oxygen isotope to changes in surface water temperature and palaeoclimatology. *Geophysical Research Letters* **32**: L07708.

Moschen R, Lücke A, Parplies J, Radtke U, Schleser GH. 2006. Transfer and early diagenesis of biogenic silica oxygen isotope signals during settling and sedimentation of diatoms in a temperate freshwater lake (Lake Holzmaar, Germany). *Geochimica et Cosmochimica Acta* **70**: 4367-4379.

Mulitza S, Boltovskoy D, Donner B, Meggers H, Paul A, Wefer G. 2003. Temperature:$\delta^{18}O$ relationships of planktonic foraminifera collected from surface waters. *Palaeogeography, Palaeoclimatology, Palaeoecology* **202**: 143-152.

Müller PJ, Schneider R. 1993. An automated leaching method for the determination of opal in sediments and particulate matter. *Deep-Sea Research I* **40**: 425-444.

Nakagawa T, Kitagawa H, Yasuda Y, Tarasov P, Nishida K, Gotanda K, Sawai Y, Yangtze River Civilization Program Members. 2003. Asynchronous Climate Changes in the North Atlantic and Japan During the Last Termination. *Science* **299**: 688-691.

Nelson DM, Tréguer P, Brzezinski MA, Leynaert A, Quéguiner B. 1995. Production and dissolution of biogenic silica in the ocean: Revised global estimates, comparison with regional data and relationship to biogenic sedimentation. *Global Biogeochemical Cycles* **9**: 359-372.

NGRIP members. 2004. High-resolution record of Northern Hemisphere climate extending into the last interglacial period. *Nature*. Doi:10.1038/NATURE02805.

Okazaki Y, Timmermann A, Menviel L, Harada N, Abe-Ouchi A, Chikamoto MO, Mouchet A, Asahi H. 2010. Deepwater Formation in the North Pacific During the Last Glacial Termination *Science* **329**: 200-204.

Okumura YM, Deser C, Hu A, Timmermann A, Xie S-P. 2009. North Pacific Climate Response to Freshwater Forcing in the Subarctic North Atlantic: Oceanic and Atmospheric Pathways. *Journal of Climate* **22**: 1424-1444.

Onodera J, Takahashi K, Honda MC. 2005. Pelagic and coastal diatom fluxes and the environmental changes in the northwestern North Pacific during December 1997 - May 2000. *Deep-Sea Research II* **52**: 2218-2239.

Parrenin F, Masson-Delmotte V, Köhler P, Raynaud D, Paillard D, Schwander J, Barbante C, Landais A, Wegner A, Jouzel J. 2013. Synchronous Change of Atmospheric CO_2 and Antarctic Temperature During the Last Deglacial Warming. *Science* **339**: 1060-1063.

Pike J, Swann GEA, Leng MJ, Snelling AM. 2013. Glacial discharge along the west Antarctic Peninsula during the Holocene. *Nature Geoscience* **6**: 199-202.

Rasmussen SO, Andersen KK, Svensson AM, Steffensen JP, Vinther BM. 2006. A new Greenland ice core chronology for the last glacial termination. *Journal of Geophysical Research* **111**: D06102.

Reimer PJ, Bard E, Bayliss A, Beck JW, Blackwell PG, Bronk Ramsey C, Buck CE, Cheng H, Edwards RL, Friedrich M, Grootes PM, Guilderson TP, Haflidason H, Hajdas I, Hatté C, Heaton TJ, Hoffman DL, Hogg AG, Hughen KA, Kaiser KF, Kromer B, Manning SW, Niu M, Reimer RW, Richards DA, Scott EM, Southon JR, Staff RA, Turney CSM, Van der Pflicht J. 2013.

INTCAL13 and MARINE13 radiocarbon age calibration curves 0-50,000 years cal BP. *Radiocarbon* **55**: 1869-1887.

Ren J, Gersonde R, Esper O, Tiedemann R. In preparation for Paleoceanography. Late Pleistocene paleoceanographic variability in the northern North Pacific: evidence from diatom records.

Reynolds BC, Aggarwal J, Brzezinski MA, Cardinal D, Engström E, Georg RB, Land M, Leng M, Opfergelt S, Vroon PZ. 2007. An inter-laboratory comparison of Si isotope reference materials. *Journal of Analytical Atomic Spectrometry* **22**: 561–568.

Reynolds BC, Frank M, Halliday AN. 2006. Silicon isotope fractionation during nutrient utilization in the North Pacific. *Earth and Planetary Science Letters* **244**: 431-443.

Reynolds BC, Frank M, Halliday AN. 2008. Evidence for a major change in silicon cycling in the sucarctic North Pacific a 2.73 Ma. *Paleoceanography* **23**: PA4219.

Riethdorf J-R, Max L, Nürnberg D, Lembke-Jene L, Tiedemann R. 2013a. Deglacial development of (sub) sea surface temperature and salinity in the subarctic northwest Pacific: Implications for upper-ocean stratification. *Paleoceanography* **28**: 91-104.

Riethdorf J-R, Nürnberg D, Max L, Tiedemann R, Gorbarenko SA, Malakhov MI. 2013b. Millennial-scale variability of marine productivity and terrigenous matter supply in the western Bering Sea over the past 180 kyr. *Climate of the Past* **9**: 1345-1373.

Rohling EJ, Marsh R, Wells NC, Siddall M, Edwards NR. 2004. Similar meltwater contributions to glacial sea level changes from Antarctic and northern ice sheets. *Nature* **430**: 1016-1021.

Ruth U., Bigler M, Röthlisberger R, Siggaard-Andersen M-L., Kipfstuhl S, Goto-Azuma K, Hansson ME, Johnsen, SJ. Lu H, Steffensen JP. 2007. Ice core evidence for a very tight link between North Atlantic and east Asian glacial climate. *Geophysical Research Letters* **34**: L03706.

Sabin AL, Pisias NG. 1996. Sea Surface Temperature Changes in the Northeastern Pacific Ocean during the Past 20,000 Years and Their Relationship to Climate Change in Northwestern North America. *Quaternary Research* **46**: 48-61.

Saenko OA, Schmittner A, Weaver AJ. 2004. The Atlantic-Pacific Seesaw. *Journal of Climate* **17**: 2033-2038.

Sancetta C. 1982. Distribution of diatom species in surface sediments of the Bering and Okhotsk seas. *Micropaleontology* **28**: 221-257.

Sancetta C. 1987. Three species of *Coscinodiscus* Ehrenberg from North Pacific sediments examined in the light and scanning electron microscopes. *Micropaleontology* **33**: 230-241.

Sancetta C, Heusser L, Labeyrie L, Naidu AS, Robinson SW. 1985. Wisconsin-Holocene Paleoenvironment of the Bering Sea: Evidence from Diatoms, Pollen, Oxygen Isotopes and Clay Minerals. *Marine Geology* **62**: 55-68.

Sarmiento JL, Gruber N, Brzezinski MA, Dunne JP. 2004. High-latitude controls of thermocline nutrients and low latitude biological productivity. *Nature* **427**: 56-60.

Sarnthein M, Gebhardt H, Kiefer T, Kucera M, Cook M, Erlenkeuser H. 2004. Mid Holocene origin of the sea-surface salinity low in the subarctic North Pacific. *Quaternary Science Reviews* **23**: 2089-2099.

Sarnthein M, Grootes PM, Kennett JP, Nadeau M-J. 2007. ^{14}C Reservoir Ages Show Deglacial Changes in Ocean Currents and Carbon Cycle. *Geophysical Monograph Series 173*: 175-196.

Sarntheim M, Schneider B, Grootes PM. 2013. Peak glacial ^{14}C ventilation ages suggest major drawdown of carbon into the abyssal ocean. *Climate of the Past* **9**: 2595-2614.

Schmidt M, Botz R, Stoffers P, Anders T, Bohrmann G. 1997. Oxygen isotopes in marine diatoms: A comparative study of analytical techniques and new results on the isotope composition of recent marine diatoms. *Geochimica et Cosmochimica Acta* **61**: 2275-2280.

Schmidt M, Botz R, Rickert D, Bohrmann G, Hall SR, Mann S. 2001. Oxygen isotopes in marine diatoms and relations to opal-A maturation. *Geochimica et Cosmochimica Acta* **65**: 201-211.

Schmitt J, Schneider R, Elsig J, Leuenberger D, Lourantou A, Chappellaz J, Köhler P, Joos F, Stocker TF, Leuenberger M, Fischer H. 2012. Carbon Isotope Constraints on the Deglacial CO_2 Rise from Ice Cores. *Science* **336**: 711-714.

Seki O, Ishiwatari R, Matsumoto K. 2002. Millennial climate oscillations in NE Pacific surface waters over the last 82 kyr: New evidence from alkenones. *Geophysical Research Letters* **29**: 2144.

Shemesh A, Charles CD, Fairbanks RG. 1992. Oxygen Isotopes in Biogenic Silica: Global Changes in Ocean Temperature and Isotopic Composition. *Science* **256**: 1434-1436.

Shemesh A, Burckle LH, Hays JD. 1994. Meltwater Input to the Southern Ocean During the Last Glacial Maximum. *Science* **266**: 1542-1544.

Shemesh A, Burckle LH, Hays JD. 1995. Late Pleistocene oxygen isotope records of biogenic silica from the Atlantic sector of the Southern Ocean. *Paleoceanography* **10**: 179-196.

Sheppard SMF, Gilg HA. 1996. Stable isotope geochemistry of clay minerals. *Clay Minerals* **13**: 1-24.

Sigman DM, Hain MP, Haug GH. 2010. The polar ocean and glacial cycles in atmospheric CO_2 concentration. *Nature* **466**: 47-55.

Skinner LC, Fallon S, Waelbroeck C, Barker S. 2010. Ventilation of the Deep Southern Ocean and Deglacial CO_2 Rise. *Science* **328**: 1147-1151.

Stabeno PJ, Bond NA, Hermann AJ, Kachel NB, Mordy CW, Overland JE. 2004. Meteoroly and oceanography of the Northern Gulf of Alaska. *Continental Shelf Research* **24**: 859-897.

Studer AS, Ellis KK, Oleynik S, Sigman DM, Haug GH. 2013. Size-specific opal-bound nitrogen isotope measurements in North Pacific sediments. *Geochimica et Cosmochimica Acta* **120**: 179-194.

Stuiver M, Reimer PJ. 1993. Extended ^{14}C data base and revised CALIB 3.0 ^{14}C age calibration program. *Radiocarbon* **35**: 215-230.

Sutton JN, Varela DE, Brzezinski MA, Beucher CP. 2013. Species-dependent silicon isotope fractionation by marine diatoms. *Geochimica et Cosmochimica Acta* **104**: 300-309.

Svensson A, Andersen KK, Bigler M, Clausen HB, Dahl-Jensen D, Davies SM, Johnsen SJ, Muscheler R, Parrenin F, Rasmussen SO, Röthlisberger R, Seierstad I, Steffensen JP, Vinther BM. 2008. A 60 000 year Greenland stratigraphic ice core chronology. *Climate of the Past* **4**: 47-57.

Svensson A, Andersen KK, Bigler M, Clausen HB, Dahl-Jensen D, Davies SM, Johnsen SJ, Muscheler R, Rasmussen SO, Röthlisberger R, Steffensen JP, Vinther BM. 2006. The Greenland Ice Core Chronology 2005, 15-42 ka. Part 2: comparison to other records. *Quaternary Science Reviews* **25**: 3258-3267.

Swann GEA. 2010. Salinity changes in the North West Pacific Ocean during the late Pliocene/early Quaternary from 2.73 Ma to 2.52 Ma. *Earth and Planetary Science Letters* **297**: 332-338.

Swann GEA, Leng MJ. 2009. A review of diatom $\delta^{18}O$ in palaeoceanography. *Quaternary Science Reviews* **28**: 384-398.

Swann GEA, Leng MJ, Sloane HJ, Maslin MA, Onodera J. 2007. Diatom oxygen isotopes: Evidence of a species effect in the sediment record. *Geochemistry Geophysics Geosystems* **8**: Q06012.

Swann GEA, Leng MJ, Sloane HJ, Maslin MA. 2008. Isotope offsets in marine diatom $\delta^{18}O$ over the last 200 ka. *Journal of Quaternary Science* **23**: 389-400.

Swann GEA, Leng MJ, Juschus O, Melles M, Brigham-Grette J, Sloane HJ. 2010. A combined oxygen and silicon diatom isotope record of Late Quaternary change in Lake El'gygytgyn, North East Siberia. *Quaternary Science Reviews* **29**: 774-786.

Swann GEA, Maslin MA, Leng MJ, Sloane HJ, Haug GH. 2006. Diatom $\delta^{18}O$ evidence for the development of the modern halocline system in the subarctic northwest Pacific at the onset of major Northern Hemisphere glaciation. *Paleoceanography* **21**: PA1009.

Swann GEA, Pike J, Snelling AM, Leng MJ, Williams MC. 2013. Seasonally resolved diatom $\delta^{18}O$ records from the West Antarctica Peninsula over the last deglaciation. *Earth and Planetary Science Letters* **364**: 12-23.

Takahashi K. 1986. Saesonal fluxes of pelagic diatoms in the subarctic Pacific, 1982-1983. *Deep-Sea Research* **33**: 1225-1251.

Takahashi K, Billings JD, Morgan JK. 1990. Oceanic province: Assessment from the time-series diatom fluxes in the northeastern Pacific. *Limnology and Oceanography* **35**: 154-165.

Takeda S. 1998. Influence of iron variability on nutrient consumption ratio of diatoms in oceanic waters. *Nature* **393**: 774-777.

Takeda S. 2011. Iron and Phytoplankton Growth in the Subarctic North Pacific. *Aqua-BioScience Monographs* **4**: 41-93.

Takeda S, Tsuda A. 2005. An in situ iron-enrichment experiment in the western subarctic Pacific (SEEDS): Introduction and summary. *Progress in Oceanography* **64**: 95-109.

Talley LD. 1993. Distribution and Formation of North Pacific Intermediate Water. *Journal of Physical Oceanography* **23**: 517-537.

Taylor HP Jr. 1968. The Oxygen Isotope Geochamistry of Igneous Rocks. Contr. Mineral and Petrol **19**: 1-71.

Tréguer PJ, De la Rocha CL. 2013. The World Ocean Silica Cycle. *Annual Review of Marine Science* **5**: 477-501.

Tsuda A, Takeda S, Saito H, Nishioka J, Nojiri Y, Kudo I, Kiyosawa H, Shiomoto A, Imai K, Ono T, Shimamoto A, Tsumune D, Yoshimura T, Aono T, Hinuma A, Kinugasa M, Suzuki K, Sohrin Y, Noiri Y, Tani H, Deguchi Y, Tsurushima N, Ogawa H, Fukami K, Kuma K, Saino T. 2003. A Mesoscale Iron Enrichment in the Western Subarctic Pacific Induces a Large Centric Diatom Bloom. *Science* **300**: 958-961.

Tsuda A, Takeda S, Saito H, Nishioka J, Kudo I, Nojiri Y, Suzuki K, Uematsu M, Wells ML, Tsumune D, Yoshimura T, Aono T, Aramaki T, Cochlan WP, Hayakama M, Imai K, Isada T, Iwamoto Y, Johnson WK, Kameyama S, Kato S, Kiyosawa H, Kondo Y, Levasseur M, Machida RJ, Nagao I, Nakagawa F, Nakanishi T, Nakatsuka S, Narita A, Noiri Y, Obata H, Ogawa H, Oguma K, Ono T, Sakuragi T, Sasakawa M, Sato M, Shimamoto A, Takata H, Trick CG, Watanabe YW, Wong CS, Yoshie N. 2007. Evidence for the Grazing Hypothesis: Grazing Reduces Phytoplankton Responses of the HNLC Ecosystem to Iron Enrichment in the Western Subarctic Pacific (SEEDS II). *Journal of Oceanography* **63**: 983-994.

Van Cappellen P, Dixit S, Van Beusekom J. 2002. Biogenic silica dissolution in the oceans: Reconciling experimental and field-based dissolution rates. *Global Biogeochemical Cycles* **16**: 1075.

Van Kreveld S, Sarnthein M, Erlenkeuser H, Grootes P, Jung S, Nadeau MJ, Pflaumann U, Voelker A. 2000. Potential links between surging ice sheets, circulation changes, and the Dansgaard-Oeschger cycles in the Irminger Sea, 60-18 kyr. *Paleoceanography* **15**: 425-442.

Vinther BM, Clausen HB, Johnsen SJ, Rasmussen SO, Andersen KK, Buchardt SL, Dahl-Jensen D, Seierstad IK, Siggaard-Andersen M-L, Steffensen JP, Svensson AM, Olsen J, Heinemeier J. 2006. A synchronized dating of three Greenland ice cores throughout the Holocene. *Journal of Geophysical Research* **111**: D13102.

Voelker AHL, workshop participants. 2002. Global distribution of centennial-scale records for Marine Isotope Stage (MIS) 3: a database. *Quaternary Science Reviews* **21**: 1185-1212.

Waelbroeck C, Labeyrie L, Michel E, Duplessy JC, McManus JF, Lambeck K, Balbon E, Labracherie M. 2002. Sea-level and deep water temperature changes derived from benthic foraminifera isotopic records. *Quaternary Science Reviews* **21**: 295-305.

WAIS Divide Project Members. 2013. Onset of deglacial warming in West Antarctica driven by local orbital forcing. *Nature*. Doi:10.1038/NATURE12376.

Wang P, Clemens S, Beaufort L, Braconnot P, Ganssen G, Jian Z, Kershaw P, Sarnthein M. 2005. Evolution and variability of the Asian monsoon system: state of the art and outstanding issues. *Quaternary Science Reviews* **24**: 595-629.

Warren BA. 1983. Why is no deep water formed in the North Pacific?. *Journal of Marine Research* **41**: 327-347.

Wefer G, Berger WH. 1991. Isotope paleontology: growth and composition of extant calcareous species. *Marine Geology* **100**: 207-248.

Weingartner TJ, Danielson SL, Royer TC. 2005. Freshwater variability and predictability in the Alaska Costal Current. *Deep-Sea Research II* **52**: 169-191.

Wiedmer M, Montgomery DR, Gillespie AR, Greenberg H. 2010. Late Quaternary megafloods from Glacial Lake Atna, Couthcentral Alaska, U.S.A. *Quaternary Research* **73**: 413-424.

Yoneda M, Uno H, Shibata Y, Suzuki R, Kumamoto Y, Yoshida K, Sasaki T, Suzuki A, Kawahata H. 2007. Radiocarbon marine reservoir ages in the western Pacific estimated by pre-bomb molluscan shells. *Nuclear Instruments and Methods in Physics Research Section B: Beam Interactions with Materials and Atoms* **259**: 432-437.

Ziegler K, Chadwick OA, Brzezinski MA, Kelly EF. 2005. Natural variations of δ^{30}Si ratios during progressive basalt weathering, Hawaiian Islands. *Geochimica et Cosmochimica Acta* **69**: 4597-4610.

A.1 Eolian dust records as a chronostratigraphic tool for marine sediment cores

Serno, S.[1,2], Winckler G.[1,3], **Maier E**.[4], Anderson, R.F.[1,3], Ren H., Gersonde R.[4], Haug G.H.[5]

[1]Lamont Doherty Earth Observatory, Columbia University, Palisades, New York, USA
[2]DFG-Leibniz Center for Surface Process and Climate Studies, Institute of Earth and Environmental Science, University of Potsdam, Potsdam, Germany
[3]Department of Earth and Environmental Sciences, Columbia University, New York, USA
[4]Alfred Wegener Institute, Helmholtz Centre for Polar and Marine Research, Bremerhaven, Germany
[5]Alfred Geological Institute, ETH Zürich, Zürich, Switzerland

Abstract

Dust records from the Subantarctic Atlantic, equatorial Pacific and North African margin show excellent correlations with ice core records of eolian dust supply from Greenland or Antarctica during the last ~100 yrs, providing strong evidence that the application of eolian dust records as a chronostratigraphic tool in marine sediment cores has high potential in the global ocean. Here we present a new high-resolution record for eolian dust input to the Subarctic North Pacific from sediment core SO202-07-6 (Detroit Seamount, western subarctic Pacific). ^{4}He is employed as a proxy for eolian dust in the sediment. The ^{4}He-based dust record from the subarctic Pacific shows an excellent correlation with the well-dated dust record from the NGRIP ice core in Greenland (Ruth et al., 2007) in the general pattern of abrupt dust changes, particularly at the transitions from the Younger Dryas stadial into the early Holocene at 11640 yr BP, from Heinrich Stadial (HS) 1 into the Bølling/Allerød (B/A) interstadial at 14650 yr BP and the termination of HS2 at 23323 yr BP (Figure A.1.1). These three abrupt changes in dust supply in the subarctic Pacific are tied to corresponding changes in the NGRIP dust record to provide a new chronostratigraphic technique for marine sediments. This new chronostratigraphic tool allows us to independently constrain radiocarbon paleoreservoir ages, which have been applied to a high-resolution record of planktic foraminiferal radiocarbon dates from SO202-07-6 to construct a robust age model for this sediment core. The three paleoreservoir ages from the dust tie points indicate constant paleoreservoir ages (650-750 yrs) since HS2, similar to observed modern surface reservoir ages (650-950 yrs; Kuzmin et al., 2001; Stuiver and Braziunas, 1993; Yoneda et al., 2007). Our results support recent findings from the eastern subarctic Pacific indicating constant radiocarbon paleoreservoir ages of 730 ± 200 yrs during the last deglaciation (Lund et al., 2011). Older paleoreservoir ages compared to modern surface reservoir ages during the Last Glacial Maximum and HS1, derived from radiocarbon plateau tuning in recent studies from the western (Sarnthein et al., 2013) and eastern subarctic Pacific (Gebhardt et al., 2008), are

not supported by our paleoreservoir age determinations. However, the radiocarbon paleoreservoir age derived from the dust tuning at the HS1-B/A transition (665 yrs) is consistent with the paleoreservoir age of Sarnthein et al. (2013; 720 ± 285 yrs) derived from the tuning of a ~1000 yr-long radiocarbon plateau observed in a marine sediment core from the western subarctic Pacific to a reference terrestrial radiocarbon record from Lake Suigetsu, Japan (Bronk Ramsey et al., 2012), around this climatic transition. We observe a radiocarbon plateau in the high-resolution planktic foraminiferal radiocarbon record from SO202-07-6 around the HS1-B/A transition, and tuning of this radiocarbon plateau to the corresponding

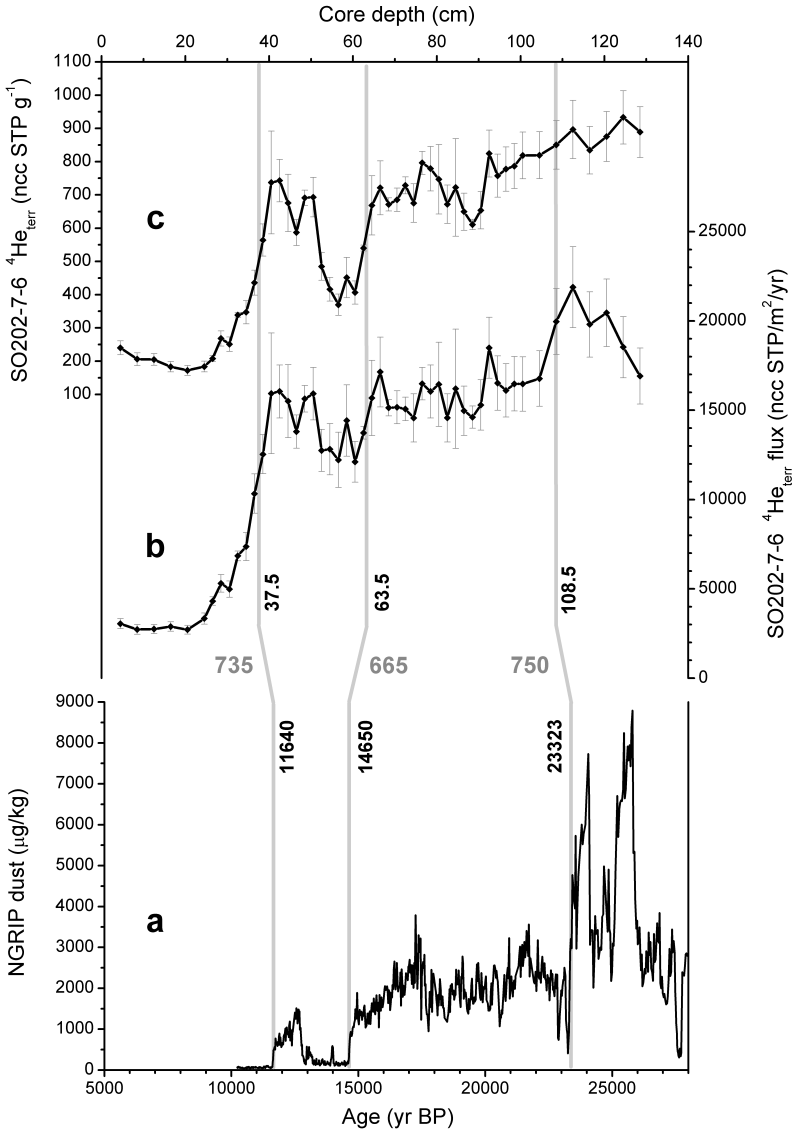

Figure A.1.1. Comparison of **a)** the NGRIP dust concentration record (Ruth et al., 2007) with **b)** the $^4He_{terr}$ flux and **c)** $^4He_{terr}$ concentration records from SO202-07-6. The dark grey lines show the match-up of the Younger Dryas-early Holocene and HS1-B/A transitions between the NGRIP dust concentration (11.640 and 14650 yr BP, respectively) and $^4He_{terr}$ concentration records (37.5 and 63.5 cm core depth, respectively), as well as the match-up of the mid-termination of HS2 in the NGRIP record at 23323 yr BP with the mid-termination in the $^4He_{terr}$ flux at 108.5 cm core depth in SO202-07-6. The paleoreservoir ages resulting from the dust tie points are shown as dark grey numbers.

plateau in the terrestrial radiocarbon record from Lake Suigetsu, Japan, provides us with age-depth constraints within the errors of the plateau tuning technique that are consistent with our independent age-depth constraints based on the paleoreservoir age reconstruction from dust tuning for this climatic transition.

Author´s contribution: I participated in (1) the selection of the depths for the high-resolution radiocarbon record from Core SO202-07-6 and (2) the ^{14}C-plateau tuning of the SO202-07-6 radiocarbon record to the high-resolution ^{14}C-record of Lake Suigetsu (Bronk Ramsey et al., 2012).

A.2 – List of Abbreviations

Institutes and projects

AWI..... Alfred Wegener Institute, Helmholtz Centre for Polar and Marine Research
BMBF..... German Federal Ministry of Education and Research (BundesMinisterium für Bildung und Forschung)
DFG ..... Deutsche ForschungsGemeinschaft
EPICA ..... European Project for Ice Coring in Antarctica
IAEA ..... International Atomic Energy Agency
INOPEX ..... Innovative NOrth Pacific EXperiment
KALMAR ..... Kurile-Kamchatka and ALeutian MARginal Sea-Island Arc Systems: Geodynamic and Climate Interaction in Space and Time
NERC ..... National Environmental Research Council
NGRIP..... North Greenland Ice Core Project
NOSAMS ..... National Ocean Science AMS facility
POLMAR ..... AWI Graduate School
WEPAMA ..... Western Pacific Margin
UCSB ..... University of California in Santa Barbara

Analytical standards, analysing techniques and definitions

AMS ..... Accelerator Mass Spectrometry
BFC ..... a lacustrine diatom standard
CT ..... Cold Trap
cps ..... counts per second
EDS ..... Energy Dispersive X-ray Spectrometry
ICP-OES ..... Inductively Coupled Plasma – Optical Emission Spectrometry
IRMS ..... Isotope Ratio Mass Spectrometer
NBS-28 ..... quartz standard from the National Institute of Standards and Technology, formerly known as the National Bureau of Standards (NBS)
NIST-19 ..... carbonate standard from the National Institute of Standards and Technology
PDB ..... Pee Dee Belemnite
PS1772-8$_{bsis}$ ..... a marine diatom standard
SEM ..... Scanning Electron Microscope
V-PDB ..... Vienna Pee Dee Belemnite
V-SMOW ..... Vienna Standard Mean Ocean Water
XRF ..... X-Ray Fluorescence (spectrometry)

Climate intervals, structures and (paleo-)climatic/-oceanographic terms

AABW ..... Antarctic Bottom Water
AC ..... Alaska Current
ACC ..... Alaskan Coastal Current
AG ..... Alaskan Gyre
AMOC ..... Atlantic Meridional Overturning Circulation
AS ..... Alaskan Stream
B/A ..... Bølling/Allerød
BP ..... Before Present
CC ..... California Current

CDW ..... Circumpolar Deep Water
CIS ..... Cordilleran Ice Sheet
D-O ..... Dansgaard-Oeschger
EDC ..... EPICA Dome C
EKG ..... East Kamchatka Current
GICC05 ..... Greenland Ice Core Chronology 2005
H ..... Heinrich Event
HNLC ..... High Nutrient-Low Chlorophyll
HS ..... Heinrich Stadial
IRD ..... Ice-Rafted Debris
LGM ..... Last Glacial Maximum
LIS ..... Laurentide Ice Sheet
LSR ..... Linear Sedimentation Rate
MAR ..... Mass Accumulation Rate
MIS ..... Marine Isotope Stage
MWP ..... Meltwater Pulse
NADW ..... North Atlantic Deep Water
NPIW ..... North Pacific Intermediate Water
OC ..... Oyashio Current
OF ..... Oberflächenwasser
SoO ..... Sea of Okhotsk
SST ..... Sea Surface Temperature
SSS ..... Sea Surface Salinity
WAIS ..... West Antarctic Ice Sheet
WSG ..... Western Subarctic Gyre
YD ..... Younger Dryas

Definitions related to isotope studies
$\delta^{13}C_{Nps}$ ..... *Neogloboquadrina pachyderma*$_{sin}$ $\delta^{13}C$
$\delta^{15}N_{diat}$ ..... diatom $\delta^{15}N$
$\delta^{18}O_{cont}$ ..... $\delta^{18}O$ of non-biogenic silica contamination
$\delta^{18}O_{diat}$ ..... diatom $\delta^{18}O$
$\delta^{18}O_{GIV}$ ..... glacial ice-volume $\delta^{18}O$
$\delta^{18}O_{model}$ ..... mass-balance corrected diatom $\delta^{18}O$
$\delta^{18}O_{Nps}$ ..... *Neogloboquadrina pachyderma*$_{sin}$ $\delta^{18}O$
$\delta^{18}O_{sw}$ ..... seawater $\delta^{18}O$
$\delta^{30}Si_{cont}$ ..... $\delta^{30}Si$ of non-biogenic silica contamination
$\delta^{30}Si_{diat}$ ..... diatom $\delta^{30}Si$
$\delta^{30}Si_{model}$ ..... mass-balance corrected diatom $\delta^{30}Si$
%cont ..... remaining percentage of contamination in a purified diatom sample
n ..... number of isotopic measurements
SD ..... Standard Deviation

Other
MIROC ..... Model for Interdisciplinary Research on Climate
NE ..... North-East
NW ..... North-West
W-E ..... West-East
r.sp. ..... resting spores

A.3 – List of figures

A.4 – List of tables